

Technical University of Munich
TUM School of Engineering and Design

Investigation of Bubble Collapse and Metal Droplet Breakup by Shock Tube Experiments

Thomas Hopfes

Vollständiger Abdruck der von der TUM School of Engineering and Design der Technischen Universität München zur Erlangung eines

Doktors der Ingenieurwissenschaften (Dr.-Ing.)

genehmigten Dissertation.

Vorsitz: Prof. Dr. Peter Mayr

Prüfer*innen der Dissertation:

1. Prof. Dr.-Ing. Nikolaus A. Adams
2. Prof. Dr. Hans G. Hornung

Die Dissertation wurde am 09.12.2021 bei der Technischen Universität München eingereicht und durch die TUM School of Engineering and Design am 03.05.2022 angenommen.

Declaration of authorship

I hereby declare that except where specific reference is made to the work of others, the contents of this dissertation are original and have not been submitted in whole or in part for consideration for any other degree or qualification in this, or any other university. This dissertation is my own work and contains nothing which is the outcome of work done in collaboration with others, except as specified in the text and acknowledgements.

Thomas Hopfes
December 6, 2021

© Thomas Hopfes, 2021
thomas.hopfes@tum.de

All rights reserved. No part of this publication may be reproduced, modified, re-written, or distributed in any form or by any means, without the prior written permission of the author.

Released December 6, 2021
Typesetting **L^AT_EX**

Acknowledgement

I truly enjoyed working on my thesis over the last four years. Conducting experiments was always at the center of it, but I learned equally much by supervising students, by lecturing and teaching, by discussing with colleagues, and by investigating new topics. I truly appreciate the great opportunity I had, and the wide freedom in choosing interesting research topics.

For this, I want to thank first of all my supervisor Prof. Adams. Thank you for your trust and support. I feel grateful for your feedback on my research work, be it in the weekly meeting or when finishing paper manuscripts. You always took your time when questions came up and helped to provide the necessary perspective. I also want to thank Prof. Hornung for offering to be my second examiner and for welcoming us in Pasadena. I'm grateful for all the interesting talks that provided me with great insight into shock tubes and shock waves.

I am very fortunate to have had a great team in Marcus Giglmaier and Zhaoguang Wang that made work fun and interesting, and that pushed me onwards when needed. Thank you, Marcus, for your support, for your guidance, especially at the beginning, and the good times spent together in the office, and in the evenings. Thank you, Wang, for all the hours we spent working in the lab, coding, discussing results, or planning the next steps. I could not imagine the last years without your almost daily company. Special thanks are extended to Steffen Schmidt. You brought me into this many years ago with your great lecture on gas dynamics. Thank you for valuable feedback on my research work, as well as for the discussions and talks in the office, during coffee breaks, or during dinners at Mimo's. I also want to thank Jingyu, it was a pleasure getting to know you and I wish you the best for the rest of your PhD.

The experimental work would not have been possible without the support of Wolfgang Lützenburg, Martin Banzer, and Luigi Findanno. You found the best solutions for our ideas and helped develop the shock tube facility in many ways. Thank you for your efforts and for always welcoming me downstairs. Further, I want to thank Angela Grygier and Hua Liu for their helpful hands in the organizational work, be it with contract extensions, management of lectures and rooms, or the delivery of our orders. Many thanks to all the colleagues I worked with over the years. The times together at conferences, during lunch or coffee breaks, or during chats in the office were an ideal balance to the work. In addition, talking with you was a great way to learn about other research topics and different approaches, which has given me valuable experiences and has widened my view. A special shout-out goes to the ACFD team for the good mood and teamwork even during long correction hours in summer.

Lastly, I want to thank my family and friends. Thank you for all the great times spent together, all the fun and the fantastic memories from the last years. I'm very grateful for the unconditional love and support I received on my journey and for the trust that I would find my way. I want to especially thank my parents and my sister with her family. You brought me tremendous joy, support, and balance over the years, and this is a big reason why I'm here today. Many thanks to you, Sonia, for believing in me, pushing me, and trusting in me. Whether it was from far or from close, you were always beside me. I'm looking forward to our future together.

Garching b. München, December 6, 2021

Thomas Hopfes

Abstract

This thesis investigates two multiphase flow phenomena experimentally: the collapse of gas bubbles in a liquid surrounding and the breakup of liquid metal droplets in a gas flow. Both topics are defined by the interaction of a gaseous and a liquid phase, and both topics are studied using the shock tube facility at the Chair of Aerodynamics and Fluid Mechanics at the Technical University of Munich. This shock tube facility and related experimental methods are introduced in this thesis along with a summary of background and literature of the two topics. In addition, the results of the experimental investigations are presented by including three first-author publications, which have been published in international, peer-reviewed journals. They constitute this publication-based thesis.

The first publication investigates the collapse of gas bubbles in a gelatinous, water-like liquid. A novel experimental setup is used that exploits the capability of the shock tube to generate an instantaneous pressure rise through shock wave impact and reflection. The bubbles react to the high-pressure surrounding by contracting and deforming. Image recordings and data processing show that the collapse of the bubbles is not significantly influenced by the gelatin, even when changing the gelatin strength. Reference calculations with the Rayleigh-Plesset equation highlight that the collapse in gelatin is comparable to a collapse in water. In addition to single bubble collapse, also the interaction of collapsing bubble pairs is investigated. Four types of bubble interactions are observed that depend on the size ratio of the bubbles and the normalized bubble distance. Some types show aspherical collapse features and develop liquid jets. Such jets can be used as transport or destruction mechanisms and thus are of interest for example in microfluidics or in medical applications.

The second and third publications investigate the breakup of single liquid metal droplets in a high-speed gas flow. This process plays an essential role for a variety of applications ranging from spray forming to metal powder production. Nevertheless, data on the influence of the specific properties of metals on the breakup remain rare. Therefore, the shock tube is used to study this topic. A well-defined, constant free stream flow is generated over a wide range of conditions and interacts with single droplets of Galinstan and Field's metal - two metals with low melting points that are apt to form surface oxide layers. Using image sequences and deformation data, it is shown that metal droplet breakup has the same breakup modes as other liquids. The transition between the modes is a continuous process with gradual changes that is in accordance with the concept of the Rayleigh-Taylor instability. However, metal droplets also show characteristic differences like an earlier breakup, a different rupture mechanism that is reminiscent of solid mechanics, and larger, irregularly-shaped fragments. These aspects clearly distinguish the breakup of metal droplets from that of common, water-like liquids. The reason for the differences is found in the surface oxidation. To generalize the observations, breakup data of the two metals are summarized in Weber number dependent fits of droplet deformation and breakup timing. In addition, a time-dependent fit of the cross-stream deformation is provided. The data fits can be used directly, for example in numerical simulations, or help adapt breakup models to account for the influence of the oxide layer. Lastly, the fits can represent other oxide-forming metals like aluminum, where no breakup data are currently available.

Contents

Declaration of authorship	iii
Acknowledgement	v
Abstract	vii
Contents	x
Acronyms	xi
Nomenclature	xiii
1 Introduction and background	1
1.1 Overview	1
1.2 Shock tube theory	3
1.3 Bubble collapse	6
1.3.1 Background	6
1.3.2 Bubble pair interaction	6
1.3.3 Methods of investigation	7
1.4 Droplet breakup	8
1.4.1 Background	8
1.4.2 Non-dimensional parameters	8
1.4.3 Breakup modes	9
1.4.4 Physical mechanisms	11
1.4.5 Metal droplet breakup	12
2 Experimental methods	13
2.1 Shock tube facility	13
2.1.1 Diaphragm clamping and rupture	13
2.1.2 Measurement equipment and control system	15
2.1.3 Test section	15
2.1.4 Visualization	16
2.2 Bubble collapse in gelatinous fluids	17
2.2.1 Experimental setup and procedure	17
2.2.2 Data processing	19
2.3 Droplet breakup of liquid metals	20
2.3.1 Experimental setup and procedure	20
2.3.2 Data processing	22
3 Summary of the publications	27
3.1 Collapse dynamics of bubble pairs in gelatinous fluids	27
3.1.1 Summary of the publication	27

3.1.2	Individual contributions of the candidate	28
3.2	Secondary atomization of liquid metal droplets at moderate Weber numbers .	29
3.2.1	Summary of the publication	29
3.2.2	Individual contributions of the candidate	30
3.3	Experimental investigation of droplet breakup of oxide-forming liquid metals .	31
3.3.1	Summary of the publication	31
3.3.2	Individual contributions of the candidate	32
4	List of peer-reviewed journal articles	33
5	Discussion	35
A	Original peer-reviewed publications	39
A.1	Collapse dynamics of bubble pairs in gelatinous fluids	41
A.2	Secondary Atomization of Liquid Metal Droplets at Moderate Weber Numbers	55
A.3	Experimental investigation of droplet breakup of oxide-forming liquid metals .	73
B	Copyright permissions for reproduced material	93
	Bibliography	97

Acronyms

AER	Chair of Aerodynamics and Fluid Mechanics
CC	cookie-cutter
FM	Field's metal
fps	frames per second
KHI	Kelvin-Helmholtz instability
RP	Rayleigh-Plesset
RTI	Rayleigh Taylor instability
SIE	shear induced entrainment
TAB	Taylor analogy breakup
TUM	Technical University of Munich
1D	one-dimensional

Nomenclature

Greek letters

$\Delta\Theta$	Phase difference
ϵ	Density ratio between liquid and gas
γ	Normalized bubble distance
κ	Ratio of specific heats
μ	Dynamic viscosity
ρ	Density
τ	Non-dimensional time

Roman letters

Δd	Diameter inaccuracy
ΔR	Radius inaccuracy
Δt	Time difference or temporal inaccuracy
Δx	Distance
A	Area
a	Speed of sound
d	Diameter
M	Mach number
n	Refractive index
Oh	Ohnesorge number
p	Pressure
R	Radius
Re	Reynolds number
S	Size ratio of bubble pairs
T	Temperature
t	Time

u	Velocity
We	Weber number
x	Position or location

Super- and subscripts

'	Conditions after shock reflection
''	Conditions after the reflection of the compression wave
$\ddot{\square}$	Second time derivative
$\dot{\square}$	First time derivative
$_0$	Initial condition; used, for example for the initial droplet diameter d_0
$_1$	Condition in the driven section of the shock tube
$_2$	Condition after shock passage through the driven gas in the shock tube
$_3$	Condition after expansion of the driver gas in the shock tube
$_4$	Condition in the driver section of the shock tube
$_\infty$	Freestream Mach number M_∞ , or farfield pressure p_∞
$_b$	Onset of breakup
$_{crit}$	Critical value
$_c$	Cross-stream value, used to describe the cross-stream diameter d_c
$_{FM}$	Value for Field's metal
$_{Gal}$	Value for Galinstan
$_g$	Gas phase
$_{ini}$	Initial deformation
$_L$	Large; used to describe the radius of the larger bubble for bubble pairs
$_l$	Liquid phase
$_{max}$	Maximum value; used to describe the maximum cross-stream diameter $d_{c,max}$
$_{mc}$	Mass center
$_r$	Conditions related to the reflected shock wave
$_S$	Small; used to describe the radius of the smaller bubble for bubble pairs
$_s$	Conditions related to the incident shock wave
$_v$	Vapor; used to describe the vapor pressure p_v
$_x$	Value in x-direction; used to describe the streamwise diameter d_x

Chapter 1

Introduction and background

The work presented in this thesis is based on experiments that were conducted using the shock tube facility at the Chair of Aerodynamics and Fluid Mechanics (AER) at the Technical University of Munich (TUM). Shock tubes are experimental facilities that are ideally suited to study different flow phenomena due to the unique features of the generated shock waves. Studies on shock waves have a long history and many related works are available in the literature. A selection of topics and representative references includes investigations on producing stronger shocks [145, 161], on shock reflection, e.g. in [14, 62, 69, 70], on shock interaction with boundary layers or gas inhomogeneities, e.g. in [38, 118] and [55], respectively, and on wave propagation in gas-liquid mixtures, e.g. in [16, 99]. Shock waves also provide a step-change in fluid properties like pressure, density, and temperature, and they induce a sudden change in flow velocity. This discontinuity can be exploited to achieve very defined and controlled experimental conditions that drive key findings in experimental fluid mechanics. The sudden change to high temperatures can for example be used to study relaxation times of heated gases [18, 86], reaction kinetics [50, 109], or flame propagation [124]. Following the shock wave is a region of uniform flow [19, 49] that can be used to study a variety of flow phenomena, for example the transonic flow around airfoils [34] or the determination of drag coefficients in transient flows [75].

This doctoral thesis exploits the features of shock tube to study two multiphase flow phenomena experimentally: bubble collapse and droplet breakup of liquid metals. Both topics are defined by the interaction of a gaseous and a liquid phase. For bubble collapse the focus lies on the gas phase, which is surrounded by a liquid phase that is at a shock-induced, high pressure. For droplet breakup, the phases are reversed and the focus lies on the liquid phase, which is affected by a shock-induced, surrounding gas flow. Both investigations build on previous work in the literature but also show novelties in the experimental methods and in the observation of physical mechanisms. It is the purpose of this thesis to introduce the work and present the obtained results in a complete and insightful manner.

1.1 Overview

This doctoral thesis is composed of three first-author publications in international, peer-reviewed journals. As noted, the publications present results of experimental work on multiphase flow phenomena that are investigated at the shock tube facility at AER.

The first publication studies gas bubbles which are positioned in a gelatinous, water-like liquid. The mixture is exposed to a high pressure by means of shock impact and reflection, which in turn drives the dynamic response of the bubbles. We study how bubbles react to the change in pressure by contracting and deforming, analyze the influence of the properties of the gelatin on the deformation, and study the interaction of bubble pairs. If two bubbles are placed next to each other they interact depending on the size ratio and distance and

show distinct collapse features. An example showing the interaction of two differently sized bubbles in close proximity is presented in fig. 1.1. Especially the aspherical collapse behavior with the development of a liquid jet is of interest for applications ranging from microfluidics to the medical field. An introduction into the topic is presented in section 1.3, while the problem-specific experimental methods are presented in section 2.2. Further details of the work can be found in the corresponding publication [68]

- **Thomas Hopfes**, Zhaoguang Wang, Marcus Giglmaier, and Nikolaus A. Adams: "Collapse dynamics of bubble pairs in gelatinous fluids". In: *Experimental Thermal and Fluid Science* 108 (2019), p.104-114. [68]

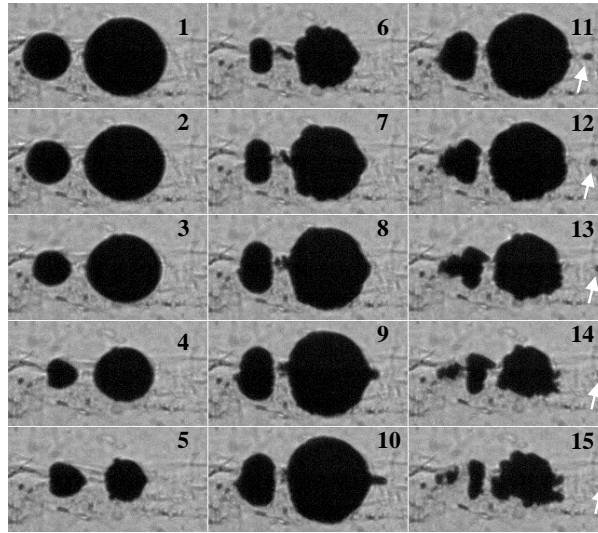


Figure 1.1: Collapse and interaction of two gas bubbles in a gelatinous surrounding exposed to a shock-induced rise in pressure. The interframe time is $16\mu\text{s}$, and white arrows highlight the detachment of a small bubble due to aspherical collapse and jet formation. The image series is taken from [68].

The second and third publications take advantage of the well-defined, shock-induced, constant freestream flow that can be generated in the shock tube for a wide range of conditions. Both studies investigate how the gas flow behind the shock interacts with liquid metal droplets, and how the aerodynamic force of the flow deforms the drops and breaks them into fragments.

The first publication on metal droplet breakup focuses on the characteristic features that distinguish the breakup of liquid metal droplets from that of water droplets or similar common liquids. Therefore, the breakup of metal Galinstan droplets is presented for a wide range of flow conditions. Results show the typical breakup modes that are also observed for other liquids and the continuous transition between the modes is discussed in detail. Then, we compare the Galinstan data to water experiments qualitatively, using image series, and quantitatively, using representative breakup parameters. Results show an earlier breakup for metal droplets, a different breakup mechanism that is reminiscent of solid mechanics, and larger, irregularly-shaped fragments. We conclude that the reactive surface oxidation of the liquid metal plays an essential role in causing the observed differences. An example for rupturing Galinstan and water droplets at similar non-dimensional flow conditions is shown in figure 1.2. An introduction into the topic of droplet breakup is presented in section 1.4, while the problem-specific experimental methods are presented in section 2.3. Further details of the work can be found in the corresponding publication [65]

- **Thomas Hopfes**, Julia Petersen, Zhaoguang Wang, Marcus Giglmaier, and Nikolaus A.

Adams: "Secondary Atomization of Liquid Metal Droplets at Moderate Weber Numbers". In: *International Journal of Multiphase Flow* 143 (2021) 103723.

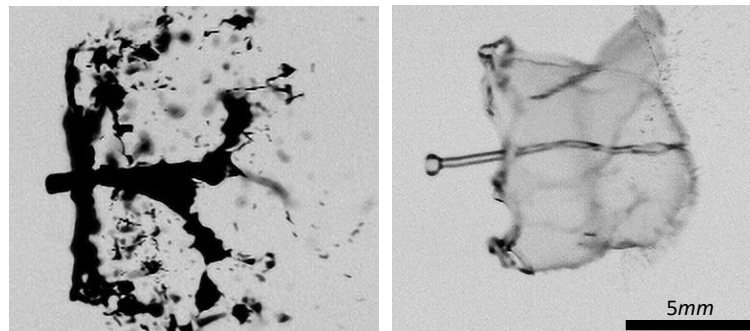


Figure 1.2: Fragmenting Galinstan metal drop (left) and water drop (right). Flow is from left to right in both images. A bar shows a reference length of 5mm.

The second publication on metal droplet breakup expands previous data by studying the breakup of Field's metal (FM) droplets. FM droplets melt at a higher temperature, and show slight differences in details of the breakup that are expected to be related to a different oxidation rate. For example, they break into a larger number of smaller fragments. However, in general the similarities in breakup behavior to Galinstan droplets are high. Thus, we summarize the collective breakup data and provide Weber number dependent fits that describe the droplet deformation and the timing of the breakup. In addition, a time-dependent empirical fit of the droplet cross-stream deformation is derived and evaluated against models from the literature. The fits represent the data accurately and can be used directly, for example in numerical simulations. In addition, we propose that they also represent other oxide-forming metals like aluminum. Further details of the work are presented in the corresponding publication [66]

- **Thomas Hopfes**, Zhaoguang Wang, Marcus Giglmaier, and Nikolaus A. Adams: "Experimental investigation of droplet breakup of oxide-forming liquid metals". In: *Physics of Fluids* 33 (2021), 102114.

In addition to presenting the publications in appendix A, this thesis features several additional sections. The following section 1.2 introduces the theory of shock tubes, while sections 1.3 and 1.4 summarize background, theory, and literature for droplet breakup and bubble collapse, respectively. A detailed overview of the shock tube facility is presented in section 2.1, while sections 2.2 and 2.3 discuss the problem-specific setups and methods of investigation for experiments on bubble collapse and droplet breakup. A summary of the publications is presented in chapter 3 along with a list of the publications in chapter 4. To conclude the thesis, the collective work is discussed with respect to the literature and main findings in chapter 5.

1.2 Shock tube theory

A sketch of a simplified shock tube is presented in fig. 1.3 (a). As shown, a shock tube consists of two main tube parts: a driver section, and a driven section. Initially, at time $t < 0$, the two sections are separated by a diaphragm and can feature different initial conditions, such as different pressures, temperatures, or gas contents. In this work, only experiments using

air at surrounding temperature are presented. In addition, the pressure in the driven section is kept at atmospheric level for all experiments, while the pressure in the driver section is increased to higher values. This simplification is included in the following considerations. The initial conditions before diaphragm rupture in the driver and driven section are labeled as regions ④ and ①, respectively. A graph for the pressure and velocity distribution in the two parts is presented below the sketch. Subscripts for the variables are associated with the region number.

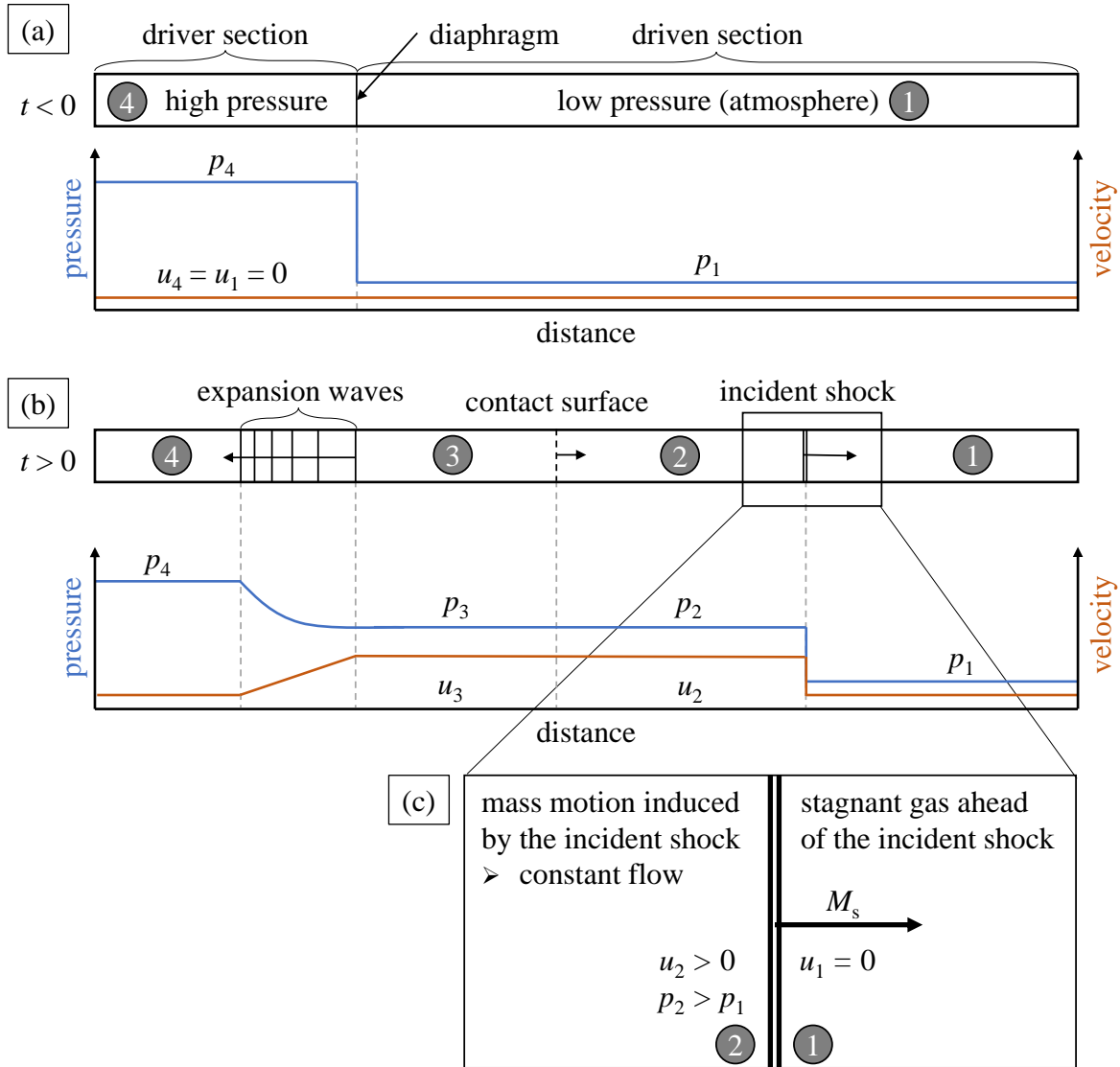


Figure 1.3: Simplified sketch of a shock tube.

A shock tube experiment starts when the diaphragm breaks and wave motions are initiated. Figure 1.3 (b) shows a time instant $t > 0$ sometime after the diaphragm rupture. Starting from the position of the ruptured diaphragm, an incident shock wave travels towards the right side of the tube, and a fan of expansion waves to the left. Thus, we now distinguish four separate regions of different flow conditions. Regions ④ and ① still represent the initial conditions, while the region behind the shock is labeled as region ②, and the region right of the expansion waves as region ③. As shown in the corresponding graph, the expansions accelerate the gas from the driver section, while continuously lowering temperature, pressure, and density. Important for this work are, however, the changes induced by the

shock wave. A detailed view of it is presented in fig. 1.3 (c). It shows the stagnant gas ahead of the shock wave which travels at shock Mach number M_s . The shock wave is a natural step function that leads to a step change in pressure ($p_2 > p_1$), and induces a mass motion of velocity u_2 in the direction of the shock. This change of flow conditions is also presented in the graph in fig. 1.3 (b). A similar increase in temperature T and density ρ occurs, but is not displayed here. Regions ② and ③ are separated by a contact surface. It separates shocked gas of the driven section and expanded gas of the driver section. As shown in the graph, pressure and velocity are equal on both sides of the interface, but density and temperature vary.

Relevant for this work are two effects related to the shock wave, the stepwise increase in pressure and the induced freestream flow. Both changes can be calculated using moving shock relations [5]. Apart from the ratio of specific heats of the gas, κ , it is only required to know the conditions in front of the shock (p_1 , T_1 , or ρ_1) and the shock Mach number, M_s . The pressure increase over the shock wave can be calculated as

$$\frac{p_2}{p_1} = 1 + \frac{2\kappa}{\kappa + 1}(M_s^2 - 1). \quad (1.1)$$

The induced velocity over the shock wave is

$$u_2 = a_1 \frac{2M_s^2 - 2}{(\kappa + 1)M_s}. \quad (1.2)$$

Here, the speed of sound in the driven section, a_1 , can be calculated from initial conditions. The change in temperature and density over the shock wave can also be calculated, but is not further discussed here. Details can be found, for example, in the book of Anderson [5].

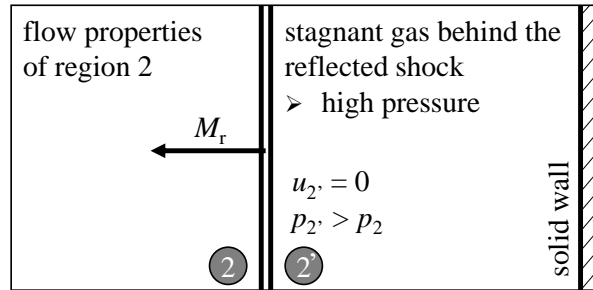


Figure 1.4: Shock reflection at a solid wall.

When the shock wave hits a solid wall, for example at the end of the tube, the shock is reflected. The strength of this reflected shock is such that the induced mass motion with velocity u_2 is stopped and that the boundary condition of zero wall-normal velocity is fulfilled. A sketch of a time instant shortly after the shock reflection is sketched in fig. 1.4. The fluid flow is stopped, but a high-pressure region of stagnant gas results. For an ideal reflection at the boundary, the reflected shock Mach number M_r can be calculated as [5]

$$\frac{M_r}{M_r^2 - 1} = \frac{M_s}{M_s^2 - 1} \sqrt{1 + \frac{2(\kappa - 1)}{(\kappa + 1)^2}(M_s^2 - 1) \left(\kappa + \frac{1}{M_s^2} \right)}. \quad (1.3)$$

Fluid properties in region ② behind the reflected shock wave, for example the pressure, can be calculated with the moving shock relations shown for the pressure in eq. (1.1) by using p_2 and the calculated M_r as input values.

1.3 Bubble collapse

1.3.1 Background

Studying bubble dynamics is subject to a long history in fluid mechanics and goes back to the work of Rayleigh [143] in 1917 who is considered the first to theoretically analyze cavitation bubbles. Ever since, the topic has been investigated by many researchers. For some applications, the collapse of spherical bubbles is interesting. In targeted drug delivery, coated microbubbles are excited by ultrasound fields to break apart and release the drug at the target location [93, 104, 132]. In addition, high temperatures and pressures are encountered inside collapsing bubbles [20, 39, 151], which can be used in sonochemistry and is even considered in relation to thermonuclear fusion [104].

However, most applications relate to bubbles that show aspherical collapse behavior. Bubbles collapse aspherically when they are next to interfaces such as solid walls or free surfaces [15, 128, 137], when they are subject to strong shock loading [132, 136], or when they are subject to external force fields such as gravity [15, 130]. In all cases, the reason is a non-uniform pressure field in the surrounding liquid. In the case of a bubble collapse next to a solid wall, the collapse is directed towards the wall. The bubble side close to the wall does not move significantly, while the opposite side shows a hollow that rapidly develops into a liquid jet with increasing velocity towards the wall. This jet enters the bubble and often drives through it to strike the opposite bubble side or the solid wall. Its impact causes high pressure, can emit strong shock waves, and has a strong damage potential that can cause erosion even on the surface of hard materials [46, 139]. This is a problem, for example for rotating ship propellers where the violent collapse of cavitation bubbles can lead to surface erosion [104]. It is often tried to avoid such adverse effects, but the potential of the bubble collapse can also be exploited for beneficial effects in microfluidics [41, 107, 185], ultrasound cleaning [119], or medical applications [93, 104, 121]. For example, extracorporeal shock wave lithotripsy [27, 33] is a non-invasive medical procedure where shock waves are focused on urinary stones or gallstones in the human body. The shock waves and the collapse of cavitation bubbles near the target area disintegrate the stones. Remaining pieces can then be removed naturally by the body.

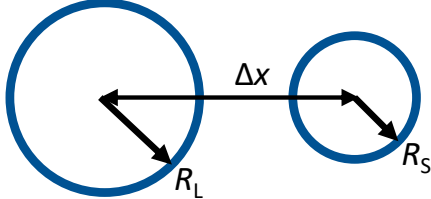
1.3.2 Bubble pair interaction

Bubbles often appear in clouds or clusters in many practical applications. Therefore, the effect of bubble interaction needs to be considered. The simplest type of interaction - that of two bubbles - is investigated in the literature by many researchers [29, 35, 45, 57, 91, 103, 113, 116, 159, 177]. The works show that bubble pairs have different types of interactions like collapsing towards each other or away from each other. In addition, bubbles modify the surrounding pressure and screen each other [23]. To describe and predict the behavior and the interaction type, important non-dimensional parameters are the normalized bubble distance, γ , and the size ratio of the two bubbles, S . The definition of the parameters along with a sketch is presented in table 1.1. Note that R_L constitutes the radius of the larger of the two bubbles, and R_S that of the smaller one. A third parameter is often considered to account for inception time differences of the bubbles. It is formulated as a relative initiation time [57] or a phase difference, $\Delta\Theta$ [29, 45]. For this work, the phase difference is used in a modified form to describe gas bubbles that are initially at rest. It can be reduced to a form solely depending on the initial bubble size ratio as shown in table 1.1.

Ultimately, the idea is to extrapolate from bubble pair interaction to larger clusters and

bubble clouds. Such clusters are investigated experimentally [22, 23] and numerically [142, 157], but the complex, large-scale interactions are difficult to analyze and generalize. Thus, additional work on multi-bubble arrangements is required.

Table 1.1: Non-dimensional parameters describing the interaction of bubble pairs. The phase difference is modified from literature for the experimental setup in this work [68].

Normalized bubble distance	$\gamma = \Delta x / (R_L + R_S)$	
Size ratio	$S = R_L / R_S$	
Phase difference	$\Delta\theta = 1 - 1/S$	

1.3.3 Methods of investigation

Due to the interesting effects and the relevant applications, bubble collapse is studied extensively in the literature. While numerical investigations provide great insight [12, 81, 89, 94, 131, 142, 146, 162–164], the summary in this work focuses on experimental investigations.

There are several established methods to investigate bubble collapse experimentally. The most common method is to focus a laser into a liquid and trigger optical breakdown [57, 102, 103, 116, 130, 137, 159, 177]. The focused laser creates a plasma region that expands and grows into a bubble. The dynamic behavior of the bubble during the ensuing collapse can then be investigated. This setup has the advantage of providing high temporal and spatial independence, repeatability, and perfectly spherical bubble shapes. However, the initial state in the plasma cannot easily be assessed, the gas content cannot be changed, and the initial growth of the bubble can affect the surrounding pressure and flow field. Hence, these experiments are suitable only to a limited extent for numerical test cases.

Spark generation is a related method, where instead of the laser, a high voltage is discharged in the liquid at the point of two connecting wires. Again, plasma forms and expands into a bubble. The method is applied in slightly different variations by many researchers [45, 107, 116, 128, 158, 181]. It provides similar advantages and disadvantages as the method of laser-production, but additional advantages are that it can be operated at lower costs and that it allows production of larger bubbles. On the other hand, another disadvantage is that the electrodes remain in the flow field and can affect the bubble collapse.

There are investigations that target air and gas bubbles. However, to initiate a collapse, the bubbles are often exposed to strong pressure pulses. These pulses are generated by laser focussing [92], spark discharge [158, 160], lithotrippers [132, 136], or explosive pellets [91]. Peak pressures of up to 100MPa can be achieved for a very short time, but the pressure does not stay constant. An additional way to study other gases is to create bubbles from gas nuclei by controlled expansion [15, 22]. However, due to the expansion, the gas pressure in the bubble is low.

1.4 Droplet breakup

1.4.1 Background

Gas atomization processes play an important role in a variety of applications ranging from fuel injections to pharmaceutical applications [9, 144]. Regarding metal atomization, also the fields of spray coating and powder metallurgy are of increasing importance [9, 63, 166], while other applications like the printing of electronics are emerging [80, 180].

Atomization processes can be separated into two core mechanisms: primary and secondary atomization. Primary breakup describes the breakup of bulk liquid into ligaments and large drops due to surface instabilities that are induced, for example, by high-velocity, relative gas flows. Secondary breakup, or secondary atomization, ensues, and describes the breakup of single droplets by aerodynamic forces. It is well understood, that this second stage of the breakup defines the final fragment size distributions of atomization processes more than the first stage [44, 120, 165, 178], which highlights its importance for many applications. Studies of the full atomization process or of the two stages individually are numerous in the literature, but the focus of this work lies on secondary atomization.

Droplet breakup is investigated in the literature numerically [42, 58, 59, 77–79, 84, 85, 87, 122, 174], theoretically and in terms of modelling [76, 83, 97, 148, 150, 154, 167], and experimentally. Experimental studies are typically conducted either in shock tubes [17, 30, 37, 48, 64, 72–74, 82, 83, 141, 154–156, 172] or continuous wind tunnels [26, 77, 97, 105, 115, 133, 140, 175, 182–184]. Some setups also use falling drops accelerated by gravity [101, 117, 167]. Continuous wind tunnel experiments can be operated at a high experiment rate, but the droplet must pass the boundary flow of the free jet before entering defined flow conditions of the core jet. In contrast, shock tube experiments are more time-consuming and complex to set up. However, they are considered superior from a scientific perspective, due to the well-defined initial and boundary conditions [53]. In addition, the step-change in flow conditions makes the results more suitable to validate theoretical and numerical studies.

1.4.2 Non-dimensional parameters

Independent of the method of investigation, it is well-established that secondary atomization can be classified by a set of non-dimensional parameters. Two parameters, the Weber number (We) and the Ohnesorge number (Oh) are considered as having the most significant influence on the breakup morphology [53, 64, 72, 138]. The Weber number provides the ratio of the aerodynamic forces onto the droplet to the opposing surface tension forces. It is written as

$$We = \rho_g u^2 d_0 / \sigma. \quad (1.4)$$

The density and flow velocity of the freestream gas flow is expressed as ρ_g and u , respectively. The initial droplet diameter is expressed by d_0 , while σ represents the surface tension of the liquid. The Ohnesorge number relates the relative importance of liquid viscous forces to the surface tension forces and is written as

$$Oh = \mu_l / \sqrt{\rho_l d_0 \sigma}. \quad (1.5)$$

Here, μ_l and ρ_l represent the viscosity and the density of the liquid drop, respectively. For $Oh < 0.1$, numerous experiments have shown that the influence of the Ohnesorge number on the breakup morphology is negligible [53]. However, it can still affect details of the breakup. For example, Chou et al. [31] find that even below this threshold, higher Oh values cause longer ligaments during the breakup that lead to larger fragments.

Also other non-dimensional parameters can have an influence on the breakup behavior, but the effect typically remains small. Aalburg et al. [1] state that the effect of the freestream Reynolds number ($Re = \rho_g u d_0 / \mu_g$) on the breakup is negligible for $Re > 100$. Lee et al. [105] confirm that the breakup does not depend on the Reynolds number for their investigation at $Re = 990 - 8088$, as do Liu and Reitz [115] in their experimental investigation at $Re = 509 - 2488$. Guildenbecher et al. [53] conclude in their review of secondary atomization that droplet breakup is relatively independent of Re . Han and Tryggvason [58, 59] study droplet breakup at low density ratios of $\epsilon = 1.15$ and $\epsilon = 10$ numerically and observe a significant change in critical Weber number and breakup morphologies. However, this rather represents liquid-liquid systems. At the higher values found in liquid-gas systems, the density ratio has a negligible effect on droplet breakup when above a certain threshold. Aalburg et al. [1] determine a value of $\epsilon = \rho_l / \rho_g > 32$, while Jain et al. [78] propose $\epsilon > 150$. The freestream Mach number (M_∞) can also influence the breakup. When reaching transonic and supersonic flow conditions, changes in the morphology are observed [154, 169], as well as a delayed initial deformation time [174] and time of onset of breakup [169].

A summary of the non-dimensional parameters for experiments in this thesis is shown in table 1.2. The table shows that apart from the Weber number, all other considered parameters fall in ranges where they are not expected to influence the breakup behavior.

Table 1.2: Range of non-dimensional parameters for presented experiments.

Liquid	We	Oh	Re	ϵ	M_∞
Galinstan	11 – 104	< 0.001	$5.9 - 28.5 \cdot 10^3$	$4.0 - 4.7 \cdot 10^3$	0.19 – 0.35
Field's metal	10 – 78	< 0.008	$5.7 - 18.0 \cdot 10^3$	$4.7 - 5.8 \cdot 10^3$	0.14 – 0.33
Water	25 – 151	< 0.003	$3.4 - 9.6 \cdot 10^3$	$7.3 - 8.2 \cdot 10^2$	0.06 – 0.17

While the mentioned parameters define the flow properties or relate the two phases, a very important parameter is the temporal evolution. To enhance comparability between studies, the work of Ranger and Nicholls [141] introduces a non-dimensional time (τ) for droplet breakup. It follows the assumption of a constant acceleration of a spherical droplet and can be written as

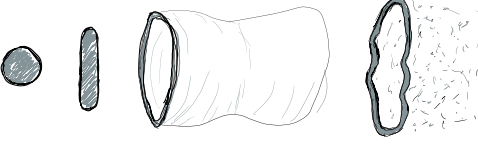
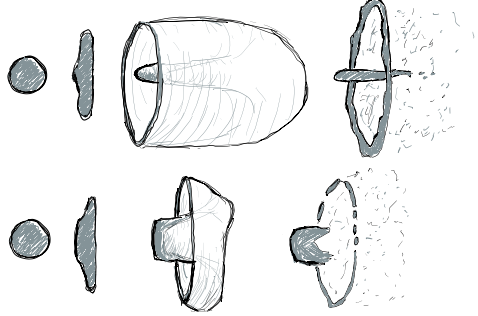

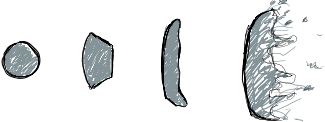
$$\tau = \frac{u}{d_0} \sqrt{\frac{\rho_g}{\rho_l}} t. \quad (1.6)$$

1.4.3 Breakup modes

Droplet fragmentation is characterized by different modes of breakup. The different modes are correlated to different ranges of the non-dimensional numbers. As discussed in the previous section 1.4.2, the classification can be reduced to be dependent solely on the Weber number for a wide range of conditions. An overview of the different breakup modes is presented in table 1.3. The table follows the typical sequence of bag, bag-and-stamen, multimode, and shear stripping breakup. Corresponding transition Weber numbers are adopted after Dai and Faeth [37] and Guildenbecher et al. [53] as $We \sim 15$, $We \sim 35$, and $We \sim 80$, respectively. However, depending on the literature, different values are found, and the names of the modes can vary [26, 31, 37, 73, 77, 78, 96, 138].

Table 1.3 also shows sketches of each mode that highlight representative and notable features. In the bag mode, the droplet first deforms into a flat disk before a hollow bag structure inflates in the downstream direction. This structure consists of a thicker toroidal

Table 1.3: Droplet breakup modes with Weber number range and sketch of the morphology of the deformation. Mode names and ranges are adopted from references [37, 53].

Mode	Range	Sketch
Bag	$We = 10 - 15$	
Bag-and-stamen	$We = 15 - 35$	
Multimode	$We = 35 - 80$	
Stripping	$We = 80+$	

rim (also called ring) at the upstream edge to which a thin sheet of liquid is attached that forms the bag [30]. The bag-and-stamen mode is related to the bag mode but develops an additional element in the stamen. The initial deformation remains similar to the bag mode, but a bulge on the disk can appear, especially at higher We . Surrounded by the inflating bag, this bulge develops into a cylindrical stamen that is parallel to the flow direction [78, 183]. With increasing Weber number, the stamen develops earlier, is thicker, and wider [26, 37, 182]. In contrast, the bag structure inflation is reduced [37, 65]. Two examples of the bag-and-stamen mode are presented in table 1.3 at lower and higher Weber number that highlight the mentioned changes throughout the regime. The multimode breakup regime is a transition regime that displays aspects of different breakup modes. With increasing We , the stamen becomes increasingly shorter and thicker until it is more appropriate to speak of a core droplet and sheets instead of a stamen and rim. During breakup, small bags form as multiple lobes on the sheets and break up continuously [77] in a more asymmetric and chaotic fashion than in the bag-and-stamen mode [26, 96]. After the inflation and rupture of multiple bags, only a core droplet is left. At lower We , this core droplet can break up again in a two-stage breakup process [138, 173] that Cao et al. [26] term dual-bag breakup mode. At higher We the core droplet is continuously eroded at the periphery similar to the stripping breakup. The stripping breakup is characterized by a thin peripheral sheet that develops around the droplet equator, bends downstream and decomposes into ligaments. As shown in table 1.3, micro fragments are stripped off directly at the droplet periphery and are entrained in the flow continuously. This process continues until the entire droplet is eroded [72].

The description of the breakup modes and the presented sketches highlight that the transi-

tion between the modes cannot be separated by a single value of We . Instead, it should rather be understood as a continuous process [53]. Aspects of different breakup modes overlap and show up more or less dominantly depending on the Weber number. This partly explains why the mode descriptions and transition values in the literature deviate between researchers.

1.4.4 Physical mechanisms

The physical mechanisms causing the different breakup modes are discussed controversially in the literature. Jackiw and Ashgriz [76] state that there are three main modelling approaches that provide insight into physical mechanism of droplet breakup: mass-spring-damper analogies, instability models, and internal flow models.

Mass-spring-damper models like the Taylor analogy breakup (TAB) model simplify droplet deformation to a one-dimensional (1D) problem where the surface tension acts as a spring and viscosity as a damper that interact with the aerodynamic forces of the gas flow. The TAB model was originally proposed by O'Rourke and Amsden [129], and has been developed and improved continuously. It is one of the most widely used droplet breakup models in numerical simulations [53, 178]. While it is performant in simulations, it is not a sophisticated model and typically not considered when focusing solely on secondary atomization.

Instability models are common approaches to describe single droplet breakup. Theofanous et al. [153–156] state two competing instabilities: the Rayleigh Taylor instability (RTI) and the Kelvin-Helmholtz instability (KHI). The RTI is the first criticality and affects breakup at low We [156]. Surface waves develop at the flattening windward side of the droplet, which leads to piercing of gas into the liquid mass and the inflation of bags. An increasing Weber number corresponds to a higher number of critical waves across the diameter. This explains the different breakup modes where the morphology changes from a single bag, to the development of the stamen at a wave peak of the instability [183], to the inflation of multiple bags [53, 154, 182]. The theory of the RTI is supported in the literature, e.g. in references [77, 78, 82, 83, 134, 182, 183].

For higher We , the breakup mechanism is discussed controversially. As mentioned, Theofanous et al. [153–156] consider that the KHI causes a second criticality and a breakup type termed shear induced entrainment (SIE). This second instability competes with the RTI in a transition range of $We = 100 - 1000$ but becomes dominant at higher We values. The mechanism of SIE starts with developing KHIs that lead to a peripheral sheet that is peeled off at the droplet equator due to viscous shearing. The sheet then breaks locally due to capillary effects. However, other authors propose other mechanisms to describe the breakup at higher Weber numbers. Ranger and Nicholls [141] suggest that the ambient shear flow induces a liquid boundary layer which becomes unstable and sheds fragments at the droplet periphery. This mechanism is typically termed 'shear stripping' and is adopted, for example, in references [31, 72–74, 96, 172]. Liu and Reitz [115] propose another alternative mechanism termed 'sheet-thinning'. Here, the inertia of the ambient flow causes sheets at the droplet periphery to deflect downstream. These sheets then break into ligaments and fragments. Guildenbecher et al. [53] conclude that the stripping breakup mode is an effect of 'sheet-thinning', and that the 'shear stripping' model is incorrect. This is further supported by numerical simulations of droplet breakup that observe the forming sheets and the independence from shear effects [42, 58, 79, 84, 87, 122]. However, the origin of the sheet and its rupture mechanism remain controversial.

A different approach to describe droplet breakup is presented by internal flow models. They model the flow that goes from the poles to the equator inside the droplet. At low We , the relatively high surface tension resists this flow which leads to the formation of the toroidal ring in bag breakup. At higher We , the surface tension is insufficient and the elongated rim

is carried away by the ambient flow and breaks [53]. This approach has led to several quantitative modeling efforts. For example, Villermaux and Bossa [167] solve the axisymmetric Euler equations for the 1D radial flow in a droplet by assuming a stagnation-point flow on its windward face. The solution is used to predict the droplet deformation and bag growth. Although it is the least studied model approach, it has found some traction recently [76, 97, 150].

1.4.5 Metal droplet breakup

Metal atomization is an important feature in a variety of emerging applications like spray forming, spray coating, or metal powder production for additive manufacturing [10, 51, 63, 100, 166]. Those applications rely on having metal melt or metal powder of well-controlled size and shape. However, poor quality remains an issue and leads to deficiencies in the final products, while low efficiencies in the processes lead to high costs [4]. To evolve the applications further, details of the atomization process need to be understood better by conducting more fundamental research [4].

Reference work on secondary atomization of liquid metals is often carried out in liquid-liquid systems. There are several experimental [32, 61, 95, 135], numerical [152], or analytical [61] studies. However, the findings in these works are not representative for the behavior in gas-liquid systems due to much lower density ratios (see section 1.4.2), different orders of magnitude in heat transfer, and different interface mechanisms like the generation of vapor bubbles [95].

With respect to metal droplet breakup in gas, there are single experiments available for mercury [72, 173], but the data are insufficient to draw conclusions. More recent works use Galinstan, an oxide-forming metal, to study metal column breakup in a cross-flow [8, 28], and some interesting phenomena can be observed. In general, Galinstan columns show breakup morphologies similar to that of water with similar breakup modes. However, breakup occurs earlier in non-dimensional time, and rupture occurs more violently with fracture lines that remind of solid mechanics. In addition, sharp-edged, non-spherical fragments appear after breakup. The authors attribute the differences to the oxide layer that Galinstan forms on the surface when in contact with oxygen [8, 28].

Despite these efforts, additional data on the breakup of metal droplets in gas are much needed. This thesis provides such data, investigates the different breakup behavior of oxide-forming metals, and generalizes the findings. The details of the experimental methods are presented in section 2.3, while the achievements are summarized in chapter 3 and attached in appendix A.

Chapter 2

Experimental methods

This section describes the experimental methods that are used in the three publications that constitute this doctoral thesis. The shock tube facility and key additional systems are presented along with a practical guideline to the shock tube operation in section 2.1. In addition, the problem-specific experimental setups and procedures for the two topics of this thesis are presented in sections 2.2 and 2.3, respectively.

2.1 Shock tube facility

Compared to the simplified considerations of section 1.2, the actual shock tube facility at AER consists of more than the two tube parts. A sketch of the facility that includes additional, connected systems is presented in figure 2.1, while table 2.1 provides an overview of the dimensions of the facility. Both the figure and table give an overview of additional systems, which are discussed individually in the following. The discussion includes systems to clamp and rupture diaphragms, to control valves and measurement equipment, and to visualize experiments. In addition, the design and setup of the test sections and the measurement of experiment conditions are key aspects of the operation.

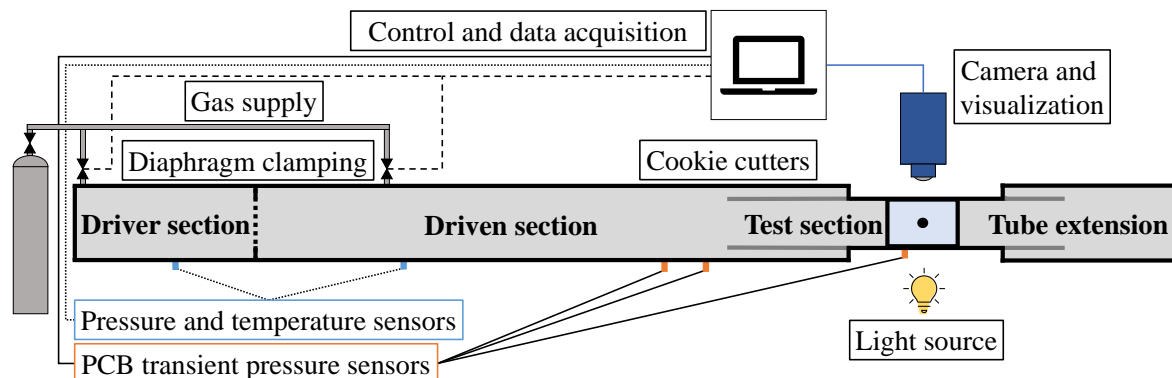


Figure 2.1: Sketch of the shock tube facility and connected systems.

2.1.1 Diaphragm clamping and rupture

A hydraulic system is installed to open and close the intersection between driver and driven sections. It allows to replace diaphragms in between experiments and clamps the tube parts together at up to 200bars during experiments. The cross-section of the clamping is square at $190 \times 190 \text{ mm}^2$. This reduced cross-section compared to the $d = 290 \text{ mm}$ round tubes is not

Table 2.1: Main tube parts and corresponding dimensions of the inner cross-section and length. The last column provides additional information.

Tube part	Cross-section	Length	Comment
Driver section	$d = 290\text{mm}$	3m	All main tube parts are made of 17mm -thick solid steel
Driven section	$d = 290\text{mm}$	19.5m	-
Tube extension	$d = 290\text{mm}$	1.5m	Replaced by solid end-wall for bubble collapse experiments
Diaphragm clamping	$190 \times 190\text{mm}^2$	-	Includes a hydraulic system
Cylindrical test section	$190 \times 190\text{mm}^2$	0.4m	$d = 100\text{mm}$ glass windows
Multi-purpose test section	$190 \times 190\text{mm}^2$	0.6m	$240 \times 190\text{mm}^2$ glass windows
Cookie-cutter upstream	$190 \times 190\text{mm}^2$	$0.4/0.8\text{m}$	$0.4/0.8\text{m}$ depending on experiments
Cookie-cutter downstream	$190 \times 190\text{mm}^2$	0.4m	sometimes not used, depending on experiments

ideal regarding the performance, but it facilitates operation and lessens the strain on the diaphragms.

For the shock tube at AER, several different options can be employed to break the diaphragms. One option, applied for aluminum diaphragms, is to use the pressure difference between the driver and driven section to press the diaphragms against an X-shaped blade, which is similar to other setups that use mechanical plungers [3, 13, 101, 154]. As an alternative, we use diaphragms that are scored in an X-shape. Due to the scoring, they break in a defined way without the need for a blade [71, 161]. The defined breaking in both methods helps to avoid that fragments detach from the diaphragms and damage the tube. Unscored diaphragms of 0.1mm and 0.5mm were used with the X-shaped blade and 1mm diaphragms scored between $0.4 - 0.6\text{mm}$ deep were used without blade for the experiments of the first publication. Depending on the thickness, pressure differences of up to 7bar were achieved. A disadvantage of this setup is that the time of diaphragm rupture cannot be controlled accurately. The pressure in the driver section is continuously increased until diaphragms rupture, which happens approximately at the same pressure differences. However, differences in blade sharpness, material properties or manufacturing inaccuracies lead to a variance that does not allow precise timing.

Another option overcomes the timing disadvantage by employing soft plastic membranes that are melted by heating wires. This is also a common method to break diaphragms [16, 72, 123]. For typical droplet breakup studies, mylar sheets of $0.05 - 0.15\text{mm}$, or 0.2mm PVC sheets are employed depending on the desired pressure ratios across driver and driven sections. Diaphragms are placed next to a pair of 0.1mm -thick, nichrome heating wires that are spanned in an X-shape across the rectangular cross-section. The wires are attached to a 55V power supply and are subject to an electric current of 3A when a trigger signal activates the apparatus. Due to the current, the wires heat up and melt the diaphragms locally, which then break in a controlled fashion. The time from signal to shock arrival in the test section depends on the applied diaphragm material and initial pressure difference between the sections, but it is highly repeatable for experiments under the same conditions. For a standard case of 0.1mm mylar diaphragms at 1bar pressure difference, the timing lies at approximately

100ms. Approximately half of the time is taken up by the diaphragm rupture, while the other half is required for the shock wave to travel to the test section. The high repeatability of the timing of this method ensures that the deformation of droplets can be captured in mid-flight.

2.1.2 Measurement equipment and control system

As highlighted earlier, the initial conditions are defining for the resulting experimental conditions. Therefore, several sensors are installed along the tube. To measure the pressure in the driver section, an absolute capacitance manometer by Setra (model 730) is used. In the driven section, an AccuSense high accuracy pressure transducer is installed, and the hydraulic pressure is monitored with a Compact OEM pressure transmitter by Gems (3100-3200 series). The temperature can be measured inside both tube parts with two Omega transition joint copper-constantan thermocouples (model TJ10-CPSS-IM15E). In addition, the surrounding pressure and temperature is measured by several sensors outside the tube for additional reference.

Data of the installed sensors are collected by a National Instruments cDAQ data acquisition system and several data points per second are saved continuously in a LabVIEW program. The program also serves to control experiments. It leads through all steps of an experiment with an interactive user interface. The program controls valve settings, fills the tube parts to desired pressure values, monitors acquired data to provide adequate updates or warnings, and documents the experiments. Details of the control system can be found in a term project report by Hopfes [67].

The actual bubble collapse or droplet breakup experiments take place in a time span of milliseconds, which exceeds the data frequency of the mentioned sensors. Therefore, several transient ICP® pressure sensors (model 113B21) by PCB Piezotronics are installed along the tube and in the test section. Their data are recorded by an LTT transient recorder and multi-functional data acquisition device, typically at a sample rate of 1 million samples per second. The transient recorder saves the data once the shock wave forms and a trigger value is exceeded in one of the pressure sensors. The trigger also serves to start the camera recordings of the experiments for which the setup is further discussed in the following section 2.1.4.

2.1.3 Test section

A notable difference to the theoretical shock tube is the designated area for the test section. It is placed at the end of the driven part of the shock tube and offers two different configurations for which the specifications are presented in table 2.1. In the first configuration, a thick-walled, cylindrical test section is used that it is closed with a solid end wall on the downstream side. This setup is used to conduct bubble collapse experiments. A second configuration allows to conduct experiments that require constant free stream flow. A multi-purpose test section is used and an additional extension tube after the test section is installed. This tube part provides sufficient space for the flow to continue after passing the test section. As the end wall of the tube is moved further downstream, the shock reflection is delayed and does not affect the flow conditions during experiments.

Another difference is indicated in table 2.1. In contrast to the round tubes, the test sections are of a rectangular cross-section of $190 \times 190 \text{ mm}^2$. This design follows pragmatic reasons, as a rectangular test section facilitates installation of experiment and measurement equipment and allows to install planar glass windows for optical access. However, a direct change of cross-section from tube to test section or test section to extension tube would lead to reflections of the incident shock wave, which in turn affects the constant flow conditions

of region ②. To avoid this, or rather to delay it, a so-called cookie-cutter (CC) is installed. It is a square steel frame of the same cross-section as the test section but features sharp-edged fronts. It cuts out the incident shock and the following freestream flow, thus providing a clean transition of the cross-section change. Effectively, it prolongs the square test section and helps to avoid unwanted wave reflections. The longer the CC, the longer do the flow conditions remain steady. Several options are available, a shorter version of $0.4m$ and a longer of $0.8m$. For bubble collapse experiments, the $0.4m$ version was used upstream of the test section. Apart from providing an ideal incident shock, it supported the gelatine in the test section. More details on this setup are provided in section 2.2. Early droplet breakup studies also used the $0.4m$ version upstream. However, installing the $0.8m$ CC upstream and the $0.4m$ CC downstream doubled the time of constant flow conditions. This is discussed further in section 2.3.2.

2.1.4 Visualization

A Shimadzu HyperVision HPV-X high speed camera is used to capture the experiments. It records 128 images at a resolution of 400×250 pixels at up to 5 million frames per second (fps). For the bubble collapse and droplet breakup experiments in this work, it was operated at a rate of 25 – 350kfps.

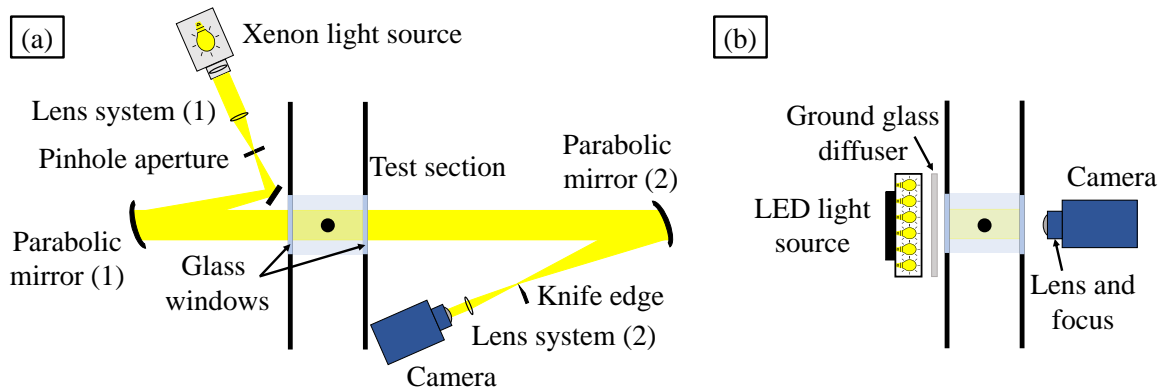


Figure 2.2: Z-type Schlieren and focused shadowgraph setup (a), and background light setup (b).

The camera is used in two optical configurations. The first is a Z-type Schlieren system for which a sketch is shown in fig. 2.2 (a). It consists of a 150W Xenon lamp, and a set of lenses and mirrors. The parallel light from the light source is focused by a first lens on a pinhole aperture, which is positioned in the focal point of an aluminum-coated parabolic mirror of $26cm$ diameter and $2.5m$ focal length. Due to limited space in the experimental hall, the light path is redirected by a planar mirror in between. A parallel light beam is reflected at the first parabolic mirror, passes through the test section, and hits the second parabolic mirror. This mirror focuses the parallel light beam onto the second focal point, in which a knife edge can be positioned to cut a part of the light. The light beam after the focal point passes through additional lenses which focus a sharp image of the observed objects on the focal plane of the camera.

Schlieren objects in the test section cause refractive differences and bend the light rays, which are partially cut at the knife edge. This causes areas of different illumination on the final image which correlate with the first spatial derivative of the refractive index $\partial n / \partial x$. The refractive index can be correlated directly to the density in the case of gases and liquids. Thus, the Schlieren setup can visualize the density gradient of the flow, which is especially

useful to visualize shock waves. If no light is cut, a focused shadowgraph setup results, which visualizes the second spatial derivative of the refractive index $\partial^2 n / \partial^2 x$. This latter setup is applied for most of the experiments presented in this thesis. Shocks are still visualized in the focused shadowgraph, and the setup produces a sharp and accurate image of the target of the observation. [149]

A second optical setup is shown in fig. 2.2 (b). It consists of a LED light panel and a ground glass diffuser that illuminate the test section with a uniform background light. The camera is positioned on the other side of the test section perpendicular to the flow direction. An Irix Dragonfly macro lens is mounted on the camera and used to focus on the plane of interest. This background light setup was only used for some experiments investigating droplet breakup. It captures sharp images at a good resolution but does not visualize the shock wave and flow field.

2.2 Bubble collapse in gelatinous fluids

For the bubble collapse experiments in this thesis, a novel experimental approach was employed that can be distinguished from experiment setups that were highlighted in section 1.3.3. The new approach relies on two main aspects: a planar shock wave to provide an instantaneous pressure jump, and a gelatinous mixture as a water-like carrier medium for gas bubbles. Combining the two aspects expands the methodology in bubble dynamics research although both aspects – using shock tube facilities and producing bubbles in gelatin – have been used individually in previous studies (e.g. in [47, 168] and [20, 39, 151], respectively). The combination of both aspects allows to investigate gas bubbles in a constant high-pressure surrounding with well-defined boundary conditions.

2.2.1 Experimental setup and procedure

For bubble collapse experiments, aluminum diaphragms are used to separate driver and driven sections (section 2.1.1). In addition, the thick-walled, cylindrical test section is installed and closed with a solid end wall (section 2.1.3). A sketch of the test section filled with gelatin is shown in fig. 2.3 (a).

To form the gelatin, we mix Gelrite™ Gellan Gum with demineralized water, heat up the mixture, and add magnesium sulfate ($MgSO_4$). After stirring until everything is dissolved, the warm mixture is poured into the test section, which is closed and sealed with a 30mm-thick back wall and turned vertically. After cooling down, the resulting gelatin is clear and behaves solid when only low pressure is applied. A thin plastic foil is placed on top of the gelatin and fixed by mounting the cookie-cutter. This helps keeping the gelatin block in place when the test section is flipped back horizontally and mounted to the end of the driven section of the shock tube.

To produce bubbles, a needle attached to a syringe is inserted through a small, closeable hole in the back wall. A defined amount of gelatin is extracted first, before the needle is removed, filled with air, and carefully inserted again. The air is then released to form spherical bubbles of up to 1.5mm radius. Figure 2.3 shows a direct photograph (c) and shadowgraph recording (d) of two bubbles surrounded by the gelatin in the test section.

The bubbles are at rest until the experiment starts with the arrival of the shock wave. Starting with the incident shock wave, the ideal wave motion in air and gelatin is presented in fig. 2.3 (b) in an $x-t$ diagram. It shows that due to the high difference in acoustic impedance, the incident shock wave reflects at the gelatin interface like at a solid wall [21]. Thus,

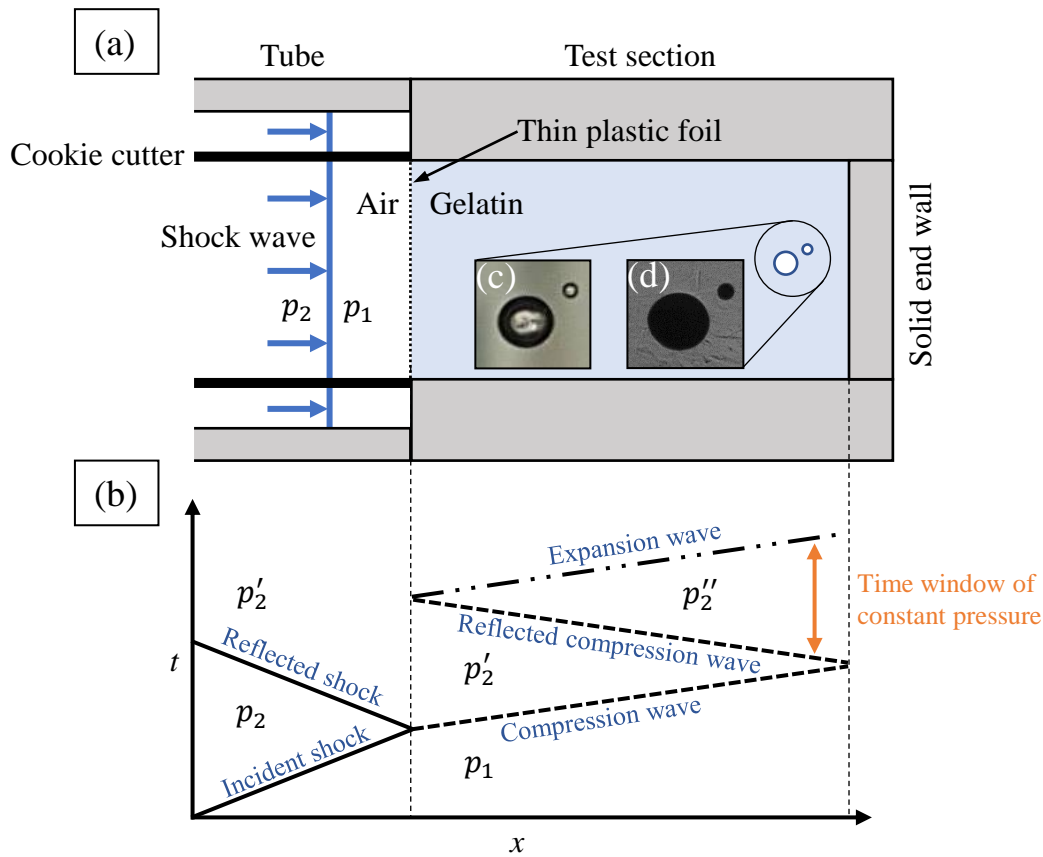


Figure 2.3: Sketch of the gelatin-filled test section with end wall and cookie cutter (a). The wave motion and pressure change during an experiment after shock arrival is presented in a wave diagram (b). A bubble pair in gelatin is depicted as a direct photograph (c) and as a shadowgraph image (d).

eq. (1.3) for the reflected shock Mach number can be used to calculate the pressure behind the reflected shock as p'_2 . To maintain an equal pressure at the interface, a compression wave propagates into the gelatin. This wave reflects at the solid end wall and further increases the pressure to p''_2 . This pressure stays constant until a reflected expansion wave returns. The time-window of constant pressure is approximately 0.4ms long, which is sufficient to conduct bubble collapse experiments.

However, conducted experiments have shown that the theory of ideal wave motion does not allow to calculate the pressure accurately. Therefore, several PCB pressure sensors are distributed along the test section and the end wall to monitor the pressure in the gelatin during all experiments. While the wave motion can be tracked as expected, the actual pressure is lower due to deformation of the test section and due to inclusion of gas in the gelatin. Nevertheless, the pressure increases step wise with the arrival of the compression wave and stays at a constant, high level throughout the collapse.

The present method features two main advantages. First, it allows to study gas bubbles in contrast to cavitation bubbles. This can provide a more realistic setting for some applications and also allows to study how different gases affect the collapse. For example, it is interesting to compare the behavior of condensable gases or vapor in contrast to gases that do not condense under the experiment conditions. Second, the setup guarantees stable initial and boundary conditions. The highly dynamic process of other bubble production methods with rapid energy deposition and complex plasma formation is avoided. In the current setup, the gas bubbles are at rest before the pressure rise, and they are exposed to a constant high

pressure during the collapse. A positive side effect of placing the bubbles in the gelatin is that bubbles of different sizes and at various distances can be produced without much additional effort. This allows to better reproduce application scenarios, where bubbles appear in clusters and interact during the collapse.

In this work, the setup is used to study the influence of the non-Newtonian properties of the gelatin on the collapse behavior by varying the gelatin concentration. In addition, the interaction of gas bubble pairs is investigated. A summary of the findings is presented in chapter 3, and the corresponding publication is attached in appendix A.1.

2.2.2 Data processing

Conducted experiments provide video recordings and pressure signals for further analysis. Videos are processed in an automated Matlab script to extract data of the time-dependent equivalent bubble radius. First, pixels that constitute the bubble are identified and summed up. The sum of the pixels is then converted into a bubble area A using a reference length. Then, the equivalent radius R is calculated from the area as

$$R = (A/\pi)^{0.5}. \quad (2.1)$$

This method is exact for spherical bubbles but also provides a good representation for slightly deformed bubbles. The data are used to provide time-dependent radius plots, to derive collapse times, and to identify the minimum radii of the bubble collapse.

Recorded pressure data are used mainly for two aspects. An average of the measured pressure over the collapse time is used to summarize the collapse behavior, for example in terms of minimum radii or collapse times. In addition, the transient pressure signal measured at the end wall close to the bubbles is used as an input for reference calculations with the Rayleigh-Plesset (RP) equation. The RP equation describes the collapse of a spherical bubble with a time dependent radius $R(t)$ in an infinite liquid domain of pressure $p_\infty(t)$ far from the bubble. Some simplifications are considered in its derivation. The liquid is considered incompressible, the gas content in the bubble is constant, external forces like gravity are neglected, and the process is considered adiabatic [46]. In this work, it is used in the form of

$$\rho_l \left[R\ddot{R} + \frac{3}{2}\dot{R}^2 \right] = p_v - p_\infty(t) + p_{g,0} \left(\frac{R_0}{R} \right)^{3\kappa} - \frac{2\sigma}{R} - 4\mu_l \frac{\dot{R}}{R}. \quad (2.2)$$

Here, p_v is the vapor pressure, $p_{g,0}$ represents the initial gas pressure in the bubble, R_0 is the initial bubble radius, and σ the surface tension. We use material properties of water for the liquid density, ρ_l , and viscosity, μ_l , and properties of air for κ in order to have a general reference. The calculations provide a valuable tool, especially as they use input values from the experiments for $p_\infty(t)$ and R_0 . Thus, a direct comparison of experiment and theory is enabled, which allows to check for differences of the applied setup and to detect potential effects of the gelatin.

Regarding the accuracy of the data analysis, both the spatial and temporal resolutions have to be considered. Typically, images are recorded at $30 - 63 \mu\text{m}/\text{pixel}$, and with around $40 - 80$ pixels per initial diameter [68]. Assuming an error within one pixel, an inaccuracy for the radius, ΔR , in a range of $\pm 1.25\%$ to $\pm 2.5\%$ results. However, this should represent the upper limit of the error, because calculating $R(t)$ with eq. (2.1) is a very robust method. The collapse of the bubbles is usually captured with $20 - 40$ images, giving an inaccuracy for the collapse time, Δt , in a range of $\pm 1.25\%$ to $\pm 2.5\%$ when assuming an error within half an interframe time.

This estimate shows that the error from the spatial and temporal resolution has only a limited influence. More difficult is assessing how a potentially inhomogeneous gelatin surrounding influences the bubble collapse. Such inhomogeneities can arise from non-uniform cooling of the gelatin or from inserting the needle. They can cause disturbances and affect the sphericity of the initial bubble or the shape during collapse. To minimize the risk, the sphericity of the bubble, also in the direction normal to the image plane, is inspected carefully before each experiment. Nevertheless, some uncertainty remains.

2.3 Droplet breakup of liquid metals

The previous overview in section 1.4 has shown that droplet breakup is a complex phenomenon with relevance in a number of applications. Despite the number of studies available in the literature, additional work is needed, especially regarding the breakup of metal droplets. This section provides an overview over the experimental work that was conducted as part of this thesis to advance this topic. The section highlights adjustments of the experimental setup and presents the methods of the investigation.

2.3.1 Experimental setup and procedure

To investigate metal droplet breakup, the shock tube setup as discussed in section 2.1 is applied. The multi-purpose test section and the tube extension are used, and mylar or PVC diaphragms separate driver and driven section. However, some additional aspects need to be discussed.

Materials

Three different liquids are used for the droplet breakup experiments in this thesis: water, Galinstan, and Field's metal. Fluid properties of the materials are summarized in table 2.2.

Galinstan is a non-toxic metal alloy of 68.5% gallium, 21.5% indium, and 10.0% tin and retains a liquid state at temperatures as low as -19°C [28, 114]. Similar to other metals like aluminum [106], it reacts with oxygen and forms an oxide layer on the surface. This layer has a thickness in the order of nanometers [40], but it imparts non-Newtonian rheological properties to the metal [36]. Dickey [40] finds that the oxide skin of gallium alloys is elastic and provides mechanical stabilization until a critical yield stress of approximately $0.500 - 0.600\text{N/m}$. This presence affects the effective surface tension of the metal. A value of $\sigma_{\text{Gal}} = 0.718\text{N/m}$ is measured for Galinstan when exposed to oxygen in its surrounding [28, 90], but it drops to 0.535N/m when the oxygen trace is below 1ppm [114]. The present experiments were conducted under atmospheric conditions and thus the higher surface tension under the effect of oxidation is used.

Field's metal is another non-toxic alloy that oxidizes [95, 111]. It has component percentages by weight of 32.5% bismuth, 51% indium, and 16.5% tin, and has a melting point of 62°C [56]. The density is temperature dependent and follows the relation [112]

$$\rho_{\text{FM}} = 10.6555 - 0.0085T. \quad (2.3)$$

Here, the density of FM is in g/cm^3 , and the temperature T in Kelvin is considered unitless. The viscosity shows shear thinning behavior and measurements provide values of $\mu_{\text{FM}} = 10 - 30\text{mPas}$ for the current temperature range [56, 110, 112]. An intermediate value of $\mu_{\text{FM}} = 21\text{mPas}$ is used in this work [110]. Only a few reference values are provided in the literature

Table 2.2: Material properties of water, Galinstan and Field's metal. Listed are values for the liquid density (ρ_l), surface tension (σ), viscosity (μ_l), and the freezing temperature (T_{freeze}). Values for Galinstan are taken from Kocourek et al. [90]. *The density of FM is temperature dependent and calculated with eq. (2.3).

Liquid	$\rho_l[kg/m^3]$	$\sigma[N/m]$	$\mu_l[mPa \cdot s]$	Oxidation	T_{freeze}
Water	998	0.072	1	non-oxidizing	0°C
Galinstan	6440	0.718	2.4	oxidizing	-19°C
Field's metal	7570 – 7700*	0.565	21	oxidizing	62°C

for the surface tension of FM. Hadj-Achour et al. [56] use a value of $\sigma_{\text{FM}} = 0.410N/m$ without source, while a corresponding work states a value of $0.500N/m$ [43]. Kouraytem et al. [95] obtain theoretical and experimental values of $\sigma_{\text{FM}} = 0.400N/m$ and $0.410N/m$ at 108°C, respectively. However, in their measurement, they note a rapid succession of a few drops to minimize oxide formation. This is critical for the applied pendant drop method [6, 171], and it is not representative for the present experiments as drops are exposed at least for some seconds to the ambient air before atomization. Thus, oxidation effects need to be taken into account.

Due to the uncertainty, the surface tension was assessed experimentally for this work. It is measured for all three liquids using the pendant drop method [6, 60]. For Galinstan and water, the average of the measurements confirm the literature values, as provided in table 2.2, within 2.5% and 1%, respectively. For FM, a mean value and standard deviation of $\sigma_{\text{FM}} = 0.565 \pm 0.067N/m$ is obtained at 90°C. This value is higher than the reference values, but this is an expected effect of the surface oxidation. The mean of $\sigma_{\text{FM}} = 0.565N/m$ is used for this work and provides a good estimate of the breakup behavior.

The gallium content in Galinstan reacts strongly with aluminum and also wets to glass surfaces [125]. As the test section is made of an aluminum alloy frame and includes large glass windows, it was necessary to protect it. Thus, a thin film of rubber spray by mibenco[®] covered the inner surfaces of the test section during experiments, and the glass windows were cleaned carefully with water after experiments. The same approach was used for experiments with FM. While there is no reaction with aluminum, the rubber spray helped to avoid that FM melt or solid particles could damage parts of the section or the glass window.

Droplet generation

A droplet generator is installed on top of the test section to produce single droplets. Depending on the desired liquid, its design changes. For experiments with water and Galinstan, a syringe with an attached needle is mounted on an aluminum profile. The syringe can be moved vertically to insert the needle into the test section through a 1mm bore hole. To generate the droplet, the syringe plunger can be advanced with a linear actuator in the micrometer range. This actuator can be controlled manually or with a step motor. It allows to precisely generate one single droplet. Depending on the needle width, droplets of different sizes can be produced. Best results in terms of sphericity of the drop, and avoiding droplet oscillation were achieved with needle diameters of 0.4 – 0.6mm.

Generating a FM drop requires a different setup that is shown in fig. 2.4. It consists of a furnace that is mounted to the top wall of the test section. To heat up the furnace, two heating cartridges are installed along with a temperature sensor and a temperature control. The furnace temperature is held within $\pm 2^\circ\text{C}$ of the target temperature, which was set to 90°C for the majority of the experiments. This temperature allowed smooth, repeatable droplet generation. The fluid chamber inside the furnace has a funnel shape that connects to a luer

lock needle adapter and steel capillaries, mainly of size G30 (outer diameter of 0.3mm). To generate a droplet, a pressure puls is created in the fluid chamber that pushes the metal melt through the needle into the test section.

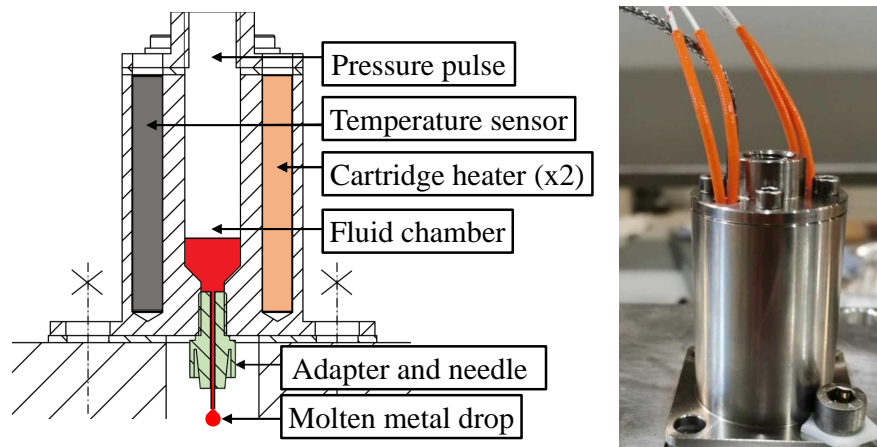


Figure 2.4: Droplet generator for Field's metal. A sketch highlighting the different parts is on the left, and a picture of the droplet generator mounted on the test section is to the right. Adopted from Hopfes et al. [66].

Workflow

Generated droplets in experiments fall through a laser beam that is spanned directly under the needle tip by an aligned pair of laser emitter and receiver. The interruption of the laser signal is captured by an Arduino micro controller. After a set delay, the controller connects a 55V power supply to the heating wires that are adjacent to the plastic diaphragm between driver and driven section (see section 2.1.1). After the diaphragm ruptures, the shock wave forms and propagates downstream to the test section. Image recording is started after the pressure sensor in the test section detects the shock arrival.

Delicate timing is required to match the shock arrival and falling droplet within the fixed frame of video recording. Experience values for the time of shock formation are required and pre-tests for the timing of the falling droplet must be conducted. However, the repeatability of all processes allows to capture the deforming drop consistently.

2.3.2 Data processing

Flow conditions

To analyze a conducted experiment, the exact flow conditions in the region behind the shock wave are required. For this thesis, these flow conditions are calculated with the moving shock relations as discussed in section 1.2. In order to do this accurately, exact knowledge of the initial conditions before shock formation is required. This was discussed in section 2.1.2. In addition, the shock Mach number of the incident shock wave must be captured. To determine it accurately, we first calculate the shock velocity u_s by dividing the spatial separation (Δx) of two pressure sensors directly upstream of the test section by the time-lag (Δt) of the measurement of the shock passage.

$$u_s = \Delta x / \Delta t \quad (2.4)$$

M_s then follows as

$$M_s = u_s / a_1. \quad (2.5)$$

With this information, all other flow conditions like the induced flow velocity or the pressure can be calculated. This method is very accurate and has been evaluated, for example, by conducting total pressure measurements of the flow [170].

To complement the calculation, we measure the transient pressure during experiments with high-frequency pressure transducers (see section 2.1.2). At least two pressure sensors are installed directly upstream of the test section and at least one transducer is installed close to the droplet position. It is ideally suited to evaluate the calculated flow conditions by comparing the measured value to the calculated value. A graph of two pressure measurements that are normalized by the respective calculated values is presented in fig. 2.5. The figure shows an instant increase to a value ~ 1 after shock passage at $t = 0$ for both signals, confirming that measured and calculated values are matching.

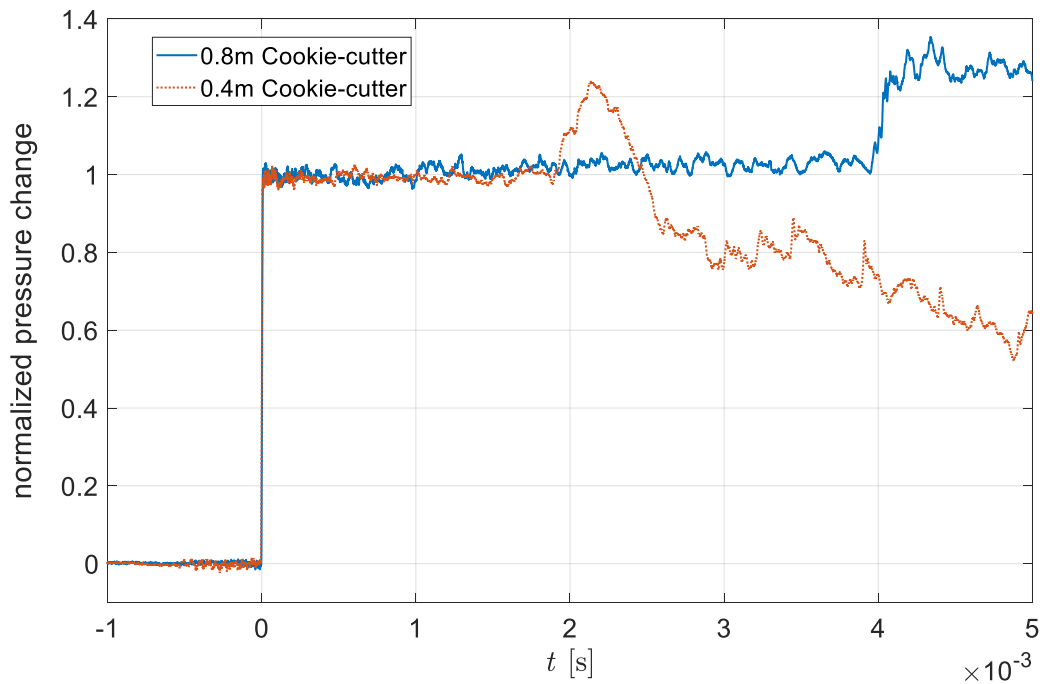


Figure 2.5: Measured pressure signal normalized by the pressure calculated with eqs. 2.5 and 1.1. The dotted, orange line represents an experiment with the 0.4m cookie-cutter installed upstream of the test section. The blue line represents an experiment with the 0.8m CC installed upstream and the 0.4m CC installed downstream of the test section. Both experiments feature 3bar in the driver section, and atmospheric pressure in the driven section.

In addition to validating the calculation of the flow properties, the shown pressure signals help evaluate the time-window of constant flow conditions. Figure 2.5 shows measurements for two different setups. The dotted, orange line represents an experiment where the short 0.4m CC is installed upstream of the test section and no CC is installed at the transition from test section to tube extension. It shows that the pressure, and the general flow conditions, remain constant for approximately 2ms. A second, blue signal represents an experiment with the 0.8m CC installed upstream and the 0.4m CC installed downstream of the test section. The time of constant flow conditions is now extended to 4ms, which allows to study metal droplet breakup under a wider range of conditions.

Image processing

Raw images from the HPV-X camera are processed in Matlab with self-developed programs. The first step is to subtract the background of the image using an image recorded shortly before the experiment. This eliminates areas of different brightness and removes visible

stains that are, for example, on the glass windows. To brighten and sharpen the images, contrast stretching is applied at different levels depending on the recording. The resolution of these images is then doubled using the super-resolution capability of Matlab's Very Deep Super-Resolution convolutional neural network [88].

The processed images are analyzed using automated Matlab scripts. They use a fixed reference length to determine values for the equivalent diameter of the drop d , the cross-stream diameter d_c , the streamwise diameter d_x , and the position of the mass center x_{mc} . Figure 2.6 shows three time instants of a deforming drop and the corresponding analysis. A '0' subscript denotes initial conditions, while $d_{c,max}$ denotes the cross-stream diameter at the end of the initial deformation time τ_{ini} . The collected data are used and processed further depending on the goal of the investigation.

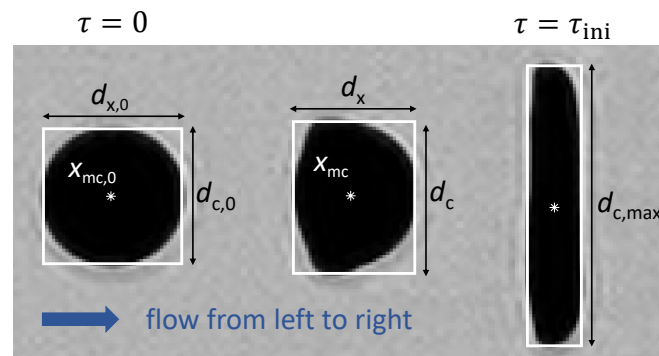


Figure 2.6: Data analysis from image processing. Provided are three time instants of droplet deformation: the start of the experiment (left, with subscript '0'), during the deformation phase (middle), and at the end of initial deformation (right). Captured variables include the cross-stream diameter d_c , the streamwise diameter d_x , and the position of the mass center x_{mc} . Flow direction is from left to right. Taken from Hopfes et al. [66]

A comment on the accuracy

The accuracy of test results is a very important aspect of experimental work, but it is commonly accepted in engineering that all measurements are subject to errors [2]. Consequently, this section provides an overview regarding the accuracy of the droplet breakup experiments of this thesis.

A typical droplet breakup experiment is subject to several uncertainties. First, the flow conditions need to be assessed. The previous section 2.3.2 has shown that an accurate calculation of flow conditions depends on an accurate measurement of initial conditions in the driven section and of the shock Mach number. Regarding the initial conditions, we regularly re-calibrate the sensors in the tube and check the surrounding ambient sensors for reference. In addition, the accuracy of, for example, the pressure transducer in the driven section is on the level of a few Pascal. Overall, the error cannot be assessed in detail, but it is reasonable to assume it is negligible. The calculation of M_s depends on an accurate measurement of the time-lag Δt . Transient pressure measurements are typically conducted at 1MHz, providing a time-resolution of $1\mu s$. Assuming a shock velocity of $400m/s$ for the distance between the two sensors of $0.75m$, a time lag of $\Delta t = 1875\mu s$ results. With a measurement uncertainty of one data point ($1\mu s$), only a minor variation of the shock Mach number would result. While the shock Mach number affects all following calculations of the flow conditions, the overall error remains low. For an experiment similar to the example case, the effect on the calculation of the Weber number would be $< 1\%$.

In addition to the flow conditions, the video processing is a source of uncertainty. The initial droplet diameter d_0 is calculated from the area A of the drop as $d_0 = \sqrt{4A/\pi}$. This is

a robust method that provides a good accuracy. Great care is taken to record the droplets with well-adjusted, sharp video settings, but the resolution remains as the limiting factor. Final images typically resolve the initial droplets at a minimum of 30 pixels per diameter. The average, for example, in the first droplet breakup study [65] is ~ 43 . Assuming an error within one pixel at the resolution of 30 pixels per diameter results in an uncertainty of $\Delta d = \pm 3.3\%$. This value changes throughout the deformation for the cross-stream and stream-wise diameter, as they increase and decrease during the experiment.

The sources of uncertainty for this work remain small overall and do not influence the results significantly. There are some limitations to the accuracy that should be considered, but they are well understood and continuously monitored.

Chapter 3

Summary of the publications

In this chapter, the three first-author, peer-reviewed publications, on which this dissertation is based, are summarized.

3.1 Collapse dynamics of bubble pairs in gelatinous fluids

Thomas Hopfes, Zhaoguang Wang, Marcus Giglmaier, Nikolaus A. Adams

3.1.1 Summary of the publication

In this publication, we study the collapse of gas bubbles in a gelatinous surrounding, as well as the interaction of collapsing bubble pairs. The experiments are conducted using a novel experimental setup. It uses the shock tube at AER to generate a stepwise increase in pressure through shock wave impact and reflection at a gelatin interface. The gelatin fills the whole test section and is formed by dissolving Gelrite™ Gellan Gum in demineralized water under the addition of magnesium sulfate (MgSO_4). Placed within the gelatin are millimeter-sized air bubbles. Their deformation and collapse is recorded with a high-speed camera.

We study single air bubbles that collapse spherically to evaluate the setup and to determine the influence of the gelatin. We apply four different gelatin mixtures. The standard mixture contains 0.6g of Gelrite™ and 0.5g of MgSO_4 per liter of demineralized water, while the other mixtures are scaled at 70%, 130%, and 160%. For all experiments, we compare image sequences of the bubble oscillations and provide normalized collapse times and minimum radii. The results show that changing the gelatin strength does not influence bubble dynamics significantly. Moreover, we show that all four applied mixtures lead to a bubble collapse that is very similar to a bubble collapse in water by using normalized data and reference calculations with the Rayleigh-Plesset equation [24].

In addition to evaluating the methodology and the influence of the gelatin, the setup is used to study the interaction of bubble pairs in the free field. We identify four types of bubble pair interaction, which can be characterized using non-dimensional parameters similarly to previous works [29, 45, 57]. Those parameters are the normalized bubble distance γ and the phase difference $\Delta\Theta$, which can be calculated from the size ratio of the two bubbles S .

A $\gamma - \Delta\Theta$ map of the four types of bubble pair interaction is presented in fig. 3.1, along with exemplary image series representing two interaction types. The first image series depicts two bubbles in very close proximity ($\gamma \sim 1$) and of very different size ratio, and thus high phase difference ($\Delta\Theta = 0.76$). We can see that the big bubble slowly collapses spherically while the small bubble quickly collapses towards the big bubble until the two bubbles merge (frames 1-3). While the remaining bubble maintains a spherical shape initially, we see that a funnel-shaped protrusion develops at the side opposite to the original position of the small bubble

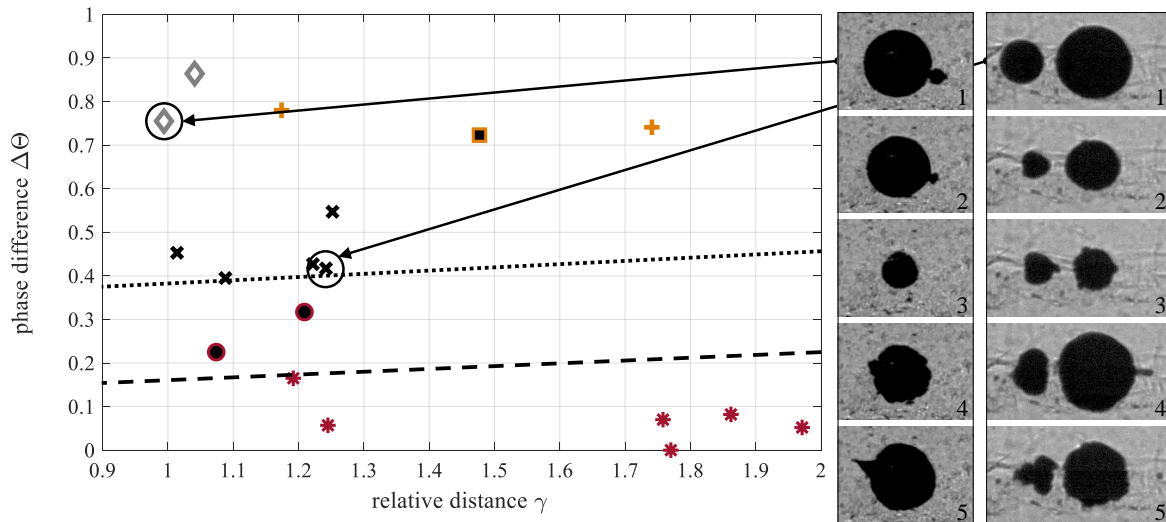


Figure 3.1: Overview of bubble pair interaction depending on the relative distance of the bubbles γ and the phase difference $\Delta\Theta$. Weak interaction (orange plus icon), shooting through (gray diamond), reversing collapse (black cross), collapse towards (red star), and mixed type behavior (black dot in red circle and black square surrounded by an orange line). The dashed and dotted lines present the critical $\Delta\Theta_{\text{crit}}$ value after Chew et al. [29] that separates the types of 'jet away' ($\Delta\Theta > \Delta\Theta_{\text{crit}}$) and 'jet towards' ($\Delta\Theta < \Delta\Theta_{\text{crit}}$) for bubbles of similar and different size, respectively. Example image sequences of shooting through and reversing collapse are presented on the right. Adapted from Hopfes et al. [68]

(frames 4-5). It is caused by a liquid jet that 'shoots through' the big bubble and penetrates the surface on the far side. The second image series shows an example for a 'reversing collapse' with bubbles at $\gamma = 1.24$ and $\Delta\Theta = 0.42$. Here, the medium-sized bubble collapses aspherically and shows a jetting behavior towards the big bubble (frames 2-3). After the collapse, the motion reverses and the medium-sized bubble expands in the opposite direction (frames 4-5). The large bubble collapses spherically, but shows a jet away from the medium-sized bubble upon rebound (frame 4). A small satellite bubble detaches from the jet and continues to move to the right (frame 5).

The characteristic bubble interactions shown in 3.1 have similarities and differences compared to the classification in the literature. The type of jetting towards each other is well known [35, 45, 57] and for the 'weak interaction' only the larger bubble dominates the behavior. However, the 'shooting through' behavior is, as such, not presented in the literature. The 'reversing collapse' has some similarities to previous observations of a 'catapult' type [29] and anti-phase bubble pairs [57] but also shows different aspects. As shown, several interaction types generate a controlled and directed liquid jet, which can be exploited for applications ranging from microfluidics and ultrasound cleaning to medical applications [104].

3.1.2 Individual contributions of the candidate

This article [68] was published in the peer-reviewed journal *Experimental Thermal and Fluid Science*. My contributions to this publication include the conceptualization and the design of the experimental methodology that allows to study gas bubble collapse in a gelatinous surrounding. I conducted the investigation by performing the experiments, processing and analyzing the study data, and visualizing the results. The original manuscript of the publication was written by me.

3.2 Secondary atomization of liquid metal droplets at moderate Weber numbers

Thomas Hopfes, Julia Petersen, Zhaoguang Wang, Marcus Giglmaier, Nikolaus A. Adams

3.2.1 Summary of the publication

A main part of all atomization process is the breakup of single droplets, termed secondary atomization. This topic is widely investigated in the literature for common liquids like water or ethanol [42, 76, 77, 84, 97, 184]. However, data on the breakup of metal droplets are scarce, even though metals feature significantly different fluid properties. They have higher ranges of density and surface tension [28], can be subject to the formation of an oxide layer [176], and temperature effects typically play a more significant role due to high melting points. It stands to reason that findings obtained in experiments with liquids like water cannot be transferred on molten metals without further investigation [10]. Therefore, this publication investigates this topic experimentally by exposing single droplets of the liquid metal Galinstan to a shock-induced crossflow. Galinstan is liquid at room temperature and oxidizes strongly.

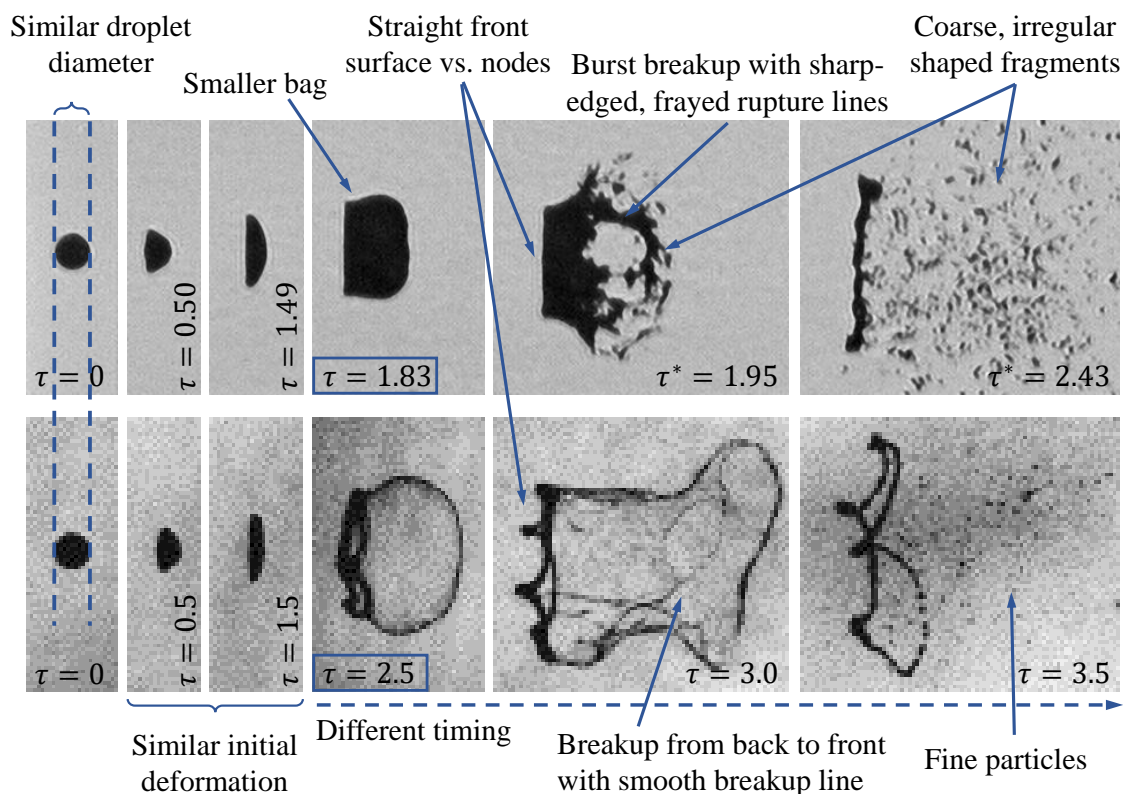


Figure 3.2: Comparison of a bag rupture of a Galinstan droplet at $We = 13.2$ and a water droplet at $We = 15$. Images of the water droplet are taken from Dai and Faeth [37] with permission from Elsevier, and the figure is adapted from Hopfes et al. [65].

The first part of this publication focusses on the breakup morphology of Galinstan droplets over different flow conditions covering a Weber number range of 11-104. Results confirm the known breakup mode sequence of bag, bag-and-stamen, multimode, and shear stripping

breakup also for liquid metal droplets. We identify corresponding transition Weber numbers between the modes of ~ 15 , ~ 35 , and ~ 80 , respectively. The transition between modes is a continuous process with gradual changes, and it is in accordance with the theory of the Rayleigh-Taylor instability. This is shown by focusing on the initial deformation and on the appearance and evolution of the stamen as the most dominant breakup feature for $We = 15 - 50$.

The second part of this publication compares the droplet breakup of Galinstan to that of common, water-like liquids. A comparison is conducted qualitatively using image series and quantitatively using summaries of representative breakup parameters. Figure 3.2 summarizes the findings and highlights the observed similarities and differences on the example of a Galinstan droplet at $We = 13.2$ compared to the breakup of a water droplet at $We = 15$. The figure and the general analysis show that the initial deformation is very similar with respect to the shape and timing of the breakup. Own reference experiments are matched, and the data compares well with correlations from the literature for the initial deformation time τ_{ini} and the maximum cross-stream diameter $d_{c,max}$. Neither different fluid properties, nor the presence of the oxide layer noticeably influence the initial drop deformation. In contrast, we observe significant differences in the breakup behavior at later stages. Those differences are highlighted in figure 3.2 and can be summarized as:

- Galinstan droplets break up significantly earlier compared to other liquids. This is confirmed for the full range of investigated Weber number by comparing to own water experiments and data of water and ethanol experiments in the literature.
- Bags burst open suddenly and show sharp-edged rupture lines that are reminiscent of solid mechanics.
- Deformation of Galinstan droplets appears limited. This is visible, for example, at the smaller bag extension and at the straight frontal side of the drop.
- Coarse, irregularly shaped fragments result from the breakup.

These observations along with previous studies [8, 28] suggest the oxide layer forming on Galinstan as the main cause for the different behavior. This finding is an important step to better understand, and ultimately control, metal atomization processes.

3.2.2 Individual contributions of the candidate

This article [65] was published in the peer-reviewed *International Journal of Multiphase Flow*. My contribution to this publication includes conceiving the idea for the study and adapting the experimental setup to allow to study liquid metal droplet breakup. I conducted the investigation by performing experiments, processing and analyzing the study data, and presenting the results. The original manuscript of the publication was written by me.

3.3 Experimental investigation of droplet breakup of oxide-forming liquid metals

Thomas Hopfes, Zhaoguang Wang, Marcus Giglmaier, Nikolaus A. Adams

3.3.1 Summary of the publication

This publication continues our previous work [65] and investigates the breakup of liquid metal droplets experimentally in the shock tube. A special focus lies on generalizing the effect of surface oxidation on the breakup behavior.

In the literature, investigations of breakup of metal droplets in gas are scarce. There are some studies using mercury [72, 173], but only single experiments are presented and mercury does not form an oxide layer when exposed to atmosphere [108]. In more recent studies, the oxide-forming metal Galinstan is used to study column breakup [8, 28] and droplet breakup [65]. However, additional data are required to estimate how the observed effects can be generalized and whether the findings are representative also for other oxide-forming liquid metals. Therefore, this work employs Field's metal, a low melting point, eutectic metal alloy that also is subject to oxidation [95, 111].

We compare the breakup of Galinstan and FM droplets by means of image sequences and deformation data. Small differences are identified. FM bags inflate slightly more and show a slightly delayed rupture. In addition, FM droplets break into a larger number of smaller and more uniform fragments, especially at low Weber numbers. We expect this to be related to a higher oxidation rate of Galinstan compared to FM. However, apart from these small differences regarding details of the breakup, we identify a strong overall similarity of the two metals with respect to the breakup morphology, transition between modes, and timing and extent of droplet deformation. In addition, Field's metal, like Galinstan, shows distinct breakup features such as sharp-edged rupture lines and an earlier breakup, which distinguishes both metals from other liquids like water.

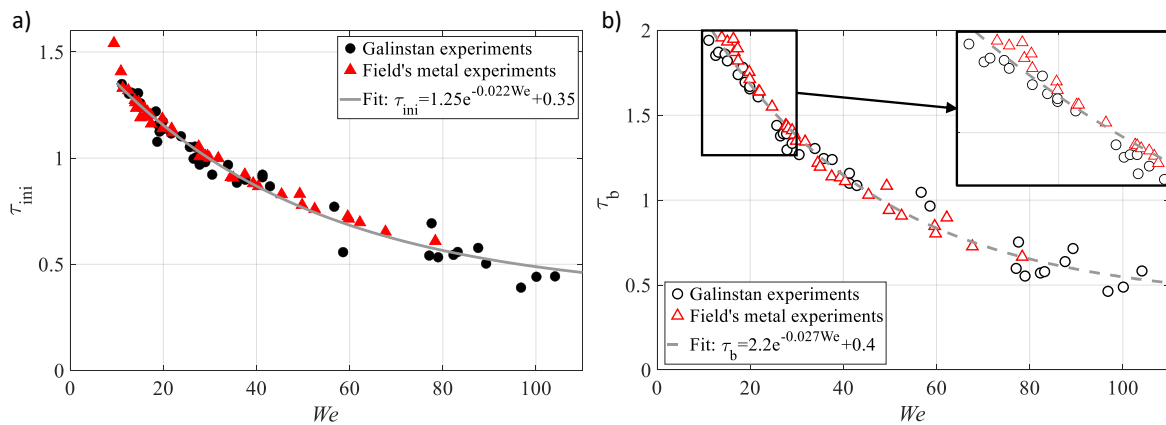


Figure 3.3: Initial deformation time τ_{ini} (a) and time of onset of breakup τ_b (b) for droplet breakup experiments with Galinstan and Field's metal. The data fits to the experiments are shown as a solid and broken gray line, respectively. The box inlet in (b) provides a zoom-in to data points in the range of $We = 10 - 30$. It highlights the slightly delayed rupture for FM droplets. Adapted from Hopfes et al. [66].

Based on the similarities and the distinction from other liquids, we use the collective data of Galinstan and FM droplet breakup to provide Weber number dependent fits for the initial deformation time τ_{ini} and the time of the onset of breakup τ_b as presented in figure 3.3 (a)

and (b), respectively. Experiment data are displayed along with the derived data fits. The corresponding equations to the fits are presented in the figure legends. The graphs show the high accordance between the data points and the empirical fits and confirm previous observations that oxide-forming metals show a similar initial deformation time, but an earlier onset of breakup compared to more common, water-like liquids.

Regarding the droplet deformation, we summarize the normalized cross-stream deformation d_c/d_0 taken at τ_{ini} across the studied Weber number range. The derived empirical fit compares favorably with a correlation derived from experiments with water and ethanol by Zhao et al. [182]. However, we observe some differences for higher We . We also provide an empirical fit of the time-dependent cross-stream deformation of the droplets. The fit is validated against experimental data for different Weber numbers and compared to models from the literature that are based on droplet breakup of more common liquids [76, 150]. While our empirical fit describes the time-dependent droplet deformation accurately, models from the literature tend to underestimate the deformation consistently at later stages of the droplet deformation.

Providing an accurate representation of the data, the presented fits can be used directly, or can help adapt other breakup models to account for the different behavior of oxide-forming metals. In addition, we propose to use the fits as a representation also for other oxide-forming metals like titanium alloys [54] or the chemically very similar aluminum [52, 106].

3.3.2 Individual contributions of the candidate

This article [66] was published in the peer-reviewed journal *Physics of Fluids*. My contributions to this publication include adapting the experimental methodology to allow to study metals with higher melting points. In addition, I conducted the experiments, processed and analyzed the study data, performed data fitting to derive empirical models, and visualized the results. The original manuscript of the publication was written by me.

Chapter 4

List of peer-reviewed journal articles

- **Thomas Hopfes**, Zhaoguang Wang, Marcus Giglmaier, and Nikolaus A. Adams: "Collapse dynamics of bubble pairs in gelatinous fluids". In: *Experimental Thermal and Fluid Science* 108 (2019), p.104-114. [[68](#)]
- **Thomas Hopfes**, Julia Petersen, Zhaoguang Wang, Marcus Giglmaier, and Nikolaus A. Adams: "Secondary Atomization of Liquid Metal Droplets at Moderate Weber Numbers". In: *International Journal of Multiphase Flow* 143 (2021) 103723. [[65](#)]
- **Thomas Hopfes**, Zhaoguang Wang, Marcus Giglmaier, and Nikolaus A. Adams: "Experimental investigation of droplet breakup of oxide-forming liquid metals". In: *Physics of Fluids* 33 (2021), 102114. [[66](#)]

Chapter 5

Discussion

As highlighted in the introduction and throughout this work, the publications constituting this thesis are based on experiments conducted with the shock tube facility of AER at TUM. The features of this facility are exploited to investigate two multiphase flow phenomena that are defined by the interaction of a gas and a liquid phase. A shock wave generated in the shock tube provides a step-change in pressure, which is used to study the collapse of air bubbles in a gelatinous surrounding. Generated shock waves also induce a high-speed gas flow. This aspect is used to investigate the deformation and breakup of single metal droplets.

There are several key achievements related to the bubble collapse investigation presented in this thesis [68]. They are summarized in section 3.1 and presented in detail in appendix A.1. The experimental setup features some novelties, although aspects like the use of shock tubes [47, 168], or the application of gelatin [20, 39, 151] have been shown previously. Their combination into the setup of this work is promising, but has to be developed further to reach the reliability and precision of other experimental setups like laser focus [57, 102, 103, 116, 130, 137, 159, 177], or spark discharge [45, 107, 116, 128, 158, 181]. Nevertheless, in contrast to those established methods, the new setup opens up interesting possibilities and provides several advantages:

- Bubbles are at rest until the impinging shock wave provides an instant change to a constant, high pressure in the surrounding gelatin.
- The setup allows the investigation of bubbles filled with gases, e.g. air, instead of cavitation bubbles that are filled with vapor.
- It is possible to study single bubbles or multi-bubble configurations with well-defined positions, either in the free field or next to a solid wall.

These advantages are used in this work to investigate two different aspects. First, the influence of a gelatinous surrounding on the collapse behavior is evaluated, which extends previous works that investigate the influence of non-Newtonian fluid properties on bubble collapse, e.g. [11, 25]. However, in the present work, this influence is marginal and the bubble collapse is similar to a collapse in water. Second, the advantage of the setup to produce multiple bubbles is used to investigate bubble pair interaction. Compared to the interaction of cavitation bubbles, similarities and differences are observed. Interaction types like the 'collapse towards' are well known [35, 45, 57], but due to using gas bubbles at rest in the free field, also new aspects of bubble interaction are found. Notable is for example the type of 'shooting through', which is not observed in the same way in the literature. Apart from improving the general understanding of bubble interaction, the findings are especially valuable for applications where gas bubbles and not vapor bubbles are present.

A well-defined, constant flow can be generated in the shock tube for a wide range of flow conditions. Owing to this advantage, two publications presented in this thesis investigate metal droplet breakup. The findings are summarized in sections 3.2 and 3.3, and presented

in detail in appendix A.2 and appendix A.3. The main achievement lies in the fact that much needed experimental breakup data is provided. A variety of emerging applications like spray forming, spray coating, or metal powder production [10, 51, 63, 166] rely on such data to better understand the physical mechanisms of the atomization process. A key aspect in all atomization processes is the breakup of single droplets, as it defines the final size and shape of fragments [44, 120, 165, 178]. Controlling this atomization step can help to overcome issues like poor quality, low efficiencies, or high costs that are observed in many applications [4, 100]. However, experimental data on the breakup of single metal droplets in gas flow are limited to a few data points with mercury [72, 173] and related investigations of column breakup with the liquid metal Galinstan [8, 28], which is not sufficient. Therefore, this thesis investigates this topic in detail.

Results of this investigation include a detailed description of the influence of oxidation effects on the breakup of the investigated metal droplets. The formation of an oxide layer on the surface leads to a different breakup mechanism with droplets bursting open in a way that reminds of the rupture of solid shells [126, 127]. This behavior has been observed for metal columns [8, 28], but it is shown here for the first time for metal droplets. On a more general level, the first droplet breakup study [65] investigates continuous transition between breakup modes and the evolution within a mode at increasing Weber number. A continuous transition has been identified previously, e.g. by [53], but it is shown here in great detail for a wide range of Weber numbers. A special focus is put on the appearance and evolution of the stamen structure. How it is formed, and how it changes in length and width with changing We is put in relation with the theory of Rayleigh-Taylor instability. It is shown that the predicted wave patterns of the RTI match the observed bag formations. This adds to the discussion in the literature on the physical breakup mechanisms, and supports the works that identify the RTI as the dominant mechanism [77, 78, 82, 83, 134, 153–156, 182, 183].

The second droplet breakup study [66] employs two oxidizing liquid metals in an effort to generalize the observed behavior. The generated data are summarized in empirical fits, and it is proposed that the findings are representative also for other oxide-forming liquid metals. A similar behavior is especially plausible for aluminum, because it is in the same group in periodic table of elements as gallium and indium, which are the main components, respectively, of the applied metals Galinstan and FM [52]. Generalized fits provide a large benefit for other works. For example, holistic approaches to simulate gas atomization processes of liquid metals are very complex. They require to simulate the high-speed, compressible gas flow, the interaction of liquid and gas phases, and primary and secondary atomization, which results in a demanding, multi-scale problem. To reduce the complexity, secondary breakup is often not simulated directly, but instead modelled, e.g. in [7, 44, 98, 147, 178, 179]. The present work can help such models to better account for oxidation effects, especially regarding breakup times and the droplet deformation.

In conclusion, this thesis shows that a shock tube facility can be used in various, flexible setups and that different features can be exploited to investigate different topics and effects. In addition, a shock tube features a wide range of operating conditions, and the shock-induced step-change of fluid properties allows to conduct experiments that are an ideal reference for numerical or analytical considerations. These advantages highlight once more that shock tubes are a valuable tool to investigate fluid mechanics problems, and that the work with the facility at AER should be continued. Besides the opportunity to use the existing setup to investigate new flow problems, also the present work provides additional potential for follow-up projects. Bubbles of different gas content can be investigated, which is especially interesting if gases are applied that condense under increased pressure. Other options are to investigate bubble collapse next to a solid wall or near soft materials, or to continue the work on multi-bubble interaction. The background light setup as in section 2.1.4 can provide

direct visual insight into the collapsing bubbles. For metal droplet breakup, future work can use metals with higher melting points to target the influence of temperature change or solidification on secondary atomization. Another option is to change the gas content in the tube, for example to nitrogen, in an effort to reduce or inhibit oxidation effects.

Appendix A

Original peer-reviewed publications

The three peer-reviewed journal articles presented in this thesis are attached here.

A.1 Collapse dynamics of bubble pairs in gelatinous fluids

Thomas Hopfes, Zhaoguang Wang, Marcus Giglmaier, Nikolaus A. Adams

In: *Experimental Thermal and Fluid Science* 108 (2019), p.104-114.
<https://doi.org/10.1016/j.expthermflusci.2019.05.023>.

Contributions: My contributions to this publication include the conceptualization and the design of the experimental methodology that allows to study gas bubble collapse in a gelatinous surrounding. I conducted the investigation by performing the experiments, processing and analyzing the study data, and visualizing the results. The original manuscript of the publication was written by me.



Collapse dynamics of bubble pairs in gelatinous fluids

Author: Thomas Hopfes,Zhaoguang Wang,Marcus Giglmaier,Nikolaus A. Adams

Publication: Experimental Thermal and Fluid Science

Publisher: Elsevier

Date: November 2019

© 2019 The Authors. Published by Elsevier Inc.

Journal Author Rights

Please note that, as the author of this Elsevier article, you retain the right to include it in a thesis or dissertation, provided it is not published commercially. Permission is not required, but please ensure that you reference the journal as the original source. For more information on this and on your other retained rights, please visit: <https://www.elsevier.com/about/our-business/policies/copyright#Author-rights>

BACK

CLOSE WINDOW



Collapse dynamics of bubble pairs in gelatinous fluids[☆]

Thomas Hopfes^{*}, Zhaoguang Wang, Marcus Giglmaier, Nikolaus A. Adams

Chair of Aerodynamics and Fluid Mechanics, Technical University of Munich, Boltzmannstr. 15, D-85748 Garching bei München, Germany



ARTICLE INFO

Keywords:

Experimental bubble dynamics
Gelatin
Shock tube
Bubble pairs

ABSTRACT

Bubble dynamics is relevant in a variety of research fields that range from material science to medical applications. It is studied extensively, and researchers apply very established and reliable experimental methods. Although these methods provide many advantages and are constantly modified and adapted, there are also some limitations on which aspects can be analyzed. Thus, we present in this study a novel experimental setup that uses a shock tube and applies a gelatinous mixture as a water-like carrier medium. Millimeter-sized air bubbles, placed in the gelatin and exposed to an instantaneous pressure increase, are analyzed under two different aspects. First, we show that single bubbles in the gelatin behave very similarly to bubbles in water during the collapse and that different gelatin concentrations do not significantly affect the behavior. In a second part, we study interacting bubble pairs and differentiate four main types of interaction that can also be characterized by non-dimensional parameters. A well-known type, jetting towards each other, is reproduced and a type termed 'reversing collapse' shows similarities to previous work as well as new aspects. The interaction of bubbles of large size ratios is either dominated by the large bubble if bubbles are far apart or leads to a pronounced liquid jet if the bubbles are close to each other. The presented results demonstrate that the applied experimental setup can provide insight into bubble interaction and jet formation. This could help, for example, to establish controlled and directed jetting of microbubbles in targeted drug delivery, which would play a major role in anti-cancer research.

1. Introduction

Research on bubble dynamics has a long history in fluid mechanics. Initially, cavitation and related phenomena were noticed due to their destructive potential, for example in the surface erosion on ship propellers [3]. However, there are not only adverse, but also beneficial aspects. Medical procedures, such as lithotripsy and targeted drug delivery, try not only to understand and avoid, but rather to exploit bubble dynamics. Lithotripsy, for example, is an established medical procedure for non-invasive destruction of gallstones in the human body by focusing extracorporeally generated shock waves on the target [4]. Cavitation bubbles are formed in the liquid surrounding the gallstone by a focused tensile wave that follows the preceding shock wave. These bubbles then interact with following shock waves and an aspherical collapse can lead to strong erosive effects through liquid jets and shock wave emission. Thus, transient cavitation is a dominant mechanism that strongly determines the overall effectiveness of the treatment [5]. One major idea behind targeted drug delivery is to use coated microbubbles as drug carriers in the human body. Ligands on the bubble

surface target specific cells before ultrasound pressure pulses, generated outside the body, break the bubbles apart and release the carried drug at the targeted location [6].

To improve the mentioned applications, bubble dynamics has been studied extensively. Fong et al. [7] speak of three widely used experimental methods to generate oscillating cavitation bubbles under reasonably controlled conditions: laser-focus, spark discharge and acoustic waves. They mention, however, that acoustic waves do not allow a high-level of accuracy for bubble positioning. In contrast, laser-generated cavitation is a very prominent method that is favored for its reproducibility and the ability to create nearly perfect spheres [8]. Cavities are created by focusing strong light pulses into a liquid, which creates a plasma at the focus point. The related phenomenon is called dielectric breakdown or, in the context of bubble generation, also optic cavitation [9]. Generating cavities with a laser has several major advantages. Cavities can be produced at any given time and at any accessible position in a liquid. It is therefore possible to produce cavities right before the impact of a shock wave [10], to change the distance of the bubble from a solid wall continuously [11] or to produce the bubble

[☆] This work is based on two contributions that were presented at the 5th International Conference on Experimental Fluid Mechanics, Munich, Germany, July 2–4, 2018 [1,2].

^{*} Corresponding author.

E-mail address: thomas.hopfes@tum.de (T. Hopfes).

<https://doi.org/10.1016/j.expthermflusci.2019.05.023>

Received 27 January 2019; Received in revised form 10 May 2019; Accepted 30 May 2019

Available online 31 May 2019

0894-1777/ © 2019 The Authors. Published by Elsevier Inc. This is an open access article under the CC BY-NC-ND license (<http://creativecommons.org/licenses/by-nc-nd/4.0/>).

next to a spherical particle [12]. This technique can produce bubbles that are perfectly spherical, so that Obreschkow et al. [13] can even study the small effect of gravity-induced pressure gradients on bubble collapse during parabolic flights. Spark generation is an alternative method that has been widely used for bubble dynamic experiments by many researchers [14–17]. It uses wires to discharge electric energy, which again leads to the formation of a plasma point that then expands to form the cavitation bubble. In general, both methods are well established and provide similar advantages and restrictions. The processes work repeatedly, reliably and offer a high level of precision in respect to the bubble shape and position. However, the mentioned methods can only study vapor bubbles. Research on pure, non-condensable gas bubbles is rarer and often has other drawbacks. The applied bubbles are, for example, rising [18], attached to a solid surface [19–21] or have to be kept in position by other means (e.g. a plastic foil [22]). In addition, often very strong pressure pulses are used to collapse the bubbles in such setups. The pulses are created by micro-explosives [18,19,21], optical breakdown [20] or a lithotripter [22,23], which results in very short term pressure peaks, rather than a constant surrounding pressure.

A constant surrounding pressure and well-defined boundary conditions are, however, desirable. To achieve that, a novel experimental method is used for the present study. The approach relies on two aspects. First, a shock tube generates a planar shock front which provides an instantaneous pressure jump to a constant high pressure. Second, a gelatinous mixture is used as a water-like carrier medium to contain pure gas bubbles rather than vapor bubbles. This distinguishes the setup from experiments with gas bubbles under strong shock-loading and from research that uses vapor bubbles. The combination expands the methodology in bubble dynamics research, although both aspects – using a shock tube and placing bubbles in gelatin – have been used individually in previous studies (e.g. [24,25] and [26,27] respectively).

Some advantages can be achieved with the present setup. The initial configuration shows the bubble and surrounding gelatin completely at rest at atmospheric pressure. In addition, the gelatin is enclosed by rigid boundaries on all sides except at the interface to the air within the driven section of the shock tube. This creates a well-defined surrounding and conditions that are favorable when the experiments serve as a reference for numerical simulations. Another positive aspect is that multiple bubbles of different sizes and at various distances can be produced without additional effort. This allows a much better representation of application scenarios, where bubbles often are present in clusters and interact with each other.

The paper is structured so that Section 2 presents the general experimental setup. On a side note, Section 2.2 shows aspects of the different applied test sections and highlights the impact of fluid-structure interaction in experimental work on bubble dynamics. In Section 3, we discuss advantages and restrictions of the setup and analyze to what extent an increasing gelatin concentration affects bubble oscillation by comparing the results to the case of bubbles in water. First results of experiments on interacting bubble pairs are presented in Section 4, while Section 5 summarizes and concludes the present work.

2. Methods

2.1. Experiment

Fig. 2-1 shows a sketch of the experimental setup used in the present study. Main parts are the shock tube, the test section filled with the gelatin and the measurement equipment, such as pressure transducers and the optical system. The shock tube, with an overall length of 22.5 m and an inner diameter of 290 mm, consists of three parts: the driver, the driven and the test section. A diaphragm separates the high-pressure driver section (used in this study at pressures of up to 8 bar) from the driven section at atmospheric pressure (p_1). Upon diaphragm rupture, a shock wave is created which propagates towards the test section at

shock Mach number M_s . It induces an instantaneous pressure and temperature rise as well as a flow velocity in the driven gas. The pressure behind the shock, p_2 can be calculated after [28] as

$$p_2 = p_1 \left(1 + \frac{2\kappa}{\kappa + 1} (M_s^2 - 1) \right) \quad (1)$$

with the heat capacity ratio of air, κ , taken at a value of $\kappa = 1.4$.

Fig. 2-2(a) shows the shock wave propagating into the test section of a cross section of $190 \times 190 \text{ mm}^2$ that is partially filled with gelatin. A sketch shows the corresponding wave motion. When the shock wave arrives at the air-gelatin interface, it reflects almost ideally due to the high difference in acoustic impedance of the two materials and travels upstream at a shock Mach number M_R that can be calculated solely from M_s . The reflected shock causes the gas flow to halt and increases the pressure to $p_{2'}$ which can be calculated with Eq. (1) by substituting M_s with M_R and p_1 with p_2 . Since the pressure must be equal at the interface, a compression wave propagates into the gelatin and increases the pressure to the value behind the reflected shock ($p_{2'}$). The compression wave reflects at the solid end wall of the test section, which further increases the pressure ($p_{2''}$). Assuming ideal wave motion and acoustic theory, the pressure increase over the reflected compression wave is equal to the increase over the initial compression wave, calculated as $\Delta p_{12'} = p_{2'} - p_1$, to lead to an ideal pressure increase at the back wall of $\Delta p_{\text{ideal}} = 2\Delta p_{12'}$. The pressure stays constant in the liquid and the bubbles, shown exemplarily in Fig. 2-2(b–c), collapse and oscillate. The constant conditions last until the reflected compression wave reaches the air-gelatin interface and reflects as an expansion wave that induces a pressure reduction. Consequently, the test time is limited to about 0.4 ms for a gelatin-filled test section of 300 mm length and a speed of sound in gelatin of $a_{\text{gel}} = 1500 \text{ m/s}$. However, Section 2.2 will show that this ideal wave motion does not predict the measured pressure accurately. The pressure is affected by the type and rigidity of the used test section.

To create the gelatin, we dissolved Gelrite™ Gellan Gum within demineralized water and added magnesium sulfate (MgSO_4) after heating. The mixture was poured into the test section, cooled off and formed a clear, agar-like gelatin. In contrast to the ideal setup depicted in Fig. 2-2, a thin plastic foil was placed between gelatin and air since it significantly facilitates the handling of the gelatin without noticeable influencing the experiment. Bubbles were produced by first inserting the needle of a syringe through a small closable hole in the back wall and extracting a small amount of gelatin. The needle was removed and carefully inserted again to then release a defined amount of air. We found that bubbles of up to 1.5 mm radius could be produced in a very spherical shape, whereas bigger radii tended to enhance non-spherical deviations. After production, the bubbles rested under well-defined initial conditions such as constant pressure (p_1), constant temperature, and zero initial velocity until the experiment started. Bubbles were positioned near the centerline of the test section and thus were far from the side walls to avoid any interaction. To take advantage of the ideal pressure rise Δp_{ideal} , bubbles were positioned towards the end of the test section. However, the distance of the bubbles to the back wall was kept at around 10 times the bubble diameter to minimize wall effects [29].

For visualization, we applied a Z-type schlieren system without cutting light at the second focal point to create ‘focused shadowgraph’ images [30]. Powered by a 150 W constant Xenon light source, the optical system projected the visualized section along the line-of-sight on the camera focal plane. This gave a two-dimensional representation of the three-dimensional bubble. The collapse was recorded by a Shimadzu HyperVision HPV-X ultra-high-speed camera that produces videos of 128 consecutive frames with a resolution of 400×250 pixels at up to 5 million frames per second. Simultaneously, PCB Piezotronics ICP® fast-response pressure sensors, connected to an LTT transient recorder, monitored and recorded the pressure during the experiment at six locations at a frequency of 1 MHz per channel. Two sensors along the tube were always connected to allow accurate measurement of the

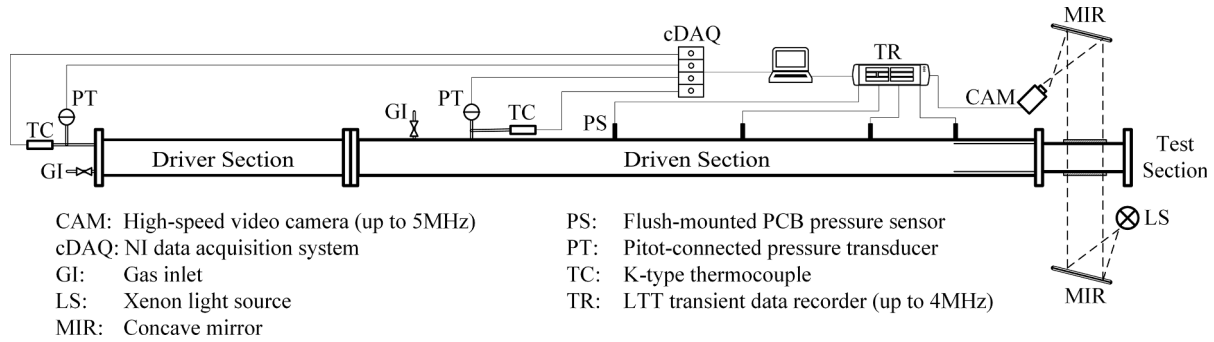


Fig. 2-1. Sketch of the shock tube and connected systems that were used for bubble experiments.

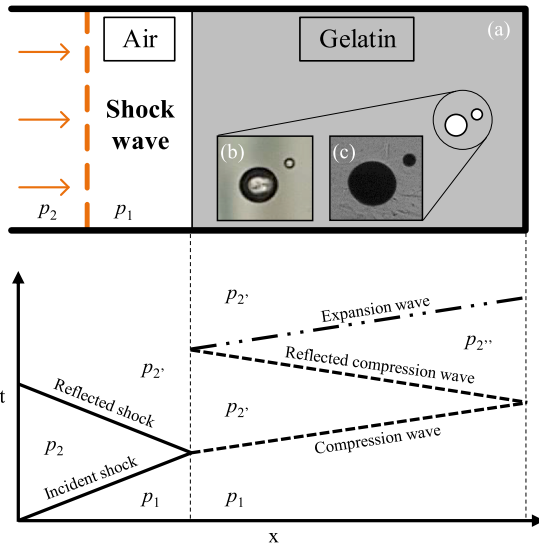


Fig. 2-2. Sketch of the test section filled with gelatin (a). Two bubbles in gelatin are depicted as a direct photograph (b) and as a shadowgraph image (c). The wave motion and pressure change during the experiment is presented in a wave diagram.

shock speed in front of the test section. Typically, three sensors monitored the pressure in the gelatin at the side of the test section and one sensor at the back wall of the test section.

2.2. Influence of the test section

To conduct the experiments, three different types of setups were available:

- Acrylic glass box: a box, made of 10 mm thick acrylic glass plates that was placed inside the test sections and exposed to the shock wave.
- Test section 1 (TS1): A test section formed out of a solid aluminum alloy cylinder with a wall thickness of up to 130 mm.
- Test section 2 (TS2): A multi-purpose test section that featured side walls made of 40 mm thick aluminum alloy plates.

One main objective of the experiments is to establish a high and constant surrounding pressure after a short rise time to initiate the bubble collapse. However, rise time and evolution of the pressure were strongly dependent on the applied setup. Fig. 2-3 shows the transient pressure signals at the back wall for all three cases. The measured pressure change $\Delta p(t) = p(t) - p_1$ is normalized by the expected ideal pressure change after the reflected compression wave Δp_{ideal} . The figure shows an instantaneous pressure rise in all three signals after the arrival of the compression wave. Apart from this instantaneous rise, the ideal

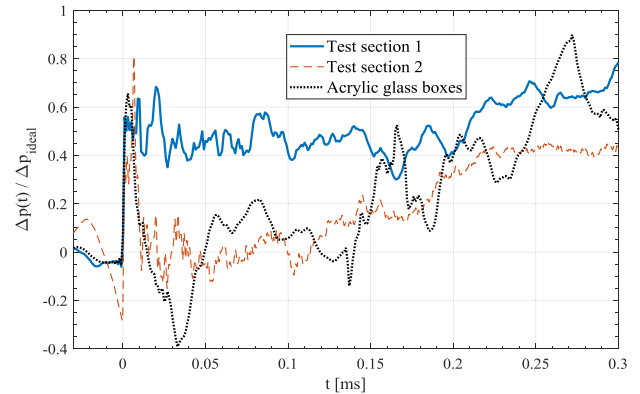


Fig. 2-3. Comparison of the pressure signal at the back wall of test section 1, test section 2, and of the acrylic glass box.

one-dimensional wave motion with constant post shock conditions is poorly reproduced and the expected pressure value $\Delta p(t)/\Delta p_{ideal} = 1$ is not reached. In addition, only the pressure in TS1 stays at a comparatively constant high level, whereas the pressure drops rapidly after the initial peak in the other cases. The short pressure peaks for the acrylic glass box and TS 2 are insufficient in this setup to initiate the bubble collapse and neither is the sustainable but slow pressure rise that occurs after more than 0.1 ms. However, good results were achieved with TS1. The pressure signal shows a significant increase and a constant value within the range of $0.4 < \Delta p(t)/\Delta p_{ideal} < 0.6$. Bubbles react to the fast rise time and the constant, high driving pressure and collapse strongly. Consequently, TS1 was used for all experiments that are presented in this work.

The reason for the untypical pressure signals was found to be the deformation of the structure that surrounds the liquid. A high pressure in the test section is reached behind the compression wave. This applies a strong load on the solid structure, which reacts by outward deformation. Since water, or gelatin in this case, is an almost incompressible liquid, a small expansion results in an immediate and strong decrease of pressure. Overall, the pressure only increases slowly, which prevents the bubbles from collapsing strongly. While a deformation of the acrylic glass box was expected, a relevant deformation of metal came as a surprise.

However, at this point the authors would like to point out that the value Δp_{ideal} , cannot be achieved even with infinitely thick sidewalls. Taking the compressibility of the metal back wall into account, a part of the shock is transmitted into the metal and the maximum pressure rise Δp_{max} can be calculated from one-dimensional acoustic theory (e.g. Brekhovskikh [31]) by

$$\Delta p_{max} = \frac{1 + R}{2} \Delta p_{ideal} \quad (2)$$

with

$$R = \frac{\rho_{Al} a_{Al} - \rho_W a_W}{\rho_{Al} a_{Al} + \rho_W a_W} \quad (3)$$

Taking the speed of sound a and the density ρ of water and aluminum, this results in $\Delta p_{\max} \approx 0.9 \Delta p_{\text{ideal}}$. The estimation can be extended from a 1D to a 3D problem, by taking the compressibility of the side walls into account. Doing this, the value is expected to be even lower. Consequently, the actual pressure rise is strongly limited in all experimental works that apply similar setups. For the present work, it results in a pressure signal that is not perfect but provides a sharp pressure jump followed by a high-pressure plateau.

3. Influence of the gelatin

Gelatinous fluids are used occasionally to study bubble dynamics. Dear et al. [26,32] produce arrays of two-dimensional cavities in gelatin and induce the collapse with a strong shock wave to investigate the liquid jet development. A similar setup is employed by Bourne and Field [33,34] to study the collapse of differently shaped cavities and the associated luminescence. Another work by Swantek and Austin [27] examines the interaction of voids in gel with a stress wave and measures the surrounding velocity field. For such experiments and the corresponding high pressures, it is usually stated that the gelatin behaves as a liquid (e.g. [32]). The shear-thinning property of the gelatin may affect bubble dynamics, especially in the present study with only moderate pressure levels of less than 1 MPa. Therefore, we compare the results using gelatin with the standard case of bubbles in water. Different gelatin mixtures are used and compared at different pressure levels.

3.1. Rayleigh-Plesset equation

A well-known formula, often serving as the standard reference to describe spherical cavitation bubbles, is the Rayleigh-Plesset equation. We use the general form of the equation after Brennen [3] but modify it to describe bubbles filled with non-condensable gas. We expect that only air at atmospheric pressure is present at the collapse initiation. Furthermore, we assume that the gas compresses and expands adiabatically, i.e. without heat transfer between bubble and surrounding liquid. The time-dependent gas pressure $p_G(t)$ within the bubble can then be written as [3]:

$$p_G = p_{G0} \left(\frac{R_0}{R} \right)^{3\kappa} \quad (4)$$

with p_{G0} as the initial pressure in the gas bubble, R_0 as the initial radius and R as the time-dependent radius of the bubble. The mentioned assumptions result in the modified equation

$$\frac{p_{G0} \left(\frac{R_0}{R} \right)^{3\kappa} - p_\infty(t)}{\rho_L} = R \frac{d^2 R}{dt^2} + \frac{3}{2} \left(\frac{dR}{dt} \right)^2 + \frac{4\nu_L}{R} \frac{dR}{dt} + \frac{2S}{\rho_L R} \quad (5)$$

with t as the time, $p_\infty(t)$ as the pressure in the fluid, ρ_L and ν_L as the density and kinematic viscosity of the liquid respectively and S as the surface tension of the liquid. Along with the measured initial radius from the images and the recorded pressure $p(t)$ at the end wall, this formula provides a valuable tool. It allows to calculate a reference for each experiment individually. The properties of water are taken to describe the liquid to further assure a general and well-known reference. Comparing results of the theory with experiments can show differences and thus the influence of the gelatin.

3.2. Experiments

The influence of the gelatin on the bubble collapse was evaluated for Gelrite™ concentrations between 0.42 and 0.96 g/l mixed with

Table 3-1

Test matrix to evaluate gelatin influence, providing the respective Gelrite and MgSO_4 concentrations as c_{Gelrite} and c_{MgSO_4} , a ratio to the standard case c_2 and the number of conducted experiments n_{exp} .

Mixture	c_{Gelrite} [g/l]	c_{MgSO_4} [g/l]	c/c_2	n_{exp}
1	0.42	0.35	70%	9
2	0.6	0.5	100%	14
3	0.78	0.65	130%	5
4	0.96	0.8	160%	14

0.35–0.8 g/l MgSO_4 , respectively. Table 3-1 presents an overview of the tested mixtures. Mixture 1 represents a lower limit below which bubbles start to rise. Mixture 4 represents an upper limit for which the gelatin is very solid, and bubbles tend to be of an aspherical shape. To allow additional insight, experiments with the four mixtures were conducted at different pressures. The pressure rise Δp , averaged over the collapse time, reached values between $\Delta p = 0.36$ bar as a lower limit and up to $\Delta p = 3.38$ bar as a higher limit.

3.2.1. High-speed imaging

Essential qualitative features of the bubble oscillation are presented with exemplary photographic sequences. Note that for all presented images, the compression wave arrives from the left but is reflected at the back wall, which is to the right of the images but out of the view. Fig. 3-1 shows bubble compression and expansion for a high-pressure increase of $\Delta p = 2.82$ – 3.38 bar for different gelatin mixtures. Fig. 3-1(a) shows the oscillation for gelatin of mixture 1 and a bubble of $R_0 = 1.27$ mm. The gelatin is very clear, and the bubble shape appears perfectly spherical. After the passage of the compression wave, the bubble starts to contract spherically (frames 1–6) until it reaches a minimum value (frame 7). The spherical shape is disturbed along the equator of the bubble during the rebound (frames 8–14). An extrusion develops and stays pronounced, while the shape stays symmetric otherwise. The bubble collapses and rebounds a second time in the following frames. Here, the shape changes significantly and the bubble shows aspherical behavior.

Fig. 3-1(b) shows results with mixture 2. The bubble of $R_0 = 1.28$ mm is of almost spherical shape, but surrounding gelatin is not completely clear due to scattered dirt particles. Comparable to the previous case, the bubble remains spherical during the collapse (frames 1–7) and develops a small extrusion along the equator at the beginning of the rebound (frame 8). This deformation remains visible during the rebound (frames 9–14) and the second collapse (frames 15–19). Again, the bubble starts to deform stronger during the second oscillation.

Different phenomena can be observed, when the Gelrite™ concentration is further increased. A bubble of $R_0 = 1.23$ mm, placed in gelatin of mixture 3, is presented in Fig. 3-1(c). The initial shape is not completely spherical but slightly elongated horizontally. In addition, the gelatin shows a non-uniform structure at the bottom of the images. Nevertheless, the dynamic response is similar as before with a uniform collapse (frames 1–7), a slightly deformed rebound (frames 8–13) and an enhanced deformation afterwards (frames 14–20).

Fig. 3-1(d) shows an experiment with mixture 4, the densest gelatin. The figure shows a bubble with an initial radius of $R_0 = 1.42$ mm that appears slightly deformed. As in the previous case, a structure in the gelatin is visible around the bottom half of the bubble. The bubble initially collapses uniformly (frames 1–8) but develops an indentation on the left side during the rebound (frames 9–16). The larger size and the lower driving pressure of that case prolong the collapse and the rebound phase.

One example for a collapse under a lower pressure is presented in Fig. 3-2. The sequence shows a very spherical bubble of $R_0 = 1.27$ mm in a gelatin of mixture 2. After the pressure increase follows an oscillating motion with a contraction (frames 1–11) and an expansion (frames 12–20). In contrast to the previously shown experiments, only a

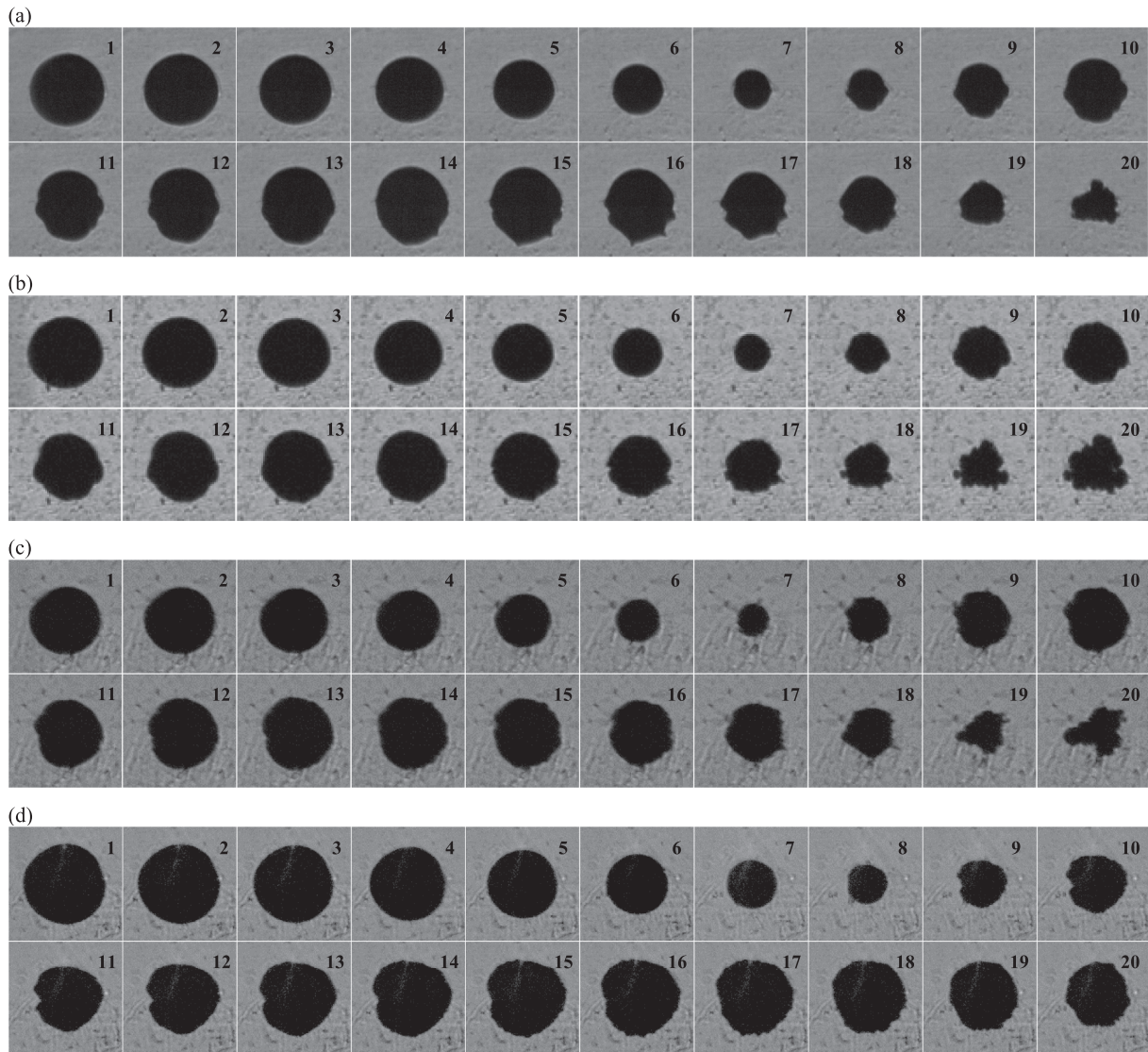


Fig. 3-1. Oscillation of air bubbles in gels of different mixtures. The frame size is $4.0 \times 4.0 \text{ mm}^2$ and the interframe time is $12 \mu\text{s}$. (a) mixture 1 (70% c_2), $R_0 = 1.27 \text{ mm}$, $\Delta p = 3.25 \text{ bar}$; (b) mixture 2 (standard mixture), $R_0 = 1.28 \text{ mm}$, $\Delta p = 3.26 \text{ bar}$; (c) mixture 3 (130% c_2), $R_0 = 1.23 \text{ mm}$, $\Delta p = 3.38 \text{ bar}$; (d) mixture 4 (160% c_2), $R_0 = 1.42 \text{ mm}$, $\Delta p = 2.82 \text{ bar}$.

weak oscillation amplitude is observed, and the bubble always stays in a very spherical shape. We omit here image sequences for other mixtures, as they show a similar weak, and spherical oscillation.

3.2.2. Radius data

To allow a quantitative analysis, we deduce a time-dependent equivalent bubble radius from all image sequences. Pixels that are part of the bubble were counted and a pixel size was provided with a reference length. An area A was calculated, and the equivalent radius R

was taken as $R = (A/\pi)^{0.5}$. This method is exact only for bubbles of perfect sphericity, but it also provides a good representation for bubbles that are only slightly deformed.

As an example, Fig. 3-3 shows the equivalent radius along with the calculated reference for the experiment that was shown in Fig. 3-1(a). The reference calculation is based on Eq. (5) and uses the measured pressure $p(t)$ as an input. The result is plotted as a solid blue line while data points for each of the 128 frames of the captured video are depicted as black crosses. An initial time of $t = 0$ is assigned to the first

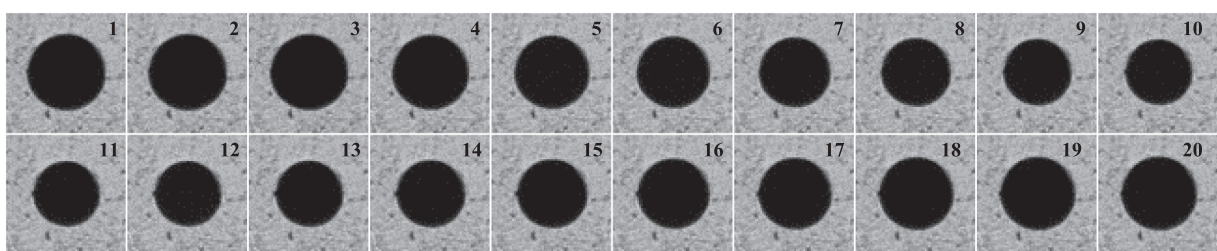


Fig. 3-2. Oscillation of an air bubble in gelatin of mixture 2 (standard mixture) after a low-pressure increase ($\Delta p = 0.44 \text{ bar}$). The interframe time is $16 \mu\text{s}$, the frame size $4.00 \times 4.00 \text{ mm}^2$ and the initial radius is $R_0 = 1.27 \text{ mm}$.

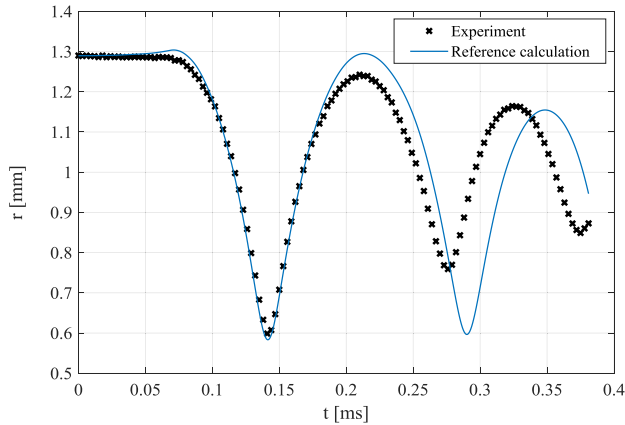


Fig. 3-3. Time-dependent equivalent radius for a single bubble in gelatin of mixture 2 under a high pressure. The corresponding image sequence is displayed in Fig. 3-1 (b). The reference calculation uses the presented Rayleigh-Plesset equation with the case-specific pressure signal $p(t)$ and the properties of water for the liquid.

frame, while the pressure increase that starts the oscillation occurs later. There is a good agreement between the two curves during the first collapse and rebound. For both curves the value and the time of the minimum radius match almost perfectly. Notably, the calculation initially shows a small increase of the radius. This increase reflects the pressure drop before the arrival of the compression wave (compare Fig. 2-3), whereas no visibly growth was detected for this experiment. After the first oscillation, the two curves show a different behavior. The experimental result shows a lower oscillation amplitude at a higher frequency. Both effects are even more pronounced during the following motion until the recording of the video ends.

A comparable behavior, from a qualitative point of view, is visible for experiments at a lower pressure. Fig. 3-4 shows the radius data that corresponds to the experiment presented in Fig. 3-2. The oscillation is much slower and of a much lower amplitude than for higher pressures, but still exhibits the same overall behavior. The curves match very well during the initial phase and during the beginning of the collapse. Towards the end, the curves deviate and the experimentally observed bubble oscillation in gelatin is dampened stronger than the calculated reference in water.

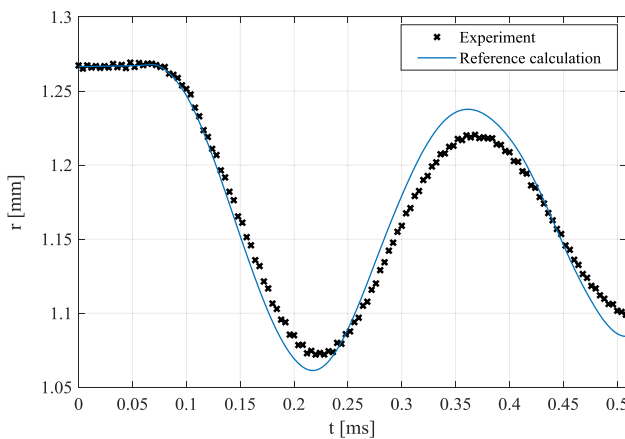


Fig. 3-4. Time-dependent equivalent radius for a single bubble in gelatin of mixture 2 under a lower pressure. The corresponding image sequence is displayed in Fig. 3-2. The reference calculation uses the presented Rayleigh-Plesset equation with the case-specific pressure signal $p(t)$ and the properties of water for the liquid.

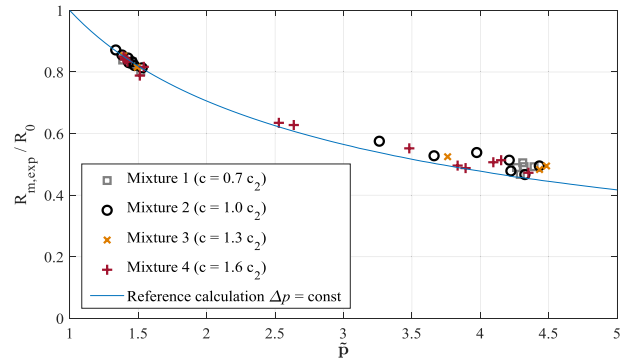


Fig. 3-5. Minimum radius $R_{m,exp}$, normalized by the initial radius R_0 in dependency of the normalized driving pressure during the collapse phase \tilde{p} . Different gelatin mixtures are highlighted according to the legend.

3.2.3. Non-dimensional parameters

Several non-dimensional parameters can be deduced from the radius data to describe the collapse behavior. A first overview is shown in Fig. 3-5 and presents the ratio between the minimum radius $R_{m,exp}$ and the initial radius R_0 for each experiment over a normalized driving pressure \tilde{p} . Here, \tilde{p} is calculated as the ratio between the average pressure during the collapse \bar{p}_c and the initial pressure in the driven section p_1 . Different gelatin concentrations are indicated by different symbols according to the legend. In addition, a reference calculation is plotted that, in this case, uses a constant Δp as the input for the calculation. The figure shows that a smaller radius is reached for an increasing driving pressure. The slope of this trend is steep at the beginning but starts to flatten out at a higher pressure. In general, the experimental results are very close to the theory. At a higher pressure, a difference starts to appear, and the experimental data indicates higher values of the ratio than the theory. Although indicated in the figure, different Gelrite™ concentrations do not show a different behavior.

To investigate the behavior in more detail, we can normalize each experiment with the corresponding calculation. The normalized minimum radius, R^* , is then defined as

$$R^* = \frac{R_{m,exp}}{R_{m,RP}} \quad (6)$$

with $R_{m,RP}$ as the minimum radius from the case-specific calculation with the Rayleigh-Plesset equation. In addition, we calculate a collapse time to provide a temporal reference. The collapse time is defined as the time from the arrival of the compression wave at the bubble position until the moment when the minimum radius is reached. The collapse time of the experiment $t_{c,exp}$ is normalized by the collapse time of the reference calculation $t_{c,RP}$ to give

$$t^* = \frac{t_{c,exp}}{t_{c,RP}} \quad (7)$$

Fig. 3-6 gives an overview of R^* plotted with respect to \tilde{p} . Due to the normalization, the differences appear enhanced. The experimental results match the calculated reference value very accurately for a low-pressure increase. All data points are in a range between $R^* = 0.99$ and $R^* = 1.015$. For increasing pressure, the figure shows a wider range of R^* with data points spread out at a higher level of $R^* = 1-1.15$. Again, the data points for different gelatin concentrations do not show any tendencies but appear randomly distributed.

The corresponding overview for the collapse time is presented in Fig. 3-7. In contrast to the previous case, the data points are not only spread around for the higher, but also for the lower pressure. The value of t^* ranges between $t^* = 0.91$ and $t^* = 1.11$ and data points are well-distributed in between. Calculating the average gives a value of $t^* = 1.01$, which verifies the general similarity to water. However, the evaluation of the impact of the gelatin concentration is difficult since a

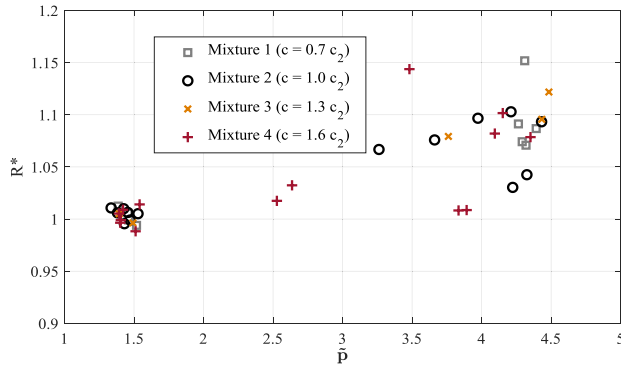


Fig. 3-6. Normalized minimum radius R^* plotted in dependency of the normalized driving pressure during the collapse phase \tilde{p} . Different gelatin mixtures are highlighted according to the legend.

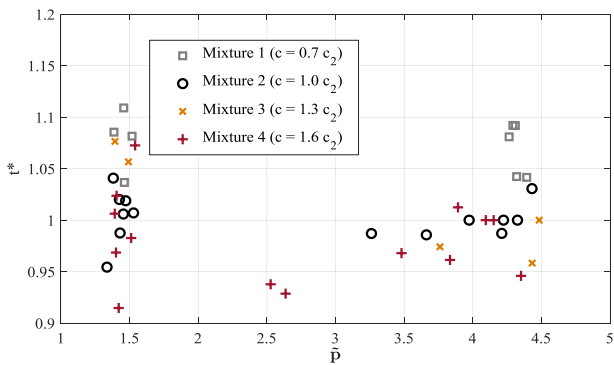


Fig. 3-7. Normalized collapse time t^* plotted in dependency of the normalized driving pressure during the collapse phase \tilde{p} . Different gelatin mixtures are highlighted according to the legend.

clear statement is not possible. At first glance, it looks like increasing the gelatin concentration leads to decreased collapse times. But some data points clearly contradict this impression. Thus, we expect that this is an effect of general uncertainty and the limited number of experiments. Especially, no corresponding effect is observed with respect to R^* , and comparable work with cavitation bubbles shows that adding polymer additives to water for non-Newtonian behavior does not significantly affect the growth and collapse of a bubble [35,36].

3.3. Discussion

3.3.1. A comment on the accuracy

Before assessing the bubble behavior in detail, it is worth highlighting some uncertainties and inaccuracies of the presented method.

- **Resolution:** The experimental setup limits the accuracy of the optical measurement data. Both a spatial and a temporal limit results directly from the camera system. Typically, the bubble is resolved at a resolution of $30\text{--}63 \mu\text{m pixel}^{-1}$ with around 40–80 pixels per diameter. This results in a spatial inaccuracy for the radii of $\Delta r = \pm 1.25\text{--}2.5\%$ when assuming an error within one pixel. The temporal evolution of the collapse is typically captured between 20 and 40 images, which gives a temporal inaccuracy for the collapse time of $\Delta t_c = \pm 1.25\text{--}2.5\%$ when considering an error of half the interframe time.
- **Minimum radius:** The temporal inaccuracy includes an additional drawback onto the spatial error. Due to the limited number of frames, it cannot be assured that the minimum radius is always captured. This directly results in a systematic error that overestimates the minimum radius. The error depends on the curvature of $r(t)$ close to the minimum. For example, the minimum radius

$r_{m,\text{exp}}$ is overestimated up to $\Delta r = 0.77\%$ for the experiment presented in Fig. 3-3 and up to $\Delta r = 0.016\%$ for the experiment of Fig. 3-4.

- **Bubble shape:** The application of gelatin in this setup leads to inhomogeneities in the liquid surrounding the bubble, whether through a non-uniform cool-down or the insertion of the needle for bubble production. These disturbances affect the symmetry of the bubble collapse and introduce an error when calculating the equivalent radius. Special care was taken to maximize the level of sphericity of the initial bubble and minimize deformation during the oscillation. To account for a potential deformation in the direction normal to the image plane, we inspected the bubbles carefully before the experiments. Nevertheless, some uncertainty with respect to the bubble shape remains and is difficult to assess.

3.3.2. Assessment of the gelatin influence

One main aspect of this study was to compare the behavior of the bubbles in gelatin with the reference case of bubbles in water. Overall, it was shown that bubbles in both cases behave similarly, especially during the first collapse. Representative image sequences show that bubbles initially collapse in a spherical shape, and the corresponding radius plots agree well with the theory (see Figs. 3-3 and 3-4). Furthermore, non-dimensional parameters shown in Figs. 3-5–3-7 confirm the overall similarity, but also highlight some differences. Overall, two main aspects stand out.

- Despite qualitatively very different gelatin mixtures, the results show that the gelatin concentration does not influence the bubble behavior noticeably. This indicates that non-Newtonian properties play a minor role. Although it is difficult to compare to previous work, this result agrees with other research on non-Newtonian liquids. Brujan and Williams [35] investigate for example the effect of polymer additives on cavitation bubbles and note that no different behavior is noticed when bubbles of a radius larger than 0.5 mm are studied. Further support stems from measurements of fluid properties. Deasy et al. [37] provide a yield (shear) stress of 1150 Pa for a Gelrite™ mixture similar to mixture 2. This value is small compared to the driving pressure levels of 0.36–3.38 bar, which supports the reduced influence.
- At lower driving pressures, the bubbles in gelatin behave similarly to water. Applying a higher driving pressure leads to larger deviations between experiment and theory with respect to the minimum radius (Figs. 3-5 and 3-6). As afore mentioned, non-Newtonian behavior is expected to be minor, but the discrepancy can be explained by the aspherical behavior of the bubble during the collapse. Deformation is enhanced for higher driving pressures and often starts to appear when the minimum radius is reached. For example, often a deformation along the equator of the bubble appears directly after the first collapse (compare Fig. 3-1(a–b)). This makes it difficult to identify the minimum radius accurately and in general leads to an overestimation of the calculated equivalent radius, which explains the observed trend.

The presented conclusions apply for the first collapse, while subsequent oscillations differ significantly from the performed reference calculation. Besides the mentioned increased asymmetry of the bubble in time, the higher viscosity of the gelatin lowers the oscillation amplitude and affects the oscillation frequency.

In summary, the shown cases demonstrate that gelatin is a suitable surrogate for water and can be utilized for studies of bubble dynamics that focus on the initial bubble collapse. Care must be taken to assure a spherical bubble shape, but the obtained results for collapse time and minimum radius show no dependency with respect to the gelatin concentration.

4. Bubble pairs

A conclusion of the previous section is that limitations of the setup do not limit the possibility to conduct research on a more general level. Thus, we use the experimental setup to produce multiple bubbles and study the interaction of gas bubble pairs.

4.1. Non-dimensional parameters

Typically, three non-dimensional parameters are defined to characterize bubble pairs: a relative distance, a size ratio and a phase difference. Chew et al. [38] define the relative initial bubble distance as

$$\gamma = \frac{d}{R_1 + R_2} \quad (8)$$

where d is the distance between the bubble centers and R_1 and R_2 are the maximum radii of the two interacting bubbles. Furthermore, the size difference is defined as

$$S = \frac{R_L}{R_S} \quad (9)$$

with R_L and R_S as the maximum radius of the large and the small bubble respectively. The third parameter, $\Delta\theta$, indicates the phase difference of the two bubbles, but the definition in the literature cannot be easily applied here, due to the different experimental setups. Experiments in related literature produce vapor cavities by means of laser-focus or electric discharge, while in this study, gas bubbles are present in an initially stationary setup. This leads, for example, to the problem that no well-defined time difference Δt of bubble initiation exists. Thus, the definition of Chew et al. [38]

$$\Delta\theta = \left| \left(\frac{t_1}{t_{osc,1}} - \frac{t_2}{t_{osc,2}} \right) \right| + \frac{\Delta t}{t_{osc,1}} \quad (10)$$

simplifies for the current case to

$$\Delta\theta = \left| \left(\frac{t_{osc,1}}{t_{osc,1}} - \frac{t_{osc,1}}{t_{osc,2}} \right) \right| = 1 - \frac{t_{osc,S}}{t_{osc,L}} \quad (11)$$

where t_{osc} gives an oscillation period, taken here as the time from maximum to minimum bubble radius in contrast to the duration from bubble nucleation to bubble collapse in the original definition. With the oscillation time of the smaller bubble, $t_{osc,S}$, being shorter than the oscillation time of the bigger bubble, $t_{osc,L}$, always a positive value for the phase difference results. Consequently, a value of $\Delta\theta = 0$ results as the minimum for equally sized and equally oscillating bubbles. A value of $\Delta\theta$ close to 1 represents bubbles of largely different sizes. Han et al. [39] note that $\Delta\theta$, in its original definition, is not independent of S . Instead, they propose a different parameter, τ , as a relative initiation time difference. Applied to the present setup, this parameter would always give a value of $\tau = 0$, as bubbles are initially present. However, following their initial reasoning, we can assume a linear relation between radius and collapse time that can be justified by the Rayleigh collapse time for single bubbles [3]. This results in the phase difference solely depending on the size ratio, and Eq. (11) transforming to:

$$\Delta\theta = 1 - \frac{R_S}{R_L} = 1 - \frac{1}{S} \quad (12)$$

It should be noted, that the normalized distance γ is calculated from the two-dimensional image, so the value is only accurate if the centers of the two bubbles are in the same plane normal to the light path. The distance can be underestimated if one bubble is displaced along the light path.

4.2. Types of interaction

The behavior of bubble pairs was investigated for differently sized

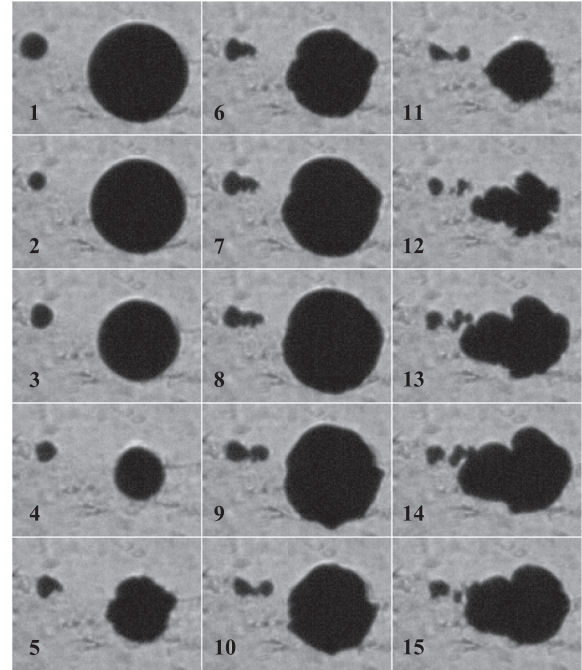


Fig. 4-1. Interacting bubble pair with $R_L = 1.0$, $R_S = 0.26$, $S = 3.86$, $\Delta\theta = 0.74$ and $\gamma = 1.74$. The interframe time is 16 μs .

bubbles of $S = 1.0$ –7.36 ($\Delta\theta = 0.0$ –0.87) at various distances of $\gamma = 0.99$ –1.97. All experiments were conducted in the high-pressure range and, except for two cases, only gelatin of mixture 2 was used. In general, the bubble interaction can be observed clearly during the first oscillation, whereas bubbles often show an irregular shape after the second collapse. This is in accordance to results of the previous section. In addition, liquid jets are not observed directly in the presented image sequences, but there are clear indications for them. Identifying the jets serves as a main feature to separate different bubble behavior and helps to define four types of bubble pair interaction that are presented in the following.

4.2.1. Weak interaction

The first type describes a bubble pair that does not interact strongly due to the large size ratio and relative distance. Fig. 4-1 presents a corresponding example with a big bubble and a small bubble ($S = 3.86$) that are a certain distance apart ($\gamma = 1.74$). The small bubble on the left collapses immediately after the pressure increase (frame 2) and oscillates at a high frequency. It follows the motion of the collapse of the big bubble (frames 1–4) and starts to elongate once the big bubble rebounds (frames 5–8). As soon as the big bubble contracts again, the small bubble follows this movement, whereas the big bubble seems not affected by any interaction. Consecutive frames show that the small bubble starts to split into two parts (frames 9–12). A tiny bubble fragment remains, but the closer part eventually is captured by the big bubble that now has a very aspherical shape (frame 15). For this case, the general dynamics is dominated by the big bubble. It creates a periodic movement that, combined with the high-frequency oscillation of the small bubble, leads to bubble splitting.

4.2.2. Shooting through

For small bubbles that are close to the main bubble, we observe a ‘shooting through’ behavior. Fig. 4-2, shows an image sequence with a similar size ratio as the previous case ($S = 4.08$), but now with the two bubbles close together ($\gamma = 0.99$). After the pressure increase, the big bubble collapses spherically (frames 1–6), while the small bubble contracts and follows the boundary of the big bubble. The two bubbles merge (frame 4) and the remaining bubble maintains a spherical shape

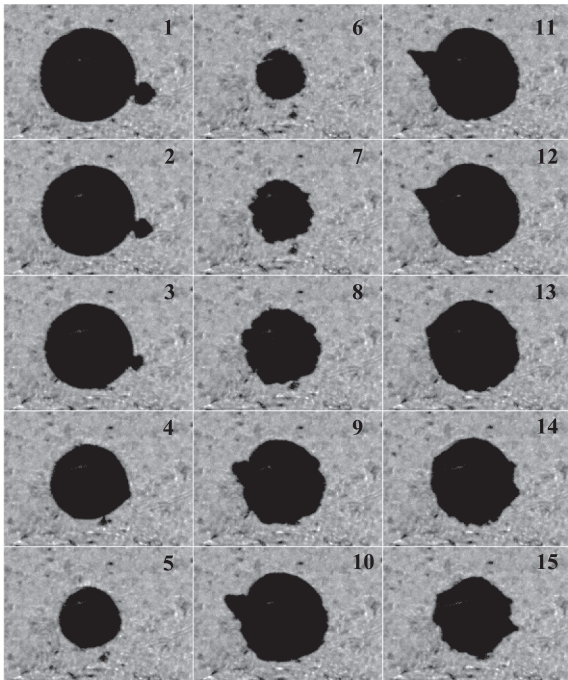


Fig. 4-2. Interacting bubble pair with $R_L = 1.51$, $R_S = 0.37$, $S = 4.08$, $\Delta\theta = 0.76$ and $\gamma = 0.99$. The interframe time is $16 \mu\text{s}$.

during the collapse and initial rebound. However, the collapse of the small bubble into the big bubble induces a liquid jet that shoots through the big bubble and penetrates the surface on the far side during the rebound. The effect is seen as a funnel-shaped protrusion that develops at the side opposite to the original position of the small bubble (frames 9–13). This type of behavior is, as such, not presented in the literature, but setting up bubbles in this constellation provides an opportunity to generate a controlled and directed liquid jet.

4.2.3. Reversing collapse

A reversing collapse is observed for the combination of a large and a medium-sized bubble. An example of this case is presented in Fig. 4-3 with $S = 1.71$ and $\gamma = 1.24$. Both bubbles contract spherically in the initial phase (frames 1–3), but the medium-sized bubble collapses faster due to the smaller size. This collapse is aspherical and creates a jet on

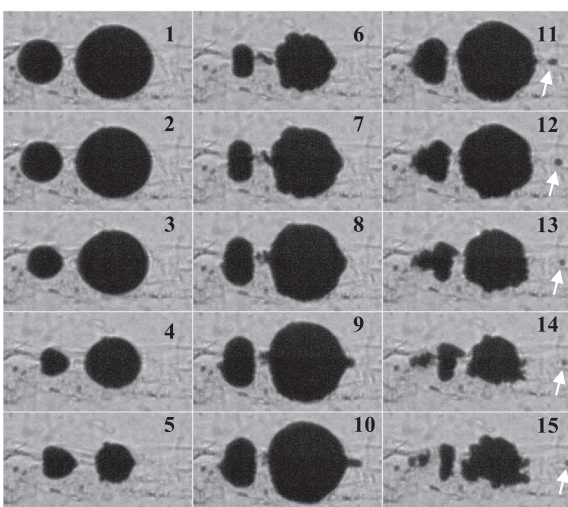


Fig. 4-3. Interacting bubble pair with $R_L = 1.09$, $R_S = 0.63$, $S = 1.71$, $\Delta\theta = 0.42$ and $\gamma = 1.24$. The interframe time is $16 \mu\text{s}$. White arrows highlight a small bubble that detaches from the main bubble.

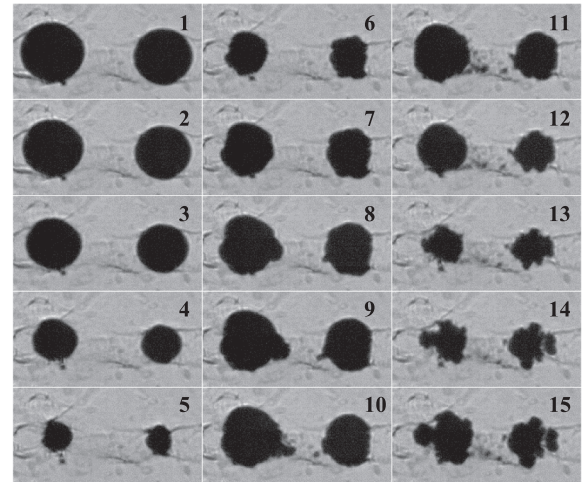


Fig. 4-4. Interacting bubble pair with $R_L = 0.91$, $R_S = 0.84$, $S = 1.09$, $\Delta\theta = 0.08$ and $\gamma = 1.86$. The interframe time is $12 \mu\text{s}$.

the right side towards the other bubble (frame 5–6). A part of this jet quickly disconnects from the bubble and remnants remain visible in between the two bubbles. After this collapse, the motion reverses and the medium-sized bubble expands in the opposite direction (frames 7–10). The medium-sized bubble first shows a shape that points away from the big bubble (frames 11–12) and then splits into two parts (frames 13–15). Meanwhile, the large bubble behaves similarly to the previous case and again shows a jet away from the smaller bubble. A small satellite bubble detaches from that jet and continues to move to the right (frames 11–15, highlighted by white arrows). The aspect of both bubbles jetting away from each other provides some similarities to previous work. Chew et al. [38] simply define one interaction type as ‘jet away’. However, the reversing motion also indicates some differences and in some way shows more similarities to what Chew et al. [38] label the ‘catapult’ type and Han et al. [39] describe as anti-phase bubble pairs.

4.2.4. Collapse towards

A final type describes bubbles that collapse towards each other. For the presented example in Fig. 4-4, the bubbles are of similar size ($S = 1.09$) and farther apart ($\gamma = 1.86$). Both bubbles collapse spherically (frames 1–5) but show an aspherical behavior during the rebound. They develop a liquid jet directed to the other bubble that is visible as a protrusion (frames 8–10). The bubble motion is largely in phase and often appears symmetric. The following oscillation still shows a directional behavior that slowly brings the bubbles closer together. This behavior is well known and has also been shown more recently in other experimental work [7,29,39].

4.3. Characterization with non-dimensional parameters

Having classified different types of bubble interaction we can display the type for each conducted experiment with respect to $\Delta\theta$ and γ (Fig. 4-5). Three experiments are characterized as in between, because they show a mixed behavior with aspects of two other types.

The figure shows that the same interaction behavior is associated to distinct regions of $\Delta\theta$ and γ . This indicates that there is a relation between the non-dimensional parameters and the interaction type. This would allow a prediction of the bubble behavior that solely depends on the initial configuration of the bubble pair. It is difficult to compare these results to previous findings in the literature due to the different experimental setup, but Chew et al. [38] apply a similar classification with respect to $\Delta\theta$ and γ for their experiments. For $1 < \gamma < 2$ their work identifies two distinct regions of different behavior as ‘jet towards’ and ‘jet away’. The regions are separated by a critical phase difference

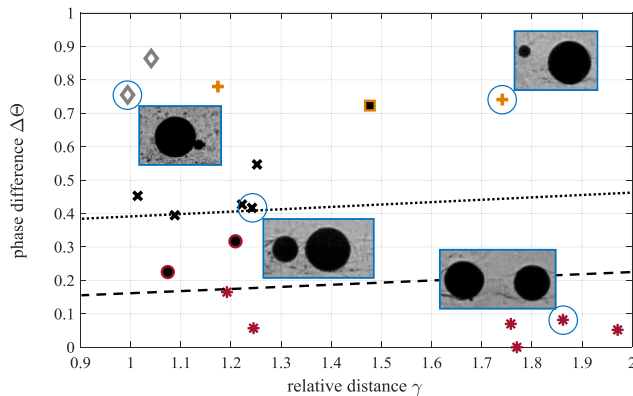


Fig. 4-5. Types of bubble pair interaction with respect to $\Delta\theta$ and γ : Weak interaction (orange plus icon), shooting through (gray diamond), reversing collapse (black cross), collapse towards (red star), and mixed type behavior (black dot in red circle and black square surrounded by an orange line). The dashed and dotted lines present, for reference, the critical $\Delta\theta_c$ value after Chew et al. [38] that separates the types of ‘jet away’ ($\Delta\theta > \Delta\theta_c$) and ‘jet towards’ ($\Delta\theta < \Delta\theta_c$) for bubbles of similar and different size respectively. (For interpretation of the references to color in this figure legend, the reader is referred to the web version of this article.)

$\Delta\theta_c$ that is around 0.2 for similarly-sized bubbles (dashed line) and around 0.45 for differently-sized bubbles (dotted line). Bubbles collapse towards each other when $\Delta\theta$ is below the critical value, and away from each other when a $\Delta\theta$ higher than the critical value. This behavior agrees well with the separation in Fig. 4-5 between the type of collapse towards and of reversing collapse. Chew et al. [38] also define two other distinct regions of the types coalescence and catapult, but they are located at $\gamma < 1$. Such a value cannot be reproduced in the present study. In contrast, the interaction of a very small bubble with a larger bubble is only discussed in the present work and is not mentioned specifically in the literature.

5. Conclusion

In this work, we present a new type of experimental setup and discuss its advantages and limitations. In a first part, the setup is used to investigate the influence of gelatin on bubble dynamics. Results show that bubbles in gelatin behave very similarly to bubbles in water during the first oscillation and that changing the gelatin concentration does not have a noticeable influence on the bubble collapse. In a second part, we study the interaction of gas bubble pairs in the free field and find four types of bubble pair interaction that can be defined by non-dimensional parameters. This classification differs from the literature in some respects due to the use of pure gas bubbles instead of vapor bubbles.

The results of this work indicate the potential of the setup, but also show some limitations. One remaining challenge is the production of a uniform gelatin and a perfectly spherical bubble. In addition, further improvements in the optical system can help to reduce the uncertainty and provide deeper insight into the collapse behavior. Future investigations can take advantage of these improvements and of the possibilities of the setup. An interesting option is to create bubbles of different gas content and study the effect on the bubble behavior or to study the interaction of a collapsing bubble with soft material. However, more work on bubble-bubble interaction should also be aimed for to study a wider range of S and γ or possibly expand from bubble pairs to several interacting bubbles.

Declaration of Competing Interest

There is no financial or personal relationship between authors and other people or organizations that could inappropriately influence or bias the work.

Acknowledgements

The authors acknowledge funding by the European Research Council (ERC) under the European Union’s Horizon 2020 research and innovation program (grant agreement No. 667483).

References

- [1] Z. Wang, T. Hopfes, M. Giglmaier, N.A. Adams, Influence of non-Newtonian gelatinous fluids on bubble collapse dynamics, 5th Int. Conf. Exp. Fluid Mech. (2018).
- [2] T. Hopfes, Z. Wang, M. Giglmaier, N.A. Adams, Dynamics of collapsing multi-bubble arrangements, 5th Int. Conf. Exp. Fluid Mech. (2018).
- [3] C.E. Brennen, Fundamentals of Multiphase Flow, Cambridge University Press, Cambridge, 2005 <https://doi.org/10.1017/CBO9780511807169>.
- [4] K. Chaussy, W. Brendel, E. Schmiedt, Extracorporeally induced destruction of kidney stones by shock waves, Lancet (London, England). 2 (1980) 1265–1268.
- [5] A.J. Coleman, J.E. Saunders, A review of the physical properties and biological effects of the high amplitude acoustic fields used in extracorporeal lithotripsy, Ultrasonics 31 (1993) 75–89, [https://doi.org/10.1016/0041-624X\(93\)90037-Z](https://doi.org/10.1016/0041-624X(93)90037-Z).
- [6] E. Unger, T. Porter, J. Lindner, P. Grayburn, Cardiovascular drug delivery with ultrasound and microbubbles, Adv. Drug Deliv. Rev. 72 (2014) 110–126, <https://doi.org/10.1016/j.addr.2014.01.012>.
- [7] S.W. Fong, D. Adhikari, E. Klaseboer, B.C. Khoo, Interactions of multiple spark-generated bubbles with phase differences, Exp. Fluids 46 (2009) 705–724, <https://doi.org/10.1007/s00348-008-0603-4>.
- [8] O. Lindau, W. Lauterborn, Cinematographic observation of the collapse and rebound of a laser-produced cavitation bubble near a wall, J. Fluid Mech. 479 (2003) 327–348, <https://doi.org/10.1017/S0022112002003695>.
- [9] W. Lauterborn, T. Kurz, Physics of bubble oscillations, Rep. Prog. Phys. 73 (2010) 106501, <https://doi.org/10.1088/0034-4885/73/10/106501>.
- [10] G.N. Sankin, P. Zhong, Interaction between shock wave and single inertial bubbles near an elastic boundary, Phys. Rev. E - Stat. Nonl. Soft Matter Phys. 74 (2006) 1–4, <https://doi.org/10.1103/PhysRevE.74.046304>.
- [11] A. Philipp, W. Lauterborn, Cavitation erosion by single laser-produced bubbles, J. Fluid Mech. 361 (1998) 75–116, <https://doi.org/10.1017/S0022112098008738>.
- [12] Y. Zhang, F. Chen, Y. Zhang, Y. Zhang, X. Du, Experimental investigations of interactions between a laser-induced cavitation bubble and a spherical particle, Exp. Therm. Fluid Sci. 98 (2018) 645–661, <https://doi.org/10.1016/j.expthermflusci.2018.06.014>.
- [13] D. Obreschkow, M. Tinguely, N. Dorsaz, P. Kobel, A. De Bosset, M. Farhat, Universal scaling law for jets of collapsing bubbles, Phys. Rev. Lett. 107 (2011) 3–6, <https://doi.org/10.1103/PhysRevLett.107.204501>.
- [14] K.S.F. Lew, E. Klaseboer, B.C. Khoo, A collapsing bubble-induced micropump: an experimental study, Sens. Actuat. A Phys. 133 (2007) 161–172, <https://doi.org/10.1016/j.sna.2006.03.023>.
- [15] C.F. Naudé, A.T. Ellis, On the mechanism of cavitation damage by nonhemispherical cavities collapsing in contact with a solid boundary, J. Basic Eng. 83 (1961) 648, <https://doi.org/10.1115/1.3662286>.
- [16] Y. Tomita, A. Shima, Mechanisms of impulsive pressure generation and damage pit formation by bubble collapse, J. Fluid Mech. 169 (1986) 535–564, <https://doi.org/10.1017/S0022112086000745>.
- [17] A.M. Zhang, P. Cui, Y. Wang, Experiments on bubble dynamics between a free surface and a rigid wall, Exp. Fluids 54 (2013), <https://doi.org/10.1007/s00348-013-1602-7>.
- [18] Y. Tomita, Interaction of a shock wave with a single bubble, Shock Wave Sci. Technol. Ref. Libr. Springer Berlin Heidelberg, Berlin, Heidelberg, 2007, pp. 35–66, https://doi.org/10.1007/978-3-540-35846-6_2.
- [19] T. Kodama, K. Takayama, N. Nagayasu, The dynamics of two air bubbles loaded by an underwater shock wave, J. Appl. Phys. 80 (1996) 5587–5592, <https://doi.org/10.1063/1.363605>.
- [20] T. Kodama, Y. Tomita, Cavitation bubble behavior and bubble-shock wave interaction near a gelatin surface as a study of in vivo bubble dynamics, Appl. Phys. B Lasers Opt. 70 (2000) 139–149, <https://doi.org/10.1007/s003400050022>.
- [21] T. Kodama, K. Takayama, Dynamic behavior of bubbles during extracorporeal shock-wave lithotripsy, Ultrason. Med. Biol. 24 (1998) 723–738, [https://doi.org/10.1016/S0301-5629\(98\)00022-2](https://doi.org/10.1016/S0301-5629(98)00022-2).
- [22] A. Philipp, M. Delius, C. Scheffczyk, A. Vogel, W. Lauterborn, Interaction of lithotripter-generated shock waves with air bubbles, J. Acoust. Soc. Am. 93 (1993) 2496–2509, <https://doi.org/10.1121/1.406853>.
- [23] C.D. Ohl, R. Ikink, Shock-wave-induced jetting of micron-size bubbles, Phys. Rev. Lett. 90 (2003) 4, <https://doi.org/10.1103/PhysRevLett.90.214502>.
- [24] S. Fujikawa, T. Akamatsu, Experimental investigations of cavitation bubble collapse by a water tube, Japan Soc. Mech. Eng. 21 (1978) 223–230.
- [25] K. Vokurka, The use of a shock tube in bubble dynamics studies, Czechoslov. J. Phys. 42 (1992) 291–302, <https://doi.org/10.1007/BF01598426>.
- [26] J.P. Dear, J.E. Field, A study of the collapse of arrays of cavities, J. Fluid Mech. 190 (1988) 409–425, <https://doi.org/10.1017/S0022112088001387>.
- [27] A.B. Swantek, J.M. Austin, Collapse of void arrays under stress wave loading, J. Fluid Mech. 649 (2010) 399–427, <https://doi.org/10.1017/S0022112009993545>.
- [28] J.D. Anderson, Modern Compressible Flow: With Historical Perspective, McGraw-Hill, New York, 1990.
- [29] P. Cui, Q.X. Wang, S.P. Wang, A.M. Zhang, Experimental study on interaction and coalescence of synchronized multiple bubbles, Phys. Fluids 28 (2016), <https://doi.org/10.1063/1.4944444>.

- [org/10.1063/1.4939007](https://doi.org/10.1063/1.4939007).
- [30] G.S. Settles, *Schlieren and Shadowgraph Techniques*, Springer Berlin Heidelberg, Berlin, Heidelberg, 2001 <https://doi.org/10.1007/978-3-642-56640-0>.
- [31] L. Brekhovskikh, *Waves in Layered Media*, Elsevier, 2012.
- [32] J.P. Dear, J.E. Field, A.J. Walton, Gas compression and jet formation in cavities collapsed by a shock wave, *Nature* 332 (6164) (1988) 505–508, <https://doi.org/10.1038/332505a0> <http://www.nature.com/articles/332505a0> <https://doi.org/10.1038/332505a0>.
- [33] N.K. Bourne, J.E. Field, Shock-induced collapse of single cavities in liquids, *J. Fluid Mech.* 244 (1992) 225–240, <https://doi.org/10.1017/S0022112092003045>.
- [34] N.K. Bourne, J.E. Field, Shock-induced collapse and luminescence by cavities, *R. Soc. Soc.* 357 (1999) 295–311.
- [35] E.A. Brujan, P.R. Williams, Cavitation phenomena in non-Newtonian liquids, *Chem. Eng. Res. Des.* 84 (2006) 293–299, <https://doi.org/10.1205/cherd05054>.
- [36] A.V. Bazilevskii, D.D. Meier, A.N. Rozhkov, Dynamics of a spherical microcavity in a polymeric liquid, *Fluid Dyn.* 38 (2003) 351–362.
- [37] P.B. Deasy, K.J. Quigley, Rheological evaluation of deacetylated gellan gum (Gelrite) for pharmaceutical use, *Int. J. Pharm.* 73 (1991) 117–123, [https://doi.org/10.1016/0378-5173\(91\)90034-L](https://doi.org/10.1016/0378-5173(91)90034-L).
- [38] L.W. Chew, E. Klaseboer, S.W. Ohl, B.C. Khoo, Interaction of two differently sized oscillating bubbles in a free field, *Phys. Rev. E - Stat. Nonl. Soft Matter Phys.* 84 (2011), <https://doi.org/10.1103/PhysRevE.84.066307>.
- [39] B. Han, K. Köhler, K. Jungnickel, R. Mettin, W. Lauterborn, A. Vogel, Dynamics of laser-induced bubble pairs, *J. Fluid Mech.* 771 (2015) 706–742, <https://doi.org/10.1017/jfm.2015.183>.

A.2 Secondary Atomization of Liquid Metal Droplets at Moderate Weber Numbers

Thomas Hopfes, Julia Petersen, Zhaoguang Wang, Marcus Giglmaier, Nikolaus A. Adams

In: *International Journal of Multiphase Flow* 143 (2021) 103723.
<https://doi.org/10.1016/j.ijmultiphaseflow.2021.103723>.

Contributions: My contributions to this publication include conceiving the original idea of the study and adapting the experimental setup to allow to study liquid metal droplet breakup. I conducted the investigation by performing the experiments, processing and analyzing the study data, and visualizing the results. The original manuscript of the publication was written by me.



Secondary Atomization of Liquid Metal Droplets at Moderate Weber Numbers

Author: T. Hopfes, J. Petersen, Z. Wang, M. Giglmaier, N.A. Adams

Publication: International Journal of Multiphase Flow

Publisher: Elsevier

Date: October 2021

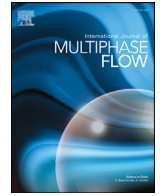
© 2021 Elsevier Ltd. All rights reserved.

Journal Author Rights

Please note that, as the author of this Elsevier article, you retain the right to include it in a thesis or dissertation, provided it is not published commercially. Permission is not required, but please ensure that you reference the journal as the original source. For more information on this and on your other retained rights, please visit: <https://www.elsevier.com/about/our-business/policies/copyright#Author-rights>

BACK

CLOSE WINDOW



Secondary Atomization of Liquid Metal Droplets at Moderate Weber Numbers

T. Hopfes*, J. Petersen, Z. Wang, M. Giglmaier, N.A. Adams

Chair of Aerodynamics and Fluid Mechanics, Technical University of Munich, Boltzmannstr. 15, D-85748 Garching bei München, Germany



ARTICLE INFO

Article history:

Received 3 December 2020

Revised 15 May 2021

Accepted 10 June 2021

Available online 17 June 2021

Keywords:

Secondary atomization

Droplet breakup

Galinstan

Liquid metal

Shock tube

ABSTRACT

Atomization of liquid metal is an essential process in a variety of production methods such as spray forming or laser sintering. A critical part of all atomization processes is the breakup of single droplets, also termed secondary atomization. While it has been widely analyzed for conventional liquids, studies focusing on the influence of the specific properties of liquid metals remain rare. To identify differences, this work investigates single liquid metal Galinstan droplets exposed to a shock-induced crossflow by recording the breakup with a high-speed camera. The experimental test series covers a Weber number range of 11–104, and results show that the breakup morphology of Galinstan droplets follows the known sequence of bag, bag-and-stamen, multimode, and shear stripping breakup. We identify transition Weber numbers of ~15, ~35, and ~80, respectively, but also show that transition between modes is a continuous process with gradual changes. Compared to conventional liquids, the initial deformation of Galinstan droplets is very similar with respect to the shape, the initial deformation time, and the maximum cross-stream diameter. In contrast, later stages of the breakup process show clear differences. We observe that the onset of breakup appears significantly earlier in non-dimensional time, that Galinstan bags inflate much less, and that the bag breakup does not exhibit the same phenomenology as that of a water droplet. Further differences in the droplet shape and fragmentation suggest that the elastic oxide layer forming on Galinstan plays an essential role.

© 2021 Elsevier Ltd. All rights reserved.

1. Introduction

Atomization of molten metal enables a large variety of applications and future technology like spray forming or spray deposition processes that use a liquid-solid spray mixture to form a new part (Henein et al., 2017) or to coat an existing part (Grant, 1995). In addition, atomized liquid metal is cooled down, collected as powder, and is either directly used, e.g. in rocket propulsion (Galfetti et al., 2007), or serves as feedstock in secondary applications and processing methods like additive manufacturing and sintering (Bauckhage, 1992; Van der Schueren and Kruth, 1995). These new applications produce near-final shaped parts, allowing a higher agility from design to product and production of complex parts in resource saving and economical processes (Anderson et al., 2018; Henein et al., 2017). However, atomization of metallic alloys remains challenging. In additive manufacturing, for example, insufficient quality of the powder feedstock can lead to deficiencies in the final product. At the same time, a low efficiency in powder production also leads to high costs (Anderson et al., 2018). To over-

come these limitations, a key factor is to conduct more fundamental research on atomization in areas where sufficient understanding is currently lacking (Anderson et al., 2018).

Independent of the exact application or atomization approach, the core atomization process can be separated into two main mechanisms: primary breakup and secondary breakup (Firmansyah et al., 2014; Ünal, 1989; Zeoli and Gu, 2006). Primary breakup comprises the formation of ligaments and large droplets from bulk liquid through surface oscillations that are induced, for example, by high-velocity relative gas flows. The subsequent secondary breakup refers to the fragmentation of a single droplet by aerodynamic forces (Firmansyah et al., 2014; Guildenbecher et al., 2009). Secondary breakup greatly reduces the droplet size. It is well understood that it defines the final fragment size distributions more than the primary breakup (Firmansyah et al., 2014; Mates and Settles, 2005; Watanawanyoo et al., 2011; Zeoli and Gu, 2006). However, secondary atomization of liquid metals is rarely studied in the literature. Therefore, to provide a fundamental basis, we investigate this topic experimentally using single liquid metal Galinstan droplets. We emphasize specific properties and effects that differentiate metals from previously analyzed liquids.

* Corresponding author.

E-mail address: thomas.hopfes@tum.de (T. Hopfes).

Table 1

Transition We for Newtonian drops with $Oh < 0.1$ adopted from references (Dai and Faeth, 2001; Guildenbecher et al., 2009). Note that Guildenbecher et al. (2009) define bag breakup for $We = 11-35$ and discuss bag-and-stamen as part of the multimode breakup.

Breakup Mode	Range
Bag	$\sim 11 < We < \sim 18$
Bag-and-stamen (or bag/plume)	$\sim 18 < We < \sim 40$
Multimode	$\sim 40 < We < \sim 80$
Shear stripping (or sheet-thinning)	$\sim 80 < We$

For more conventional liquids, the fragmentation of single droplets has been studied extensively and it has been well established that the breakup morphology is mainly determined by the Weber number (We) and the Ohnesorge number (Oh) (Hinze, 1955; Pilch and Erdman, 1987).

$$We = \rho_g u_\infty^2 d_0 / \sigma \quad (1)$$

$$Oh = \mu_d / \sqrt{\rho_d d_0 \sigma} \quad (2)$$

Here, ρ_g and u_g represent the density and velocity of the gas flow, while d_0 , σ , μ_d , and ρ_d represent the initial diameter, the surface tension, the dynamic viscosity, and the density of the liquid drop, respectively. The Weber number represents the ratio between the disruptive aerodynamic force and the restorative surface tension. The Ohnesorge number compares the viscous force to the surface tension and when below a value of 0.1, the influence of liquid viscosity on the breakup regime diminishes, and the Weber number is the dominating factor (Guildenbecher et al., 2009).

The morphology of droplet breakup varies strongly with changing Weber number. Several breakup modes are observed and the transition between them is often characterized by a transition Weber number. Depending on the literature, different values for the transition values are found and the names of the modes vary slightly (Cao et al., 2007; Chou et al., 1997; Dai and Faeth, 2001; Hsiang and Faeth, 1995; Jain et al., 2015, 2019; Krzeczowski, 1980; Pilch and Erdman, 1987). For the current work, we adopt the transition values of Dai and Faeth, (2001) and add terminology after Guildenbecher et al. (2009) as shown in Table 1. The presented single transition values do not strictly separate the modes as we will show later. Instead, transition should rather be understood as a continuous process (Guildenbecher et al., 2009).

The bag and bag-and-stamen modes are well understood as a result of the Rayleigh-Taylor (R-T) instability developed at the accelerated droplet front (Joseph et al., 1999), but some studies also identify other physical mechanisms. In discussion are the pressure imbalance between the front and rear side of the drop (Opfer et al., 2014), the stress repartition around the surface (Villermaux and Bossa, 2009), and the structure of flow vortices in the wake (Inamura et al., 2009). Following the bag-and-stamen mode, the multimode breakup is an intermediate regime, in which the R-T instability is superimposed by aspects of shear stripping. Shear stripping is the next breakup mode, but the exact physical mechanisms behind it are still unclear. No agreement has been achieved on whether the viscous shear or the aerodynamic drag is the driving force. Correspondingly, the name of this regime varies among shear stripping (Ranger and Nicholls, 1969), sheet thinning (Liu and Reitz, 1997) and shear-induced entrainment (Theofanous and Li, 2008). For the current work, the terminology of shear stripping is adopted.

While this classification for conventional liquids is backed by extensive work in the literature, liquid metal aerobreakup is rarely singled out as an investigated topic. This is interesting because several additional aspects must be considered. Often, high tempera-

tures are necessary to melt metals and the temperature difference to the surrounding gas can lead to thermal effects that can strongly influence the breakup. Notable is for example the change of fluid properties like thermal conductivity, viscosity, and surface tension with temperature, which becomes especially critical near the solidification temperature (Assael et al., 2006; Leitner et al., 2017). Differences exist even when, like in the current work, a metal like Galinstan is used that is liquid at room temperature. In that case, liquid metals still provide significantly different properties such as higher ranges of density and surface tension (Chen et al., 2018), and are subject to the formation of an oxide layer (Yim, 1996). Consequently, findings obtained in experiments with conventional liquids like water cannot, without further ado, be transferred on molten metals (Bauckhage, 1992). Instead, experiments targeting the specific properties of liquid metals need to be conducted.

Reference work on the breakup of liquid metal droplets is often carried out in liquid-liquid systems. For example, Patel and Theofanous (1981) investigate the fragmentation of mercury, gallium and acetylene tetrabromide drops in water accelerated by a shock wave in a hydrodynamic shock tube. Ciccarelli and Frost (1994) also study molten metal droplets in an ambient flow of water. They differentiate between cold drops that break up due to stripping by the relative flow, and hot drops where the growth and collapse of vapor bubbles dominate the fragmentation. Validating against both these works, Thakre and Ma (2015) present numerical investigations and highlight various deformation patterns. Haraldsson et al. (2001) analyze molten alloy drop fragmentation in a water pool experimentally and analytically. They highlight the competing processes of fragmentation and solidification that lead to a fragmentation-controlled and a freezing-controlled breakup regime. By conducting an instability analysis of the crust breakup, they derive a modified aeroelastic number and provide a critical value that separates the regimes. In contrast to experiments in gas-liquid systems, these works show differences in the fragmentation process. The differences probably are due to the low-density ratio and the high heat transfer between the liquids, as well as the effect of the growth and collapse of vapor bubbles at the interfaces (Kouraytem et al., 2016). Thus, the investigation of fluid-fluid systems can only provide a first glimpse at the breakup of molten metal, but it does not represent the gas atomization process accurately.

A more appropriate reproduction of gas atomization is achieved by analyzing fluid-gas systems. However, only few works focus on metals. In a very detailed report, Wolfe and Andersen (1964) present some experiments with mercury. Hsiang and Faeth (1992) also use mercury, but only a single data point in a figure is shown. Apart from that, secondary atomization of liquid metal has been studied only recently. Chen et al. (2018) present the aerobreakup of a Galinstan liquid metal column in a shock-induced air flow for moderate Weber numbers up to $We = 100$. They note a strong similarity to the breakup morphologies of water, but also highlight key differences. Breakup occurs earlier in non-dimensional time for Galinstan, while also appearing to be more violently. Furthermore, local bag formation and breakup occurs in a different form with fracture lines more akin to solid mechanics than to breakup of liquids. After breakup, non-spherical fragments appear, and remaining sheets exhibit sharp edges. The different behavior is attributed to the oxide layer that Galinstan forms on its surface when exposed to oxygen. Complementing simulations by Arienti et al. (2019) highlight an initially strong similarity in the deformation and cross-flow acceleration of columns in the range of $We = 10-12$, when normalizing the time by the characteristic transport time after Ranger and Nicholls (1969). The authors conclude that substantial differences between a liquid metal and a conventional liquid such as water arise when the bag membrane ruptures. However, these differences could not be repro-

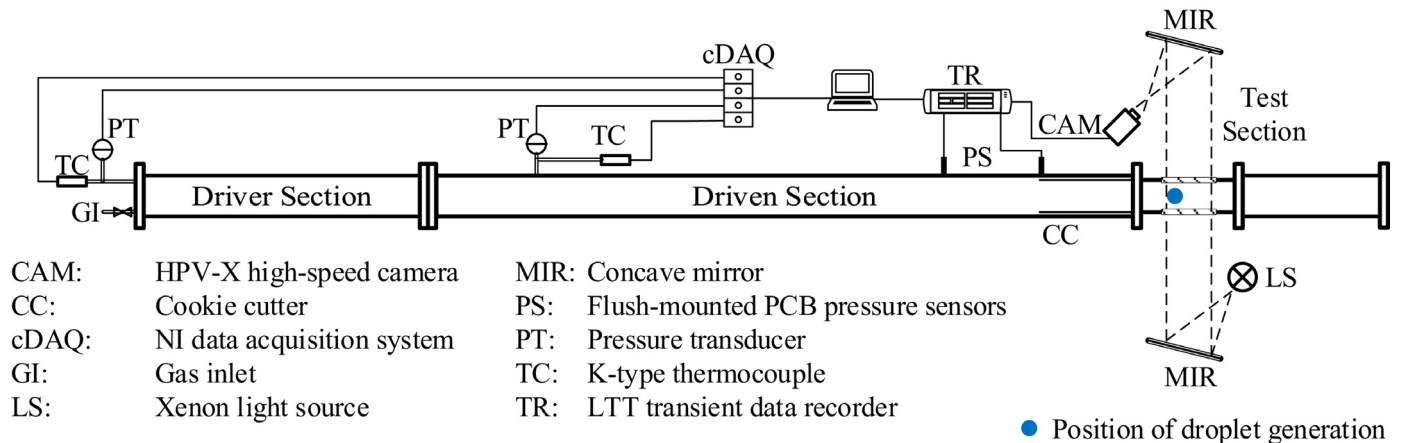


Fig. 1. Layout of the shock tube and connected measurement systems.

duced in the simulation because oxidation of Galinstan was not considered (Arienti et al., 2019).

The highlighted studies provide a good, but limited, discussion of secondary atomization of liquid metals. Differences between liquid-liquid and gas-liquid systems were already pointed out, and columns evolve differently than spherical drops. To extend previous investigations and get closer to the setting in applications, we use Galinstan to study secondary atomization of single liquid metal droplets in an experimental test series. The work covers droplet breakup in a range of $We = 11 - 104$ and analyzes the breakup morphology (section 4.1), transition between modes (section 4.2), underlying physical mechanisms (section 4.3), while also pointing out similarities and differences to conventional liquids (section 5). We hope to contribute to a profound understanding of the involved physical phenomena and provide a reference for future work.

2. Methods

2.1. Experimental facility

Experiments are conducted with a shock tube that has been adapted recently to study droplet breakup in sub- and supersonic flow (Wang et al., 2020). A corresponding layout for the current experiments is depicted in Fig. 1. The tube, with an overall length of 24 m and an inner diameter of 290 mm, consists of three segments: the driver section, the driven section, and the test section. In experiments, Mylar diaphragms of 0.15 mm thickness separate the driver section from the driven section, before each section is filled with air to pressure levels corresponding to desired flow conditions. Single droplets are produced in the test section by expelling Galinstan through hypodermic needles with an outer diameter of 0.4 - 0.6 mm. After detaching from the needle tip, falling droplets interrupt a laser beam, which generates an electrical signal. A switch is flipped, and an electric current of 3 A is supplied to a pair of crossed 0.1 mm-thick NiCr heating wires that are in contact with the Mylar diaphragm between driver and driven section. Locally melted by the wires, the diaphragm ruptures, and a planar shock wave forms, propagates towards the downstream test section and induces a flow with uniform flow conditions. A cookie-cutter is installed upstream of the test section to remove boundary flows and to enable the transition from the tube to the 190 mm x 190 mm square test section.

The pressure variation inside the shock tube is measured by PCB Piezotronics ICP® fast-response pressure sensors flush mounted along the tube. The measured signals are acquired by an LTT transient data recorder at a sampling frequency of 1 MHz. We calculate the shock velocity from the time lag of the inci-

dent shock passing two pressure sensors directly upstream of the test section. The combination of the shock velocity and initial pre-shock conditions yields post-shock flow properties based on moving shock relations. A sensor in the test section measures the pressure rise across the incident shock and serves as a trigger for the image recording. For the current experiments, the shock-induced flow remains steady over approximately 2.0-2.2 ms depending on the shock strength. After that, reflected waves lead to a slightly varying pressure and a continuous ramp up of flow velocity. Unless otherwise specified the constant time-window covers deformation and breakup of droplets for all presented results.

For visualization, we use a Z-type focused shadowgraph (Settles, 2001), and image sequences are recorded with a Shimadzu HyperVision HPV-X ultra-high-speed camera. The camera can record 128 consecutive images with a resolution of 400×250 pixels at a framing rate of up to 5 Mfps.

2.2. Preparation and post-processing

Experiments were conducted with Galinstan, a non-toxic eutectic alloy of gallium, indium and tin that retains a liquid state well below 0°C and has a very low vapor pressure (Liu et al., 2012). It chemically reacts with aluminum, and strongly wets to glass surfaces (Morley et al., 2008), which made it necessary to protect the aluminum alloy in the test section by applying a thin film of rubber spray and to carefully clean the glass windows with water after experiments. Galinstan has a reported surface tension of 535 mN/m when the oxygen trace is below 1 ppm (Liu et al., 2012). However, like many other liquid metals such as aluminum or titanium alloy (Guleryuz and Cimenoglu, 2009; Leitner et al., 2017), it reacts with oxygen and forms an oxide layer, which imparts non-Newtonian rheological properties to the metal (Daeneke et al., 2018). This distinguishes Galinstan from Mercury, which is not apt to form an oxide layer (Li et al., 2014), and makes Galinstan uniquely suited to study this effect. According to Dickey (2014), the oxide skin of gallium alloys is elastic and provides mechanical stabilization until its critical yield stress of approximately 0.5 - 0.6 N/m is reached. As a result, a surface tension of 718 mN/m is measured for Galinstan in standard conditions (Chen et al., 2018; Kocourek et al., 2006). This value is used in the present work, because Galinstan drops were completely exposed to air before the breakup.

During post-processing, recorded raw images are processed with subtraction of background noise, contrast stretching and super resolution using MATLAB's Very Deep Super-Resolution convolutional neural network (Kim et al., 2016). It was ensured that this does not alter the data analysis. The analysis was conducted auto-

Table 2
Range of operating conditions for presented Galinstan experiments. Values for fluid properties of Galinstan after Kocourek et al. (2006) ($\rho_d = 6440 \text{ kg/m}^3$, $\sigma = 718 \text{ mN/m}$, $\mu_d = 2.4\text{e-}3 \text{ kg/m}\cdot\text{s}$).

We	Oh	Re_∞
11 - 104	0.65 - 1.01 •1E-3	5.9 - 28.5 •1E+3
M_∞	ρ_d/ρ_g	μ_d/μ_g
0.19 - 0.35	3970 - 4660	117 - 122

matically in MATLAB using a fixed reference length, and provides droplet data like the initial droplet diameter d_0 , cross-stream diameter d_c , the streamwise diameter d_x , or the position of the mass center x_{mc} .

The experimental time t is defined to be zero at the moment of shock-impact on the droplet. For consistency and comparability with previous literature, t is normalized by the characteristic transport time after Ranger and Nicholls (Ranger and Nicholls, 1969), yielding the dimensionless time τ :

$$\tau = t \frac{u_g}{d_0} \sqrt{\rho_g/\rho_d} \quad (3)$$

We consider two characteristic breakup times within this work – the end of initial deformation τ_{ini} , and the onset of breakup τ_b . For the bag and the bag-and-stamen mode, τ_{ini} defines the time instant when the deformed droplet resembles a flat disc, right before the bag starts to inflate (Pilch and Erdman, 1987; Zhao et al., 2010). For the shear stripping mode, τ_{ini} is identified as the first incidence of a sheet at the droplet periphery being drawn downstream of the drop (Pilch and Erdman, 1987). In practice, this time instant is found by comparing images and simultaneously monitoring the droplet diameter in streamwise direction, because a sharp rise in d_x indicates that bag inflation or shear stripping is initiated. The second characteristic time τ_b describes the onset of breakup and is taken at the first sign of bag rupture for lower Weber numbers, and at the first sign of shedding of fragments from sheets or ligaments for higher Weber numbers.

3. Breakup morphology of Galinstan droplets

A total of 34 experiments with Galinstan droplets were analyzed in detail for the present study. Corresponding ranges of critical non-dimensional numbers are presented in Table 2. Apart from the Weber and Ohnesorge number, also the flow Reynolds number $Re_\infty = \rho_g \cdot u_\infty \cdot d_0 / \mu_g$, Mach number $M_\infty = u_\infty / a_\infty$, liquid-gas density ratio ρ_d / ρ_g , as well as the liquid-gas viscosity ratio μ_d / μ_g are included. Initial droplet diameters d_0 range from 1.22 mm to 2.98 mm.

In addition to the Galinstan test series, experiments with water droplets were conducted for reference. All presented experiments are checked for constant flow conditions, but there are some exceptions, especially during late-stage fragmentation. If at any point flow conditions are not constant, this is mentioned in the text or figure description. In addition, throughout this work we mark the time with an asterisk '*' as a method of highlighting when flow conditions become non-constant.

3.1. Classification

An overview of the breakup behavior is presented in Fig. 2. We observe a transition of the breakup morphology for Galinstan droplets from bag, to bag-and-stamen, and shear stripping with increasing Weber number. Both the morphologies and transition values are similar to that of conventional liquids (Dai and Faeth, 2001).

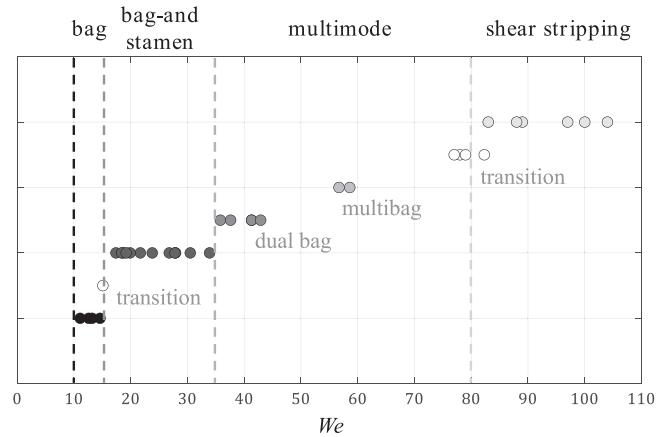


Fig. 2. Classification of breakup behavior of Galinstan droplets for varying Weber number. Main modes are bag, bag-and-stamen, multimode, and shear stripping with transition values of ~15, ~35, and ~80, respectively. Multimode shows several sub-features like the dual-bag and multibag breakup.

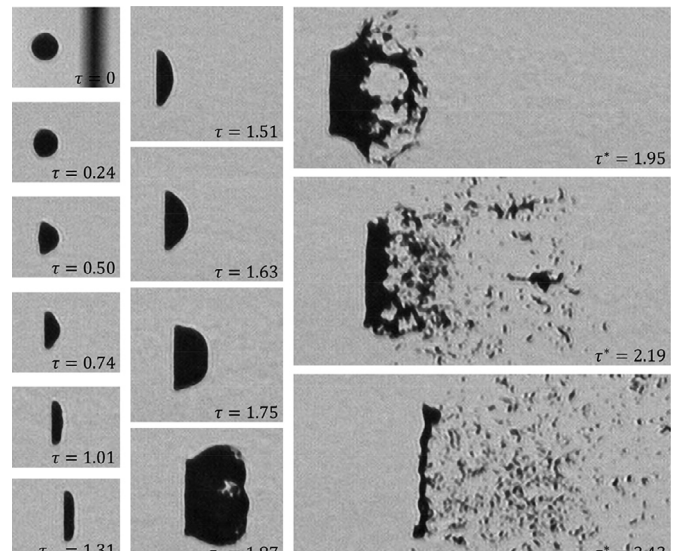


Fig. 3. Bag breakup of a Galinstan droplet with an initial diameter of $d_0 = 1.32 \text{ mm}$ at $We = 13.2$. The three columns represent initial deformation, bag inflation, and rupture and fragmentation, respectively. Critical time instants are the end of initial deformation at $\tau_{ini} = 1.31$ and the onset of bag rupture at $\tau_b = 1.87$. An asterisk at later times indicates non-constant flow conditions. A high-speed video of this breakup mode is included with this paper in Video 1.

Detailed similarities and differences of Galinstan droplets will be discussed in section 5, while the following section focuses on the morphology and presents exemplary image sequences for each mode. In addition, we highlight that the transition between modes is a continuous process with different features developing under the changing aerodynamic pressure. Especially the range from $We = 35 - 80$, often termed multimode regime, displays several transition types like dual-bag and multibag breakup that are further discussed in section 4.2.

3.1.1. Bag

Fig. 3 shows a bag breakup for a Galinstan droplet at $We = 13.2$ with an initial diameter of $d_0 = 1.32 \text{ mm}$. The first column shows the droplet until the end of the deformation period when the droplet shape equals a flat disc. Until that moment at $\tau_{ini} = 1.31$, the droplet is squeezed by the flow, flattens in the streamwise direction, and stretches in cross-stream direction. After the initial deformation, the bag inflates as is shown in the second col-

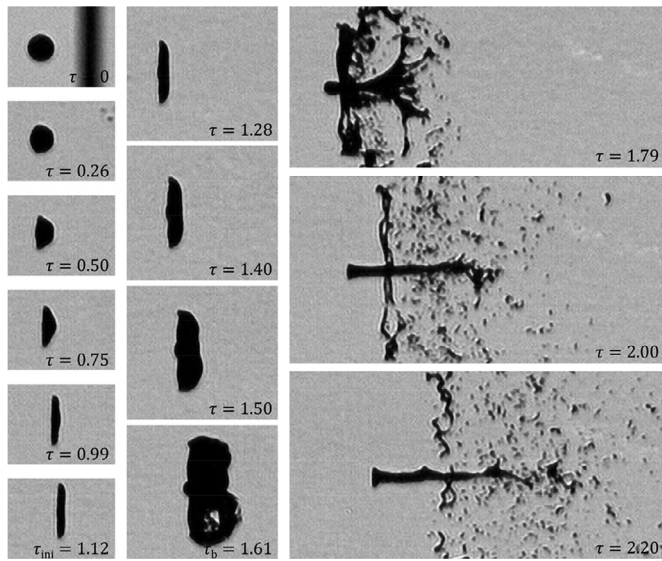


Fig. 4. Bag-and-stamen breakup of a Galinstan droplet with an initial diameter of $d_0 = 1.32$ mm at $We = 21.7$. The three columns represent initial deformation, bag inflation, and rupture and fragmentation, respectively. Critical time instants are the end of initial deformation at $\tau_{ini} = 1.12$ and the onset of bag rupture at $\tau_b = 1.61$. A high-speed video of this breakup mode is included with this paper in [Video 2](#).

umn. Here, the upstream side of the bag remains straight, while the downstream side inflates into a symmetric bag. Symmetry is lost when the first indication of bag rupture can be seen at $\tau_b = 1.87$. Complete bag rupture and droplet disintegration is shown in the third column, but changing flow conditions make the time-normalization inaccurate (as indicated by the asterisk). At $\tau_b = 1.87$, the bag ruptures and bursts open in an outwards splashing motion ($\tau^* = 1.95$). The bag disintegrates further in a flapping motion, and coarse, irregularly shaped fragments are torn off at the fracture line. Bag disintegration is completed at $\tau^* = 2.43$, but a toroidal rim (also called ring) remains that disintegrates at even later time instants. With respect to the morphology, Galinstan droplets break up very similarly to conventional liquids. Image sequences for comparisons are found, for example in references (Dai and Faeth, 2001; Guildenbecher and Sojka, 2011; Jain et al., 2015; Villermaux and Bossa, 2009; Zhao et al., 2010).

3.1.2. Bag-and-stamen

Bag-and-stamen breakup is shown in [Fig. 4](#) for a Galinstan droplet of $d_0 = 1.32$ mm at $We = 21.7$. Again, the droplet initially deforms into what appears as a flat disc at $\tau_{ini} = 1.12$. The deformation period is shorter than in the bag mode but features a very similar shape throughout. A bag structure starts to form and inflates between $\tau = 1.28$ and $\tau = 1.61$, while the formation of the stamen becomes apparent through the appearance of a small bulge at the windward side ($\tau = 1.28$) and an indentation of the bag at the leeward side ($\tau = 1.50$). The bag starts to disintegrate at $\tau_b = 1.61$ and once fragmented, a clear separation of stamen and toroidal rim is revealed. At $\tau = 2.00$ only a thin ring and a straight stamen in the center remain. The ring disintegrates and resulting fragments at $\tau = 2.2$ appear larger than fragments resulting from the rupture of the bag. In contrast, the stamen does not fragment easily and remains coherent for a long time despite elongating in the streamwise direction. Again, the morphology of the breakup of Galinstan droplets is like that of conventional liquids. Image sequences for comparisons are found, for example in references (Dai and Faeth, 2001; Guildenbecher and Sojka, 2011; Jain et al., 2015; Zhao et al., 2013).

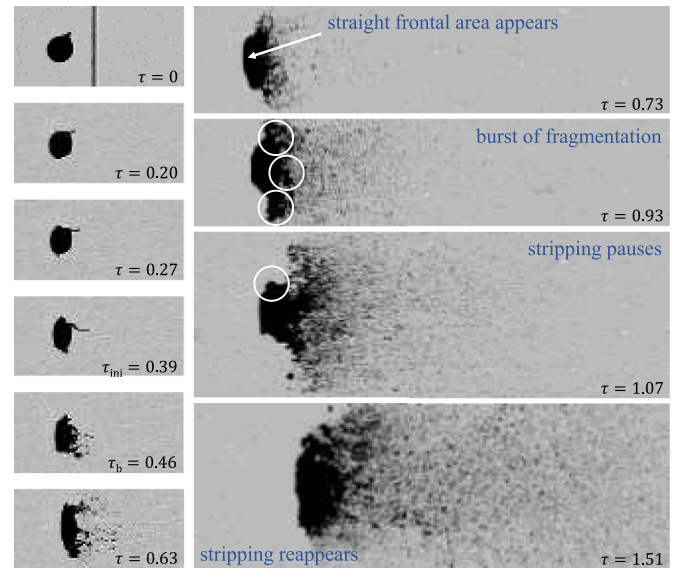


Fig. 5. Shear stripping breakup of a Galinstan droplet with an initial diameter of $d_0 = 2.72$ mm at $We = 96.8$. A straight frontal surface is pointed out at $\tau = 0.73$ and a wave of shedding is highlighted for $\tau = 0.93 - 1.07$. A high-speed video of this breakup mode is included with this paper in [Video 3](#).

3.1.3. Shear stripping

[Fig. 5](#) shows the breakup process for a Galinstan droplet of $d_0 = 2.72$ mm at $We = 96.8$ representing the shear stripping mode. The first image of the sequence highlights that Galinstan droplets in some experiments featured an appendix on top of the droplet that was typically aligned parallel to the falling direction. This phenomenon is also observed by [Dickey \(2014\)](#), [Liu et al. \(2012\)](#), and [Chen et al. \(2018\)](#) who all present droplets with a similar shape. The reason is that the droplet elongates while forming at the needle tip, and reacts with the surrounding air to form an oxide layer on the Galinstan surface ([Liu et al., 2012](#)). The oxide layer then hinders the contraction of the droplet to a perfect sphere in flight and thus the droplet remains in the aspherical shape it had at the moment of detachment. For our experiments, this asymmetry appeared for some experiments, mostly at higher Weber number in the shear stripping regime. For these experiments we used a wider needle, which allows to produce larger droplets but also leads to a more pronounced appendix ([Li et al., 2014](#)). The image sequence shows that after the shock wave passes, the appendix is bent and stretched in flow direction. To reduce the effect of the appendix on the analysis, we focus on the lower hemisphere of the drop and assume symmetry to find τ_{ini} and the corresponding maximum cross-stream diameter $d_{c,max}$.

As for the breakup, in contrast to lower Weber number experiments, the drop does not reach the shape of a flat disc. Instead, the droplet initially deforms into an ellipsoid ($\tau = 0.0 - 0.29$), with a thin sheet developing at the periphery. Then, the thin sheet is directly drawn downstream of the drop, which marks a significantly earlier end of initial deformation at $\tau_{ini} = 0.39$. The bending sheet starts to decompose into ligaments that are stretched in streamwise direction and break quickly ($\tau_b = 0.46$). After the ligaments break, fragments are stripped off directly at the droplet periphery and are entrained in the flow in a continuous erosion of the core droplet ($\tau = 0.73$ and later). Several experiments show a tendency of recurring shedding similar to what [Dorschner et al. \(2020\)](#) describe for water droplets in the same breakup regime. Here, shedding manifests as a large number of fragments detaching at the same time. An example for that behavior is highlighted in the figure for $\tau = 0.93 - 1.07$. The first image shows a burst of frag-

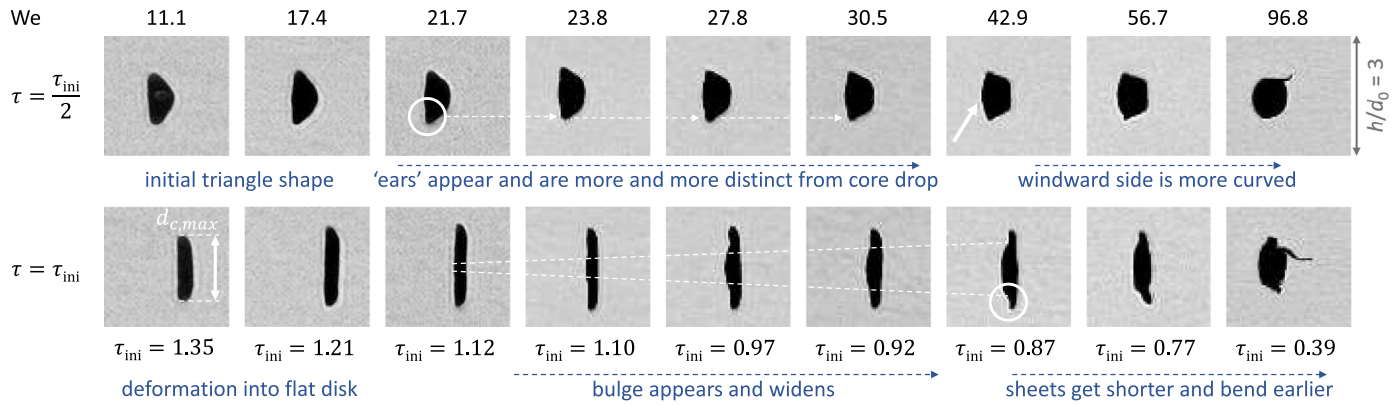


Fig. 6. Initial droplet deformation through the regimes of bag breakup ($We = 11.1$), bag-and-stamen breakup ($We = 17.4 - 30.5$), dual bag breakup ($We = 42.9$), multibag breakup ($We = 56.7$) and shear stripping breakup ($We = 96.8$). Provided are frames at $\tau = \tau_{ini}/2$ and at the end of initial deformation τ_{ini} . Frames in the second row also show the maximum cross-stream diameter $d_{c,max}$. All frames are scaled to have a height h of three times the initial diameter d_0 . Flow is from left to right and within one experiment the x-position of the left edge of the image is fixed to show droplet movement. As a second aspect, the figure shows that the basis for the breakup morphology we observe at later times is already set during the initial deformation.

mentation, while the latter shows that stripping pauses momentarily. Such waves of fragmentation appear repeatedly, but an exact analysis is difficult only using shadowgraph images and with the appendix breaking the symmetry. Several time instants show that the windward side of the disintegrating droplet flattens to a straight, even surface ($\tau = 0.73 - 0.93$). This behavior is not typical for other liquids but is observed at least shortly for all experiments with Galinstan at higher Weber number. We expect this to be an effect of the oxide layer and discuss it along with other differences in section 5.2. Apart from this observation, the breakup morphology of Galinstan droplets in the shear stripping regime matches that of more conventional liquids. For comparison, see for example the work of Dai and Faeth (2001) (Fig. 7, ethyl alcohol, $We = 81$), or Jain et al. (2015) (Figures 12 and 13, water, $We = 120$).

3.2. Transition between modes

The three presented examples show the typical behavior for the most prominent breakup modes. However, there is not a single transition point separating the modes, instead it is a continuous transition process. Showing this in detail can be very beneficial for understanding the underlying physics in secondary atomization and can help modelling efforts. Especially considering that the presented results are the first that are based on the breakup of liquid metal droplets.

3.2.1. Initial deformation of the droplet

Fig. 6 presents the initial deformation of droplets for experiments ranging from bag mode to shear stripping at two representative time instants – one at $\tau_{ini}/2$ to show intermediate deformation and one at τ_{ini} to show the shape at the end of the deformation phase. With increasing Weber number, τ_{ini} decreases significantly, which is consistent to correlation for conventional liquids as section 5.1 will show. However, the figure is important because of two additional aspects: highlighting the continuous transition with increasing Weber number and showing that the initial deformation sets the basis for later breakup patterns.

Following the first aspect, we can see that the shape of the deformed droplet changes with increasing Weber number in a continuous transition process. Several characteristic features can be observed that appear and change gradually. The most prominent ones are:

- A rim, visible as ‘ears’ in the images, develops as soon as $We = 21.7$ and appears distinct from the core droplet. At high

Weber number, a more ellipsoidal shape with a curved front develops and the rim recedes to thin sheets.

- At τ_{ini} we first observe the shape of a flat disk, but with increasing Weber number, we also see that along with the rim formation outside, a bulge develops in the center of the droplet ($We = 21.7$ and higher).
- With increasing Weber number, the bulge widens, while the rim becomes shorter and thinner. At higher Weber numbers we observe a hat-like shape ($We = 42.9$), and the rim starts to bend in streamwise direction showing some asymmetric behavior ($We = 56.7 - 96.8$).
- The deformation of the drop into a flat disk for low Weber numbers triggers the R-T instability which then leads to an inflating bag (Fig. 3).
- The bulge that appears for higher Weber numbers corresponds to a higher mode of the R-T instability. It is easy to see that this bulge develops into the stamen, and that the rim inflates into a bag structure with an enclosing ring (Fig. 4).
- A wider bulge leads to larger stamen structures and the correspondingly shorter rim develops only small bags. We will see that effect clearly in the following sections, but it can already be expected from the shape seen in Fig. 6.
- Shorter and thinner sheets at high Weber number, such as shown for $We = 96.8$, cannot always support a bag formation, instead they bend in the flow direction. The bent sheets rupture directly, and the breakup mode transitions to shear stripping (Fig. 5).

3.2.2. From bag to bag-and-stamen

Apart from the initial deformation, also aspects of the breakup morphology appear and change gradually. As an example, the transition from the bag to the bag-and-stamen mode is shown in the first three rows of Fig. 7. In our experiments, this transition is marked by a changing shape of the bag and by the appearance of the stamen in a range of $We = 14.6 - 17.4$.

For the bag breakup shown earlier in Fig. 3, we can see that the bag features a small indentation on the leeward side ($\tau_b = 1.87$). This could be considered as the first mark of transition towards the bag-and-stamen mode. However, a first clear appearance of the stamen can be seen for the experiment with $We = 14.6$ in Fig. 7. The image sequence shows that after the bag breaks, an inside structure becomes visible indicating that the bag is curved inwards in the center ($\tau = 1.93$). Some sheets of the bag are initially connected to the ring, but they bend in streamwise direction, fold around the point of curvature, and collide to form a first stamen-

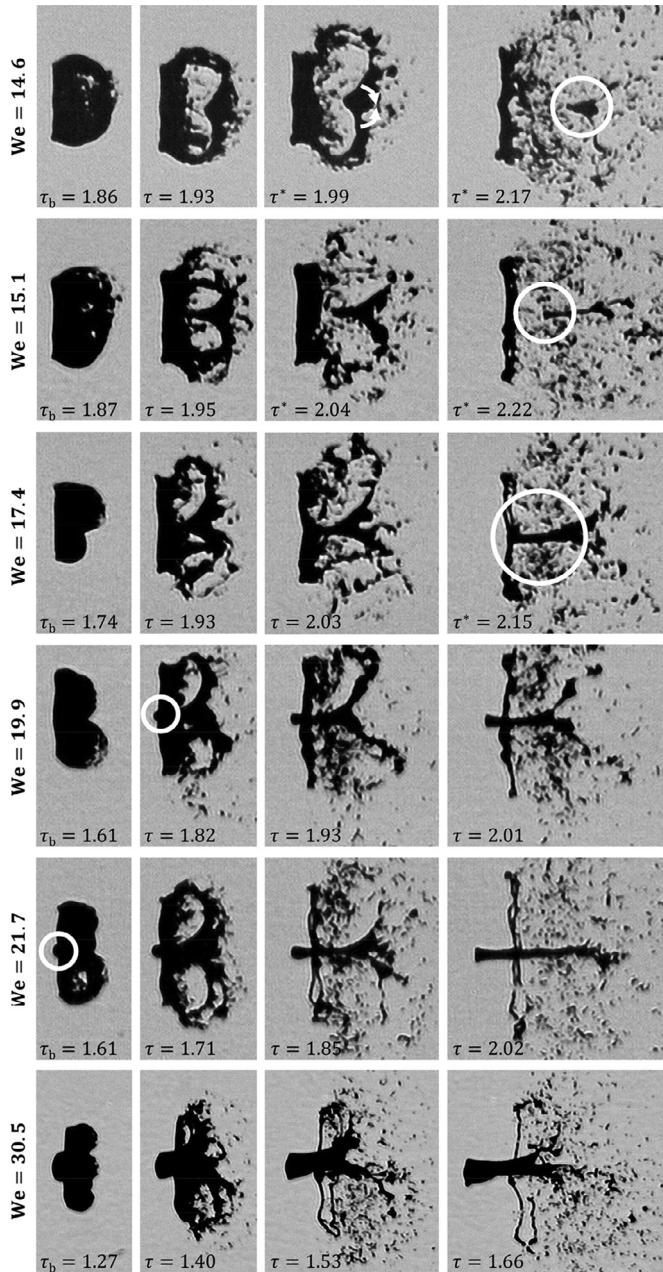


Fig. 7. Transition from bag to bag-and-stamen mode for $We = 14.6$ to 17.4 , and evolution of the stamen throughout the bag-and-stamen mode for $We = 17.4$ to 30.5 . Images in the first column present the onset of breakup at τ_b while the last column shows the shape approximately $\Delta\tau = 0.4$ later in time. For $We = 14.6$ and $We = 15.1$ this value is lower to show the stamen. Intermediate time instants are chosen to show the developing features.

like structure (highlighted at $\tau^* = 1.99 - 2.17$). For $We = 15.1$ and 17.4 a similar sequence repeats, but the inwards curvature of the bag is much stronger. For $We = 17.4$, already the initial bag is split at the onset of breakup at $\tau_b = 1.74$. A more prominent stamen evolves that is clearly separated from the ring (highlighted at $\tau^* = 2.22$ and 2.15 , respectively).

The stamen is established after this transition regime, but still changes in size, shape, and position with increasing Weber number. Two main aspects can be found. First, the stamen forms more prominently with increasing Weber number. Hardly visible initially, it becomes longer and wider, and concentrates more of the liquid. The fourth column of Fig. 7 shows this process nicely for the range of $We = 14.6 - 30.5$. Secondly, the stamen position is shifted more

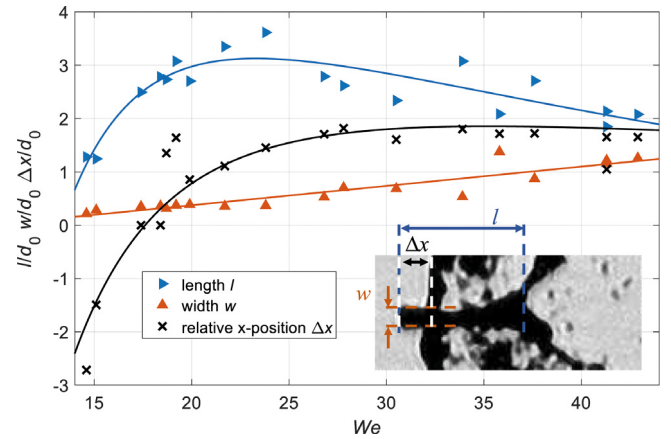


Fig. 8. Stamen length, width, and relative position to the toroidal rim at $\tau = 1.2 \bullet \tau_b$ for different Weber numbers in the bag-and-stamen and dual bag mode. Data points are from measurements, while corresponding trendlines are generated by curve fitting.

and more upstream in relation to the bags and the ring. Initially, the stamen forms downstream of the ring, but with increasing Weber number, the stamen head appears at the same position as the ring ($We = 17.4$ at $\tau^* = 2.15$) and then exceeds it. For $We = 21.7$ the stamen is visible even before the bag breakup (highlighted at $\tau_b = 1.61$). With respect to the development in time, we observe that as soon as the stamen forms properly, the ring always travels downstream faster than the stamen due to a higher drag.

With the stamen forming more prominently and shifting in relative position, the bags become smaller and break earlier. Correspondingly, also the ring becomes thinner and accumulates less liquid. Although it is not always shown at the same level of detail, many other authors observe a similar transition within the bag-and-stamen mode also for conventional liquids. For example, images presented by Zhao et al. (2013) for water droplets at $We = 18$ and $We = 29$ show comparable trends and shapes.

3.2.3. Stamen appearance and evolution

The appearance and evolution of the stamen is the dominant feature of transition for lower Weber numbers. Because of its importance, the stamen shape is analyzed quantitatively in Fig. 8. The figure shows the length, width, and relative position of the stamen to the ring as a function of the Weber number. An inserted image illustrates the defined variables. The ring position is fixed as zero and the upstream direction is defined as the positive x-axis. All values are normalized by d_0 . Data points were generated by analyzing the two frames closest to a time of $\tau = 1.2 \bullet \tau_b$ and averaging the value. This time instant was chosen exemplarily but represents a consistent trend. A rectangular box was fit onto the stamen by hand to calculate an approximate width and length. The upstream edge was fit to the head of the stamen, while the downstream edge was fixed at the end of the stamen or the position that first indicated that the stamen was hollow. Trendlines were generated with MATLAB's curve fitting toolbox but only serve to visualize the development with changing Weber number.

The figure confirms the qualitative observations earlier. The stamen width increases linearly with the Weber number within the shown range of up to $We = 42.9$. The stamen length also increases initially but decreases after a peak around $We \sim 23$. A comparable analysis by Dai and Faeth (2001) reveals that the volume of the stamen (plume in their work) peaks at $We \sim 30$ similar to what results for our observations when calculating the volume with the assumption of a cylindrical stamen. They also observe that the volume of bag and ring decreases to almost zero at this Weber

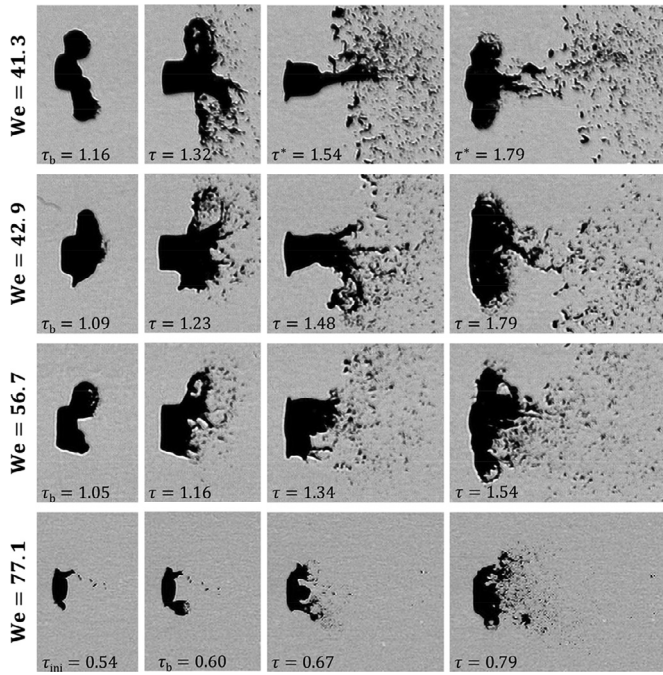


Fig. 9. Breakup morphology in the multimode regime, including dual bag breakup ($We = 41.3$), multibag breakup ($We = 56.7$) and transition to shear stripping with small bags forming locally ($We = 77.1$).

number, similar to what we mentioned about the bags becoming smaller and the toroidal rim becoming thinner.

From $We > 35$, calculating the volume of the stamen with the provided values would result in a value larger than the initial volume. Clearly, the assumption of a solid cylinder-shaped stamen is not valid anymore from this point on. What we observe as a solid stamen is actually a hollow construct with sheets of metal or sheets of oxide layer enclosing gas in the center. Videos of the experiments, for example the ones shown in the last row of Fig. 7 and the first rows of Fig. 9, seem to confirm that assumption. While the upstream part seems to be a solid core drop, we observe sharp changes in stamen width further downstream because of folding sheets. Additionally, the stamen sometimes breaks apart in the middle and reveals its hollow inside. The hollow stamen appears symmetric, but along with other details, we cannot judge this clearly from the shadowgraph images.

Fig. 8 also shows that the stamen head position in relation to the ring position changes with the Weber number as observed before. The transition from down- to upstream position occurs for $We \sim 18$, and the upstream position then stabilizes at $\Delta x/d_0 \sim 1.7$ for increasing Weber number.

3.2.4. Multimode

Summarized as multimode breakup, different unique characteristics appear for $We > 35$. To show this, Fig. 9 serves as a continuation of Fig. 7 in the sense that the Weber number increases, and the gradual change and transition continues.

We have seen in Fig. 7 and in the quantitative analysis in Fig. 8 that the stamen becomes increasingly shorter, and thicker with higher Weber numbers. The continuation of this trend can be seen in Fig. 9 for $We = 41.3$ and 42.9 . While we still see bag inflation and a stamen and ring structure for the experiment in the first row, the second row already shows that this behavior ceases for slightly higher Weber numbers. Bags inflate only shortly, and the ring starts to disappear. In addition, the breakup becomes increasingly asymmetric. Reaching $We = 42.9 - 56.7$, the stamen becomes so short and the rim so thin that it is more appropriate to speak

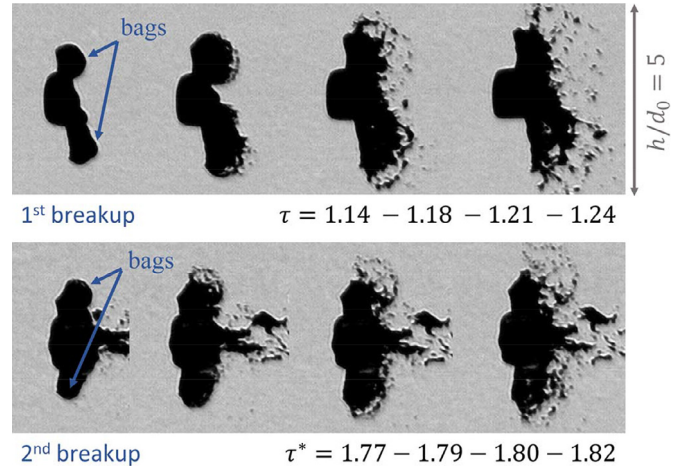


Fig. 10. Characteristic breakup pattern in the dual bag mode shown for a Galinstan droplet at $We = 41.3$. A high-speed video of this breakup mode is included with this paper in Video 4.

of a core droplet and sheets instead of a stamen and rim (Dai and Faeth, 2001). Continuing the transition, multiple bags still form for $We = 56.7$, but only a few, small bags form once the breakup transitions towards the shear stripping regime ($We = 77.1$).

Looking more into detail, the breakup morphology of the experiment shown in the first row of Fig. 9 for $We = 41.3$ matches well with the breakup morphology that some authors describe as a two-stage process (Pilch and Erdman, 1987; Wolfe and Andersen, 1964) and that Cao et al. (2007) term the dual bag breakup. Cao et al. (2007) define the breakup mode in the range of $We = 28-41$ and characterize it by two subsequent bag breakups of which they name the second one as the major distinguishing criterion to the bag-stamen mode. In our opinion this breakup pattern precisely follows the trends we observed for the bag-and-stamen regime. The stamen becomes thicker and only small bags form and break quickly. Consequently, a large droplet core remains that can reach a high enough Weber number to undergo a second bag-like breakup. An example for such a dual bag breakup for a Galinstan droplet is shown in Fig. 10. Both breakups appear quite similar and remain quite symmetric.

After the dual bag breakup, the pattern transitions to the multi-bag breakup ($We = 56.7$). Here, bags form as multiple lobes on the bag membrane and subsequently break up similarly to the bag breakup for lower Weber number (Jain et al., 2015). Jain et al. (2015) argue that the R-T instability characterizes this behavior, but that nonlinear effects and asymmetric undulations lead to differences to the bag-and-stamen regime. We can only observe that multiple bags break repeatedly in a seemingly random fashion, and that symmetry is mostly lost. However, a lack of experiments in that range and the chaotic nature of this regime in general (Krzczkowski, 1980) do not allow a detailed analysis.

At higher Weber number, the erosion of the core droplet transitions to shear stripping at the periphery. However, small bags still form at the early stage of the breakup from sheets that emerge at the rim and are drawn downstream of the drop ($We = 77.1$ at $\tau = 0.60$ and $\tau = 0.67$). No further bags appear after these initial bags, and the drop breaks up like in the shear stripping mode. This transition period, where bags appear initially ceases quickly as the Weber number is increased above a value of $We = 80$.

3.3. Rayleigh-Taylor analysis

R-T waves are considered to be the dominant physical breakup mechanism for low Weber numbers. The instability is triggered at

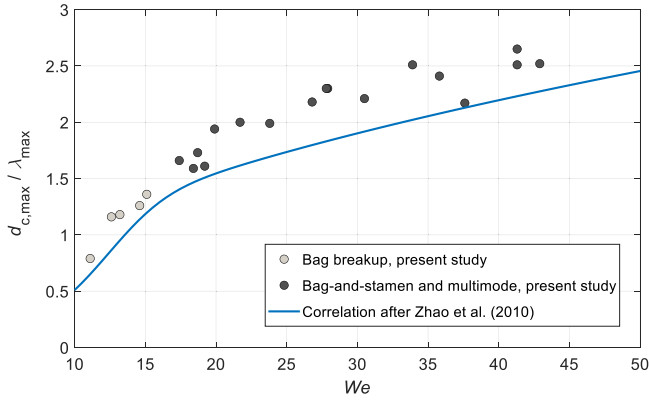


Fig. 11. Number of critical waves n_{RT} across the deformed droplet diameter according to classical R-T instability analysis and depending on the Weber number. Data points are calculated with equation (4), and the correlation after Zhao et al. (2010) follows equations (6) and (7).

the accelerated drop front during the initial deformation of the drop into a flat disk. Classical R-T analysis can provide a wavelength λ_{max} for the fastest-growing wave on the deforming drop. When comparing the result with the maximum cross-stream diameter of the drop $d_{c,max}$ taken at τ_{ini} , the number of waves across the deformed droplet results as (Guildenbecher et al., 2009):

$$n_{RT} = \frac{d_{c,max}}{\lambda_{max}} = \frac{1}{4\pi} \left(\frac{d_{c,max}}{d_0} \right)^2 \sqrt{C_D \cdot We} \quad (4)$$

Here, C_D represents the drag coefficient. In experiments, $d_{c,max}$ is measured at τ_{ini} (compare Fig. 6), and C_D can be calculated using the assumption of constant drop acceleration after Ranger and Nicholls (1969) as

$$C_D = \frac{8}{3} \cdot \frac{X_{ini}}{\tau_{ini}^2} \quad (5)$$

with $X_{ini} = x_{mc}/d_0$ as the normalized x-position of the mass center at τ_{ini} . The calculated number of waves n_{RT} across the deformed drop is shown in Fig. 11. There, the reference line follows the correlation for the maximum cross-stream diameter of Zhao et al. (2010)

$$\frac{d_{c,max}}{d_0} = \frac{2}{1 + \exp(-0.0019 We^{2.7})}, \quad (6)$$

and calculates the drag coefficient after Liu et al. (1993) as

$$C_D = C_{D, Sphere} \cdot \left(1 + 2.632 \left(1 - \left(\frac{d_0}{d_{c,max}} \right)^2 \right) \right). \quad (7)$$

For the drag coefficient of a sphere we assume $C_{D, Sphere} = 0.4$ similarly to previous works (Guildenbecher et al., 2009; Zhao et al., 2010).

Fig. 11 shows that an increasing Weber number leads to a higher number of critical waves across the diameter. In addition, data points of n_{RT} for liquid metal droplets match well with the correlation based on equations (6) and (7) for conventional liquids. This indicates that the physical mechanism and the effect of the R-T instability is not influenced by the special properties of Galinstan.

In the literature, the bag type corresponds to a half or single critical wave across the droplet diameter, whereas bag-and-stamen corresponds to 1.5-3 waves across the droplet diameter depending on the source (Guildenbecher et al., 2009; Theofanous et al., 2004; Zhao et al., 2010). For our experiments, the figure shows that the transition occurs around a value of $n_{RT} \sim 1.5$, but as previously shown, the transition is gradual. This is reflected by the fact that

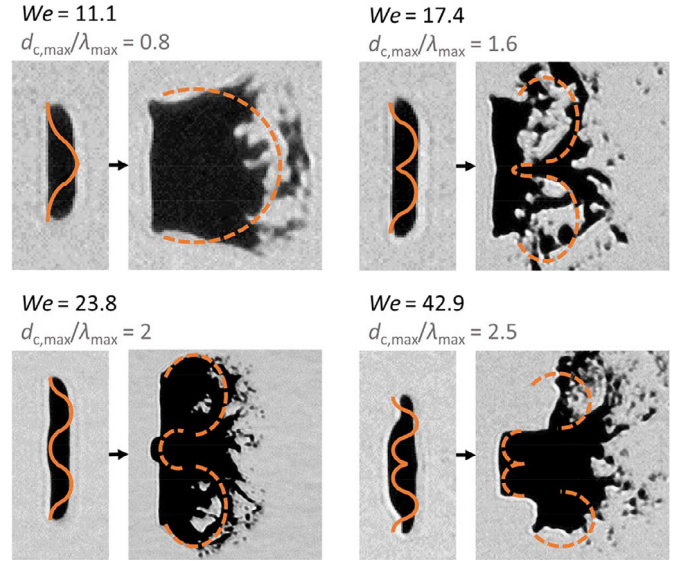


Fig. 12. Sketch of R-T waves across the deformed drop at τ_{ini} and after onset of breakup for four different Weber numbers. Values for the number of waves across the droplet diameter are calculated with equation (4). The sketched waves show how initial instabilities develop into inflating bags and stamens. Images in this case only highlight the breakup morphology and are not scaled to equal sizes.

experiments in the transition range of $We = 15-20$ show values of $n_{RT} \sim 1.3$ to $n_{RT} \sim 1.7$, indicating that aspects of both breakup morphologies manifest weaker and stronger dependent on the specific value. Similarly, transition between bag-and-stamen and dual bag appears gradually. Zhao et al. (2010) state a value of $n_{RT} \sim 2$ as the lower limit for dual-bag breakup. For this study, dual-bag mode is rather clustered around a value of $n_{RT} \sim 2.5$, but elements of the dual bag certainly also appear for lower Weber numbers and correspondingly lower values of n_{RT} .

Fig. 12 shows four representative examples of Galinstan droplets at the end of initial deformation and after onset of breakup. Here, the focus lies on the breakup pattern, so images are not scaled equally. Sketched on the images are waves according to the calculated number of waves across the deformed droplet diameter. The waves are sketched in radial direction in a sectional view assuming a zero gradient at the droplet periphery. This leads to a singular point in the center for which radial symmetry is applied. While the sketched waves suggest a curved surface, we initially do not see the extent because of shadowgraph imagery and the opacity of Galinstan. However, we can judge retrospectively that the grooves and bulges of the sketched instabilities develop into bags and stamens, respectively. The breakup morphology of the bag ($We = 11.1$), bag-and-stamen ($We = 17.4-23.8$), and dual bag modes ($We = 42.9$) are accurately predicted by the calculated wave number. In the bag-and-stamen mode, the higher value of n_{RT} also correlates with the increase in the stamen thickness as shown in the figure.

The presented examples and the summary in Fig. 11 are in accordance with the theory of R-T instability. In addition, the good agreement between Galinstan and conventional liquids further emphasizes the similarity of the breakup morphology shown in previous sections.

4. Breakup of Galinstan droplets compared to conventional liquids

The previous section has shown that both the breakup morphology and transition Weber numbers of Galinstan droplets are

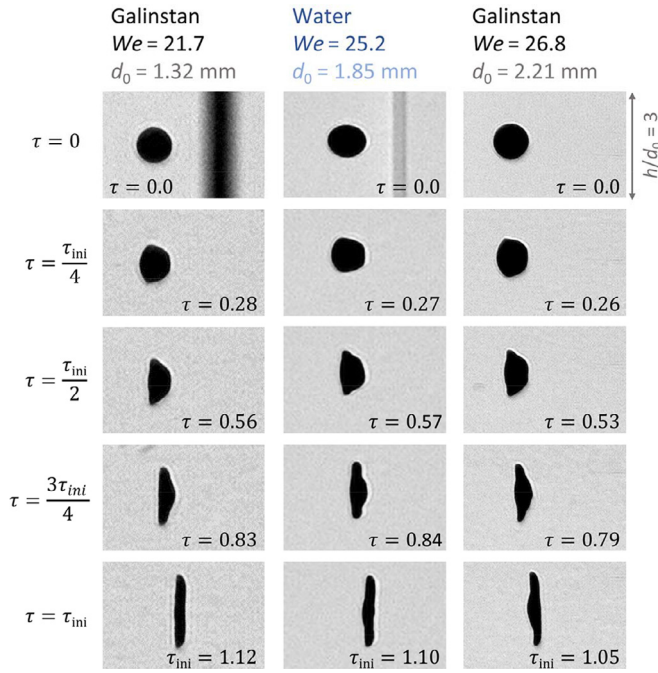


Fig. 13. Initial deformation of Galinstan droplets compared to a water droplet.

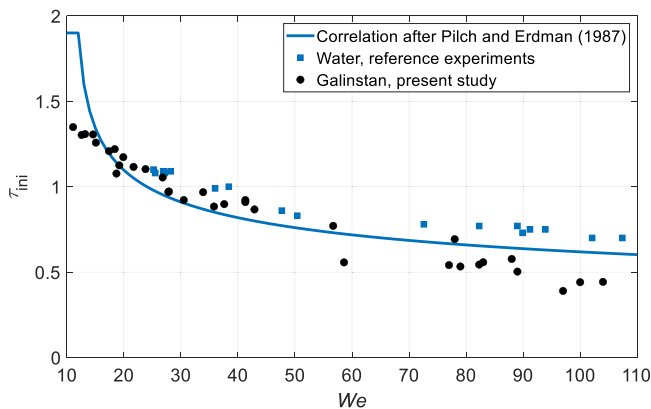


Fig. 14. Initial deformation time τ_{ini} of Galinstan droplets compared to the empirical correlation of Pilch and Erdman (1987) and own reference experiments with water droplets.

very similar to conventional liquids. However, a direct comparison of the two liquids in the following section reveals further details.

4.1. Similarities during the initial deformation

With respect to the initial deformation, Fig. 13 provides a representative direct comparison for $We \sim 25$ in a sequence of images. Weber numbers are not matched exactly, so both lower and higher Weber number experiments are shown for Galinstan ($We = 21.7$ and $We = 26.8$). Initial deformation ends at almost the same non-dimensional time with $\tau_{ini} = 1.12$ and $\tau_{ini} = 1.05$ for Galinstan at lower and higher Weber number, respectively, compared to $\tau_{ini} = 1.10$ for water. Although the water droplet has a slightly oval shape at the beginning, deformation is very similar between the two liquids, and the droplet shapes at different time instants match very well throughout. A quantitative analysis of the normalized cross-stream and streamwise diameters confirms the good agreement for the two liquids until τ_{ini} .

While Fig. 13 compares only single experiments, Fig. 14 and Fig. 15 expand the analysis from a single case to the full range of inves-

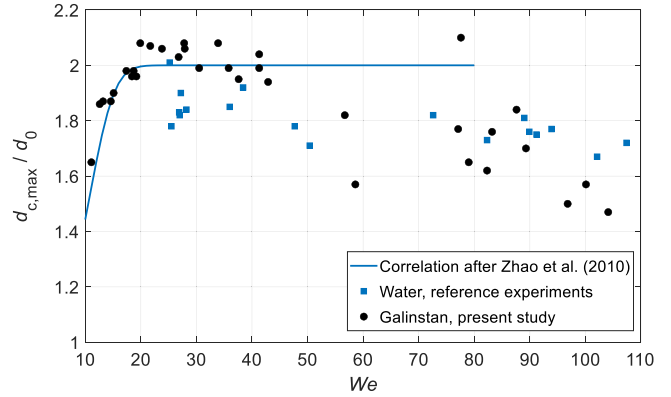


Fig. 15. Normalized cross-stream diameter $d_{c,max}/d_0$ at end of initial deformation for Galinstan experiments in comparison to the correlation of Zhao et al. (2010) (equation 6) and own reference experiments with water droplets. For $We > 58$, Galinstan droplets featured an appendix, which leads to increased uncertainty.

tigated Weber number by summarizing the time of initial deformation τ_{ini} and the maximum cross-stream diameter $d_{c,max}$, respectively. Both parameters play a critical role in defining the evolving breakup patterns and provide a good way to characterize and generalize initial droplet deformation.

The time of initial deformation for present Galinstan experiments decreases with increasing Weber number as shown in Fig. 14. While the decrease is stronger in the lower Weber number range, it becomes weaker with increasing Weber number. This tendency and the absolute values of τ_{ini} match well with the correlation given by Pilch and Erdman (1987) except at very low Weber numbers. For $We > 58$, Galinstan droplets have slightly lower values of τ_{ini} , likely because they feature an appendix that influences deformation and breakup (compare Fig. 5). Own water reference experiments confirm the similarity for the investigated Weber number range.

Fig. 15 shows the maximum cross-stream diameter $d_{c,max}$ normalized by d_0 for the investigated Weber number range. For Galinstan droplets, we observe a rise from 1.6 to 2.0 in the range of $We = 10$ -20, followed by constant plateau at a value of ~ 2.0 until $We \sim 40$. This behavior matches the correlation of Zhao et al. (2010) for conventional liquids and data points in that range of water reference experiments. As mentioned before, Galinstan experiments for $We > 58$ are subject to a higher uncertainty because of the appendix. Nevertheless, we identify a trend towards lower values of $d_{c,max}/d_0$, which is matched by the water reference experiments. A similar behavior can also be seen in the measurement points of Zhao et al. (2010) despite their fit suggesting a constant value. In fact, starting at $We \sim 40$, their data points suggest a trend down to approximately 1.7 for $We \sim 80$, similar to the measurements in the present study.

Studying a similar Weber number range, Chen et al. (2018) state that τ_{ini} is lower by a factor of ~ 0.6 for Galinstan columns compared to water columns. However, we cannot confirm this trend with the present study. In our experiments, both the initial deformation time and the maximum cross-stream deformation of Galinstan droplets are well in accordance with correlation for conventional liquids and own water reference experiments. In addition, an exemplary image sequence of a Galinstan and water droplet shows a good agreement throughout the deformation phase. Overall, it appears that neither the different fluid properties of the liquid metal, nor the oxide layer change the droplet deformation, provided that the Weber number is matched and that the time is nondimensionalized. This remarkable similarity is also observed by Arienti et al. (2019) by means of experiments and simulations for

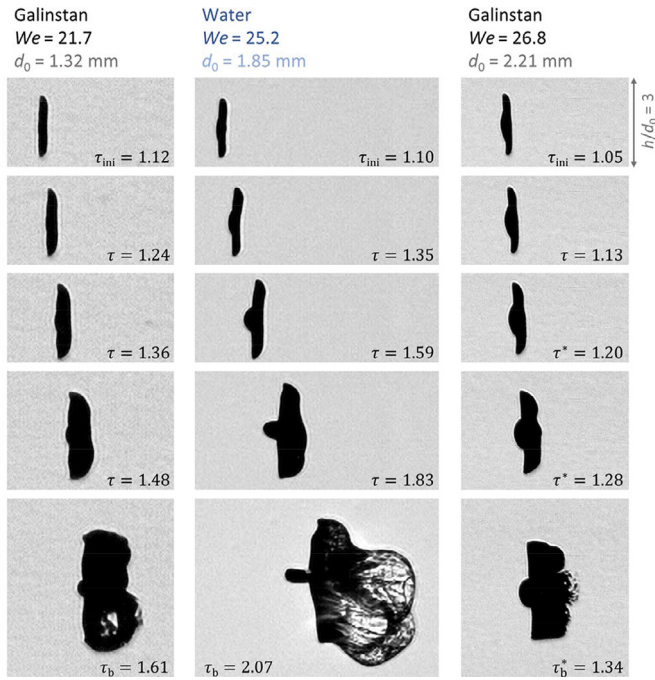


Fig. 16. Bag inflation and breakup of Galinstan droplets compared to a water droplet at $We \sim 25$.

Galinstan and water columns at $We = 10-12$. It is confirmed here for spherical droplets and for a wide range of Weber numbers.

4.2. Differences during the breakup

Previous sections have shown strong similarities between Galinstan and conventional liquids with respect to the morphology and initial deformation. However, we also observe significant differences. These differences appear after the initial deformation when the breakup is initiated.

4.2.1. Onset of breakup

Fig. 16 picks up where Fig. 13 ended and shows the bag inflation up to the moment of onset of breakup for Galinstan and water droplets at $We \sim 25$. As shown earlier, the morphology of the breakup is very similar, but the direct comparison also highlights clear differences for the two cases, most notably in the timing. Onset of breakup occurs significantly earlier for Galinstan with $\tau_b = 1.61$ and $\tau_b^* = 1.34$ compared to $\tau_b = 2.07$ for water. Overall, the shape appears similar, but Galinstan deforms much faster than water.

Especially the last two rows highlight that water droplets can sustain a much higher level of deformation and seem to adapt better to the flow. We can see this in the stamen, which remains very thick and with a constant curvature for Galinstan ($\tau^* = 1.28$, $We = 26.8$) but thins out and prolongs for the water droplet ($\tau = 1.83$). We also observe that the water bag inflates significantly more, especially in streamwise direction.

The single comparison is again expanded to the full range of investigated Weber numbers to confirm the observation on a more general level. Fig. 17 shows the time of onset of breakup τ_b for present Galinstan experiments in comparison to own water reference experiments and experiments with water and ethanol by Dai and Faeth (2001). The figure confirms the earlier onset of breakup for Galinstan, providing a difference of $\Delta\tau \sim 0.5$ to own water experiments and $\Delta\tau \sim 1$ compared to the values of Dai and Faeth (2001). Chen et al. (2018) also note a shorter bag inflation time for Galinstan columns compared to water columns and state

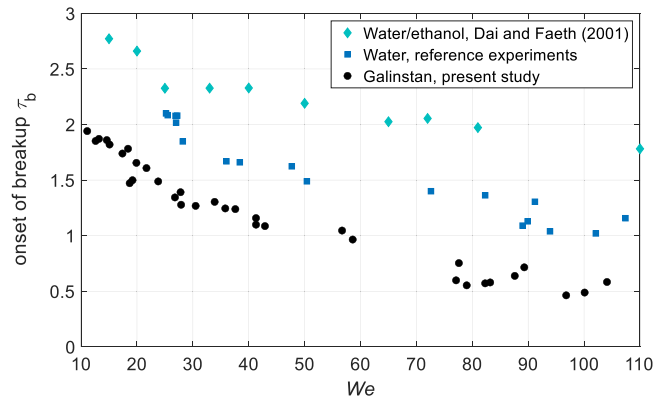


Fig. 17. Time of onset of breakup τ_b for Galinstan droplets compared to own reference experiments with water and experiments with water/ethanol droplets by Dai and Faeth (2001).

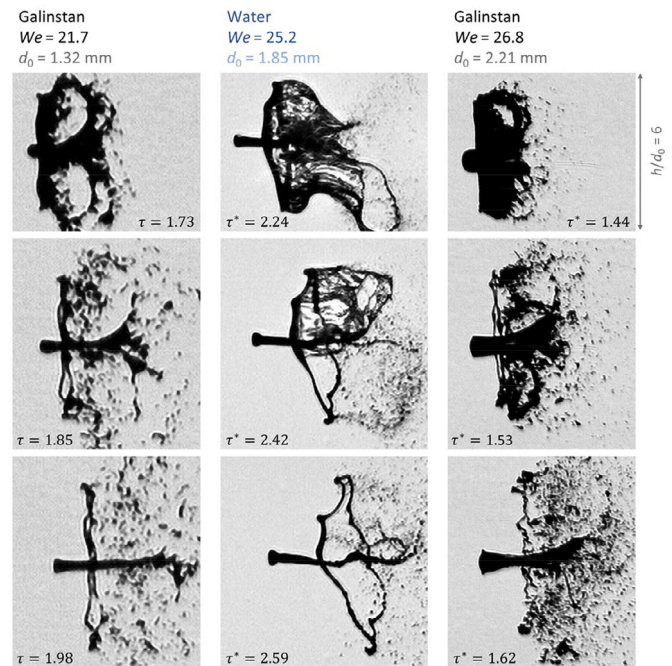


Fig. 18. Bag rupture and fragmentation of Galinstan and water droplets at $We \sim 25$.

that the onset of breakup occurs $\Delta\tau = 0.5 - 0.7$ earlier, which compares well with the present findings.

4.2.2. Rupture and fragmentation

Fig. 18 extends the image sequence of Galinstan and water droplets at $We \sim 25$ to later time instants. Flow conditions are now not constant for the water and the higher Weber number Galinstan case, so the analysis must be conducted carefully and can only provide qualitative impressions. Nevertheless, the direct comparison helps to highlight several further differences.

Most importantly, water bags break up from back to front in a continuous fashion along a smooth breakup line ($\tau^* = 2.24 - 2.59$). The breakup starts at a small hole, and sheets roll up along the edges while the hole widens (Chen et al., 2018). Galinstan bags on the other hand burst open across the whole bag surface almost simultaneously. Rupture lines are frayed and sharp-edged, reminiscent of solid mechanics (Fig. 18, first row).

Other effects are also notable. As observed before, the stamen for the higher We Galinstan experiment is clearly thicker than for the water experiment at similar Weber number. In addition, the

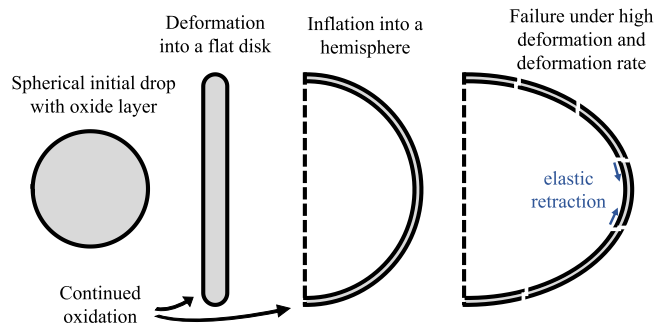


Fig. 19. Sketch of a deforming Galinstan droplet (grey) covered by an oxide layer (black) during bag breakup.

inwards curvature and folding of separated sheets discussed in section 4.2.2 distinguishes the Galinstan case from the water case which shows a clearer separation of stamen and bag (Fig. 18, second row). With respect to the ring, we can see that the water ring is rather thick, stays intact, and develops several nodes and indentations at the windward side ($\tau^* = 2.59$). Zhao et al. (2010) state that five to eight nodes appear for the bag-stamen mode. The presented water case reflects this behavior, but an exact number of nodes is difficult to obtain as the nodes do not form clearly. In contrast, the Galinstan rings are thinner, rather straight and do not form nodes before breakup (Fig. 18, second row). Lastly, Fig. 18 shows that fragments of the Galinstan breakup are coarse, aspherical, and sharp-edged, whereas bag rupture for water produces a fine mist.

4.3. Influence of the oxide layer

The previous section has highlighted several characteristic differences in breakup behavior that distinguish Galinstan from conventional liquids. Galinstan has a higher range of density and surface tension, but both property variations are accounted for through non-dimensional parameters. Previous sections have shown that this normalization eliminates differences with respect to the breakup morphology and early-stage deformation. Similarly, Chen et al. (2018) note that the influence of the density ratio is minimal.

However, in contrast to conventional liquids, Gallium alloys are covered by a connected oxide layer when exposed to oxygen, which can influence the breakup mechanism. Literature provides that the oxide layer forms rapidly even at low oxygen exposure but is self-limiting at a thickness of several nanometers (Daeneke et al., 2018). The oxide is an elastic solid that has a critical yield stress (Dickey, 2014), imparts mechanical stabilization to the liquid metal (Dickey, 2014), and increases the effective dynamic viscosity (Li et al., 2014). In addition, continuous oxide formation likely alters droplet shapes on the millisecond timescale or faster (Chen et al., 2018), i.e. during droplet breakup in the presented experiments.

4.3.1. Change of the breakup mechanism

Fig. 19 sketches the bag breakup of a Galinstan droplet in several stages. At the beginning of the experiment, the spherical droplet is covered by a connected oxide layer. This layer remains intact during the deformation into a disk and hemisphere, either because the initial oxide skin stretches, or because the droplet deformation rate initially is low compared to the rate of new oxide formation. Due to continuous oxidation, the amount of oxide increases during the experiment.

With increasing deformation, the oxide layer might not re-form fast enough. A reduction of effective surface tension could result,

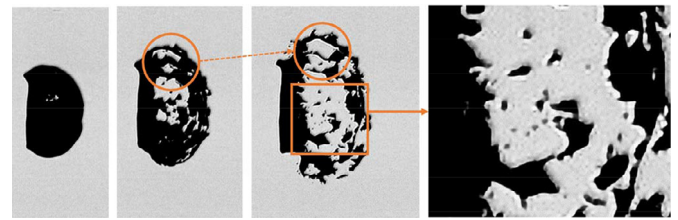


Fig. 20. Detailed record of bag fragmentation for a Galinstan droplet. The Weber number cannot be calculated accurately for this case due to inconsistent flow conditions. Circles highlight the contraction of fragments after rupture. The last image provides a zoom-in that shows the sharp-edged rupture lines and fragments.

from $\sigma \approx 0.72$ N/m at a fully oxidized interface to as low as $\sigma \approx 0.54$ N/m where liquid Galinstan is exposed. This change can cause a shift towards a higher effective Weber number, which can partly explain the observation of an earlier breakup time for Galinstan droplets. In addition, at one point, the stress in the oxide layer exceeds the critical yield stress and the layer ruptures. The remaining exposed bulk liquid cannot support the deformation, and again a significantly earlier breakup time results. Fig. 20 shows that sharp-edged, frayed rupture lines appear that are reminiscent of cracks in solid mechanics (Arienti et al., 2019; Chen et al., 2018). In the presented example, the rupture also manifests as an instantaneous burst of the whole bag surface with detached pieces of oxide layer retracting due to their inherent elasticity (Fig. 19 and Fig. 20). Overall, the breakup of the oxide skin appears more similar to a solid shell cracking under high tension (Mott, 1947; Moulinet and Adda-Bedia, 2015) than to a liquid droplet breakup.

The presented example focuses on bag breakup, but the change of the breakup mechanism occurs also in the other breakup regimes, albeit more locally. In the bag-and-stamen regime, the largest deformation and highest deformation rate appears at the inflating bags. Consequently, the critical yield stress is exceeded there, and the oxide layer in the bags breaks locally (compare Fig. 7). In the shear stripping regime, the drop does not deform strongly before breakup, but we do see strong local deformation especially at the sheets that are drawn downstream (compare Fig. 5). The oxide layer ruptures under local high strain and liquid Galinstan is exposed to the flow.

4.3.2. Fragmentation

Fig. 18 and Fig. 20 also show that coarse, irregularly shaped fragments are entrained in the flow after bag rupture. This distinguishes Galinstan from the very fine, spherical particles that are observed for water droplets. Chen et al. (2018) attribute the non-spherical shape of Galinstan fragments to the quick formation and the finite thickness of the oxide layer, which hinders the fragments from reaching a spherical shape and leads to a larger minimum fragment size. We agree, but with respect to the provided observation of burst rupture, we would like to add a further detail. Large aspherical fragments mostly appear directly after bag breakup as remnants of the ruptured oxide layer. The more the bag extends and blows up, the more pronounced are the irregularly shaped fragments. For example, Fig. 20 shows irregular shapes more clearly than Fig. 18, and a change can also be seen in image sequences presented earlier in this work. The reason is most likely the slower breakup and continuous oxidation during bag formation when the Weber number is lower. More oxide is generated, and more and larger aspherical fragments remain after rupture.

Experiments in the shear stripping regime do not show large irregularly shaped oxide fragments. However, it is possible that small oxide fragments are ripped off from the droplet periphery that cannot be identify due to the limits of the applied visualization. Similarly, we cannot judge accurately whether exposed liquid

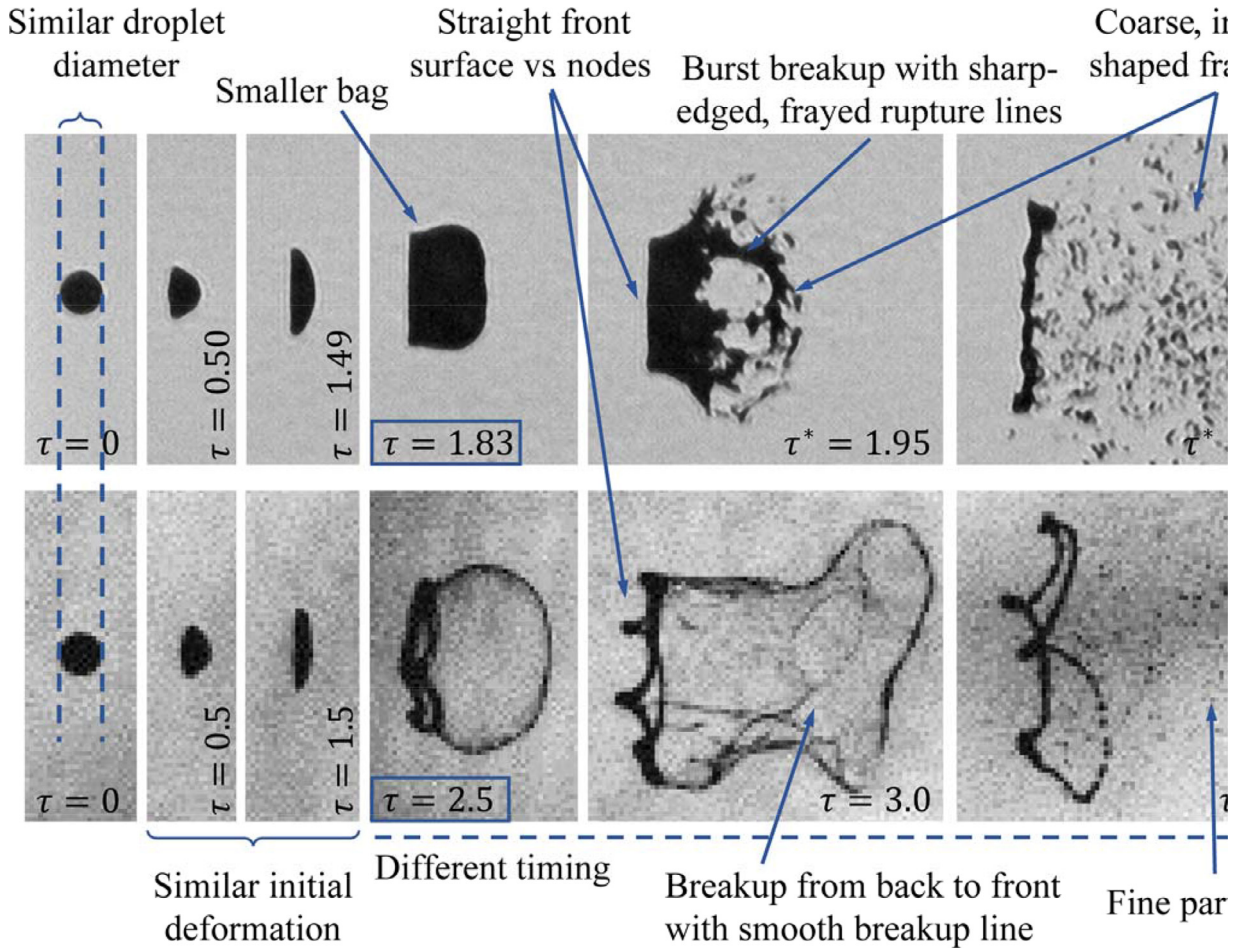


Fig. 21. Bag rupture of a Galinstan droplet at $We = 13.2$ compared to a water droplet at $We = 15$ taken from Dai and Faeth (2001) with permission from Elsevier. Images are scaled to have a similar initial droplet diameter.

Galinstan breaks into spherical or aspherical fragments when being exposed to the flow.

4.3.3. Additional effects

Apart from causing the burst breakup and aspherical fragmentation, the presence of the oxide layer seems to affect the breakup process also in other aspects.

- The oxide layer spanning the droplet limits the deformation and affects the external shape, especially when high deformation rates are reached. For example, Galinstan bags inflate less, and the stamen in the bag-and-stamen regime is wider (Fig. 16). In addition, Galinstan droplets in the shear stripping regime show a straight frontal area, which indicates that a large, connected piece of oxide layer remains intact and affects the droplet shape (Fig. 5).
- Stamen structures are generated by intact oxide sheets folding inwards after bag rupture (Fig. 7). However, because the oxide layer is solid, the sheets cannot recombine properly, and the stamen shape cannot adapt to the flow like in the case of water (Fig. 18). For thicker stamens, the oxide sheets trap air within the stamen, which explains why the stamen was found to be hollow earlier.
- There is no formation of indentations and nodes on the ring for Galinstan droplets in the bag-and-stamen regime. This could be caused by the mechanical stabilization imparted by the oxide layer. However, it could also be an effect of the faster breakup, as instabilities leading to nodes simply may not develop quickly enough in the case of Galinstan.

5. Summary and conclusion

The present work carried out experiments on secondary atomization with the liquid metal Galinstan. The first part of the analysis classified the morphology and the transition between modes, while the second part compared the results to conventional liquids.

Provided that the Weber number is matched and that the time is nondimensionalized, experimental results show that the breakup morphology of Galinstan droplets is very similar to that of conventional liquids. We observe bag, bag-and-stamen, multimode, and shear stripping breakup with corresponding transition Weber numbers of ~ 15 , ~ 35 , and ~ 80 , respectively. The multimode regime shows further sub-features associated with dual bag mode and multibag mode, similar to conventional liquids. Compared to the literature, both the type of modes as well as the transition values match previous observations, e. g. in references (Dai and Faeth, 2001; Guildenbecher et al., 2009).

The first part also shows that there is a gradual transition between the modes. Documenting this transition provides a reference for future work and helps to gain a more profound understanding of the physics. First, we present the initial deformation of droplets throughout the investigated Weber number range. The direct comparison shows how the shape at the end of deformation defines the following breakup behavior. Secondly, we focus on the appearance and evolution of the stamen as the most dominant feature up to $We \sim 50$. We observe that with increasing Weber number, the stamen:

- grows in cross-stream diameter;
- shifts upstream relative to the ring;
- first becomes longer, then becomes shorter until it is more accurate to speak of a core droplet than a stamen.

Corresponding to the stamen becoming more dominant, bags inflate less and start to show asymmetry. At one point, sheets at the droplet periphery do not support bag formation anymore, but instead directly bend downstream. After that, the breakup morphology transitions to shear stripping.

The classification, as well as the observations for the transition are in accordance with the theory of R-T instability. We observe the transition from bag to bag-and-stamen around a value of $d_{c,max}/\lambda_{max} = 1.5$ and see features of the dual bag mode around a value of 2.5.

The second part of this study provides a direct comparison of Galinstan to conventional liquids. Fig. 21 summarizes the findings and highlights the observed similarities and differences. The figure shows the breakup of a Galinstan droplet at $We = 13.2$ compared to the breakup of a water droplet at $We = 15$ taken from Dai and Faeth (2001). The initial droplet deformation is very similar both qualitatively and quantitatively, which is a trend that is confirmed for all conducted experiments. Across the full range of investigated Weber numbers, our results match correlations in the literature and own reference experiments with respect to the initial deformation time τ_{ini} and the maximum cross-stream diameter $d_{c,max}$. This shows that neither different fluid properties, nor the presence of the oxide skin noticeably influence the initial deformation of the drop.

In contrast, time instants after the initial deformation show a clearly different breakup behavior for Galinstan droplets. Main findings are highlighted exemplarily in Fig. 21 and can be summarized as:

- Galinstan droplets show an earlier onset of breakup of $\Delta\tau \approx 0.5 - 1$ compared to conventional liquids.
- When forming bags, Galinstan droplets burst open suddenly and show sharp-edged rupture lines reminiscent of solid mechanics (Fig. 21, Galinstan at $\tau^* = 1.95$).
- Deformation of Galinstan droplets appears limited. For example, bags inflate to a smaller size, stamens appear hollow, toroidal rims for Galinstan do not form nodes, and droplets in the shear stripping regime show a straight frontal area during the breakup.
- Coarse irregularly shaped fragments result from the rupture of the oxidized layer.

These observations along with results of previous studies suggest that the oxide layer covering Galinstan surfaces is the differentiating factor that changes the breakup behavior (Arienti et al., 2019; Chen et al., 2018). The oxide layer spans around the droplet and seems to limit the droplet deformation when higher deformation rates are reached. In addition, once a critical value is exceeded, the oxide layer ruptures and Galinstan droplets burst open like a solid shell rather than a liquid droplet (Mott, 1947; Moulinet and Adda-Bedia, 2015).

The present work provides an extensive look into the breakup behavior of oxide-forming liquid metal droplets. It can directly impact applications where Galinstan is atomized and sprayed on substrates, e.g., to create stretchable electronics (Jeong et al., 2015; Zhang et al., 2014). More importantly, it is a first step into studying secondary atomization of metal droplets in general. Observations of the behavior can be transferred to other oxide-forming metals, such as aluminum or titanium alloys, that are of higher practical interest in applications like powder metallurgy and additive manufacturing. In addition, the work can serve as a reference for future numerical or experimental work and can help adjust modelling ef-

forts that currently are validated against the behavior of conventional liquids. Nevertheless, further fundamental research into this topic is required to correlate the behavior of different metals and quantify the breakup. Next steps should target molten metals at higher temperatures, where the complex effect of changing fluid properties with changing temperature must be considered. Especially the behavior near the solidification point is challenging and of practical relevance in many applications.

Declaration of Competing Interest

The authors declare that they have no known competing financial interests or personal relationships that could have appeared to influence the work reported in this paper.

CRediT authorship contribution statement

T. Hopfes: Conceptualization, Formal analysis, Investigation, Methodology, Visualization, Writing – original draft. **J. Petersen:** Formal analysis, Investigation, Writing – review & editing. **Z. Wang:** Investigation, Methodology, Writing – review & editing. **M. Giglmaier:** Conceptualization, Project administration, Supervision, Writing – review & editing. **N.A. Adams:** Conceptualization, Funding acquisition, Resources, Supervision, Writing – review & editing.

Acknowledgements

The authors acknowledge funding by the European Research Council (ERC) under the European Union's Horizon 2020 research and innovation program (grant agreement No. 667483).

Supplementary materials

Supplementary material associated with this article can be found, in the online version, at doi:0.1016/j.ijmultiphaseflow.2021.103723.

References

- Anderson, I.E., White, E.M.H., Dehoff, R., 2018. Feedstock powder processing research needs for additive manufacturing development. *Curr. Opin. Solid State Mater. Sci.* 22, 8–15. doi:10.1016/j.cossms.2018.01.002.
- Arienti, M., Ballard, M., Sussman, M., Mazumdar, Y.C., Wagner, J.L., Farias, P.A., Guildenbecher, D.R., 2019. Comparison of simulation and experiments for multimode aerodynamic breakup of a liquid metal column in a shock-induced cross-flow. *Phys. Fluids* 31, 082110. doi:10.1063/1.5099589.
- Assael, M.J., Kakosimos, K., Banish, R.M., Brillo, J., Egry, I., Brooks, R., Quedest, P.N., Mills, K.C., Nagashima, A., Sato, Y., Wakeham, W.A., 2006. Reference data for the density and viscosity of liquid aluminum and liquid iron. *J. Phys. Chem. Ref. Data* 35, 285–300. doi:10.1063/1.2149380.
- Baukhage, K., 1992. Das Zerstäuben metallischer Schmelzen. *Chemie Ing. Tech.* 64, 322–332. doi:10.1002/cite.330640404.
- Cao, X., Sun, Z., Li, W., Liu, H., Yu, Z., Cao, X., Sun, Z., Li, W., Liu, H., Yu, Z., 2007. A new breakup regime of liquid drops identified in a continuous and uniform air jet flow. *Phys. Fluids* 19. doi:10.1063/1.2723154.
- Chen, Y., Wagner, J.L., Farias, P.A., DeMauro, E.P., Guildenbecher, D.R., 2018. Galinstan liquid metal breakup and droplet formation in a shock-induced cross-flow. *Int. J. Multiph. Flow* 106, 147–163. doi:10.1016/j.ijmultiphaseflow.2018.05.015.
- Chou, W.H., Hsiang, L.P., Faeth, G.M., 1997. Temporal Properties of Drop Breakup in the Shear Breakup Regime. *Int. J. Multiph. Flow* 23, 651–669.
- Ciccarelli, G., Frost, D.L., 1994. Fragmentation mechanisms based on single drop steam explosion experiments using flash X-ray radiography. *Nucl. Eng. Des.* 146, 109–132. doi:10.1016/0029-5493(94)90324-7.
- Daeneke, T., Khoshmanesh, K., Mahmood, N., De Castro, I.A., Esrafilzadeh, D., Barrow, S.J., Dickey, M.D., Kalantar-Zadeh, K., 2018. Liquid metals: Fundamentals and applications in chemistry. *Chem. Soc. Rev.* 47, 4073–4111. doi:10.1039/c7cs00043j.
- Dai, Z., Faeth, G.M., 2001. Temporal properties of secondary drop breakup in the multimode breakup regime. *Int. J. Multiph. Flow* 27, 217–236. doi:10.1016/S0301-9322(00)00015-X.
- Dickey, M.D., 2014. Emerging applications of liquid metals featuring surface oxides. *ACS Appl. Mater. Interfaces* 6, 18369–18379. doi:10.1021/am5043017.
- Dorschner, B., Biasiori-Poulanges, L., Schmidmayer, K., El-Rabii, H., Colonius, T., 2020. On the formation and recurrent shedding of ligaments in droplet aerobreakup. arXiv.

- Firmansyah, D.A., Kaiser, R., Zahaf, R., Coker, Z., Choi, T.Y., Lee, D., 2014. Numerical simulations of supersonic gas atomization of liquid metal droplets. *Jpn. J. Appl. Phys.* 53. doi:10.7567/JJAP.53.05HA09.
- Galfetti, L., DeLuca, L.T., Severini, F., Colombo, G., Meda, L., Marra, G., 2007. Pre and post-burning analysis of nano-aluminized solid rocket propellants. *Aerosp. Sci. Technol.* 11, 26–32.
- Grant, P.S., 1995. Spray forming. *Prog. Mater. Sci.* 39, 497–545. doi:10.1016/0079-6425(95)00004-6.
- Guildenbecher, D.R., López-Rivera, C., Sojka, P.E., 2009. Secondary atomization. *Exp. Fluids* 46, 371–402. doi:10.1007/s00348-008-0593-2.
- Guildenbecher, D.R., Sojka, P.E., 2011. Experimental investigation of aerodynamic fragmentation of liquid drops modified by electrostatic surface charge. *At. Sprays* 21, 139–147. doi:10.1615/AtomizSpr.2011003299.
- Guleryuz, H., Cimenoglu, H., 2009. Oxidation of Ti–6Al–4V alloy. *J. Alloys Compd.* 472, 241–246. doi:10.1016/j.jallcom.2008.04.024.
- Haraldsson, H.O., Li, H.X., Yang, Z.L., Dinh, T.N., Sehgal, B.R., 2001. Effect of solidification on drop fragmentation in liquid-liquid media. *Heat Mass Transf. und Stoffuebertragung* 37, 417–426. doi:10.1007/s002310000097.
- Henein, H., Uhlenwinkel, V., Fritsching, U., 2017. Metal Sprays and Spray Deposition. Springer International Publishing, Cham doi:10.1007/978-3-319-52689-8.
- Hinze, J.O., 1955. Fundamentals of the hydrodynamic mechanism of splitting in dispersion processes. *AIChE J* 1, 289–295. doi:10.1002/aic.690010303.
- Hsiang, L.-P., Faeth, G.M., 1995. Drop Deformation and Breakup due to Shock Wave and Steady Disturbances. *Int. J. Multiph. Flow* 21, 545–560. doi:10.1016/0301-9322(94)00095-2.
- Hsiang, L.P., Faeth, G.M., 1992. Near-limit drop deformation and secondary breakup. *Int. J. Multiph. Flow* 18, 635–652. doi:10.1016/0301-9322(92)90036-G.
- Inamura, T., Yanaoka, H., Kawada, T., 2009. Visualization of airflow around a single droplet deformed in an airstream. *At. Sprays* 19, 667–677. doi:10.1615/AtomizSpr.v19.i7.50.
- Jain, M., Prakash, R.S., Tomar, G., Ravikrishna, R.V., 2015. Secondary breakup of a drop at moderate Weber numbers. *Proc. R. Soc. A Math. Phys. Eng. Sci.* 471. doi:10.1098/rspa.2014.0930.
- Jain, S.S., Tyagi, N., Prakash, R.S., Ravikrishna, R.V., Tomar, G., 2019. Secondary breakup of drops at moderate Weber numbers: Effect of Density ratio and Reynolds number. *Int. J. Multiph. Flow* 117, 25–41. doi:10.1016/j.ijmultiphaseflow.2019.04.026.
- Jeong, S.H., Hjort, K., Wu, Z., 2015. Tape transfer atomization patterning of liquid alloys for microfluidic stretchable wireless power transfer. *Sci. Rep.* 5, 8419. doi:10.1038/srep08419.
- Joseph, D.D., Belanger, J., Beavers, G., 1999. Breakup of a liquid drop suddenly exposed to a high speed airstream. *Int. J. Multiph. Flow* 25, 1263–1303. doi:10.1016/S0301-9322(99)00043-9.
- Kim, J., Lee, J.K., Lee, K.M., 2016. Accurate Image Super-Resolution Using Very Deep Convolutional Networks. In: 2016 IEEE Conference on Computer Vision and Pattern Recognition (CVPR). IEEE, pp. 1646–1654. doi:10.1109/CVPR.2016.182.
- Kocourek, V., Karcher, C., Conrath, M., Schulze, D., 2006. Stability of liquid metal drops affected by a high-frequency magnetic field. *Phys. Rev. E - Stat. Nonlinear, Soft Matter Phys.* 74, 1–7. doi:10.1103/PhysRevE.74.026303.
- Kouraytem, N., Li, E.Q., Thoroddsen, S.T., 2016. Formation of microbeads during vapor explosions of Field's metal in water. *Phys. Rev. E* 93, 4–9. doi:10.1103/PhysRevE.93.063108.
- Krzeczkowski, S.A., 1980. Measurement of liquid droplet disintegration mechanisms. *Int. J. Multiph. Flow* 6, 227–239. doi:10.1016/0301-9322(80)90013-0.
- Leitner, M., Leitner, T., Schmon, A., Aziz, K., Pottlacher, G., 2017. Thermophysical Properties of Liquid Aluminum. *Metall. Mater. Trans. A Phys. Metall. Mater. Sci.* 48, 1–10. doi:10.1007/s11661-017-4053-6.
- Li, H., Mei, S., Wang, L., Gao, Y., Liu, J., 2014. Splashing phenomena of room temperature liquid metal droplet striking on the pool of the same liquid under ambient air environment. *Int. J. Heat Fluid Flow* 47, 1–8. doi:10.1016/j.ijheatfluidflow.2014.02.002.
- Liu, A., Mather, D., Reitz, R., 1993. Modeling the Effects of Drop Drag and Breakup on Fuel Sprays. *SAE Int. Congr. Expo. SAE* 930072.
- Liu, T., Sen, P., Kim, C.J., 2012. Characterization of nontoxic liquid-metal alloy galinstan for applications in microdevices. *J. Microelectromechanical Syst.* 21, 443–450. doi:10.1109/JMEMS.2011.2174421.
- Liu, Z., Reitz, R.D., 1997. An analysis of the distortion and breakup mechanisms of high speed liquid drops. *Int. J. Multiph. Flow* 23, 631–650. doi:10.1016/S0301-9322(96)00086-9.
- Mates, S.P., Settles, G.S., 2005. A study of liquid metal atomization using close-coupled nozzles, Part 1: Gas dynamic behavior. *At. Sprays* 15.
- Morley, N.B., Burris, J., Cadwallader, L.C., Nornberg, M.D., 2008. GaInSn usage in the research laboratory. *Rev. Sci. Instrum.* 79, 3–6. doi:10.1063/1.2930813.
- Mott, N.F., 1947. Fragmentation of shell cases. *Proc. R. Soc. London. Ser. A. Math. Phys. Sci.* 189, 300–308.
- Moulinet, S., Adda-Bedia, M., 2015. Popping Balloons: A Case Study of Dynamical Fragmentation. *Phys. Rev. Lett.* 115, 184301. doi:10.1103/PhysRevLett.115.184301.
- Opfer, L., Roisman, I.V., Venzmer, J., Klostermann, M., Tropea, C., 2014. Droplet-air collision dynamics: Evolution of the film thickness. *Phys. Rev. E* 89, 013023. doi:10.1103/PhysRevE.89.013023.
- Patel, P.D., Theofanous, T.G., 1981. Hydrodynamic fragmentation of drops. *J. Fluid Mech.* 103, 207–223. doi:10.1017/S0022112081001304.
- Pilch, M., Erdman, C.A., 1987. Use of breakup time data and velocity history data to predict the maximum size of stable fragments for acceleration-induced breakup of a liquid drop. *Int. J. Multiph. Flow* 13, 741–757. doi:10.1016/0301-9322(87)90063-2.
- Ranger, A.A., Nicholls, J.A., 1969. Aerodynamic shattering of liquid drops. *AIAA J* 7, 285–290. doi:10.2514/3.5087.
- Settles, G.S., 2001. Schlieren and Shadowgraph Techniques. Springer Berlin Heidelberg, Berlin, Heidelberg doi:10.1007/978-3-642-56640-0.
- Thakre, S., Ma, W., 2015. 3D simulations of the hydrodynamic deformation of melt droplets in a water pool. *Ann. Nucl. Energy* 75, 123–131. doi:10.1016/j.anucene.2014.07.046.
- Theofanous, G.T., Li, J.G., 2008. On the physics of aerobreakup. *Phys. Fluids* 20. doi:10.1063/1.2907989.
- Theofanous, T.G., Li, G.J., Dinh, T.N., 2004. Aerobreakup in Rarefied Supersonic Gas Flows. *J. Fluids Eng.* 126, 516. doi:10.1115/1.1777234.
- Ünal, A., 1989. Liquid break-up in gas atomization of fine aluminum powders. *Metall. Trans. B* 20, 61–69. doi:10.1007/BF02670350.
- Van der Schueren, B., Kruth, J.-P., 1995. Powder deposition in selective metal powder sintering. *Rapid Prototyp. J.*
- Villermaux, E., Bossa, B., 2009. Single-drop fragmentation determines size distribution of raindrops. *Nat. Phys.* 5, 697–702. doi:10.1038/nphys1340.
- Wang, Z., Hopfes, T., Giglmaier, M., Adams, N.A., 2020. Effect of Mach number on droplet aerobreakup in shear stripping regime. *Exp. Fluids* 61, 193. doi:10.1007/s00348-020-03026-1.
- Watanawanyoo, P., Hirahara, H., Mochida, H., Furukawa, T., Nakamura, M., Chaitep, S., 2011. Experimental investigations on spray characteristics in twin-fluid atomizer. *Procedia Eng* 24, 816–822. doi:10.1016/j.proeng.2011.11.2743.
- Wolfe, H.E., Andersen, W.H., 1964. Kinetics, mechanism, and resultant droplet sizes of the aerodynamic breakup of liquid drops. *AEROJET-GENERAL CORP DOWNEY CA.*
- Yim, P., 1996. The Role of Surface Oxidation in the Break-Up of Laminar Liquid Metal Jets.
- Zeoli, N., Gu, S., 2006. Numerical modelling of droplet break-up for gas atomisation. *Comput. Mater. Sci.* 38, 282–292. doi:10.1016/j.commatsci.2006.02.012.
- Zhang, Q., Gao, Y., Liu, J., 2014. Atomized spraying of liquid metal droplets on desired substrate surfaces as a generalized way for ubiquitous printed electronics. *Appl. Phys. A Mater. Sci. Process.* 116, 1091–1097. doi:10.1007/s00339-013-8191-4.
- Zhao, H., Liu, H., Li, W., Xu, J., 2010. Morphological classification of low viscosity drop bag breakup in a continuous air jet stream. *Phys. Fluids* 22, 114103. doi:10.1063/1.3490408.
- Zhao, H., Liu, H.F., Xu, J.L., Li, W.F., Lin, K.F., 2013. Temporal properties of secondary drop breakup in the bag-stamen breakup regime. *Phys. Fluids* 25. doi:10.1063/1.4803154.

A.3 Experimental investigation of droplet breakup of oxide-forming liquid metals

Thomas Hopfes, Zhaoguang Wang, Marcus Giglmaier, Nikolaus A. Adams

In: *Physics of Fluids* 33 (2021), 102114.
<https://doi.org/10.1063/5.0064178>

Contributions: My contributions to this publication include adapting the experimental methodology to allow to study metals with higher melting points. In addition, I conducted the experiments, processed and analyzed the study data, performed data fitting to derive empirical models, and visualized the results. The original manuscript of the publication was written by me.



LICENSE TO PUBLISH AGREEMENT FOR JOURNALS

This License to Publish must be signed, either electronically within the Peer X-Press manuscript submission system, or as a PDF to be uploaded into Peer X-Press as an alternate form, before the manuscript can be published. If you have questions about how to submit the form, please contact the journal's editorial office. For questions regarding the copyright terms and conditions of this License, please contact AIP Publishing LLC's Office of Rights and Permissions, 1305 Walt Whitman Road, Suite 300, Melville, NY 11747-4300 USA; Phone 516-576-2268; Email: rights@aip.org.

Article Title ("Work"): Experimental Investigation of Droplet Breakup of

Oxide-Forming Liquid Metals

(Please indicate the final title of the Work. Any substantive changes made to the title after acceptance of the Work may require the completion of a new agreement.)

All Author(s): Thomas Hopfes, Zhaoguang Wang, Marcus

Giglmaier, Nikolaus A. Adams

(Please list all the authors' names in order as they will appear in the Work. All listed authors must be fully deserving of authorship and no such authors should be omitted. For large groups of authors, attach a separate list to this form.)

Journal: Physics of Fluids

Manuscript ID#: POF21-AR-03063R1

All Copyright Owner(s), if not Author(s):

-

(Please list all copyright owner(s) by name. In the case of a Work Made for Hire, the employer(s) or commissioning party(ies) are the copyright owner(s). For large groups of copyright owners, attach a separate list to this form.)

Copyright Ownership and Grant of Rights

For the purposes of this License, the "Work" consists of all content within the article itself and made available as part of the article, including but not limited to the abstract, tables, figures, graphs, images, and multimedia files, as well as any subsequent errata. The Work refers to the content contained in both the Accepted Manuscript (AM) and the Version of Record (VOR). "Supplementary Material" consists of material that is associated with the article but linked to or accessed separately (available electronically only), including but not limited to data sets and any additional files.

This Agreement is an Exclusive License to Publish not a Transfer of Copyright. Copyright to the Work remains with the Author(s) or, in the case of a Work Made for Hire, with the Author(s)' employer(s). AIP Publishing LLC shall own and have the right to register in its name the copyright to the journal issue or any other collective work in which the Work is included. Any rights granted under this License are contingent upon acceptance of the Work for publication by AIP Publishing. If for any reason and at its own discretion AIP Publishing decides not to publish the Work, this License is considered void.

Each Copyright Owner hereby grants to AIP Publishing LLC the following irrevocable rights for the full term of United States and foreign copyrights (including any extensions):

1. The exclusive right and license to publish, reproduce, distribute, transmit, display, store, translate, edit, adapt, and create derivative works from the Work (in whole or in part) throughout the world in all formats and media whether now known or later developed, and the nonexclusive right and license to do the same with the Supplementary Material.
2. The right for AIP Publishing to freely transfer and/or sublicense any or all of the exclusive rights listed in #1 above. Sublicensing includes the right to authorize requests for reuse of the Work by third parties.
3. The right for AIP Publishing to take whatever steps it considers necessary to protect and enforce, at its own expense, the exclusive rights granted herein against third parties.

Author Rights and Permitted Uses

Subject to the rights herein granted to AIP Publishing, each Copyright Owner retains ownership of copyright and all other proprietary rights such as patent rights in the Work.

Each Copyright Owner retains the following nonexclusive rights to use the Work, without obtaining permission from AIP Publishing, in keeping with professional publication ethics, and provided clear credit is given to its first publication in an AIP Publishing journal. Any reuse must include a full credit line acknowledging AIP Publishing's publication and a link to the VOR on AIP Publishing's site.

Each Copyright Owner may:

1. Reprint portions of the Work (excerpts, figures, tables) in future works created by the Author, in keeping with professional publication ethics.
2. Post the Accepted Manuscript (AM) to their personal web page or their employer's web page immediately after acceptance by AIP Publishing.
3. Deposit the AM in an institutional or funder-designated repository immediately after acceptance by AIP Publishing.

4. Use the AM for posting within scientific collaboration networks (SCNs). For a detailed description of our policy on posting to SCNs, please see our Web Posting Guidelines (<https://publishing.aip.org/authors/web-posting-guidelines>).
5. Reprint the Version of Record (VOR) in print collections written by the Author, or in the Author's thesis or dissertation. It is understood and agreed that the thesis or dissertation may be made available electronically on the university's site or in its repository and that copies may be offered for sale on demand.
6. Reproduce copies of the VOR for courses taught by the Author or offered at the institution where the Author is employed, provided no fee is charged for access to the Work.
7. Use the VOR for internal training and noncommercial business purposes by the Author's employer.
8. Use the VOR in oral presentations made by the Author, such as at conferences, meetings, seminars, etc., provided those receiving copies are informed that they may not further copy or distribute the Work.
9. Distribute the VOR to colleagues for noncommercial scholarly use, provided those receiving copies are informed that they may not further copy or distribute the Work.
10. Post the VOR to their personal web page or their employer's web page 12 months after publication by AIP Publishing.
11. Deposit the VOR in an institutional or funder-designated repository 12 months after publication by AIP Publishing.
12. Update a prior posting with the VOR on a noncommercial server such as arXiv, 12 months after publication by AIP Publishing.

Author Warranties

Each Author and Copyright Owner represents and warrants to AIP Publishing the following:

1. The Work is the original independent creation of each Author and does not infringe any copyright or violate any other right of any third party.
2. The Work has not been previously published and is not being considered for publication elsewhere in any form, except as a preprint on a noncommercial server such as arXiv, or in a thesis or dissertation.
3. Written permission has been obtained for any material used from other sources, and copies of the permission grants have been supplied to AIP Publishing to be included in the manuscript file.
4. All third-party material for which permission has been obtained has been properly credited within the manuscript.
5. In the event that an Author is subject to university open access policies or other institutional restrictions that conflict with any of the rights or provisions of this License, such Author has obtained the necessary waiver from his or her university or institution.

This License must be signed by the Author(s) and, in the case of a Work Made for Hire, also by the Copyright Owners. One Author/Copyright Owner may sign on behalf of all the contributors/owners only if they all have authorized the signing, approved of the License, and agreed to be bound by it. The signing Author and, in the case of a Work Made for Hire, the signing Copyright Owner warrants that he/she/it has full authority to enter into this License and to make the grants this License contains.

1. The Author must please sign here (except if an Author is a U.S. Government employee, then please sign under #3 below):

	Thomas Hopfes	27.09.2021
Author Signature	Print Name	Date

2. The Copyright Owner (if different from the Author) must please sign here:

-		
Name of Copyright Owner	Authorized Signature and Title	Date

3. If an Author is a U.S. Government employee, such Author must please sign below.

The signing Author certifies that the Work was written as part of his/her official duties and is therefore not eligible for copyright protection in the United States.

-
Name of U.S. Government Institution (e.g., Naval Research Laboratory, NIST)

-		
Author Signature	Print Name	Date

PLEASE NOTE: NATIONAL LABORATORIES THAT ARE SPONSORED BY U.S. GOVERNMENT AGENCIES BUT ARE INDEPENDENTLY RUN ARE NOT CONSIDERED GOVERNMENT INSTITUTIONS. (For example, Argonne, Brookhaven, Lawrence Livermore, Sandia, and others.) Authors at these types of institutions should sign under #1 or #2 above.

If the Work was authored under a U.S. Government contract, and the U.S. Government wishes to retain for itself and others acting on its behalf, a paid-up, nonexclusive, irrevocable, worldwide license in the Work to reproduce, prepare derivative works from, distribute copies to the public, perform publicly, and display publicly, by or on behalf of the Government, please check the box below and add the relevant Contract numbers.

Contract #(s) _____ [1.16.1]

LICENSE TERMS DEFINED

Accepted Manuscript (AM): The final version of an author's manuscript that has been accepted for publication and incorporates all the editorial changes made to the manuscript after submission and peer review. The AM does not yet reflect any of the publisher's enhancements to the work such as copyediting, pagination, and other standard formatting.

arXiv: An electronic archive and distribution server for research article preprints in the fields of physics, mathematics, computer science, quantitative biology, quantitative finance, and statistics, which is owned and operated by Cornell University, <http://arxiv.org/>.

Commercial and noncommercial scholarly use: *Noncommercial* scholarly uses are those that further the research process for authors and researchers on an individual basis for their own personal purposes. They are author-to-author interactions meant for the exchange of ideas. *Commercial* uses fall outside the author-to-author exchange and include but are not limited to the copying or distribution of an article, either in hard copy form or electronically, for resale or licensing to a third party; posting of the AM or VOR of an article by a site or service where an access fee is charged or which is supported by commercial paid advertising or sponsorship; use by a for-profit entity for any type of promotional purpose. Commercial uses require the permission of AIP Publishing.

Embargo period: The period of time during which free access to the full text of an article is delayed.

Employer's web page: A web page on an employer's site that highlights the accomplishments and research interests of the company's employees, which usually includes their publications. (See also: Personal web page and Scholarly Collaboration Network.)

Exclusive License to Publish: An exclusive license to publish is a written agreement in which the copyright owner gives the publisher exclusivity over certain inherent rights associated with the copyright in the work. Those rights include the right to reproduce the work, to distribute copies of the work, to perform and display the work publicly, and to authorize others to do the same. The publisher does not hold the copyright to the work, which continues to reside with the author. The terms of the AIP Publishing License to Publish encourage authors to make full use of their work and help them to comply with requirements imposed by employers, institutions, and funders.

Full Credit Line: AIP Publishing's preferred format for a credit line is as follows (you will need to insert the specific citation information in place of the capital letters): "Reproduced from [FULL CITATION], with the permission of AIP Publishing." A FULL CITATION would appear as: Journal abbreviation, volume number, article ID number or page number (year). For example: Appl. Phys. Lett. 107, 021102 (2015).

Institutional repository: A university or research institution's digital collection of articles that have been authored by its staff and which are usually made publicly accessible. As authors are encouraged and sometimes required to include their published articles in their institution's repository, the majority of publishers allow for deposit of the Accepted Manuscript for this purpose. AIP Publishing also allows for the VOR to be deposited 12 months after publication of the Work.

Journal editorial office: The contact point for authors concerning matters related to the publication of their manuscripts. Contact information for the journal editorial offices may be found on the journal websites under the "About" tab.

Linking to the Version of Record (VOR): To create a link to your article in an AIP Publishing journal or proceedings, you need to know the CrossRef digital object identifier (doi). You can find the doi on the article's abstract page. For instructions on linking, please refer to our Web Posting Guidelines at <https://publishing.aip.org/authors/web-posting-guidelines>.

National Laboratories: National laboratories are sponsored and funded by the U.S. Government but have independent nonprofit affiliations and employ private sector resources. These institutions are classified as Federally Funded Research and Development Centers (FFRDCs). Authors working at FFRDCs are not considered U.S. Government employees for the purposes of copyright. The Master Government List of FFRDCs may be found at <http://www.nsf.gov/statistics/ffrdclist/>.

Personal web page: A web page that is hosted by the author or the author's institution and is dedicated to the author's personal research interests and publication history. An author's profile page on a social media site or scholarly collaboration network is *not* considered a personal web page. (See also: Scholarly Collaboration Network; Employer's web page.)

Peer X-Press: A web-based manuscript submission system by which authors submit their manuscripts to AIP Publishing for publication, communicate with the editorial offices, and track the status of their submissions. The Peer X-Press system provides a fully electronic means of completing the License to Publish Agreement. A hard copy of the Agreement will be supplied by the editorial office if the author is unable to complete the electronic version of the form.

Preprint: A version of an author's manuscript intended for publication that has not been peer reviewed and does not reflect any editorial input or publisher enhancements.

Professional Publication Ethics: AIP Publishing provides information on what it expects from authors in its "Statement of ethics and responsibilities of authors submitting to AIP Publishing journals" (<http://publishing.aip.org/authors/ethics>). AIP Publishing is also a member of the Committee on Publication Ethics (COPE) (<http://publicationethics.org/>), which provides numerous resources and guidelines for authors, editors, and publishers with regard to ethical standards and accepted practices in scientific publishing.

Scholarly Collaboration Network (SCN): Professional networking sites that facilitate collaboration among researchers as well as the sharing of data, results, and publications. SCNs include sites such as Academia.edu, ResearchGate, and Mendeley, among others.

Supplementary Material: Related material that has been judged by peer review as being relevant to the understanding of the article but that may be too lengthy or of too limited interest for inclusion in the article itself. Supplementary Material may include data tables or sets, appendixes, movie or audio clips, or other multimedia files.

U.S. Government employees: Authors working at Government organizations who author works as part of their official duties and who are not able to license rights to the Work, since no copyright exists. Government works are in the public domain within the United States.

Version of Record (VOR): The final published version of the article as it appears in the printed journal/proceedings or on the Scitation website. It incorporates all editorial input, is formatted in the publisher's standard style, and is usually viewed in PDF form.

Waiver: A request made to a university or institution to exempt an article from its open-access policy requirements. For example, a conflict will exist with any policy that requires the Author to grant a nonexclusive license to the university or institution that enables it to license the Work to others. In all such cases, the Author must obtain a waiver, which should be included in the manuscript file.




Work: The "Work" is considered all the material that comprises the article, including but not limited to the abstract, tables, figures, images, multimedia files that are directly embedded within the text, and the text itself. The Work does not include the Supplementary Material. (See also: Supplementary Material.)

Work Made for Hire: Under copyright law, a work prepared by an employee within the scope of employment, or a work that has been specially ordered or commissioned for which the parties have agreed in writing to consider as a Work Made for Hire. The hiring party or employer is considered the author and owner of the copyright, not the person who creates the work.

Experimental investigation of droplet breakup of oxide-forming liquid metals

Cite as: Phys. Fluids **33**, 102114 (2021); <https://doi.org/10.1063/5.0064178>

Submitted: 21 July 2021 • Accepted: 22 September 2021 • Published Online: 14 October 2021

 T. Hopfes,  Z. Wang (王召光),  M. Giglmaier, et al.



View Online



Export Citation



CrossMark

Physics of Fluids

SPECIAL TOPIC: Flow and Acoustics of Unmanned Vehicles

Submit Today!



Experimental investigation of droplet breakup of oxide-forming liquid metals

Cite as: Phys. Fluids **33**, 102114 (2021); doi: 10.1063/5.0064178

Submitted: 21 July 2021 · Accepted: 22 September 2021 ·

Published Online: 14 October 2021



View Online



Export Citation



CrossMark

T. Hopfes,^{a)} Z. Wang (王召光), M. Giglmaier, and N. A. Adams

AFFILIATIONS

Chair of Aerodynamics and Fluid Mechanics, Technical University of Munich, Boltzmannstr. 15, D-85748 Garching bei München, Germany

^{a)} Author to whom correspondence should be addressed: thomas.hopfes@tum.de

ABSTRACT

This work investigates the breakup of liquid metal droplets experimentally using a shock tube. Droplets of Field's metal melt are produced and their flow-induced deformation and rupture are captured by a high-speed camera. Results are compared to previous data on Galinstan droplet breakup using image sequences and deformation data. Regarding differences, we find that Field's metal droplets show slightly larger deformations and breakup into a larger number of smaller fragments, especially at low Weber numbers. We expect this to be an effect of different oxidation rates. However, both oxidizing metals show a very similar behavior with respect to the breakup morphology, transition between modes, and the timing of the deformation across the investigated Weber number range of 10–100. In addition, core features that distinguish the breakup of metals from that of conventional, water-like liquids are confirmed. Based on the similarities, we propose that the findings can be generalized to also represent other oxide-forming metals. Weber number-dependent fits are presented for the initial deformation time, the time of the onset of breakup, and the maximum cross-stream diameter. In addition, we provide an empirical fit for the time-dependent cross-stream deformation and evaluate it against experimental data and models from the literature. The fits can be used directly in numerical studies or help improve current breakup models.

Published under an exclusive license by AIP Publishing. <https://doi.org/10.1063/5.0064178>

I. INTRODUCTION

Atomization of metal melt is a core technology that enables a large variety of applications like spray forming or spray deposition processes.^{1,2} It also enables metal powder production which is used, for example, in rocket propulsion or additive manufacturing processes.^{3–5} Nevertheless, atomization of metallic alloys remains challenging with respect to the quality and controllability of the final product as well as in terms of efficiency.⁶

The atomization process can be separated into two main mechanisms: primary breakup and secondary breakup.^{7–9} Primary breakup describes the transition of a bulk liquid to ligaments and large droplets, whereas secondary breakup refers to the fragmentation of a single droplet by aerodynamic forces.^{9,10} Secondary atomization is extensively studied for liquids such as water, ethanol, or Diesel,^{11–16} which we consider as conventional liquids. However, not all related findings can directly be transferred to metal melts,⁵ because the breakup of metal droplets adds further complexities to the breakup process. Fluid properties like the thermal conductivity, viscosity, and surface tension change with temperature, especially near the solidification temperature.^{17,18} In addition, many metals, even when being liquid at room

temperature, provide significantly different properties such as higher ranges of density and surface tension¹⁹ and can be subject to the formation of an oxide layer.²⁰

For conventional liquids, it has been well established that secondary breakup is mainly determined by two non-dimensional numbers, the Weber number (We) and the Ohnesorge number (Oh).^{21,22} The Ohnesorge number relates the dynamic viscosity (μ_d) with the initial diameter (d_0), the surface tension (σ), and the density (ρ_d) of the liquid drop,

$$Oh = \mu_d / \sqrt{\rho_d d_0 \sigma}. \quad (1)$$

For $Oh \leq 0.1$, as applies for this work, the influence of liquid viscosity on the breakup regime is negligible, and the Weber number remains as the dominating parameter.¹⁰ The Weber number represents the ratio between the disruptive aerodynamic force and the restorative surface tension and is written as

$$We = \rho_g u_g^2 d_0 / \sigma. \quad (2)$$

Here, ρ_g and u_g represent density and velocity of the surrounding gas or fluid flow. Droplet breakup modes vary with increasing Weber

number. Typically, they are distinguished as bag, bag-and-stamen, multimode, and shear stripping breakup with transition We of ~ 15 , ~ 40 , and ~ 80 , respectively.²³ Depending on the literature, however, different transition Weber numbers are found, and the names of the modes can vary.^{14,22–28}

Concerning metal droplet breakup, there are several works that study liquid–liquid systems experimentally,^{29–31} numerically,³² or analytically.³¹ However, these works do not represent the fragmentation process in gas–liquid systems adequately due to much lower density ratios, different orders of magnitude in heat transfer, and different interface mechanisms like the generation of vapor bubbles.³³ With respect to metal droplet breakup in gas, there are single experiments available for mercury^{34,35} and some more recent studies using Galinstan, an oxide-forming metal that is liquid at room temperature. The breakup of Galinstan has both similarities and differences compared to liquids like water.^{19,36,37} The breakup morphology follows the same pattern of bag, bag-and-stamen, multimode, and shear stripping with increasing Weber number, and transition values match those of conventional liquids.³⁷ In addition, the initial deformation of Galinstan droplets is similar to other liquids with respect to the initial deformation time and corresponding cross-stream diameter.³⁷ However, the onset of breakup is significantly earlier for Galinstan, and the fragmentation appears more abruptly. Furthermore, bags break with fracture lines that are more akin to solid mechanics, and the resulting fragments are non-spherical and sharp-edged. All effects are related to the oxide layer forming on the surface of the Galinstan droplet.^{19,36,37}

However, only data on the breakup of Galinstan droplets are available so the question remains how well previous observations generalize and can be applied to other oxide-forming liquid metals like aluminum or titanium alloys.^{17,38} In addition, it is unclear to what extent and regarding which aspects different oxidation parameters affect or change the breakup behavior. Therefore, this work employs Field’s metal (FM), a low melting point eutectic metal alloy that also is subject to oxidation,^{33,39} to expand the data set. Using the collective data of Galinstan and FM droplet breakup, we provide empirical fits for breakup times and droplet deformation as a representation for oxidizing liquid metals. In addition, a thorough study of differences between the two metals is conducted to evaluate further influencing factors like the oxidation rate.

II. METHODS

A. Experimental facility

Experiments are conducted with a shock tube that has been established for droplet breakup studies.^{37,40,41} Details of the experimental setup can be found in the corresponding works, but an overview and an explanation of some changes are also presented here. Figure 1 shows a sketch of the shock tube and the droplet generator developed for metal melts. With respect to the shock tube, we increased the experiment time of constant flow conditions by modifying the setup compared to previous works. The cookie-cutter upstream of the test section, which is used to remove boundary flows and to enable the transition from the tube to the 190 mm × 190 mm square test section, was replaced by a longer version. In addition, a shorter cookie-cutter was installed downstream of the test section. Thus, the rectangular area of the test section was effectively prolonged, removing unwanted wave motion. Steady flow conditions last for 4.0–4.2 ms for the current experiments, covering the deformation and breakup of the droplets unless otherwise specified. In some cases, we show image series that extend to late-stage breakup when flow conditions are non-constant. To highlight this, we mark the time with an asterisk “*” in these cases.

The shock-induced flow interacts with single droplets that are expelled from a droplet generator through a needle into the test section. The droplet generator for the Field’s metal is highlighted in Fig. 1 and consists of a furnace including two heating cartridges. Connected to the funnel of the furnace is a luer lock needle adaptor and steel capillaries typically of size G30. The metal is melted in the furnace, and drops are expelled by creating a pressure pulse in the fluid chamber. A temperature sensor and a temperature control keep the furnace within $\pm 2^\circ\text{C}$ of the target temperature, which was set to 90°C for the majority of the experiments. This represents a good estimate for the temperature of the liquid in the furnace, while the temperature of the drop forming at the needle tip is expected to be slightly lower. The effect of the temperature and experiments operating at a lower target temperature is discussed in Sec. III A.

As in previous studies,^{37,40,41} we apply PCB Piezotronics ICP® fast-response pressure sensors to measure the shock velocity. Post-shock flow properties are then calculated from pre-shock conditions

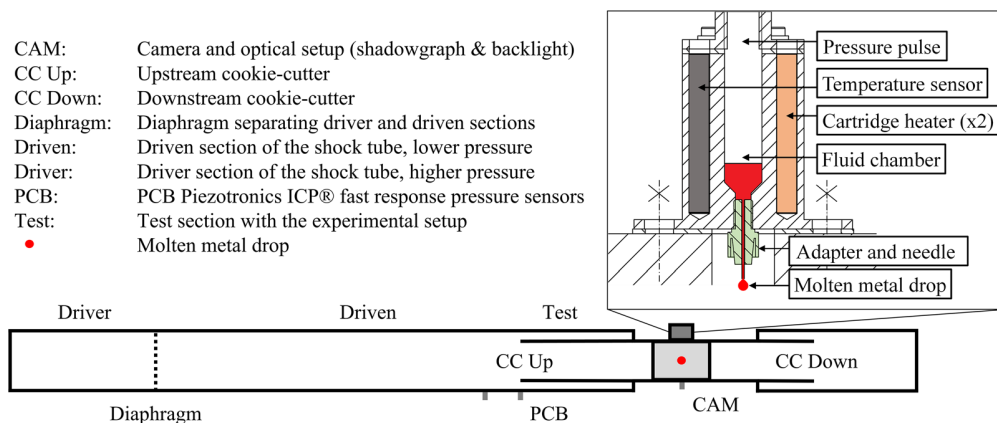


FIG. 1. Sketch of the shock tube and the droplet generator for Field’s metal.

using moving shock relations and are evaluated in comparison with the measured static pressure at the wall of the test section.

We record shadowgraph and backlight image sequences with a Shimadzu HyperVision HPV-X ultra-high-speed camera. The camera records 128 consecutive images with a resolution of 400×250 pixels and is operated at framing rates of 20–50 kfps. The z-type shadowgraph system has been used previously,^{40,41} and the backlight system follows a standard setup, with an LED array illuminating a ground glass diffuser to provide a uniform background light. The camera is set up perpendicular to the flow and uses a lens to focus on the plane of the drop.

B. Liquid metal properties

Table I provides an overview of key fluid properties of the two studied metals. Water is listed as well to represent conventional liquids and to highlight key differences. Fluid properties for Galinstan are taken as in our previous work as $\rho_{\text{Gal}} = 6440 \text{ kg/m}^3$, $\sigma_{\text{Gal}} = 718 \text{ mN/m}$, and $\mu_{\text{Gal}} = 2.4 \text{ mPa}\cdot\text{s}$ for the density, surface tension, and viscosity, respectively.³⁷ Field’s metal is a nontoxic eutectic alloy with component percentages by weight of 32.5% bismuth, 51% indium, and 16.5% tin, and a melting point at 62 °C.⁴² The density is temperature dependent and follows the relation⁴³

$$\rho_{\text{FM}} = 10.6555 - 0.0085 \cdot T. \quad (3)$$

Here, the density of FM, ρ_{FM} , is in g/cm^3 and temperature T is in Kelvin. The viscosity is shear rate dependent and shows shear thinning behavior.⁴⁴ Measurements range between 10 and 30 $\text{mPa}\cdot\text{s}$ ^{42–44} for the current temperature. With that range, the viscosity is low compared to the surface tension ($Oh < 0.01$) for the current experiments, and We remains as the dominating parameter.¹⁰

Exact data of the surface tension are important to correctly estimate the Weber number. However, measurements for the surface tension of FM are available only in few works. Hadj-Achour *et al.*⁴² provided a value of $\sigma_{\text{FM}} \sim 410 \text{ mN/m}$, but neither a source nor context is provided. In the corresponding work, a value of 500 mN/m is listed.⁴⁵ Kouraytem *et al.*³³ assumed a bimodal bismuth-indium alloy and obtained a theoretical value of $\sigma_{\text{FM}} \sim 400 \text{ mN/m}$ and measured a value of $\sigma_{\text{FM}} \sim 410 \text{ mN/m}$ at 108 °C with a pendant drop method.⁴⁶ They note a rapid succession of a few drops to minimize oxide formation on the surface, which is critical as the pendant drop method usually requires static conditions to establish equilibrium.^{47,48} It is also not representative for our experiments where drops are exposed at least for some seconds to the ambient air before the atomization and so oxidation effects need to be taken into account. Consequently, we

TABLE I. Summarized are key fluid properties of the studied liquid metals and water, which is listed to represent conventional liquids. Listed are values for the density (ρ), the surface tension (σ), the viscosity (μ), and the freezing temperature (T_{freeze}).

Liquid	ρ (kg/m^3)	σ (mN/m)	μ ($\text{mPa}\cdot\text{s}$)	Oxidation	T_{freeze}
Galinstan	6440	718	2.4	Oxidizing	−19 °C
Field’s metal	7570–7700	565	21	Oxidizing	62 °C
Water	998	72	1	Non-reactive	0 °C

measured the effective surface tension of FM in air with the pendant drop method and the relation⁴⁸

$$\sigma_{\text{PD}} = g\Delta\rho R_0^2/\beta. \quad (4)$$

Here, g is the gravitational acceleration, $\Delta\rho$ is the density difference of the two fluids (FM and air), R_0 is the radius of the apex curvature of the drop, and β is the shape factor. The shape factor was calculated after Hansen and Rodsrud⁴⁹ using the two characteristic diameters d_s and d_e ,

$$\beta = 0.12836 - 0.7577 \frac{d_s}{d_e} + 1.7713 \left(\frac{d_s}{d_e}\right)^2 - 0.5426 \left(\frac{d_s}{d_e}\right)^3. \quad (5)$$

As shown in Fig. 2, d_e is the maximum diameter of the drop and d_s is the diameter at the droplet neck taken at the height of d_e from the apex of the drop.

Validating with Galinstan, we obtain a mean value and standard deviation of $\sigma_{\text{Gal,PD}} = 700 \pm 20 \text{ mN/m}$, confirming the literature value within 2.5% of the mean. For FM, we measure $\sigma_{\text{FM,PD}} = 565 \pm 67 \text{ mN/m}$ at 90 °C. The relatively high variance results because metal droplets in our measurements could not be kept fully stationary at the needle tip. For this work, we take the surface tension of FM as $\sigma_{\text{FM}} = 565 \text{ mN/m}$ according to the mean of the measurement. Sections III B and IV A will show that the resulting Weber numbers fit well with the expected breakup behavior, confirming the chosen value.

As noted in Table I, Field’s metal, like Galinstan, but in contrast to liquids like water, is subject to oxidation when exposed to air,^{33,39} as are all its individual components.^{39,50,51} However, details of the oxidation process of FM or the properties of its oxide skin are rare. Oxidation times are noted occasionally but range from seconds⁴² (the time it takes to form a droplet) up to several minutes.³⁹ The experience of this work indicates that surface oxidation appears rather quickly. For example, an appendix forms when droplets detach from the needle tip, leading to an aspherical shape. This is also a common observation for Galinstan droplets and is associated with the formation of an oxide

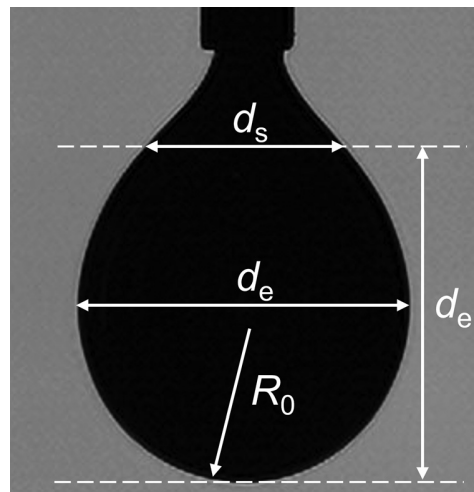


FIG. 2. Pendant metal drop illuminated in background light with parameters characterizing the droplet shape.

layer.^{52–54} In addition, Secs. III B and III C will show that several aspects of the breakup are reminiscent of Galinstan and its oxide layer, albeit not always to the same extent.

C. Data analysis

For the present experiments, the time t is defined as zero at the moment the shock passes the droplet. For consistency and comparability with previous literature, t is normalized by the characteristic transport time after Ranger and Nicholls,⁵⁵ yielding the dimensionless time τ ,

$$\tau = t \cdot u_g / d_0 \sqrt{\rho_g / \rho_d}. \quad (6)$$

Two characteristic breakup times are of importance – the end of initial deformation τ_{ini} and the onset of breakup τ_b . In the bag and the bag-and-stamen mode, τ_{ini} defines the time instant when the deformed droplet resembles a flat disk, right before the bag inflation starts.^{22,56} In the shear stripping mode, τ_{ini} is reached when a sheet or ligament at the droplet periphery is drawn downstream of the drop for the first time.²² In both cases, this time instant is found by comparing images and checking the streamwise diameter for its minimum. The second characteristic time τ_b , representing the onset of breakup, is taken at the first sign of fragmentation. For low Weber numbers, this coincides with bag rupture, and for higher We , this coincides with shedding of fragments from sheets or ligaments.

With respect to the video data, recorded images are processed with background subtraction, contrast stretching and super-resolution using MATLAB’s Very Deep Super-Resolution convolutional neural network.⁵⁷ Automated MATLAB scripts, using a fixed length as reference, provide values for the equivalent droplet diameter d , the cross-stream diameter d_c , the streamwise diameter d_x , and the position of the mass center x_{mc} . A subscript of “0” denotes respective initial conditions and $d_{c,max}$ marks the maximum cross-stream deformation which is taken at τ_{ini} . Figure 3 shows a sketch corresponding to the analysis. The flow is from left to right for this sketch and all following figures. For several FM droplets, an appendix affects the analysis, especially at the beginning of the breakup. To make the data comparable, data

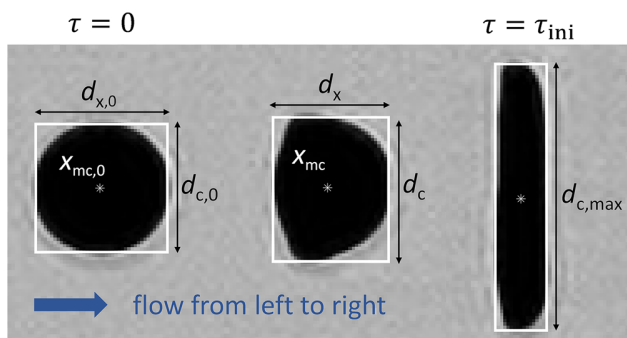


FIG. 3. The cross-stream diameter d_c , the streamwise diameter d_x , and the position of the mass center x_{mc} at the start of the experiment (left, with subscript “0”), during the deformation phase (middle), and at the end of initial deformation (right, at τ_{ini} , providing $d_{c,max}$). Flow direction is from left to right.

points are corrected by adjusting the dimension so as to omit the appendix.

To provide further analysis, we apply a simple, automated image processing and region property determination in MATLAB. The algorithm creates a binary map of the selected images and identifies fragments after the breakup. The results from one or several images are then summarized with respect to the size and quantity of the fragments. An example of a raw and processed image is shown in Fig. 4. The process is limited by the optical setup and the resolution. The smallest identifiable fragments are of the size of one pixel, which results in equivalent minimum fragment diameters of $\sim 50 \mu\text{m}$. The algorithm identifies individual particles accurately but is limited for larger connected structures or particle clusters. This method is used in this work for a direct comparison of conducted experiments and helps to determine differences as shown in Sec. III C 2.

III. EXPERIMENTS

As highlighted in the introduction, previous works have shown that Galinstan breakup shows differences compared to conventional liquids like water. These differences, e.g., an earlier rupture and the formation of aspherical fragments, are associated with the oxide layer forming on the droplet surface.^{19,36,37} The introduction also highlights that additional studies on the droplet breakup of metals are not readily available. Therefore, this work presents experiments using Field’s metal. In addition to providing necessary additional data, this can help confirm previous results and enhance their meaningfulness to a more general level. The hypothesis is that if both metals show a similar breakup, then also other oxide-forming metals are likely to show similar trends. This would be especially true for aluminum, as it is part of the same group in the periodic table of elements as gallium and indium, which are the main components of Galinstan and FM, respectively.⁵⁸ This suggests that aluminum reacts similarly and forms similar compounds to the metals studied in this work.⁵⁸

To evaluate the hypothesis, the Sec. III B provides representative image sequences for direct comparison of FM and Galinstan along with quantitative data of droplet deformation. The focus lies on determining similarities that would support a generalization of the behavior, but also on detecting differences. Studying differences helps to determine other potential influencing factors, to better understand the effect of oxidation on the breakup, and to determine potential limitations of the hypothesis.

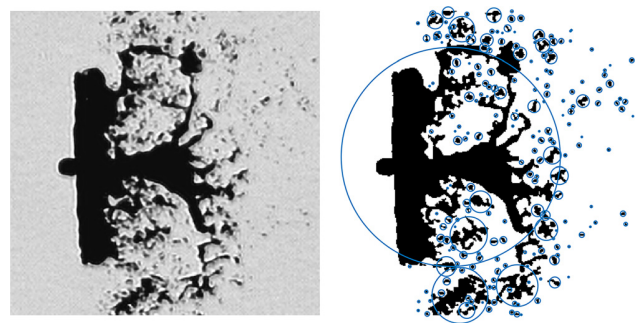


FIG. 4. Raw image (left) and binarized image (right) of a droplet breakup. The circles highlight the center and size of the detected fragments.

For Galinstan droplet breakup, we use data from our previous work,³⁷ complemented by some newly conducted experiments. For Field's metal, all experiments were conducted using the new setup.

A. Temperature effect

Before focusing on oxidation effects, it has to be evaluated whether the breakup of FM droplets is affected by thermal effects like changing fluid properties or partial solidification. In contrast to Galinstan and other liquids like water as shown in Table I, FM has a melting point that is higher than the surrounding gas temperature at the beginning of and during the experiments. However, calculating the heat transfer from dimensionless numbers shows that the temperature change of the FM melt is almost negligible.⁵⁹ The temperature drops only around ~ 1.5 K during the fall of around 10 cm into the test section before the experiment. During the experiment, a spherical droplet cools even less, due to the short experimental time on the order of milliseconds and the lower temperature difference to the surrounding gas due to the shock-induced heating. Consequently, a strong temperature effect can only be expected when droplets are close to the solidification point at the beginning of the experiment. For most experiments, the furnace temperature was set to 90°C because it provided a controllable and repeatable droplet production. However, we put great effort into producing droplets closer to the solidification

point by lowering the furnace temperature. We managed droplet production at a furnace temperature as low as 75°C , but lowering the temperature further resulted in freezing at the thin needle tip. Several experiments in the range of $75\text{--}80^\circ\text{C}$ were conducted but showed no differences to the other experiments, suggesting that temperature effects are not significant for this study. However, this topic should be considered for future studies. Partial solidification has a strong effect on the breakup morphology, and the influence on final particle shapes in gas atomizers is of high practical interest.

B. Image sequences

1. Bag breakup

The following two image series compare the bag breakup of a Galinstan droplet at $We = 14.6$ (Fig. 5, Multimedia view) and a Field's metal droplet at $We = 13.9$ (Fig. 6, Multimedia view). The cases show aspects of stamen formation and can thus be considered transition cases to the bag-and-stamen mode.

The experiment in Fig. 6 also shows that the effect of a small appendix on the droplet deformation and breakup is minimal. Within one quarter of the initial deformation time, the appendix merges into the droplet, and by half of τ_{ini} no asymmetry in the shape of the deforming drop can be observed. Thus, an accurate analysis of the deformation can be achieved.

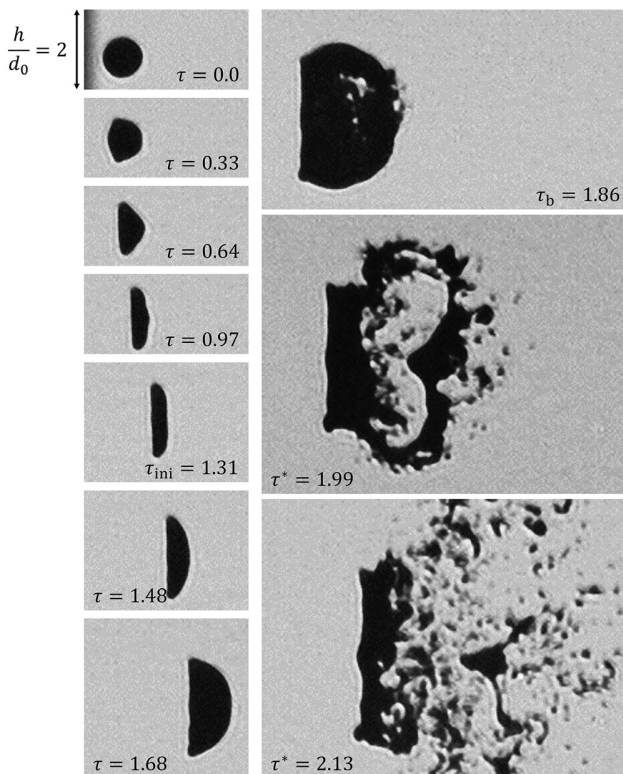


FIG. 5. Galinstan, shadowgraph, $d_0 = 1.28$, and $We = 14.6$. Multimedia view: <https://doi.org/10.1063/5.0064178.1>

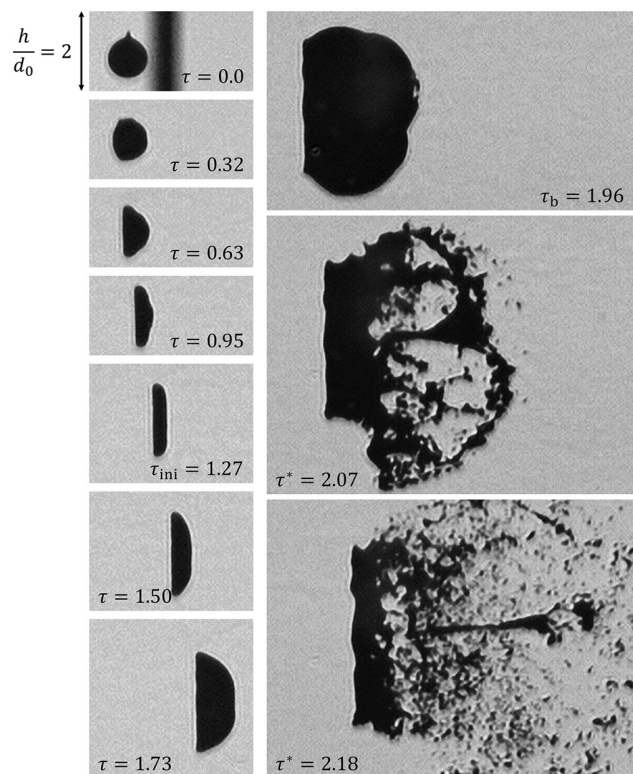


FIG. 6. FM, shadowgraph, $d_0 = 1.66$, and $We = 13.9$. Multimedia view: <https://doi.org/10.1063/5.0064178.2>

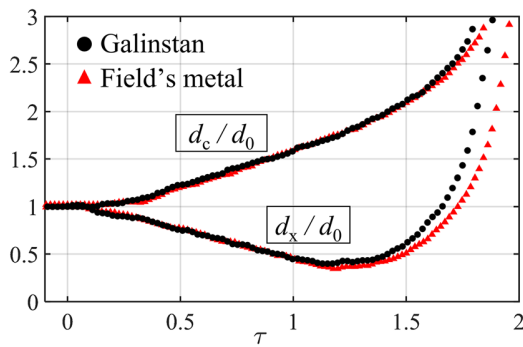


FIG. 7. Change of cross-stream diameter d_c and streamwise diameter d_x normalized by the initial diameter d_0 over normalized time τ . The data points correspond to the experiments shown in Figs. 5 and 6 with $We_{Gal} = 14.6$ and $We_{FM} = 13.9$, respectively.

Comparing the two image sequences, a strong similarity in shape and time evolution can be concluded, especially regarding the deformation before rupture as shown in the left columns. Figure 7 confirms this quantitatively by showing that the droplet deformation over time

τ with respect to the cross-stream diameter d_c , and streamwise diameter d_x , follows nearly identical lines for the two experiments. For Galinstan, both diameters increase faster toward later times, but this is likely only an effect of the slightly higher Weber number.

Regarding the right columns of the image series, we can observe that the onset of breakup at τ_b is slightly later for the FM case, and the corresponding hemisphere appears a bit larger. Fragments visible in the last frames appear smaller and more uniform for the FM case. This difference along with the later breakup and the extended bag inflation at τ_b in the FM case are minor, but noticeable. Their significance and cause are discussed in more detail in Sec. III C.

2. Bag-and-stamen

Two image sequences in this section show the breakup behavior in the bag-and-stamen mode. The Galinstan experiment is at $We = 21.7$ (Fig. 8, Multimedia view), and the FM experiment at $We = 22.0$ (Fig. 9, Multimedia view).

Again, the deformation of the two metal droplets is very similar. The time evolutions and shapes match almost exactly, and all main steps of the breakup, like the stamen appearance and the ring

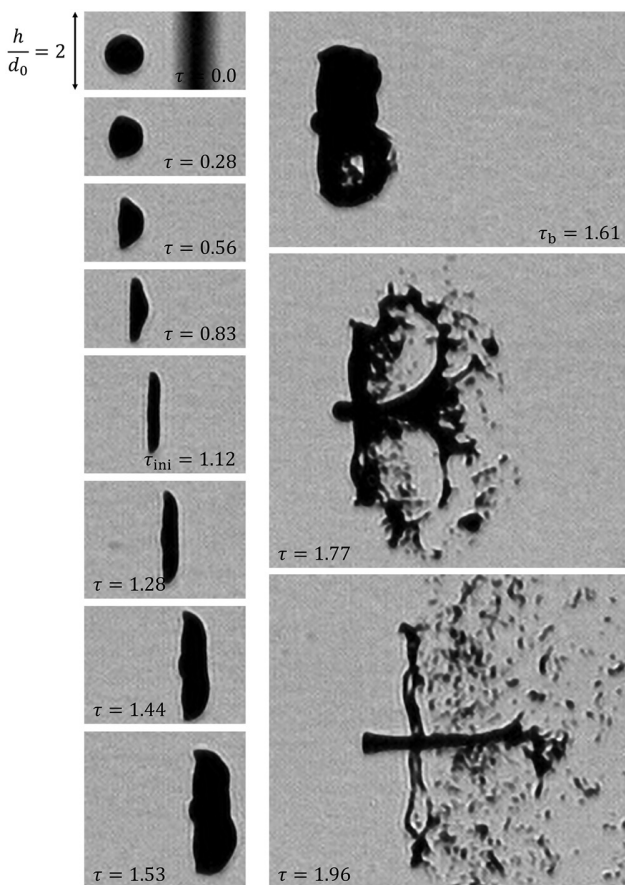


FIG. 8. Galinstan, shadowgraph, $d_0 = 1.32$, and $We = 21.7$. Multimedia view: <https://doi.org/10.1063/5.0064178.3>

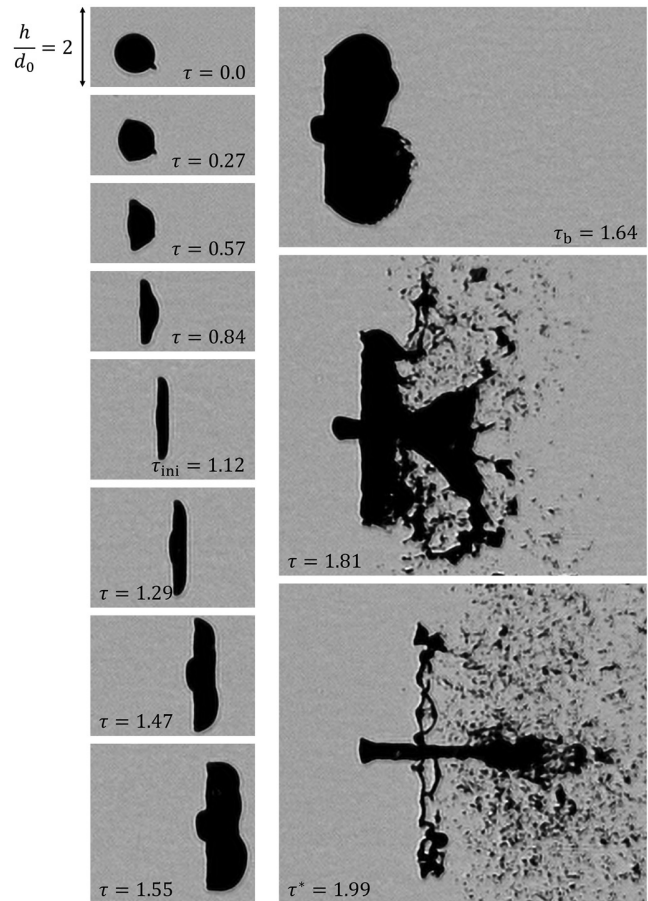


FIG. 9. FM, shadowgraph, $d_0 = 2.06$, and $We = 22.0$. Multimedia view: <https://doi.org/10.1063/5.0064178.4>

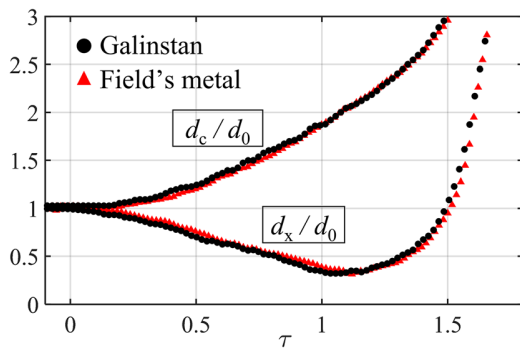


FIG. 10. Change of d_c and d_x normalized by d_0 . $We_{Gal} = 21.7$ and $We_{FM} = 22.0$ corresponding to Figs. 8 and 9, respectively.

formation, are observed equally for both metals. A quantitative analysis of the droplet deformation is presented in Fig. 10 and confirms the very similar behavior.

Nevertheless, small differences can be seen from the direct comparison. The time instant of breakup is almost equal, but a bit later for the FM experiment. The inflated bags for the FM experiment appear a bit larger and the stamen slightly thicker. As in the previous case, the fragments after bag rupture seem smaller and more uniform for the FM case.

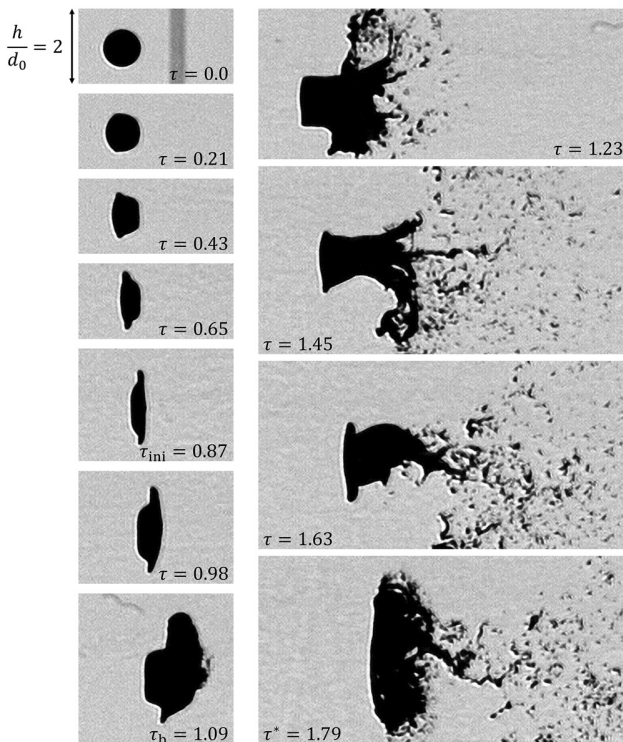


FIG. 11. Galinstan drop, shadowgraph, $d_0 = 1.99$, and $We = 42.9$. Multimedia view: <https://doi.org/10.1063/5.0064178.5>

3. Multimode

A direct comparison of the breakup of the two metals in the multimode regime is presented in Fig. 11 (Multimedia view) for Galinstan at $We = 42.9$ and in Fig. 12 (Multimedia view) for FM at $We = 40.4$.

Like for the lower Weber number cases, the qualitative similarity of the breakup is high. The initial deformation concludes at exactly $\tau_{ini} = 0.87$ in both cases and follows the expected patterns. After that, the Galinstan droplet does not breakup fully symmetrical, but this is a common observation in the chaotic nature of the multimode regime.²⁴ In addition, the time evolution of the two cases diverges slightly after the first bag rupture, but the observed breakup patterns match well throughout. Quantifying the deformation, Fig. 13 shows almost equal lines for the two experiments both for the cross-stream and the streamwise droplet deformation.

The small differences noted in Secs. III B 1 and III B 2 are more difficult to observe here. While the same trends persist, the bag inflation and onset of breakup now appear more similar than for lower We , as do the fragment shapes and sizes after rupture.

C. Comparing Field's metal and Galinstan

The exemplary experiments have shown that the general breakup behavior is very similar for the two metals with respect to the breakup morphology, the transition between the modes, and the timing of the deformation. In addition, main characteristics that distinguish

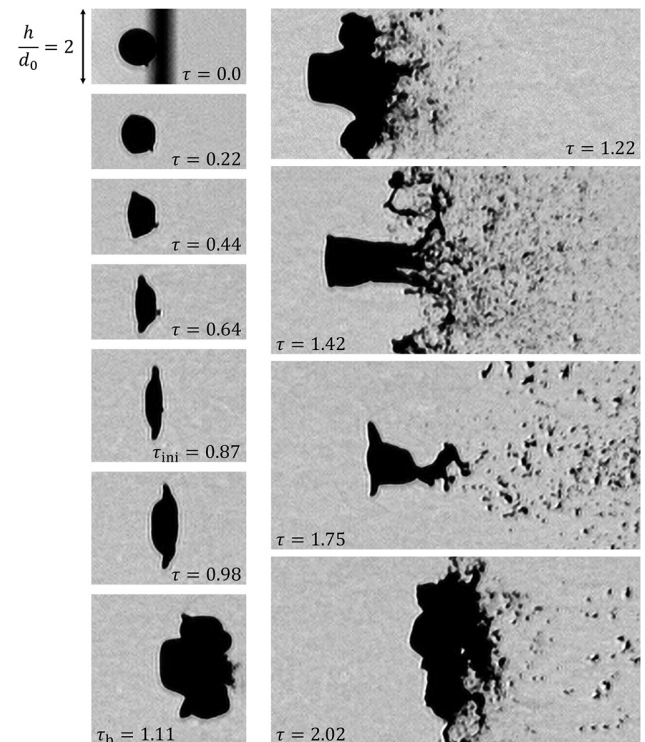


FIG. 12. FM drop, shadowgraph, $d_0 = 1.89$, and $We = 40.4$. Multimedia view: <https://doi.org/10.1063/5.0064178.6>

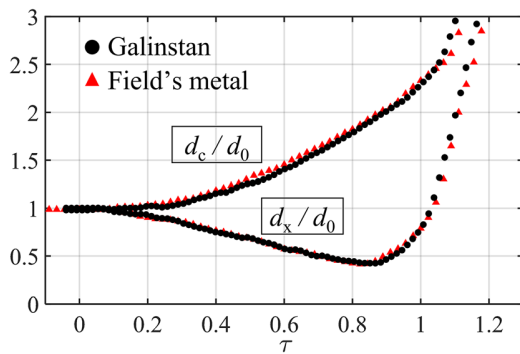


FIG. 13. Change of d_c and d_x normalized by d_0 . $We_{Gal} = 42.9$ and $We_{FM} = 40.4$ corresponding to Figs. 11 and 12, respectively.

oxidizing metals from conventional liquids like the appearance of sharp-edged rupture lines and earlier breakup³⁷ are confirmed also for FM. This suggests that a generalization of the observations is feasible. This generalization is presented in the form of empirical fits in Sec. IV and is representative also for other oxidizing liquid metals.

However, looking even at small differences can be very instructive. Differences can help determine to what extent different oxidation parameters affect the breakup behavior and they can point out potential limitations of the generalization approach. Representative experiments in Sec. III B have highlighted that the breakup of FM and Galinstan droplets differs slightly in two aspects:

- FM bags inflate a bit more before rupture and their time of onset of breakup is a bit later.
- A larger number of smaller and more uniform fragments result from the breakup of FM droplets.

Both aspects are addressed in the following for additional insight. An explanation for the differences is proposed.

1. Onset of breakup and extent of deformation

It has been shown for some examples in Sec. III B that the onset of breakup is postponed for FM. This behavior is also confirmed in Sec. IV in Fig. 18. The difference is small and limited to experiments of $We < 30$ but appears consistently.

Figure 14 provides a quantitative analysis of the drop extension at τ_b for experiments up to $We = 60$. It shows both the streamwise (d_x) and cross-stream (d_c) extension. Looking at the difference between the two metals, we can see that the deformation before rupture is higher for FM in both dimensions. The gap is clear for low Weber numbers but diminishes around $We \sim 45$ for d_x and $We \sim 35$ for d_c . For higher Weber numbers, the data points of the two metals are scarcer, but the values start to overlap and converge.

2. Fragment sizes

We apply the image processing as described in Sec. II C to quantify differences regarding the number of fragments and their sizes after rupture. For similar Weber numbers, images for both metals are selected from a timespan that starts after the higher value of τ_b and

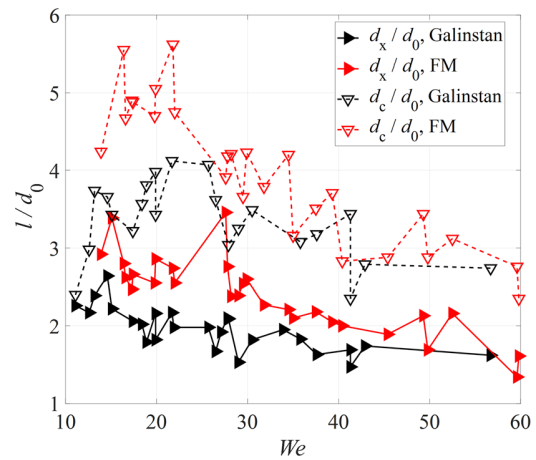


FIG. 14. Extension of the inflated drops in streamwise (d_x), and cross-stream (d_c) direction at the onset of breakup (τ_b) for different We . All values are normalized by d_0 .

lasts for $\Delta\tau = 0.3$. For example, for $We = 19.9$, the onset of breakup is at $\tau_b = 1.66$ for Galinstan and $\tau_b = 1.7$ for FM, and we choose a timespan ranging from $\tau = 1.7-2.0$ for both metals for the analysis. For the selected images, the script sums up the number and sizes of the detected fragments and filters the result for fragments smaller than a normalized equivalent diameter $d_{eqv}/d_0 = 0.2$. As an example, Fig. 15 displays the cumulative mass fraction of the detected fragments for $We = 19.9$, confirming that FM droplet breakup leads to smaller fragments compared to Galinstan droplet breakup.

Complementing the figure, Table II displays the Sauter mean diameter (SMD) and number of detected fragments for the case of Fig. 15 and several other cases at different We . It shows that the SMD of FM fragments is smaller, and that the number of fragments is significantly higher. Both trends are stronger for lower We , and differences almost diminish for the case of $We \sim 40$, confirming previous observations.

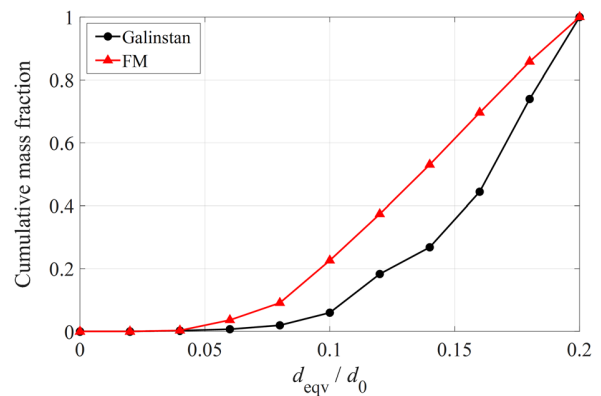


FIG. 15. Cumulative mass fraction for fragments at $We = 19.9$. A time range of $\tau = 1.7-2.0$ was chosen, and 16 images per experiment within that time range were used for the analysis.

TABLE II. Sauter mean diameter (SMD) and number of fragments n_{frag} detected for Galinstan and FM droplets.

We	Galinstan		Field's metal	
	SMD/ d_0	n_{frag}	SMD/ d_0	n_{frag}
19.9	0.146	554	0.120	3199
21.7/22.0	0.144	617	0.114	2458
26.5/28.2	0.114	1699	0.111	2211
42.9/40.4	0.116	2655	0.117	3095

3. Oxidation rate

An aspect that can explain the observed differences is the oxidation rate of the two metals. It is commonly stated that oxidation and re-formation of the oxide layer of Galinstan occur rapidly,^{19,54,60} while this is not as clear for FM. As highlighted in Sec. II B, we expect rapid oxidation also for FM, but not to the extent of Galinstan.

A reduced oxidation rate would lead to less oxide formation during the deformation of the droplet. Consequently, more pure liquid would remain. This facilitates deformation and leads to extended bag formation and later breakup times, as observed. In addition, the resulting fragments are a mix of the remnants of the oxide layer and exposed liquid. Liquid parts of the droplet can break into finer and more spherical fragments, which explains the observed differences in the number of fragments in Table II. A difference in the oxidation rate also explains why we notice a dependency on the Weber number. For low We , the breakup times are longest, while for increasing We , they are greatly reduced. In the current range, breakup times are typically halved (in milliseconds) when doubling We . Consequently, there is less time at higher We for the continuous oxidation to have an effect, and thus, differences are harder to notice. In addition, a higher We means that significantly higher forces act on the droplet rendering material differences, such as the level of oxidation, less important. Because of both aspects, differences in the oxidation rate have a stronger effect and manifest more clearly for low Weber numbers.

Overall, differences are observed mainly within the details of the breakup evolution, while general aspects of the breakup remain very similar for the two metals. However, the effect on the fragment size distribution appears significant and can be relevant in many applications. To understand the effect of the oxidation rate better, this topic should be considered for future investigations. For example, oxidation could be controlled by using inert gases.

IV. DATA FITTING

In many practical atomization applications, the secondary atomization comprises only one part of the whole process. For example, in metal powder production or spray applications, it is also important to consider other aspects like the primary breakup,⁶¹ the design of the melt tip,⁶² gas pressure,⁶³ gas selection, and vacuum conditions,⁶⁴ as well as the flow structure within the atomizer.⁹ Therefore, most holistic studies of gas atomization, especially numerical investigations, do not resolve the individual droplet breakup in detail but instead model it.^{7,9,65–67} Otherwise, the complexity of the analysis or the computational costs would exceed reasonable levels.

Regarding secondary atomization, the data for validation of breakup models are typically taken from experiments with conventional liquids. However, it has been shown that metal breakup evolves differently.^{19,36,37} In addition, Sec. III B has supported our hypothesis of a similar breakup behavior of oxide-forming metals. FM and Galinstan do show the same behavior in all main aspects of breakup, which is further confirmed by the full data set presented in this section. Thus, we use the combined data set to summarize the findings and to provide empirical fits that can be used in numerical studies or serve as data for model validation. The fits represent the behavior and trends observed for the breakup of oxide-forming liquid metals.

A. Characteristic breakup parameters

In this section, we summarize all the conducted experiments with respect to the characteristic time instants τ_{ini} and τ_b , as well as the normalized cross-stream deformation $d_{c,\text{max}}/d_0$. This confirms findings observed in Sec. III and provides fits for the use in future works.

Figure 16 summarizes the initial deformation time for all conducted experiments. Data points show that Galinstan and FM follow the same trend and complement each other, confirming their strong similarity. As shown previously,³⁷ this also means that the initial deformation time of both metals is similar to that of more conventional liquids. All data points were used to find a fit that is valid for the experimental range of $We \sim 10$ –100. It was added to the figure and can be written as

$$\tau_{\text{ini}} = 1.25 e^{-0.022 We} + 0.35. \tag{7}$$

The normalized maximum cross-stream deformation $d_{c,\text{max}}/d_0$ corresponding to τ_{ini} is shown in Fig. 17. It confirms the similarity of the two metals also with respect to the deformation. The value of $d_{c,\text{max}}/d_0$ rises quickly for low Weber numbers and then peaks at a value of ~ 2.1 at $We \sim 30$ before slowly decreasing again. An empirical fit that is valid for the experimental range can be written as

$$d_{c,\text{max}}/d_0 = 1 + \frac{We}{(We/8)^2 + 14}. \tag{8}$$

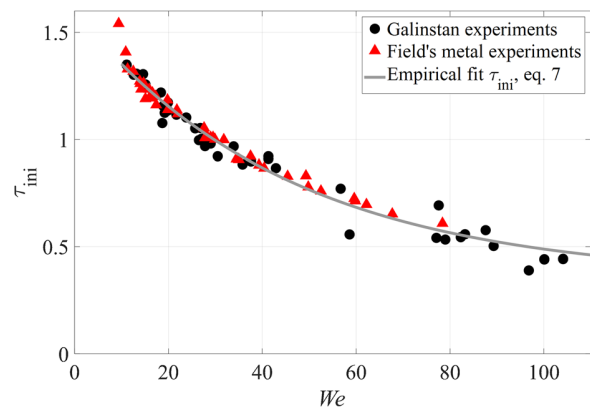


FIG. 16. Initial deformation time τ_{ini} for droplet breakup experiments with Galinstan and Field's metal. A data fit, as in Eq. (7), is plotted as a solid gray line.

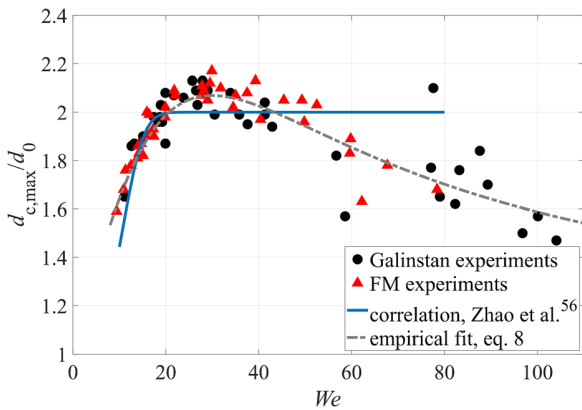


FIG. 17. Normalized cross-stream diameter $d_{c,max}/d_0$ at τ_{ini} for droplet breakup experiments with Galinstan and Field’s metal, along with the correlation of Zhao *et al.*⁵⁶ and the present empirical fit.

The data points and the empirical fit compare favorably, especially at low We , with the correlation of Zhao *et al.*⁵⁶ which is based on experiments with water and ethanol. However, we observe some differences for higher We , as the present fit now includes a decrease after the initial peak instead of a constant value.

Figure 18 shows the time of onset of breakup τ_b for the conducted experiments. Note that breakup times for some experiments at low We fall into non-constant flow conditions. Although they still show a very similar behavior, those data points are excluded from the figure. In general, the data points of the two metals match well, but for low Weber numbers, τ_b is consistently a bit higher for FM. A zoomed-in window in the figure highlights this trend that has already been observed in Sec. III B and has been discussed in Sec. III C. While it is noticeable, the overall difference remains small. Therefore, all data points are used again to obtain a fit of τ_b that is valid for the range of $We \sim 10$ –100 and is written as

$$\tau_b = 2.2 e^{-0.027 We} + 0.4. \tag{9}$$

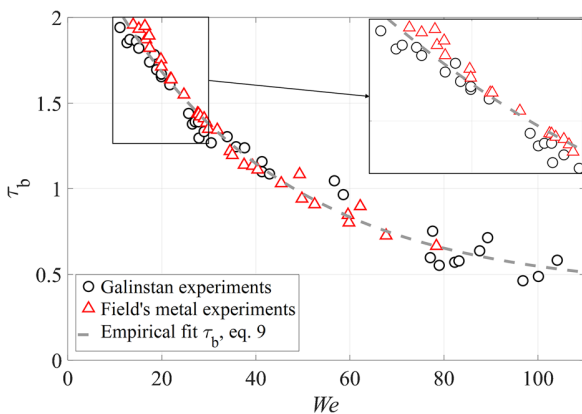


FIG. 18. Time of onset of breakup τ_b for droplet breakup experiments with Galinstan and Field’s metal. A data fit, as in Eq. (9), is plotted as a broken gray line. The box inlet provides a zoom-in to data points in the range of $We = 10$ –30.

While differences between the two metals are small, the difference to conventional liquids regarding τ_b is high. The significantly earlier rupture observed for Galinstan droplets³⁷ can be extended to Field’s metal droplets.

It should be emphasized that the present empirical fits are not validated for $We > 100$. For the cross-stream deformation, the value tends to $d_{c,max}/d_0 = 1$ for We higher than the shown range, which is not an ideal representation. In contrast, the fits for the timings provide a reasonable estimate when compared to conventional liquids⁴⁰ due to the remaining constant terms.

B. Cross-stream deformation

In addition to the time evolution of metal droplet breakup, also the deformation of the droplet is important. A summary for $d_{c,max}$ is provided in Sec. IV A, but of great interest is also the time dependent deformation, especially in the cross-stream direction. It is, for example, essential to calculate the drag force on the deforming droplet in the flow field. Large interest in this topic is reflected in the literature, notably also in recent works. For example, Stefanitsis *et al.*¹⁵ summarized empirical correlations for droplet deformation as well as theoretical and semi-analytical droplet breakup models. In addition, they propose improvements for two long existing models, namely, an improved Taylor analogy breakup (TAB) model and a modified Navier–Stokes (M-NS) model. For both models, several parameters are found by fitting to simulation results and experimental works that are based on conventional liquids. A very detailed modeling approach of the radial expansion rate is also provided by Jackiw and Ashgriz¹² following the internal flow concept of Villermaux and Bosa.⁶⁸ They also estimate some parameters based on what they observe in their experiments with water.

Here, we provide our own fit based on the experiments. In addition, we evaluate to which extent the present fit and other models from the literature can capture the cross-stream deformation of liquid metal droplets.

1. Formulation of the empirical fit

An overview for some of the experiments discussed in this work is presented in Fig. 19. It shows that the use of the dimensionless time does not collapse the experiments into a single line, but that instead there is a strong Weber number dependency. However, the lines appear self-similar to some extent, so incorporating the Weber number as part of the time axis appears promising. Hence, this was done for Fig. 20, which shows a much more uniform behavior for the sum of the experiments. While this procedure was based on the observations from our data, considering the Weber number in deformation models is common. Hsiang and Faeth³⁵ apply it for their empirical correlation as do many mathematical models such as the TAB or M-NS model.¹⁵

Stretching the time axis by $We^{0.45}$ was found to best collapse the available data. We use these data to provide an empirical fit that represents the cross-stream deformation for our experiments. We apply curve fitting in MATLAB on the base of a quadratic polynomial. The result can be simplified as

$$d_c/d_0(\tau) = 0.05 We^{0.9} \tau^2 + 1. \tag{10}$$

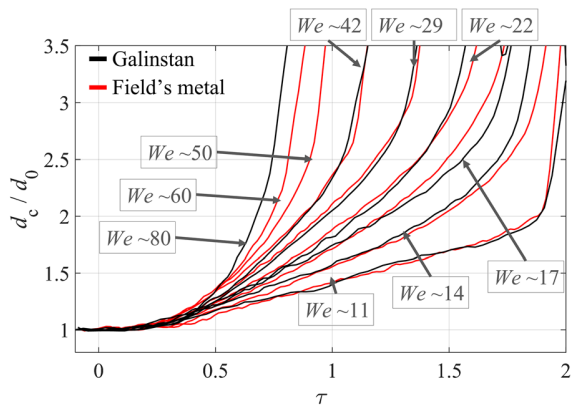


FIG. 19. Cross-stream deformation for selected experiments of Galinstan and FM. Data points are replaced by line-plots for simplicity.

The deformation in the streamwise direction can be normalized in similar fashion and is provided for completeness. Figure 21 shows that this works to some extent. The shift from flattening to growing now appears at similar values along the x -axis for the displayed experiments, but the minimum value of d_x and the curvature of the lines is different for experiments with changing We . Especially some high- We experiments stand out, as they reach a minimum of $d_x/d_0 > 0.5$ after which a sharp rise appears. A fourth-order polynomial fit capturing the main aspects of the deformation is

$$d_x/d_0(\tau) = 0.002 We^{1.8} \tau^4 - 0.0633 We^{0.9} \tau^2 - 0.015 We^{0.45} \tau + 1. \tag{11}$$

2. Validation and comparison

In the following, the fit for the cross-stream deformation is evaluated for different We in comparison to the experimental data and two deformation models from the literature. We selected the improved TAB model of Stefanitsis *et al.*¹⁵ and the model of Jackiw and Ashgriz.¹² From the experimental side, we choose a narrow range of

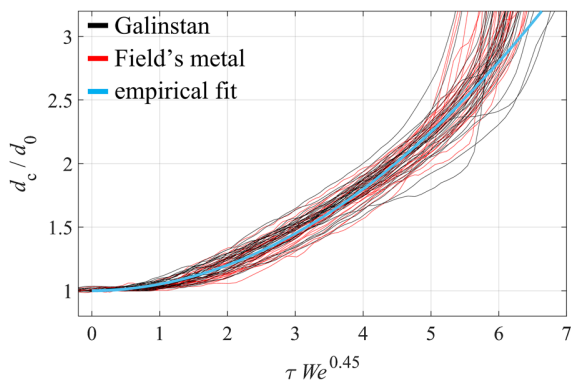


FIG. 20. Normalized cross-stream deformation of experiments in a range of $We = 10-80$. FM in red, Galinstan in black, with the quadratic fit of Eq. (10) in blue.

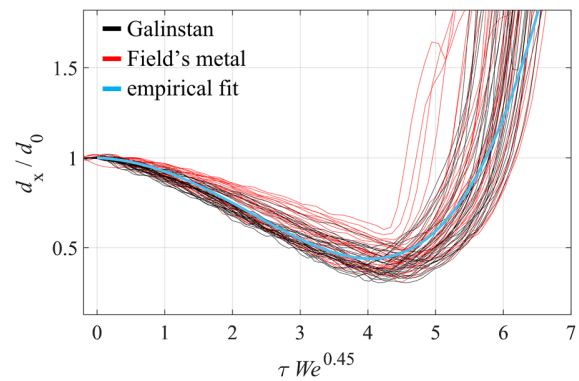


FIG. 21. Normalized streamwise deformation of FM and Galinstan droplets in a range of $We = 10-80$ with corresponding fit of Eq. (11).

We and take all experiments that fall into that range from both metals. The gathered data are averaged to provide time-dependent means and standard deviations. The different models are calculated for one Weber number in the chosen range and evaluated in comparison. For the improved TAB model, we take $Oh = 0.0044$ representing an average of the experiments.

Figure 22 presents four plots at four different Weber numbers throughout the bag ($We = 14.5$), bag-and-stamen ($We = 28.0$), and multimode regime ($We = 41.0-60.0$). The standard deviation of the experimental data is shown as a narrow band encompassing the mean value. The uncertainty is low in general and only increases for later time instants close to τ_b . This is especially visible for Figs. 22(c) and 22(d), where τ_b falls into the displayed time. The experimental data show that the deformation of metal droplet transitions from a more linear behavior at low We to a more exponential behavior at high We . For $We = 14.5$, the cross-stream deformation develops almost linearly up to $\tau = 1.5$ before it accelerates. For the other plots at $We = 28.0-60.0$, the growth is more exponential from the beginning.

The model of Jackiw and Ashgriz¹² captures the linearity of the deformation for low We very accurately, despite their work focusing on water droplets. Their model is primarily developed for the bag and bag-and-stamen regime, and the authors note greater deviation in the multimode and sheet thinning regime. This is reflected in the plots for the higher Weber numbers, where the model matches well at the beginning, but starts to underestimate the deformation already before τ_{ini} . In addition, the more exponential deformation is not captured and so a large gap develops toward τ_b .

The improved TAB model does not perform well in the bag regime [Fig. 22(a)], where it greatly underestimates the deformation of the metal droplets. In contrast, it matches the experimental data very well in the other regimes. The only minor drawback is that the model starts to underestimate the deformation at later times—slightly around τ_{ini} and more clearly toward τ_b .

The present empirical fit of Eq. (10) matches well overall but also shows some limitations. In the linear regime at $We = 14.5$, it provides an accurate representation initially and captures the accelerated deformation at later stages to some extent, but it does not capture the linearity of the deformation. The fit is very accurate for the bag-and-stamen regime represented by the case of $We = 28.0$ in Fig. 22(b) where the

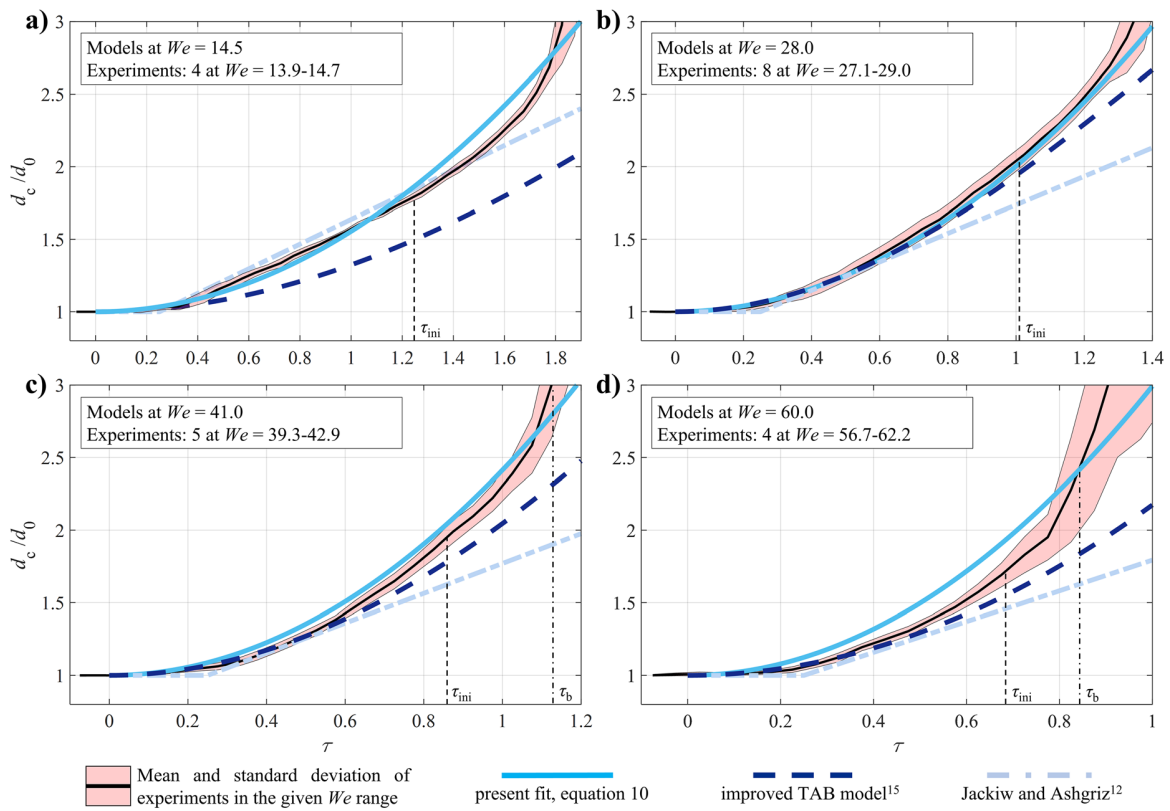


FIG. 22. Normalized cross-stream deformation of the droplets. The present fit [Eq. (10)] is presented in comparison with experiments, the improved TAB model of Stefanitsis *et al.*,¹⁵ and the model of Jackiw and Ashgriz.¹² The different plots represent deformation in the bag regime at $We = 14.5$ (a), the bag-and-stamen regime at $We = 28.0$ (b), and multimode regime at $We = 41.0$ (c), and $We = 60.0$ (d).

experimental data are matched almost exactly. For higher Weber numbers, the cross-stream deformation value around τ_b is still captured by the fit, but the initial deformation is overestimated—slightly for $We = 40.0$, and more clearly for $We = 60.0$. This discrepancy is likely due to the change of the underlying breakup mechanism with increasing We . For low We , the breakup is associated with the Rayleigh–Taylor instability,⁶⁹ before the mechanism transitions to stripping⁷⁰ starting in the multimode regime, especially when getting closer to the shear stripping mode at $We \sim 80$. Our empirical fit better captures the deformation at lower We , whereas the transition to the stripping mechanism leads to a different cross-stream deformation that is only partially captured.

3. Evaluation

Sections IV B 1 and IV B 2 provide several key insights. Finding one simple empirical fit for the cross-stream deformation in the range of investigated Weber numbers is difficult. While incorporating the Weber number as a factor is essential to match the experiments, it also has some limitations. For different Weber numbers, the cross-stream deformation shows different behaviors, more linear at low We , and more exponential at high We . The provided empirical fit covers the

investigated range decently, but a more complex fit would be necessary to adapt to the change of the curvature.

Another observation is that models developed for conventional liquids can also provide a good estimate for the present data, albeit not to the same extent as the present fit. In general, the accuracy compared to the experimental data is high initially, typically until around τ_{ini} . This can be explained by the strong similarity of oxide-forming liquid metals to other liquids during the initial deformation that has been observed previously.³⁷ In contrast, the time period after τ_{ini} corresponds to a very different behavior for oxide-forming liquid metals like a different rupture mechanism and earlier breakup.³⁷ The differences lead to a faster rise in d_c/d_0 during that time period, and consequently, the deformation models from the literature tend to underestimate the deformation.

V. SUMMARY AND CONCLUSION

The goal of this work was to extend previous efforts regarding metal droplet breakup and to provide much-needed data. Therefore, we studied the breakup of Field’s metal droplets experimentally in a shock-tube. To conduct the analysis accurately, we measured the effective surface tension value of FM in air using the pendant drop method. The breakup of FM droplets is then compared to Galinstan droplet

breakup using image sequences, deformation data, and overviews of characteristic breakup parameters; key observations are:

- Both metals show a high level of similarity with respect to the breakup morphology, transition We between modes, gradual transition between the modes, and timing and extent of initial droplet deformation.
- Field's metal, like Galinstan, shows distinct breakup features like sharp-edged rupture lines and earlier breakup. This distinguishes the two metals from more conventional liquids such as water.
- FM bags inflate slightly more and rupture a bit later. In addition, FM droplet breakup leads to a larger number of smaller and more uniform fragments. Both differences are observed primarily at low Weber numbers and are expected to be an effect of a higher oxidation rate of Galinstan compared to FM.

Despite small differences regarding details of the breakup, there is a strong overall similarity of the two metals, and their breakup behavior is distinct from that of conventional, water-like liquids. Based on these observations, we propose that the findings can be generalized to also represent other oxide-forming metals, like the chemically very similar aluminum.⁵⁸ We use the collective data of Galinstan and FM droplet breakup to provide empirical fits for the initial deformation time τ_{ini} , the corresponding normalized deformation $d_{c,max}/d_0$, and the time of the onset of breakup τ_b . In addition, an empirical fit for the time-dependent cross-stream deformation is provided, validated for different Weber numbers, and compared to models that are based on droplet breakup of conventional liquids. The main conclusions are that models developed for conventional liquids can describe the behavior of metal droplets initially, both with regard to timing and deformation. However, at later stages of the breakup, the deformation is consistently underestimated, and the normalized breakup time is overestimated. In contrast, the present empirical fits provide an accurate representation. The fits can be used directly, and the collected data can help validate or adapt other breakup models for the different behavior of oxide-forming metals. With that, the impact of this work goes beyond the direct observation of FM droplet breakup and extends to a more general level.

Nevertheless, more experimental research on metal droplet breakup is required. For example, more work on the effect of changing temperature and partial solidification is essential. The involved physical processes are complex, but their influence on the breakup morphology and fragment distribution is relevant in many practical applications.

ACKNOWLEDGMENTS

The authors acknowledge funding by the European Research Council (ERC) under the European Union's Horizon 2020 research and innovation program (Grant No. 667483).

AUTHOR DECLARATIONS

Conflict of Interest

The authors have no conflicts to disclose.

DATA AVAILABILITY

The data that support the findings of this study are available from the corresponding author upon reasonable request.

REFERENCES

- ¹H. Henein, V. Uhlenwinkel, and U. Fritsching, in *Metal Sprays and Spray Deposition*, edited by H. Henein, V. Uhlenwinkel, and U. Fritsching (Springer International Publishing, Cham, Switzerland, 2017).
- ²P. S. Grant, "Spray forming," *Prog. Mater. Sci.* **39**(4–5), 497–545 (1995).
- ³L. Galfetti, L. T. DeLuca, F. Severini, G. Colombo, L. Meda, and G. Marra, "Pre and post-burning analysis of nano-aluminized solid rocket propellants," *Aerosp. Sci. Technol.* **11**(1), 26–32 (2007).
- ⁴B. Van der Schueren and J.-P. Kruth, "Powder deposition in selective metal powder sintering," *Rapid Prototyping J.* **1**(3), 23–31 (1995).
- ⁵K. Bauckhage, "Das Zerstäuben metallischer Schmelzen," *Chem. Ing. Tech.* **64**(4), 322–332 (1992).
- ⁶I. E. Anderson, E. M. H. White, and R. Dehoff, "Feedstock powder processing research needs for additive manufacturing development," *Curr. Opin. Solid State Mater. Sci.* **22**(1), 8–15 (2018).
- ⁷N. Zeoli and S. Gu, "Numerical modelling of droplet break-up for gas atomisation," *Comput. Mater. Sci.* **38**(2), 282–292 (2006).
- ⁸A. Ünal, "Liquid break-up in gas atomization of fine aluminum powders," *Metall. Trans. B* **20**(1), 61–69 (1989).
- ⁹D. A. Firmansyah, R. Kaiser, R. Zahaf, Z. Coker, T. Y. Choi, and D. Lee, "Numerical simulations of supersonic gas atomization of liquid metal droplets," *Jpn. J. Appl. Phys. Part 1* **53**(3), 05HA09 (2014).
- ¹⁰D. R. Guildenbecher, C. López-Rivera, and P. E. Sojka, "Secondary atomization," *Exp. Fluids* **46**(3), 371–402 (2009).
- ¹¹J. W. J. Kaiser, J. M. Winter, S. Adami, and N. A. Adams, "Investigation of interface deformation dynamics during high-Weber number cylindrical droplet breakup," *Int. J. Multiphase Flow* **132**, 103409 (2020).
- ¹²I. M. Jackiw and N. Ashgriz, "On aerodynamic droplet breakup," *J. Fluid Mech.* **913**(A33), 1–46 (2021).
- ¹³B. Dorschner, L. Biasiori-Poulanges, K. Schmidmayer, H. El-Rabii, and T. Colonius, "On the formation and recurrent shedding of ligaments in droplet aerobreakup," *J. Fluid Mech.* **904**, A20 (2020).
- ¹⁴M. Jain, R. S. Prakash, G. Tomar, and R. V. Ravikrishna, "Secondary breakup of a drop at moderate Weber numbers," *Proc. R. Soc. A Math. Phys. Eng. Sci.* **471**(2177), 20140930 (2015).
- ¹⁵D. Stefanitsis, G. Strotos, N. Nikolopoulos, E. Kakaras, and M. Gavaises, "Improved droplet breakup models for spray applications," *Int. J. Heat Fluid Flow* **76**, 274–286 (2019).
- ¹⁶V. Kulkarni and P. E. Sojka, "Bag breakup of low viscosity drops in the presence of a continuous air jet," *Phys. Fluids* **26**(7), 072103 (2014).
- ¹⁷M. Leitner, T. Leitner, A. Schmon, K. Aziz, and G. Pottlacher, "Thermophysical properties of liquid aluminum," *Metall. Mater. Trans. A Phys. Metall. Mater. Sci.* **48**(6), 1–10 (2017).
- ¹⁸M. J. Assael, K. Kakosimos, R. M. Banish *et al.*, "Reference data for the density and viscosity of liquid aluminum and liquid iron," *J. Phys. Chem. Ref. Data* **35**(1), 285–300 (2006).
- ¹⁹Y. Chen, J. L. Wagner, P. A. Farias, E. P. DeMauro, and D. R. Guildenbecher, "Galinstan liquid metal breakup and droplet formation in a shock-induced cross-flow," *Int. J. Multiphase Flow* **106**(505), 147–163 (2018).
- ²⁰P. Yim, "The role of surface oxidation in the break-up of laminar liquid metal jets," Doctoral dissertation (Massachusetts Institute of Technology, 1996).
- ²¹J. O. Hinze, "Fundamentals of the hydrodynamic mechanism of splitting in dispersion processes," *AIChE J.* **1**(3), 289–295 (1955).
- ²²M. Pilch and C. A. Erdman, "Use of breakup time data and velocity history data to predict the maximum size of stable fragments for acceleration-induced breakup of a liquid drop," *Int. J. Multiphase Flow* **13**(6), 741–757 (1987).
- ²³Z. Dai and G. M. Faeth, "Temporal properties of secondary drop breakup in the multimode breakup regime," *Int. J. Multiphase Flow* **27**(2), 217–236 (2001).
- ²⁴S. A. Krzeczowski, "Measurement of liquid droplet disintegration mechanisms," *Int. J. Multiphase Flow* **6**(3), 227–239 (1980).
- ²⁵L.-P. Hsiang and G. M. Faeth, "Drop deformation and breakup due to shock wave and steady disturbances," *Int. J. Multiphase Flow* **21**(4), 545–560 (1995).
- ²⁶W. H. Chou, L. P. Hsiang, and G. M. Faeth, "Temporal properties of drop breakup in the shear breakup regime," *Int. J. Multiphase Flow* **23**(4), 651–669 (1997).

- ²⁷X. Cao, Z. Sun, W. Li *et al.*, “A new breakup regime of liquid drops identified in a continuous and uniform air jet flow,” *Phys. Fluids* **19**(5), 057103 (2007).
- ²⁸S. S. Jain, N. Tyagi, R. S. Prakash, R. V. Ravikrishna, and G. Tomar, “Secondary breakup of drops at moderate Weber numbers: Effect of density ratio and Reynolds number,” *Int. J. Multiphase Flow* **117**, 25–41 (2019).
- ²⁹P. D. Patel and T. G. Theofanous, “Hydrodynamic fragmentation of drops,” *J. Fluid Mech.* **103**, 207–223 (1981).
- ³⁰G. Ciccarelli and D. L. Frost, “Fragmentation mechanisms based on single drop steam explosion experiments using flash X-ray radiography,” *Nucl. Eng. Des.* **146**(1–3), 109–132 (1994).
- ³¹H. Ó. Haraldsson, H. X. Li, Z. L. Yang, T. N. Dinh, and B. R. Sehgal, “Effect of solidification on drop fragmentation in liquid-liquid media,” *Heat Mass. Transfer Stoffuebertrag.* **37**(4–5), 417–426 (2001).
- ³²S. Thakre and W. Ma, “3D simulations of the hydrodynamic deformation of melt droplets in a water pool,” *Ann. Nucl. Energy* **75**, 123–131 (2015).
- ³³N. Kourayem, E. Q. Li, and S. T. Thoroddsen, “Formation of microbeads during vapor explosions of Field’s metal in water,” *Phys. Rev. E* **93**(6), 063108 (2016).
- ³⁴H. E. Wolfe and W. H. Andersen, *Kinetics, Mechanism, and Resultant Droplet Sizes of the Aerodynamic Breakup of Liquid Drops* (Aerojet-General Corp., Downey, CA, 1964).
- ³⁵L. P. Hsiang and G. M. Faeth, “Near-limit drop deformation and secondary breakup,” *Int. J. Multiphase Flow* **18**(5), 635–652 (1992).
- ³⁶M. Arienti, M. Ballard, M. Sussman *et al.*, “Comparison of simulation and experiments for multimode aerodynamic breakup of a liquid metal column in a shock-induced cross-flow,” *Phys. Fluids* **31**(8), 082110 (2019).
- ³⁷T. Hopfes, J. Petersen, Z. Wang, M. Giglmaier, and N. A. Adams, “Secondary atomization of liquid metal droplets at moderate Weber numbers,” *Int. J. Multiphase Flow* **143**, 103723 (2021).
- ³⁸H. Guleryuz and H. Cimenoglu, “Oxidation of Ti–6Al–4V alloy,” *J. Alloys Compd.* **472**(1–2), 241–246 (2009).
- ³⁹A. Lipchitz, L. Laurent, and G. D. Harvel, “Suitability of eutectic Field’s metal for use in an electromagnetically-enhanced experimental two-phase flow loop,” in *ICONE20-POWER2012* (American Society of Mechanical Engineers, 2012), pp. 51–58.
- ⁴⁰Z. Wang, T. Hopfes, M. Giglmaier, and N. A. Adams, “Effect of Mach number on droplet aerobreakup in shear stripping regime,” *Exp. Fluids* **61**(9), 193 (2020).
- ⁴¹Z. Wang, T. Hopfes, M. Giglmaier, and N. A. Adams, “Experimental investigation of shock-induced tandem droplet breakup,” *Phys. Fluids* **33**(1), 012113 (2021).
- ⁴²M. Hadj-Achour, N. Rimbart, S. Castrillon-Escobar, and M. Gradeck, “A study of liquid-liquid secondary fragmentation with solidification,” in *Proceedings ICLASS–2015* (Universitat Politècnica València, Taiwan, 2015).
- ⁴³A. Lipchitz, T. Imbert, and G. D. Harvel, “Investigation of fluid dynamic properties of liquid Field’s metal,” in *Proceedings of the ASME 2013 Power Conference, POWER2013* (American Society of Mechanical Engineers, 2013), pp. 1–9.
- ⁴⁴A. Lipchitz, G. Harvel, and T. Sunagawa, “Experimental investigation of the thermal conductivity and viscosity of liquid In–Bi–Sn eutectic alloy (Field’s metal) for use in a natural circulation experimental loop,” in *Proceedings of the International Conference on Nuclear Engineering* (2015).
- ⁴⁵S. C. Escobar, “Instabilité et dispersion de jets de corium liquides: Analyse des processus physiques et modélisation dans le logiciel MC3D,” Doctoral dissertation (Université de Lorraine, 2016).
- ⁴⁶J. D. Berry, M. J. Neeson, R. R. Dagastine, D. Y. C. Chan, and R. F. Tabor, “Measurement of surface and interfacial tension using pendant drop tensiometry,” *J. Colloid Interface Sci.* **454**, 226–237 (2015).
- ⁴⁷M. Wegener, L. Muhmood, S. Sun, and A. V. Deev, “Surface tension measurements of calcia-alumina slags: A comparison of dynamic methods,” *Metall. Mater. Trans. B* **46**(1), 316–327 (2015).
- ⁴⁸J. M. Andreas, E. A. Hauser, and W. B. Tucker, “Boundary tension by pendant drops,” *J. Phys. Chem.* **42**(7), 1001–1019 (1938).
- ⁴⁹F. K. Hansen and G. Rødsrud, “Surface tension by pendant drop. I. A fast standard instrument using computer image analysis,” *J. Colloid Interface Sci.* **141**(1), 1–9 (1991).
- ⁵⁰J. Kim, H. Schoeller, J. Cho, and S. Park, “Effect of oxidation on indium solderability,” *J. Electron. Mater.* **37**(4), 483–489 (2008).
- ⁵¹L. Leontie, M. Caraman, M. Alexe, and C. Harnagea, “Structural and optical characteristics of bismuth oxide thin films,” *Surf. Sci.* **507510**, 480–485 (2002).
- ⁵²H. Li, S. Mei, L. Wang, Y. Gao, and J. Liu, “Splashing phenomena of room temperature liquid metal droplet striking on the pool of the same liquid under ambient air environment,” *Int. J. Heat Fluid Flow* **47**, 1–8 (2014).
- ⁵³T. Liu, P. Sen, and C. J. Kim, “Characterization of nontoxic liquid-metal alloy galinstan for applications in microdevices,” *J. Microelectromech. Syst.* **21**(2), 443–450 (2012).
- ⁵⁴M. D. Dickey, “Emerging applications of liquid metals featuring surface oxides,” *ACS Appl. Mater. Interfaces* **6**(21), 18369–18379 (2014).
- ⁵⁵A. A. Ranger and J. A. Nicholls, “Aerodynamic shattering of liquid drops,” *AIAA J.* **7**(2), 285–290 (1969).
- ⁵⁶H. Zhao, H. Liu, W. Li, and J. Xu, “Morphological classification of low viscosity drop bag breakup in a continuous air jet stream,” *Phys. Fluids* **22**(11), 114103 (2010).
- ⁵⁷J. Kim, J. K. Lee, and K. M. Lee, “Accurate image super-resolution using very deep convolutional networks,” in *2016 IEEE Conference on Computer Vision and Pattern Recognition (CVPR)* (IEEE, 2016), pp. 1646–1654.
- ⁵⁸N. N. Greenwood and A. Earnshaw, *Chemistry of the Elements* (Elsevier, 2012).
- ⁵⁹N. Ciftci, N. Ellendt, G. Coulthard, E. Soares Barreto, L. Mädler, and V. Uhlenwinkel, “Novel cooling rate correlations in molten metal gas atomization,” *Metall. Mater. Trans. B* **50**(2), 666–677 (2019).
- ⁶⁰T. Daeneke, K. Khoshmanesh, N. Mahmood *et al.*, “Liquid metals: Fundamentals and applications in chemistry,” *Chem. Soc. Rev.* **47**(11), 4073–4111 (2018).
- ⁶¹S. Markus, U. Fritsching, and K. Bauckhage, “Jet break up of liquid metal in twin fluid atomisation,” *Mater. Sci. Eng. A* **326**(1), 122–133 (2002).
- ⁶²J. Mi, R. S. Figliola, and I. E. Anderson, “A numerical investigation of gas flow effects on high-pressure gas atomization due to melt tip geometry variation,” *Metall. Mater. Trans. B* **28**(5), 935–941 (1997).
- ⁶³K. Hanthanan Arachchilage, M. Haghshenas, S. Park *et al.*, “Numerical simulation of high-pressure gas atomization of two-phase flow: Effect of gas pressure on droplet size distribution,” *Adv. Powder Technol.* **30**(11), 2726–2732 (2019).
- ⁶⁴S. P. Mates, S. D. Ridder, F. S. Biancaniello, and T. Zahrah, “Vacuum-assisted gas atomization of liquid metal,” *Atomization Sprays* **22**(7), 581–601 (2012).
- ⁶⁵N. Zeoli and S. Gu, “Computational simulation of metal droplet break-up, cooling and solidification during gas atomisation,” *Comput. Mater. Sci.* **43**(2), 268–278 (2008).
- ⁶⁶J. S. Thompson, O. Hassan, S. A. Rolland, and J. Sienz, “The identification of an accurate simulation approach to predict the effect of operational parameters on the particle size distribution (PSD) of powders produced by an industrial close-coupled gas atomiser,” *Powder Technol.* **291**, 75–85 (2016).
- ⁶⁷M. R. Ridolfi and P. Folgarait, “Numerical modeling of secondary breakup in molten metals gas-atomization using dimensionless analysis,” *Int. J. Multiphase Flow* **132**, 103431 (2020).
- ⁶⁸E. Villermaux and B. Bossa, “Single-drop fragmentation determines size distribution of raindrops,” *Nat. Phys.* **5**(9), 697–702 (2009).
- ⁶⁹D. D. Joseph, J. Belanger, and G. Beavers, “Breakup of a liquid drop suddenly exposed to a high speed airstream,” *Int. J. Multiphase Flow* **25**, 1263–1303 (1999).
- ⁷⁰T. G. Theofanous, G. J. Li, and T. N. Dinh, “Aerobreakup in rarefied supersonic gas flows,” *J. Fluids Eng.* **126**(4), 516 (2004).

Appendix B

Copyright permissions for reproduced material

ELSEVIER LICENSE
TERMS AND CONDITIONS

Dec 04, 2021

This Agreement between TUM, Chair of Aerodynamics and Fluid Mechanics -- Thomas Hopfes ("You") and Elsevier ("Elsevier") consists of your license details and the terms and conditions provided by Elsevier and Copyright Clearance Center.

License Number	5202081097740
License date	Dec 04, 2021
Licensed Content Publisher	Elsevier
Licensed Content Publication	International Journal of Multiphase Flow
Licensed Content Title	Temporal properties of secondary drop breakup in the multimode breakup regime
Licensed Content Author	Z. Dai,G.M. Faeth
Licensed Content Date	Feb 1, 2001
Licensed Content Volume	27
Licensed Content Issue	2
Licensed Content Pages	20
Start Page	217
End Page	236
Type of Use	reuse in a thesis/dissertation
Portion	figures/tables/illustrations

Number of figures/tables/illustrations	1
Format	both print and electronic
Are you the author of this Elsevier article?	No
Will you be translating?	No
Title	Investigation of Bubble Collapse and Metal Droplet Breakup by Shock Tube Experiments
Institution name	Chair of Aerodynamics and Fluid Mechanics, Technical University of Munich
Expected presentation date	Apr 2022
Portions	Images of Fig. 1
	TUM, Chair of Aerodynamics and Fluid Mechanics Boltzmannstr. 15
Requestor Location	Garching bei München, 85748 Germany Attn: TUM, Chair of Aerodynamics and Fluid Mechanics
Publisher Tax ID	GB 494 6272 12
Total	0.00 EUR
Terms and Conditions	

INTRODUCTION

1. The publisher for this copyrighted material is Elsevier. By clicking "accept" in connection with completing this licensing transaction, you agree that the following terms and conditions apply to this transaction (along with the Billing and Payment terms and conditions established by Copyright Clearance Center, Inc. ("CCC"), at the time that you opened your Rightslink account and that are available at any time at <http://myaccount.copyright.com>).

GENERAL TERMS

Bibliography

- [1] Aalburg, C., Van Leer, B., and Faeth, G. M. “Deformation and Drag Properties of Round Drops Subjected to Shock-Wave Disturbances”. In: *AIAA Journal* 41.12 (2003), pp. 2371–2378. ISSN: 00011452. DOI: 10.2514/2.6862. URL: <https://doi.org/10.2514/2.6862>.
- [2] Abernethy, R. B., Benedict, R. P., and Dowdell, R. B. “Asme Measurement Uncertainty.” In: *American Society of Mechanical Engineers (Paper)* 107.83 (1983). ISSN: 04021215.
- [3] Alexiou, A. “Soot formation in shock-tube pyrolysis of toluene, toluene-methanol, toluene-ethanol, and toluene-oxygen mixtures”. In: *Combustion and Flame* 104.1-2 (Jan. 1996), pp. 51–65. ISSN: 00102180. DOI: 10.1016/0010-2180(95)00004-6. URL: <https://linkinghub.elsevier.com/retrieve/pii/0010218095000046>.
- [4] Anderson, I. E., White, E. M., and Dehoff, R. “Feedstock powder processing research needs for additive manufacturing development”. In: *Current Opinion in Solid State and Materials Science* 22.1 (2018), pp. 8–15. ISSN: 13590286. DOI: 10.1016/j.cossms.2018.01.002. URL: <https://doi.org/10.1016/j.cossms.2018.01.002>.
- [5] Anderson, J. D. *Modern compressible flow: with historical perspective*. Vol. 12. McGraw-Hill New York, 1990.
- [6] Andreas, J. M., Hauser, E. A., and Tucker, W. B. “Boundary tension by pendant drops”. In: *Journal of Physical Chemistry* 42.7 (1938), pp. 1001–1019. ISSN: 00223654. DOI: 10.1021/j100903a002.
- [7] Antipas, G. “Gas atomization of aluminium melts: Comparison of analytical models”. In: *Metals* 2.2 (2012), pp. 202–210. ISSN: 20754701. DOI: 10.3390/met2020202.
- [8] Arienti, M., Ballard, M., Sussman, M., Mazumdar, Y. C., Wagner, J. L., Farias, P. A., and Guildenbecher, D. R. “Comparison of simulation and experiments for multimode aerodynamic breakup of a liquid metal column in a shock-induced cross-flow”. In: *Physics of Fluids* 31.8 (Aug. 2019), p. 082110. ISSN: 1070-6631. DOI: 10.1063/1.5099589. URL: <https://doi.org/10.1063/1.5099589> <http://aip.scitation.org/doi/10.1063/1.5099589>.
- [9] Ashgriz, N. *Handbook of Atomization and Sprays*. Ed. by Ashgriz, N. Boston, MA: Springer US, 2011. ISBN: 978-1-4419-7263-7. DOI: 10.1007/978-1-4419-7264-4. URL: <http://link.springer.com/10.1007/978-1-4419-7264-4>.
- [10] Bauckhage, K. “Das Zerstäuben metallischer Schmelzen”. In: *Chemie Ingenieur Technik* 64.4 (1992), pp. 322–332. ISSN: 15222640. DOI: 10.1002/cite.330640404.
- [11] Bazilevskii, A. V., Meier, D. D., and Rozhkov, A. N. “Dynamics of a Spherical Microcavity in a Polymeric Liquid”. In: *Fluid Dynamics* 38.3 (2003), pp. 351–362.
- [12] Beig, S. A., Aboulhasanzadeh, B., and Johnsen, E. “Temperatures produced by inertially collapsing bubbles near rigid surfaces”. In: *Journal of Fluid Mechanics* 852 (2018), pp. 105–125. ISSN: 14697645. DOI: 10.1017/jfm.2018.525.

- [13] Ben-Dor, G., Britan, A., Elperin, T., Igra, O., and Jiang, J. P. “Experimental investigation of the interaction between weak shock waves and granular layers”. In: *Experiments in Fluids* 22.5 (1997), pp. 432–443. ISSN: 07234864. DOI: 10.1007/s003480050069.
- [14] Ben-Dor, G. and Glass, I. I. “Domains and boundaries of non-stationary oblique shock-wave reflexions. 2. Monatomic gas”. In: *Journal of Fluid Mechanics* 96.4 (1980), pp. 735–756. ISSN: 14697645. DOI: 10.1017/S0022112080002339.
- [15] Benjamin, T. B. and Ellis, A. T. “The Collapse of Cavitation Bubbles and the Pressures thereby Produced against Solid Boundaries”. In: *Philosophical Transactions of the Royal Society A: Mathematical, Physical and Engineering Sciences* 260.1110 (1966), pp. 221–240. ISSN: 1364-503X. DOI: 10.1098/rsta.1966.0046. URL: <http://rsta.royalsocietypublishing.org/cgi/doi/10.1098/rsta.1966.0046>.
- [16] Beylich, A. E. and Gülhan, A. “On the structure of nonlinear waves in liquids with gas bubbles”. In: *Physics of Fluids A: Fluid Dynamics* 2.8 (1990), p. 1412. ISSN: 08998213. DOI: 10.1063/1.857590. URL: <http://scitation.aip.org/content/aip/journal/pofa/2/8/10.1063/1.857590>.
- [17] Biasiori-Poulanges, L. and El-Rabii, H. “High-magnification shadowgraphy for the study of drop breakup in a high-speed gas flow”. In: *Optics Letters* 44.23 (2019), p. 5884. ISSN: 0146-9592. DOI: 10.1364/ol.44.005884.
- [18] Blackman, V. “Vibrational relaxation in oxygen and nitrogen”. In: *Journal of Fluid Mechanics* 1.1 (1956), pp. 61–85. ISSN: 14697645. DOI: 10.1017/S0022112056000056.
- [19] Bleakney, W., Weimer, D. K., and Fletcher, C. H. “The shock tube: A facility for investigations in fluid dynamics”. In: *Review of Scientific Instruments* 20.11 (1949), pp. 807–815. ISSN: 00346748. DOI: 10.1063/1.1741395.
- [20] Bourne, N. K. and Field, J. E. “Shock-induced collapse of single cavities in liquids”. In: *Journal of Fluid Mechanics* 244 (1992), pp. 225–240. ISSN: 14697645. DOI: 10.1017/S0022112092003045.
- [21] Brekhovskikh, L. *Waves in layered media*. Vol. 16. Elsevier, 2012. ISBN: 0323161626.
- [22] Bremond, N., Arora, M., Dammer, S. M., and Lohse, D. “Interaction of cavitation bubbles on a wall”. In: *Physics of Fluids* 18.21 (2006), pp. 121505–102003. DOI: 10.1063/1.3249602. URL: <https://doi.org/10.1063/1.2396922><http://aip.scitation.org/toc/phf/18/12>.
- [23] Bremond, N., Arora, M., Ohl, C.-D., and Lohse, D. “Controlled Multibubble Surface Cavitation”. In: *Physical Review Letters* 96.22 (June 2006), p. 224501. ISSN: 0031-9007. DOI: 10.1103/PhysRevLett.96.224501. URL: <https://www.researchgate.net/publication/6982017><https://link.aps.org/doi/10.1103/PhysRevLett.96.224501>.
- [24] Brennen, C. E. *Fundamentals of Multiphase Flow*. Vol. 9780521848. January 2005. Cambridge: Cambridge University Press, Apr. 2005, pp. 1–345. ISBN: 9780521848046. DOI: 10.1017/CBO9780511807169. arXiv: arXiv:1011.1669v3. URL: <http://ebooks.cambridge.org/ref/id/CBO9780511807169><https://www.cambridge.org/core/product/identifier/9780511807169/type/book>.
- [25] Brujan, E.-a. “Cavitation Bubble Dynamics in Non-Newtonian Fluids”. In: *Polymer Engineering and Science* (2009). DOI: 10.1002/pen.
- [26] Cao, X.-k., Sun, Z.-g., Li, W.-f., Liu, H.-f., and Yu, Z.-h. “A new breakup regime of liquid drops identified in a continuous and uniform air jet flow”. In: *Physics of Fluids* 19.5 (2007). DOI: <https://doi.org/10.1063/1.2723154>.

- [27] Chaussy, C., Brendel, W., and Schmiedt, E. "Extracorporeally induced destruction of kidney stones by shock waves." In: *Lancet (London, England)* 2.8207 (Dec. 1980), pp. 1265–8. ISSN: 0140-6736.
- [28] Chen, Y., Wagner, J. L., Farias, P. A., DeMauro, E. P., and Guildenbecher, D. R. "Galinstan liquid metal breakup and droplet formation in a shock-induced cross-flow". In: *International Journal of Multiphase Flow* 106.505 (2018), pp. 147–163. ISSN: 03019322. DOI: 10.1016/j.ijmultiphaseflow.2018.05.015.
- [29] Chew, L. W., Klaseboer, E., Ohl, S. W., and Khoo, B. C. "Interaction of two differently sized oscillating bubbles in a free field". In: *Physical Review E - Statistical, Nonlinear, and Soft Matter Physics* 84.6 (2011). ISSN: 15393755. DOI: 10.1103/PhysRevE.84.066307.
- [30] Chou, W. H. and Faeth, G. M. "Temporal properties of secondary drop breakup in the bag breakup regime". In: *International Journal of Multiphase Flow* 24.6 (1998), pp. 889–912. ISSN: 03019322. DOI: 10.1016/S0301-9322(98)00015-9.
- [31] Chou, W. H., Hsiang, L. P., and Faeth, G. M. "Temporal Properties of Drop Breakup in the Shear Breakup Regime". In: *International Journal of Multiphase Flow* 23.4 (1997), pp. 651–669.
- [32] Ciccarelli, G. and Frost, D. L. "Fragmentation mechanisms based on single drop steam explosion experiments using flash X-ray radiography". In: *Nuclear Engineering and Design* 146.1-3 (1994), pp. 109–132. ISSN: 00295493. DOI: 10.1016/0029-5493(94)90324-7.
- [33] Coleman, A. and Saunders, J. "A review of the physical properties and biological effects of the high amplitude acoustic fields used in extracorporeal lithotripsy". In: *Ultrasonics* 31.2 (Jan. 1993), pp. 75–89. ISSN: 0041624X. DOI: 10.1016/0041-624X(93)90037-Z. URL: <http://www.sciencedirect.com/science/article/pii/S0041624X9390037Z>.
- [34] Cook, W. J., Presley, L. L., and Chapman, G. T. "Shock tube as a device for testing transonic airfoils at high reynolds numbers". In: *AIAA Journal* 17.7 (1979), pp. 714–721. ISSN: 00011452. DOI: 10.2514/3.61208.
- [35] Cui, P., Wang, Q. X., Wang, S. P., and Zhang, A. M. "Experimental study on interaction and coalescence of synchronized multiple bubbles". In: *Physics of Fluids* 28.1 (2016). ISSN: 10897666. DOI: 10.1063/1.4939007.
- [36] Daeneke, T., Khoshmanesh, K., Mahmood, N., De Castro, I. A., Esrafilzadeh, D., Barrow, S. J., Dickey, M. D., and Kalantar-Zadeh, K. "Liquid metals: Fundamentals and applications in chemistry". In: *Chemical Society Reviews* 47.11 (2018), pp. 4073–4111. ISSN: 14604744. DOI: 10.1039/c7cs00043j.
- [37] Dai, Z. and Faeth, G. M. "Temporal properties of secondary drop breakup in the multimode breakup regime". In: *International Journal of Multiphase Flow* 27.2 (Feb. 2001), pp. 217–236. ISSN: 03019322. DOI: 10.1016/S0301-9322(00)00015-X. URL: <http://aip.scitation.org/doi/10.1063/1.4803154%20https://linkinghub.elsevier.com/retrieve/pii/S030193220000015X>.
- [38] Davies, L. and Wilson, J. L. "Influence of reflected shock and boundary-layer interaction on shock-tube flows". In: *Physics of Fluids* 12.5 (1969). ISSN: 10706631. DOI: 10.1063/1.1692625.
- [39] Dear, J. P., Field, J. E., and Walton, a. J. "Gas compression and jet formation in cavities collapsed by a shock wave". In: *Nature* 332.6164 (1988), pp. 505–508. ISSN: 0028-0836. DOI: 10.1038/332505a0.

- [40] Dickey, M. D. “Emerging applications of liquid metals featuring surface oxides”. In: *ACS Applied Materials and Interfaces* 6.21 (2014), pp. 18369–18379. ISSN: 19448252. DOI: 10.1021/am5043017.
- [41] Dijkink, R. and Ohl, C.-D. “Laser-induced cavitation based micropump”. In: *Lab on a Chip* 8.10 (2008), p. 1676. ISSN: 1473-0197. DOI: 10.1039/b806912c. URL: <http://xlink.rsc.org/?DOI=b806912c>.
- [42] Dorschner, B., Biasiori-Poulanges, L., Schmidmayer, K., El-Rabii, H., and Colonius, T. “On the formation and recurrent shedding of ligaments in droplet aerobreakup”. In: *Journal of Fluid Mechanics* 904 (Dec. 2020), A20. ISSN: 0022-1120. DOI: 10.1017/jfm.2020.699. arXiv: 2003.00048. URL: <http://dx.doi.org/10.1017/jfm.2020.699>.
- [43] Escobar, S. C. *Instabilité et dispersion de jets de corium liquides: analyse des processus physiques et modélisation dans le logiciel MC3D*. 2016.
- [44] Firmansyah, D. A., Kaiser, R., Zahaf, R., Coker, Z., Choi, T. Y., and Lee, D. “Numerical simulations of supersonic gas atomization of liquid metal droplets”. In: *Japanese Journal of Applied Physics* 53.5 SPEC. ISSUE 3 (2014). ISSN: 13474065. DOI: 10.7567/JJAP.53.05HA09.
- [45] Fong, S. W., Adhikari, D., Klaseboer, E., and Khoo, B. C. “Interactions of multiple spark-generated bubbles with phase differences”. In: *Experiments in Fluids* 46.4 (2009), pp. 705–724. ISSN: 07234864. DOI: 10.1007/s00348-008-0603-4.
- [46] Franc, J.-P. and Michel, J.-M. *Fundamentals of cavitation*. Vol. 76. Springer science & Business media, 2006. ISBN: 1402022336.
- [47] Fujikawa, S. and Akamatsu, T. “Experimental Investigations of Cavitation Bubble Collapse by a Water Tube”. In: *Japan Society of Mechanical Engineers* 21 (1978), pp. 223–230. ISSN: 09168451.
- [48] Gel’fand, B. E., Gubin, S. A., and Kogarko, S. M. “Various forms of drop fractionation in shock waves and their special characteristics”. In: *Journal of Engineering Physics* 27.1 (July 1974), pp. 877–882. ISSN: 0022-0841. DOI: 10.1007/BF00827632. URL: <http://link.springer.com/10.1007/BF00827632>.
- [49] Glass, I. I. and Patterson, G. N. “A Theoretical and Experimental Study of Shock-Tube Flows”. In: *Journal of the Aeronautical Sciences* 22.2 (1955), pp. 73–100. DOI: 10.2514/8.3282.
- [50] Glick, H. S., Klein, J. J., and Squire, W. “Single-Pulse Shock Tube Studies of the Kinetics of the Reaction $N_2 + O_2 \rightarrow 2NO$ between 2000–3000 K”. In: *The Journal of Chemical Physics* 27.4 (Oct. 1957), pp. 850–857. ISSN: 0021-9606. DOI: 10.1063/1.1743864. URL: <http://aip.scitation.org/doi/10.1063/1.1743864>.
- [51] Grant, P. S. “Spray forming”. In: *Progress in Materials Science* 39.4-5 (1995), pp. 497–545. ISSN: 00796425. DOI: 10.1016/0079-6425(95)00004-6.
- [52] Greenwood, N. N. and Earnshaw, A. *Chemistry of the Elements*. Elsevier, 1997. ISBN: 978-0-7506-3365-9. DOI: <https://doi.org/10.1016/C2009-0-30414-6>.
- [53] Guildenbecher, D. R., López-Rivera, C., and Sojka, P. E. “Secondary atomization”. In: *Experiments in Fluids* 46.3 (Mar. 2009), pp. 371–402. ISSN: 0723-4864. DOI: 10.1007/s00348-008-0593-2. URL: <http://link.springer.com/10.1007/s00348-008-0593-2>.
- [54] Guleryuz, H. and Cimenoglu, H. “Oxidation of Ti–6Al–4V alloy”. In: *Journal of Alloys and Compounds* 472.1-2 (Mar. 2009), pp. 241–246. ISSN: 09258388. DOI: 10.1016/j.jallcom.2008.04.024. URL: <https://linkinghub.elsevier.com/retrieve/pii/S0925838808006609>.

- [55] Haas, J.-F. and Sturtevant, B. “Interaction of weak shock waves with cylindrical and spherical gas inhomogeneities”. In: *Journal of Fluid Mechanics* 181.-1 (Sept. 1987), p. 41. ISSN: 0022-1120. DOI: 10.1017/S0022112087002003. URL: http://www.journals.cambridge.org/abstract%7B%5C_%7DS0022112087002003.
- [56] Hadj-Achour, M., Rimbart, N., Castrillon-Escobar, S., and Gradeck, M. “A Study of Liquid-Liquid Secondary Fragmentation with Solidification”. In: *Proceedings ICLASS-2015*. August 2015. Taiwan: Universitat Politècnica València, Sept. 2015. ISBN: 9788490485804. DOI: 10.4995/ILASS2017.2017.5034. URL: <http://ocs.editorial.upv.es/index.php/ILASS/ILASS2017/paper/view/5034>.
- [57] Han, B., Köhler, K., Jungnickel, K., Mettin, R., Lauterborn, W., and Vogel, A. “Dynamics of laser-induced bubble pairs”. In: *Journal of Fluid Mechanics* 771 (2015), pp. 706–742. ISSN: 14697645. DOI: 10.1017/jfm.2015.183.
- [58] Han, J. and Tryggvason, G. “Secondary breakup of axisymmetric liquid drops. I. Acceleration by a constant body force; Mechanics of air-assisted liquid atomization”. In: *Atomization Sprays* 11.12 (1999), pp. 3650, 55–3667. URL: <http://aip.scitation.org/doi/abs/10.1063/1.870229>.
- [59] Han, J. and Tryggvason, G. “Secondary breakup of a axisymmetric liquid drops. II. Impulsive acceleration”. In: *Physics of Fluids* 13.6 (2001), pp. 1554–1565. ISSN: 10706631. DOI: 10.1063/1.1370389.
- [60] Hansen, F. K. and Rødsrud, G. “Surface tension by pendant drop. I. A fast standard instrument using computer image analysis”. In: *Journal of Colloid And Interface Science* 141.1 (1991), pp. 1–9. ISSN: 00219797. DOI: 10.1016/0021-9797(91)90296-K.
- [61] Haraldsson, H. Ó., Li, H. X., Yang, Z. L., Dinh, T. N., and Sehgal, B. R. “Effect of solidification on drop fragmentation in liquid-liquid media”. In: *Heat and Mass Transfer/Waerme- und Stoffuebertragung* 37.4-5 (2001), pp. 417–426. ISSN: 09477411. DOI: 10.1007/s002310000097.
- [62] Henderson, L. F. and Lozzi, A. “Experiments on transition of Mach reflexion”. In: *Journal of Fluid Mechanics* 68.1 (1975), pp. 139–155. ISSN: 14697645. DOI: 10.1017/S0022112075000730.
- [63] Henein, H., Uhlenwinkel, V., and Fritsching, U. *Metal Sprays and Spray Deposition*. Ed. by Henein, H., Uhlenwinkel, V., and Fritsching, U. Cham: Springer International Publishing, 2017. ISBN: 978-3-319-52687-4. DOI: 10.1007/978-3-319-52689-8. URL: <http://link.springer.com/10.1007/978-3-319-52689-8>.
- [64] Hinze, J. O. “Fundamentals of the hydrodynamic mechanism of splitting in dispersion processes”. In: *AIChE Journal* 1.3 (1955), pp. 289–295. ISSN: 15475905. DOI: 10.1002/aic.690010303.
- [65] Hopfes, T., Petersen, J., Wang, Z., Giglmaier, M., and Adams, N. “Secondary Atomization of Liquid Metal Droplets at Moderate Weber Numbers”. In: *International Journal of Multiphase Flow* 143 (Oct. 2021), p. 103723. ISSN: 03019322. DOI: 10.1016/j.ijmultiphaseflow.2021.103723. URL: <https://linkinghub.elsevier.com/retrieve/pii/S0301932221001713>.
- [66] Hopfes, T., Wang, Z., Giglmaier, M., and Adams, N. A. “Experimental investigation of droplet breakup of oxide-forming liquid metals”. In: *Physics of Fluids* 33.10 (Oct. 2021), p. 102114. ISSN: 1070-6631. DOI: 10.1063/5.0064178. URL: <https://aip.scitation.org/doi/10.1063/5.0064178>.

- [67] Hopfes, T. *Auslegung und Programmierung der Steuerungs- und Messtechnik für die Durchführung von Überschallexperimenten am Stoßrohr des AER*. Tech. rep. Technical University of Munich, 2016.
- [68] Hopfes, T., Wang, Z., Giglmaier, M., and Adams, N. A. “Collapse dynamics of bubble pairs in gelatinous fluids”. In: *Experimental Thermal and Fluid Science* 108.May (2019), pp. 104–114. ISSN: 08941777. DOI: 10.1016/j.expthermflusci.2019.05.023. URL: <https://doi.org/10.1016/j.expthermflusci.2019.05.023>.
- [69] Hornung, H. G., Oertel, H., and Sandeman, R. J. “Transition to Mach reflexion of shock waves in steady and pseudosteady flow with and without relaxation”. In: *Journal of Fluid Mechanics* 90.3 (1979), pp. 541–560. ISSN: 14697645. DOI: 10.1017/S002211207900238X.
- [70] Hornung, H. and Taylor, D. J. R. “Transition from regular to Mach reflection of shock waves Part 1. The effect of viscosity in the pseudosteady case”. In: *Journal of Fluid Mechanics* 123 (1982), pp. 143–153.
- [71] Hornung, H., Sturtevant, B., Belanger, J., Sanderson, S., Brouillette, M., and Jenkins, M. “Performance data of the new free-piston shock tunnel T5 at GALCIT”. In: *Shock Waves*. Springer, 1992, pp. 603–610.
- [72] Hsiang, L. P. and Faeth, G. M. “Near-limit drop deformation and secondary breakup”. In: *International Journal of Multiphase Flow* 18.5 (1992), pp. 635–652. ISSN: 03019322. DOI: 10.1016/0301-9322(92)90036-G.
- [73] Hsiang, L. P. and Faeth, G. M. “Drop Deformation and Breakup due to Shock Wave and Steady Disturbances”. In: *International Journal of Multiphase Flow* 21.4 (Aug. 1995), pp. 545–560. ISSN: 0301-9322. DOI: 10.1016/0301-9322(94)00095-2. URL: <https://www.sciencedirect.com/science/article/pii/0301932294000952>.
- [74] Igra, D. and Takayama, K. “Investigation of Aerodynamic Breakup of a Cylindrical Water Droplet”. In: *Atomization and Sprays* 11.2 (2001), p. 20. ISSN: 1044-5110. DOI: 10.1615/AtomizSpr.v11.i2.50. URL: <http://www.dl.begellhouse.com/journals/6a7c7e10642258cc,02b3b3196bd0e2a7,3de535e93ce621fb.html>.
- [75] Igra, O. and Takayama, K. “Shock tube study of the drag coefficient of a sphere in a nonstationary flow”. In: *Shock Waves*. Vol. 442. 1915. Berlin, Heidelberg: Springer Berlin Heidelberg, 1993, pp. 491–497. DOI: 10.1007/978-3-642-77648-9_77. URL: http://link.springer.com/10.1007/978-3-642-77648-9%7B%5C_%7D77.
- [76] Jackiw, I. M. and Ashgriz, N. “On aerodynamic droplet breakup”. In: *Journal of Fluid Mechanics* 913.A33 (2021), pp. 1–46. DOI: <https://doi.org/10.1017/jfm.2021.7>. URL: <https://www.cambridge.org/core/journals/journal-of-fluid-mechanics/article/on-aerodynamic-droplet-breakup/08FAF615A2CA46C828C0732A12D2D203>.
- [77] Jain, M., Prakash, R. S., Tomar, G., and Ravikrishna, R. V. “Secondary breakup of a drop at moderate Weber numbers”. In: *Proceedings of the Royal Society A: Mathematical, Physical and Engineering Sciences* 471.2177 (2015). ISSN: 14712946. DOI: 10.1098/rspa.2014.0930.
- [78] Jain, S. S., Tyagi, N., Prakash, R. S., Ravikrishna, R. V., and Tomar, G. “Secondary breakup of drops at moderate Weber numbers: Effect of Density ratio and Reynolds number”. In: *International Journal of Multiphase Flow* 117 (2019), pp. 25–41. ISSN: 03019322. DOI: 10.1016/j.ijmultiphaseflow.2019.04.026. arXiv: 1803.02989. URL: <https://doi.org/10.1016/j.ijmultiphaseflow.2019.04.026>.
- [79] Jalaal, M. and Mehravaran, K. “Transient growth of droplet instabilities in a stream”. In: *Physics of Fluids* 26.1 (2014). ISSN: 10897666. DOI: 10.1063/1.4851056.

- [80] Jeong, S. H., Hjort, K., and Wu, Z. “Tape transfer atomization patterning of liquid alloys for microfluidic stretchable wireless power transfer”. In: *Scientific Reports* 5 (2015), p. 8419. ISSN: 20452322. DOI: 10.1038/srep08419.
- [81] Johnsen, E. and Colonius, T. “Numerical simulations of non-spherical bubble collapse”. In: *Journal of Fluid Mechanics* 629 (2009), pp. 231–262. ISSN: 00221120. DOI: 10.1017/S0022112009006351.
- [82] Joseph, D. D., Beavers, G. S., and Funada, T. “Rayleigh-Taylor instability of viscoelastic drops at high weber numbers”. In: *Journal of Fluid Mechanics* 453.1992 (2002), pp. 109–132. ISSN: 00221120. DOI: 10.1017/S0022112001006802.
- [83] Joseph, D. D., Belanger, J., and Beavers, G. “Breakup of a liquid drop suddenly exposed to a high speed airstream”. In: *International Journal of Multiphase Flow* 25 (1999), pp. 1263–1303. ISSN: 03019322. DOI: 10.1016/S0301-9322(99)00043-9.
- [84] Kaiser, J., Winter, J., Adami, S., and Adams, N. “Investigation of interface deformation dynamics during high-Weber number cylindrical droplet breakup”. In: *International Journal of Multiphase Flow* 132 (Nov. 2020), p. 103409. ISSN: 03019322. DOI: 10.1016/j.ijmultiphaseflow.2020.103409. URL: <https://linkinghub.elsevier.com/retrieve/pii/S0301932220305188>.
- [85] Kékesi, T., Amberg, G., and Prahl Wittberg, L. “Drop deformation and breakup”. In: *International Journal of Multiphase Flow* 66.June (2014), pp. 1–10. ISSN: 03019322. DOI: 10.1016/j.ijmultiphaseflow.2014.06.006. URL: <http://dx.doi.org/10.1016/j.ijmultiphaseflow.2014.06.006>.
- [86] Kewley, D. J. and Hornung, H. G. “Free-piston shock-tube study of nitrogen dissociation”. In: *Chemical Physics Letters* 25.4 (1974), pp. 531–536. ISSN: 00092614. DOI: 10.1016/0009-2614(74)85360-1.
- [87] Khosla, S. and Smith, C. “Detailed Understanding of Drop Atomization by Gas Cross-flow Using the Volume of Fluid Method”. In: *ILASS Americas* May (2006).
- [88] Kim, J., Lee, J. K., and Lee, K. M. “Accurate Image Super-Resolution Using Very Deep Convolutional Networks”. In: *2016 IEEE Conference on Computer Vision and Pattern Recognition (CVPR)*. IEEE, June 2016, pp. 1646–1654. ISBN: 978-1-4673-8851-1. DOI: 10.1109/CVPR.2016.182. URL: <http://ieeexplore.ieee.org/document/7780551/>.
- [89] Koch, M., Lechner, C., Reuter, F., Köhler, K., Mettin, R., and Lauterborn, W. “Numerical modeling of laser generated cavitation bubbles with the finite volume and volume of fluid method, using OpenFOAM”. In: *Computers and Fluids* 126.November 2015 (2016), pp. 71–90. ISSN: 00457930. DOI: 10.1016/j.compfluid.2015.11.008.
- [90] Kocourek, V., Karcher, C., Conrath, M., and Schulze, D. “Stability of liquid metal drops affected by a high-frequency magnetic field”. In: *Physical Review E - Statistical, Nonlinear, and Soft Matter Physics* 74.2 (2006), pp. 1–7. ISSN: 15393755. DOI: 10.1103/PhysRevE.74.026303.
- [91] Kodama, T., Takayama, K., and Nagayasu, N. “The dynamics of two air bubbles loaded by an underwater shock wave”. In: *Journal of Applied Physics* 80.10 (1996), pp. 5587–5592. ISSN: 00218979. DOI: 10.1063/1.363605.
- [92] Kodama, T. and Tomita, Y. “Cavitation bubble behavior and bubble-shock wave interaction near a gelatin surface as a study of in vivo bubble dynamics”. In: *Applied Physics B: Lasers and Optics* 70.1 (Jan. 2000), pp. 139–149. ISSN: 0946-2171. DOI: 10.1007/s003400050022. URL: <http://link.springer.com/10.1007/s003400050022>.

- [93] Kooiman, K., Vos, H. J., Versluis, M., and Jong, N. de. "Acoustic behavior of microbubbles and implications for drug delivery". In: *Advanced Drug Delivery Reviews* 72 (June 2014), pp. 28–48. ISSN: 0169409X. DOI: 10.1016/j.addr.2014.03.003.
- [94] Koukouvinis, P., Gavaises, M., Supponen, O., and Farhat, M. "Numerical simulation of a collapsing bubble subject to gravity". In: *Physics of Fluids* 28.3 (2016). ISSN: 10897666. DOI: 10.1063/1.4944561. URL: <http://dx.doi.org/10.1063/1.4944561>.
- [95] Kouraytem, N., Li, E. Q., and Thoroddsen, S. T. "Formation of microbeads during vapor explosions of Field's metal in water". In: *Physical Review E* 93.6 (2016), pp. 4–9. ISSN: 24700053. DOI: 10.1103/PhysRevE.93.063108.
- [96] Krzeczkowski, S. A. "Measurement of liquid droplet disintegration mechanisms". In: *International Journal of Multiphase Flow* 6.3 (1980), pp. 227–239. ISSN: 03019322. DOI: 10.1016/0301-9322(80)90013-0.
- [97] Kulkarni, V. and Sojka, P. E. "Bag breakup of low viscosity drops in the presence of a continuous air jet". In: *Physics of Fluids* 26.7 (2014). ISSN: 10897666. DOI: 10.1063/1.4887817.
- [98] Kuntz, D. W. and Payne, J. L. "Simulation of powder metal fabrication with high pressure gas atomization". In: *Advances in Powder Metallurgy and Particulate Materials* 1 (1995). ISSN: 10428860.
- [99] Kuznetsov, V. V., Nakoryakov, V. E., Pokusaev, B. G., and Shreiber, I. R. "Propagation of perturbations in a gas-liquid mixture". In: *Journal of Fluid Mechanics* 85.1 (1978), pp. 85–96. ISSN: 14697645. DOI: 10.1017/S0022112078000543.
- [100] Lagutkin, S., Achelis, L., Sheikhaliev, S., Uhlenwinkel, V., and Srivastava, V. "Atomization process for metal powder". In: *Materials Science and Engineering A* 383.1 SPEC. ISS. (2004), pp. 1–6. ISSN: 09215093. DOI: 10.1016/j.msea.2004.02.059.
- [101] Lane, W. R. "Shatter of Drops in Streams of Air". In: *Industrial & Engineering Chemistry* 43.6 (1951), pp. 1312–1317. ISSN: 0019-7866. DOI: 10.1021/ie50498a022.
- [102] Lauterborn, W. "Cavitation and coherent optics". In: *Cavitation and inhomogeneities in underwater acoustics*. Springer, 1980, pp. 3–12.
- [103] Lauterborn, W. and Hentschel, W. "Cavitation bubble dynamics studied by high speed photography and holography: part one". In: *Ultrasonics* 23.6 (Nov. 1985), pp. 260–268. ISSN: 0041624X. DOI: 10.1016/0041-624X(85)90048-4. URL: <http://linkinghub.elsevier.com/retrieve/pii/0041624X85900484>.
- [104] Lauterborn, W. and Kurz, T. "Physics of bubble oscillations". In: *Reports on Progress in Physics* 73.10 (Oct. 2010), p. 106501. ISSN: 0034-4885. DOI: 10.1088/0034-4885/73/10/106501. URL: <https://iopscience.iop.org/article/10.1088/0034-4885/73/10/106501>.
- [105] Lee, C. H. and Reitz, R. D. "An experimental study of the effect of gas density on the distortion and breakup mechanism of drops in high speed gas stream". In: *International Journal of Multiphase Flow* 26.2 (2000), pp. 229–244. ISSN: 03019322. DOI: 10.1016/S0301-9322(99)00020-8.
- [106] Leitner, M., Leitner, T., Schmon, A., Aziz, K., and Pottlacher, G. "Thermophysical Properties of Liquid Aluminum". In: *Metallurgical and Materials Transactions A: Physical Metallurgy and Materials Science* 48.6 (2017), pp. 1–10. ISSN: 10735623. DOI: 10.1007/s11661-017-4053-6.
- [107] Lew, K. S. F., Klaseboer, E., and Khoo, B. C. "A collapsing bubble-induced micropump: An experimental study". In: *Sensors and Actuators, A: Physical* 133.1 (2007), pp. 161–172. ISSN: 09244247. DOI: 10.1016/j.sna.2006.03.023.

- [108] Li, H., Mei, S., Wang, L., Gao, Y., and Liu, J. “Splashing phenomena of room temperature liquid metal droplet striking on the pool of the same liquid under ambient air environment”. In: *International Journal of Heat and Fluid Flow* 47 (2014), pp. 1–8. ISSN: 0142727X. DOI: 10.1016/j.ijheatfluidflow.2014.02.002.
- [109] Lifshitz, A. and Tsang, W. “Shock Tube Techniques in Chemical Kinetics”. In: *An. Rev. Phys. Chem.* 40 (1990), pp. 559–599.
- [110] Lipchitz, A., Harvel, G., and Sunagawa, T. “Experimental Investigation of the Thermal Conductivity and Viscosity of Liquid In-Bi-Sn Eutectic Alloy (Field’s Metal) for Use in a Natural Circulation Experimental Loop”. In: *The Proceedings of the International Conference on Nuclear Engineering (ICONE) 2015.23*. December (2015). ISSN: 2424-2934. DOI: 10.1299/jsmeicone.2015.23._ICONE23-1_440.
- [111] Lipchitz, A., Laurent, L., and Harvel, G. D. “Suitability of Eutectic Field’s Metal for Use in an Electromagnetohydrodynamically-Enhanced Experimental Two-Phase Flow Loop”. In: *ICONE20-POWER2012*. American Society of Mechanical Engineers, July 2012, pp. 51–58. ISBN: 978-0-7918-4499-1. DOI: 10.1115/ICONE20-POWER2012-54103. URL: <https://asmedigitalcollection.asme.org/ICONE/proceedings/ICONE20-POWER2012/44991/51/293371>.
- [112] Lipchitz, A., Imbert, T., and Harvel, G. D. “Investigation of Fluid Dynamic Properties of Liquid Field’s Metal”. In: *Proceedings of the ASME 2013 Power Conference, POWER2013*. American Society of Mechanical Engineers, July 2013, pp. 1–9. ISBN: 978-0-7918-5606-2. DOI: 10.1115/POWER2013-98224. URL: <https://asmedigitalcollection.asme.org/POWER/proceedings/POWER2013/56062/Boston,%20Massachusetts,%20USA/282196>.
- [113] Liu, N.-N., Zhang, A.-M., Cui, P., Wang, S.-P., and Li, S. “Interaction of two out-of-phase underwater explosion bubbles”. In: *Physics of Fluids* 33.10 (2021), p. 106103. ISSN: 1070-6631. DOI: 10.1063/5.0064164.
- [114] Liu, T., Sen, P., and Kim, C. J. “Characterization of nontoxic liquid-metal alloy galinstan for applications in microdevices”. In: *Journal of Microelectromechanical Systems* 21.2 (2012), pp. 443–450. ISSN: 10577157. DOI: 10.1109/JMEMS.2011.2174421.
- [115] Liu, Z. and Reitz, R. D. “An analysis of the distortion and breakup mechanisms of high speed liquid drops”. In: *International Journal of Multiphase Flow* 23.4 (1997), pp. 631–650. ISSN: 03019322. DOI: 10.1016/S0301-9322(96)00086-9.
- [116] Luo, J. and Niu, Z. “Jet and Shock Wave from Collapse of Two Cavitation Bubbles”. In: *Scientific Reports* 9.1 (2019), pp. 1–13. ISSN: 20452322. DOI: 10.1038/s41598-018-37868-x.
- [117] Magarvey, R. H. and Taylor, B. W. “Free fall breakup of large drops”. In: *Journal of Applied Physics* 27.10 (1956), pp. 1129–1135. ISSN: 00218979. DOI: 10.1063/1.1722216.
- [118] Mark, H. “The interaction of a reflected shock wave with the boundary layer in a shock tube”. In: (1958).
- [119] Mason, T. J. “Ultrasonic cleaning: An historical perspective”. In: *Ultrasonics Sonochemistry* 29 (Mar. 2016), pp. 519–523. ISSN: 13504177. DOI: 10.1016/j.ultsonch.2015.05.004. URL: <http://dx.doi.org/10.1016/j.ultsonch.2015.05.004%20https://linkinghub.elsevier.com/retrieve/pii/S1350417715001339>.
- [120] Mates, S. P. and Settles, G. S. “A study of liquid metal atomization using close-coupled nozzles, Part 1: Gas dynamic behavior”. In: *Atomization and Sprays* 15.1 (2005). ISSN: 1044-5110.

- [121] Medwin, H. "Counting bubbles acoustically: a review". In: *Ultrasonics* 15.1 (Jan. 1977), pp. 7–13. ISSN: 0041624X. DOI: 10.1016/0041-624X(77)90005-1. URL: <https://linkinghub.elsevier.com/retrieve/pii/0041624X77900051>.
- [122] Meng, J. C. and Colonius, T. "Numerical Simulation of the Aerobreakup of a Water Droplet". In: *Journal of Fluid Mechanics* 835 (2018), pp. 1108–1135. ISSN: 14697645. DOI: 10.1017/jfm.2017.804.
- [123] Meshkov, E. E. "Instability of the interface of two gases accelerated by a shock wave". In: *Fluid Dynamics* 4.5 (1969), pp. 101–104. ISSN: 15738507. DOI: 10.1007/BF01015969.
- [124] Miller, J. A., Mitchell, R. E., Smooke, M. D., and Kee, R. J. "Toward a comprehensive chemical kinetic mechanism for the oxidation of acetylene: Comparison of model predictions with results from flame and shock tube experiments". In: *Symposium (International) on Combustion* 19.1 (1982), pp. 181–196. ISSN: 00820784. DOI: 10.1016/S0082-0784(82)80189-6.
- [125] Morley, N. B., Burris, J., Cadwallader, L. C., and Nornberg, M. D. "GaInSn usage in the research laboratory". In: *Review of Scientific Instruments* 79.5 (2008), pp. 3–6. ISSN: 00346748. DOI: 10.1063/1.2930813.
- [126] Mott, N. F. "Fragmentation of shell cases". In: *Proceedings of the Royal Society of London. Series A. Mathematical and physical sciences* 189.1018 (1947), pp. 300–308. ISSN: 0080-4630.
- [127] Moulinet, S. and Adda-Bedia, M. "Popping Balloons: A Case Study of Dynamical Fragmentation". In: *Physical Review Letters* 115.18 (Oct. 2015), p. 184301. ISSN: 0031-9007. DOI: 10.1103/PhysRevLett.115.184301. URL: <https://link.aps.org/doi/10.1103/PhysRevLett.115.184301>.
- [128] Naudé, C. F. and Ellis, A. T. "On the Mechanism of Cavitation Damage by Nonhemispherical Cavities Collapsing in Contact With a Solid Boundary". In: *Journal of Basic Engineering* 83.4 (1961), p. 648. ISSN: 00219223. DOI: 10.1115/1.3662286.
- [129] O'Rourke, P. J. and Amsden, A. A. "The Tab Method for Numerical Calculation of Spray Droplet Breakup". In: Nov. 1987. DOI: 10.4271/872089. URL: <https://www.sae.org/content/872089/>.
- [130] Obreschkow, D., Tinguely, M., Dorsaz, N., Kobel, P., Bosset, A. de, and Farhat, M. "Universal Scaling Law for Jets of Collapsing Bubbles". In: *Physical Review Letters* 107.20 (Nov. 2011), p. 204501. ISSN: 0031-9007. DOI: 10.1103/PhysRevLett.107.204501. arXiv: arXiv:1109.6141v1. URL: <https://link.aps.org/doi/10.1103/PhysRevLett.107.204501>.
- [131] Ochiai, N., Iga, Y., Nohmi, M., and Ikohagi, T. "Numerical Analysis of Nonspherical Bubble Collapse Behavior and Induced Impulsive Pressure during First and Second Collapses near the Wall Boundary". In: *Journal of Fluid Science and Technology* 6.6 (2011), pp. 860–874. ISSN: 1880-5558. DOI: 10.1299/jfst.6.860.
- [132] Ohl, C. D. and Ikink, R. "Shock-Wave-Induced Jetting of Micron-Size Bubbles". In: *Physical Review Letters* 90.21 (May 2003), p. 214502. ISSN: 0031-9007. DOI: 10.1103/PhysRevLett.90.214502. URL: <https://link.aps.org/doi/10.1103/PhysRevLett.90.214502>.
- [133] Opfer, L., Roisman, I. V., Venzmer, J., Klostermann, M., and Tropea, C. "Droplet-air collision dynamics: Evolution of the film thickness". In: *Physical Review E* 89.1 (Jan. 2014), p. 013023. ISSN: 1539-3755. DOI: 10.1103/PhysRevE.89.013023. URL: <https://link.aps.org/doi/10.1103/PhysRevE.89.013023>.

- [134] Ortiz, C., Joseph, D. D., and Beavers, G. S. "Acceleration of a liquid drop suddenly exposed to a high-speed airstream". In: *International Journal of Multiphase Flow* 30.2 (2004), pp. 217–224. ISSN: 03019322. DOI: 10.1016/j.ijmultiphaseflow.2003.11.004.
- [135] Patel, P. D. and Theofanous, T. "Hydrodynamic fragmentation of drops". In: *Journal of Fluid Mechanics* 103 (1981), pp. 207–223. ISSN: 14697645. DOI: 10.1017/S0022112081001304.
- [136] Philipp, A., Delius, M., Scheffczyk, C., Vogel, A., and Lauterborn, W. "Interaction of lithotripter-generated shock waves with air bubbles". In: *The Journal of the Acoustical Society of America* 93.5 (1993), pp. 2496–2509. ISSN: 0001-4966. DOI: 10.1121/1.406853. URL: <http://asa.scitation.org/doi/10.1121/1.406853>.
- [137] Philipp, A. and Lauterborn, W. "Cavitation erosion by single laser-produced bubbles". In: *Journal of Fluid Mechanics* 361 (1998), pp. 75–116. ISSN: 00221120. DOI: 10.1017/S0022112098008738.
- [138] Pilch, M. and Erdman, C. A. "Use of breakup time data and velocity history data to predict the maximum size of stable fragments for acceleration-induced breakup of a liquid drop". In: *International Journal of Multiphase Flow* 13.6 (1987), pp. 741–757. ISSN: 03019322. DOI: 10.1016/0301-9322(87)90063-2.
- [139] Plesset, M. S. and Chapman, R. B. "Collapse of an initially spherical Vapor Cavity in the Neighborhood of a solid Boundary". In: *Journal of Fluid Mechanics* 47.2 (1971), pp. 283–290. ISSN: 0022-1120. DOI: 10.1017/S0022112071001058.
- [140] Qian, L., Zhong, X., Zhu, C., and Lin, J. "An experimental investigation on the secondary breakup of carboxymethyl cellulose droplets". In: *International Journal of Multiphase Flow* (Nov. 2020), p. 103526. ISSN: 03019322. DOI: 10.1016/j.ijmultiphaseflow.2020.103526. URL: <https://doi.org/10.1016/j.ijmultiphaseflow.2020.103526> <https://linkinghub.elsevier.com/retrieve/pii/S0301932220306376>.
- [141] Ranger, A. A. and Nicholls, J. A. "Aerodynamic shattering of liquid drops." In: *AIAA Journal* 7.2 (1969), pp. 285–290. ISSN: 0001-1452. DOI: 10.2514/3.5087. URL: <http://arc.aiaa.org/doi/abs/10.2514/3.5087>.
- [142] Rasthofer, U., Wermelinger, F., Hadjidakis, P., and Koumoutsakos, P. "Large Scale Simulation of Cloud Cavitation Collapse". In: *Procedia Computer Science* 108 (2017), pp. 1763–1772. ISSN: 18770509. DOI: 10.1016/j.procs.2017.05.158. URL: <http://dx.doi.org/10.1016/j.procs.2017.05.158>.
- [143] Rayleigh, L. "VIII. On the pressure developed in a liquid during the collapse of a spherical cavity". In: *Philosophical Magazine Series 6* 34.200 (Aug. 1917), pp. 94–98. ISSN: 1941-5982. DOI: 10.1080/14786440808635681. URL: <http://www.tandfonline.com/doi/abs/10.1080/14786440808635681>.
- [144] Reitz, R. D. and Diwakar, R. "Effect of Drop Breakup on Fuel Sprays". In: *SAE Technical Paper Series* 1 (1986). DOI: 10.4271/860469.
- [145] Resler, E. L., Lin, S. C., and Kantrowitz, A. "The production of high temperature gases in shock tubes". In: *Journal of Applied Physics* 23.12 (1952), pp. 1390–1399. ISSN: 00218979. DOI: 10.1063/1.1702080.
- [146] Sagar, H. J. and Moctar, O. el. "Dynamics of a cavitation bubble near a solid surface and the induced damage". In: *Journal of Fluids and Structures* 92 (2020), p. 102799. ISSN: 10958622. DOI: 10.1016/j.jfluidstructs.2019.102799. URL: <https://doi.org/10.1016/j.jfluidstructs.2019.102799>.

- [147] Sarkar, S., Sivaprasad, P. V., and Bakshi, S. “Numerical modeling and prediction of particle size distribution during gas atomization of molten tin”. In: *Atomization and Sprays* 26.1 (2016), pp. 23–51. ISSN: 10445110. DOI: 10.1615/AtomizSpr.2015011680.
- [148] Schmehl, R. “Modeling droplet breakup in complex two-phase flows”. In: *9th International Conference on Liquid Atomization and Spray Systems, ICLASS 2003 c* (2003), pp. 1–3.
- [149] Settles, G. S. *Schlieren and Shadowgraph Techniques*. Berlin, Heidelberg: Springer Berlin Heidelberg, 2001. ISBN: 978-3-642-63034-7. DOI: 10.1007/978-3-642-56640-0. URL: <http://link.springer.com/10.1007/978-3-642-56640-0>.
- [150] Stefanitsis, D., Strotos, G., Nikolopoulos, N., Kakaras, E., and Gavaises, M. “Improved droplet breakup models for spray applications”. In: *International Journal of Heat and Fluid Flow* 76. January (2019), pp. 274–286. ISSN: 0142727X. DOI: 10.1016/j.ijheatfluidflow.2019.02.010. URL: <https://doi.org/10.1016/j.ijheatfluidflow.2019.02.010>.
- [151] Swantek, A. B. and Austin, J. M. “Collapse of void arrays under stress wave loading”. In: *Journal of Fluid Mechanics* 649 (2010), pp. 399–427. ISSN: 00221120. DOI: 10.1017/S0022112009993545.
- [152] Thakre, S. and Ma, W. “3D simulations of the hydrodynamic deformation of melt droplets in a water pool”. In: *Annals of Nuclear Energy* 75 (2015), pp. 123–131. ISSN: 0306-4549. DOI: <https://doi.org/10.1016/j.anucene.2014.07.046>. URL: <http://www.sciencedirect.com/science/article/pii/S0306454914003776>.
- [153] Theofanous, T. G. and Li, G. J. “On the physics of aerobreakup”. In: *Physics of Fluids* 20.5 (2008), p. 052103. ISSN: 10706631. DOI: 10.1063/1.2907989.
- [154] Theofanous, T. G., Li, G. J., and Dinh, T. N. “Aerobreakup in Rarefied Supersonic Gas Flows”. In: *Journal of Fluids Engineering* 126.4 (2004), p. 516. ISSN: 00982202. DOI: 10.1115/1.1777234. URL: <http://fluidsengineering.asmedigitalcollection.asme.org/article.aspx?articleid=1430001>.
- [155] Theofanous, T. G., Mitkin, V. V., Ng, C. L., Chang, C.-H., Deng, X., and Sushchikh, S. “The physics of aerobreakup. II. Viscous liquids”. In: *Physics of Fluids* 24.2 (Feb. 2012), p. 022104. ISSN: 1070-6631. DOI: 10.1063/1.3680867. URL: <http://aip.scitation.org/doi/10.1063/1.3680867>.
- [156] Theofanous, T. “Aerobreakup of Newtonian and Viscoelastic Liquids”. In: *Annual Review of Fluid Mechanics* 43.1 (2011), pp. 661–690. ISSN: 0066-4189. DOI: 10.1146/annurev-fluid-122109-160638. URL: <http://www.annualreviews.org/doi/10.1146/annurev-fluid-122109-160638>.
- [157] Tiwari, A., Pantano, C., and Freund, J. B. “Growth-and-collapse dynamics of small bubble clusters near a wall”. In: *Journal of Fluid Mechanics* 775 (2015), pp. 1–23. ISSN: 14697645. DOI: 10.1017/jfm.2015.287.
- [158] Tomita, Y. and Shima, A. “Mechanisms of impulsive pressure generation and damage pit formation by bubble collapse”. In: *Journal of Fluid Mechanics* 169 (1986), pp. 535–564. ISSN: 14697645. DOI: 10.1017/S0022112086000745.
- [159] Tomita, Y., Shima, A., and Sato, K. “Dynamic behavior of two-laser-induced bubbles in water”. In: *Citation: Appl. Phys. Lett. Physics of Fluids Journal of Applied Physics* 571.67 (1990), pp. 12103–3560. DOI: 10.1063/1.345305. URL: <https://doi.org/10.1063/1.103726%20http://aip.scitation.org/toc/apl/57/3>.

- [160] Tomita, Y., Shima, A., and Ohno, T. “Collapse of multiple gas bubbles by a shock wave and induced impulsive pressure”. In: *Journal of Applied Physics* 56.125 (1984). DOI: 10.1063/1.333745. URL: <https://doi.org/10.1063/1.333745%20http://aip.scitation.org/toc/jap/56/1>.
- [161] Tranter, R. S., Brezinsky, K., and Fulle, D. “Design of a high-pressure single pulse shock tube for chemical kinetic investigations”. In: *Review of Scientific Instruments* 72.7 (2001), pp. 3046–3054. ISSN: 00346748. DOI: 10.1063/1.1379963.
- [162] Trummler, T., Schmidt, S. J., and Adams, N. A. “Numerical investigation of non-condensable gas effect on vapor bubble collapse”. In: *Physics of Fluids* 33.9 (2021). ISSN: 10897666. DOI: 10.1063/5.0062399.
- [163] Trummler, T., Bryngelson, S. H., Schmidmayer, K., Schmidt, S. J., Colonius, T., and Adams, N. A. “Near-surface dynamics of a gas bubble collapsing above a crevice”. In: *Journal of Fluid Mechanics* (2020). ISSN: 14697645. DOI: 10.1017/jfm.2020.432. arXiv: 1912.07022.
- [164] Trummler, T., Schmidt, S. J., and Adams, N. A. “Effect of stand-off distance and spatial resolution on the pressure impact of near-wall vapor bubble collapses”. In: *International Journal of Multiphase Flow* 141.1966 (2021). ISSN: 03019322. DOI: 10.1016/j.ijmultiphaseflow.2021.103618. arXiv: 2104.06298.
- [165] Ünal, A. “Liquid break-up in gas atomization of fine aluminum powders”. In: *Metallurgical Transactions B* 20.1 (1989), pp. 61–69. ISSN: 03602141. DOI: 10.1007/BF02670350.
- [166] Van der Schueren, B. and Kruth, J. “Powder deposition in selective metal powder sintering”. In: *Rapid Prototyping Journal* 1.3 (Sept. 1995), pp. 23–31. ISSN: 1355-2546. DOI: 10.1108/13552549510094241. URL: <https://www.emerald.com/insight/content/doi/10.1108/13552549510094241/full/html>.
- [167] Villermaux, E. and Bossa, B. “Single-drop fragmentation determines size distribution of raindrops”. In: *Nature Physics* 5.9 (2009), pp. 697–702. ISSN: 17452481. DOI: 10.1038/nphys1340.
- [168] Vokurka, K. “The use of a shock tube in bubble dynamics studies”. In: *Czechoslovak Journal of Physics* 42.3 (Mar. 1992), pp. 291–302. ISSN: 0011-4626. DOI: 10.1007/BF01598426. URL: <http://link.springer.com/10.1007/BF01598426>.
- [169] Wang, Z., Hopfes, T., Giglmaier, M., and Adams, N. A. “Effect of Mach number on droplet aerobreakup in shear stripping regime”. In: *Experiments in Fluids* 61.9 (2020), pp. 1–17. ISSN: 1432-1114.
- [170] Wang, Z., Giglmaier, M., Hopfes, T., Köglmeier, L., and Adams, N. A. “Impact of sensor housing geometries on transient stagnation pressure measurements in impulse facilities”. In: *Experimental Thermal and Fluid Science* 109 (Dec. 2019), p. 109851. ISSN: 08941777. DOI: 10.1016/j.expthermflusci.2019.109851. URL: <https://linkinghub.elsevier.com/retrieve/pii/S0894177719301591>.
- [171] Wegener, M., Muhmood, L., Sun, S., and Deev, A. V. “Novel high-temperature experimental setup to study dynamic surface tension phenomena in oxide melts”. In: *Industrial and Engineering Chemistry Research* 52.46 (2013), pp. 16444–16456. ISSN: 08885885. DOI: 10.1021/ie4022623.
- [172] Wierzbza, A. and Takayama, K. “Experimental investigation of the aerodynamic breakup of liquid drops”. In: *AIAA Journal* 26.11 (Nov. 1988), pp. 1329–1335. ISSN: 0001-1452. DOI: 10.2514/3.10044. URL: <http://arc.aiaa.org/doi/10.2514/3.10044>.

- [173] Wolfe, H. E. and Andersen, W. H. *Kinetics, mechanism, and resultant droplet sizes of the aerodynamic breakup of liquid drops*. Tech. rep. 1964.
- [174] Xiao, F., Wang, Z. G., Sun, M. B., Liu, N., and Yang, X. “Simulation of drop deformation and breakup in supersonic flow”. In: *Proceedings of the Combustion Institute* 36.2 (2017), pp. 2417–2424. ISSN: 15407489. DOI: 10.1016/j.proci.2016.09.016.
- [175] Xu, Z., Wang, T., and Che, Z. “Droplet deformation and breakup in shear flow of air”. In: *Physics of Fluids* 32.5 (May 2020), p. 052109. ISSN: 1070-6631. DOI: 10.1063/5.0006236. URL: <https://doi.org/10.1063/5.0006236> <http://aip.scitation.org/doi/10.1063/5.0006236>.
- [176] Yim, P. “The Role of Surface Oxidation in the Break-Up of Laminar Liquid Metal Jets”. PhD thesis. 1996. URL: <http://hdl.handle.net/1721.1/10920>.
- [177] Yuan, F., Sankin, G., and Zhong, P. “Dynamics of tandem bubble interaction in a microfluidic channel”. In: *The Journal of the Acoustical Society of America* 130.5 (Nov. 2011), pp. 3339–3346. ISSN: 0001-4966. DOI: 10.1121/1.3626134. URL: <http://asa.scitation.org/doi/10.1121/1.3626134>.
- [178] Zeoli, N. and Gu, S. “Numerical modelling of droplet break-up for gas atomisation”. In: *Computational Materials Science* 38.2 (2006), pp. 282–292. ISSN: 09270256. DOI: 10.1016/j.commatsci.2006.02.012.
- [179] Zeoli, N. and Gu, S. “Computational simulation of metal droplet break-up, cooling and solidification during gas atomisation”. In: *Computational Materials Science* 43.2 (2008), pp. 268–278. ISSN: 09270256. DOI: 10.1016/j.commatsci.2007.10.005.
- [180] Zhang, Q., Gao, Y., and Liu, J. “Atomized spraying of liquid metal droplets on desired substrate surfaces as a generalized way for ubiquitous printed electronics”. In: *Applied Physics A: Materials Science and Processing* 116.3 (2014), pp. 1091–1097. ISSN: 14320630. DOI: 10.1007/s00339-013-8191-4.
- [181] Zhang, S., Wang, S. P., and Zhang, A. M. “Experimental study on the interaction between bubble and free surface using a high-voltage spark generator”. In: *Physics of Fluids* 28.3 (2016). ISSN: 10897666. DOI: 10.1063/1.4944349.
- [182] Zhao, H., Liu, H., Li, W., and Xu, J. “Morphological classification of low viscosity drop bag breakup in a continuous air jet stream”. In: *Physics of Fluids* 22.11 (2010), p. 114103. DOI: 10.1063/1.3490408.
- [183] Zhao, H., Liu, H. F., Xu, J. L., Li, W. F., and Lin, K. F. “Temporal properties of secondary drop breakup in the bag-stamen breakup regime”. In: *Physics of Fluids* 25.5 (2013). ISSN: 10706631. DOI: 10.1063/1.4803154.
- [184] Zhao, H., Liu, H.-f., Cao, X.-k., Li, W.-f., and Xu, J.-l. “Breakup characteristics of liquid drops in bag regime by a continuous and uniform air jet flow”. In: *International Journal of Multiphase Flow* 37.5 (2011), pp. 530–534. ISSN: 0301-9322. DOI: 10.1016/j.ijmultiphaseflow.2010.12.006. URL: <http://dx.doi.org/10.1016/j.ijmultiphaseflow.2010.12.006>.
- [185] Zwaan, E., Le Gac, S., Tsuji, K., and Ohl, C.-D. “Controlled Cavitation in Microfluidic Systems”. In: *Physical Review Letters* 98.25 (June 2007), p. 254501. ISSN: 0031-9007. DOI: 10.1103/PhysRevLett.98.254501. URL: <https://link.aps.org/doi/10.1103/PhysRevLett.98.254501>.